# Tuning Spin Currents with Ultrathin Heavy Metal Microstructure

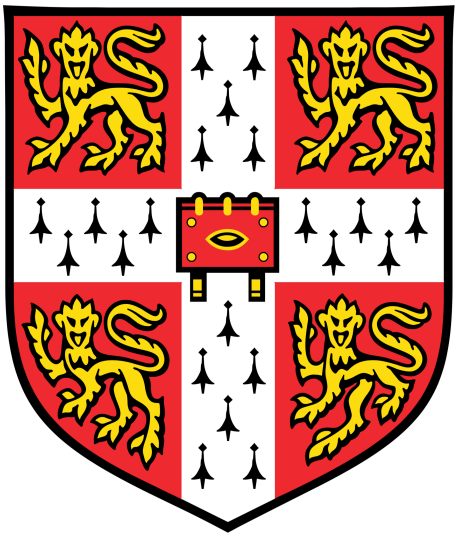


Spencer John Brennan

Department of Physics
University of Cambridge


This dissertation is submitted for the degree of
*Doctor of Philosophy*

Trinity Hall

November 2018

# Declaration

I hereby declare that except where specific reference is made to the work of others, the contents of this dissertation are original and have not been submitted in whole or in part for consideration for any other degree or qualification in this, or any other university. This dissertation is my own work and contains nothing which is the outcome of work done in collaboration with others, except as specified in the text. This dissertation contains fewer than 60,000 words including appendices, bibliography, footnotes, tables and equations, and has fewer than 150 figures.

Spencer John Brennan

November 2018

*They cannot admire you for intellect. Granted – but there are many other qualities of which you cannot say, 'but that is not the way I am made'. So display those virtues which are wholly in your own power – integrity, dignity, hard work, self-denial, contentment, frugality, kindness, independence, simplicity, discretion, magnanimity.*

Marcus Aurelius Antoninus (121 – 180 AD)

# Acknowledgements

The opportunity to study the arts, science, nature, engineering and philosophy for nearly 25 years was bestowed upon me as the greatest gift by my loving parents. Although they were not given the same chances at an early age, they had the selflessness and priority to equip me with a training that will guide me to lead a life well lived. From painfully teaching me how to read at 7 years old, driving me around the city for hockey practice, investing in my schooling and raising me as their son, they never once failed. As individuals too, I constantly look up to them. To my father for not only his despise of injustice in hope for a more equal existence amongst men, but for his heart, creativity and like-mindedness. To my mother for her courage to do whatever she aspires to, despite gender and age. And for her great sacrifice of her career to ensure a successful upbringing; for the life she gave up to be my mother and friend. Only the summed efforts of the team of us three have made this study possible.

Indeed, I owe a great debt of gratitude to those close friends around me whom I often consider to be as close as family. Aristotle said: "*In poverty as well as in other misfortunes, people suppose that friends are their only refuge. And friendship is a help … to those in their prime in performing noble actions, for 'two going together' are better able to think and to act*." For us social beings, they are the lampposts in a dark existence leading us in the right direction. The friendship, love and admiration I have for Lina and Ross makes them nothing other than family. For all the friendship I experienced on the CUIHC, I cannot imagine a life without you in it. Some of my teammates I've had the privilege to get to know more than others and here I will name the few who I was lucky enough to spend time with and what I hope to learn from their character: from Jaason Geerts, an unwavering devotion to your teammates; from Julien Gagnon, the confidence to lead a group of men; from Alan Bauer, to not rush through life, but instead direct it well; from Jeremy Reeves, the determination to do good deeds every day; from James Requeima, how to live a well-ordered life; from Patrick Gut, a pragmatic outlook on life and humility in accomplishments; from Michal Barabas, reliability and unwavering dedication to his teammates; from Oscar Wilsby, perseverance through insurmountable difficulties without guidance; from Kumaran Nathan, the self's will to be it's best at every moment; from Lucas Maddalena, the greatness in a quiet, determined soul; from Václav Beránek, a will to overcome all odds; from Cody Hanson, the loyalty in friendship, the commitment to a cause and kindness of spirit; from Cody Valdes, brotherhood and refuge in philosophy as the guide to a truly well oriented mind and soul.

And from beyond the CUIHC: from Charlie Reighard, Cristina Susanu and Clara Ceulemans, for good friends in new circumstances; from Rob Gard, to be a proponent of freedom of speech regardless of the circumstance; from Elisa Dierickx, the importance of the preservation of nature and the dedication to a just cause; from Eve Avdoulos, that true friendship is the bearer of peace and support; from Angela Wittmann, how great personal growth comes from overcoming great obstacles; from Homa Majd, the freedom in a soul which is died to the core with greatness and love for others; from Olia Zadvorna, that respect, loyalty and kindness in a soul makes for strong companionship. Especially, thank you to Tarun Vemulkar for the countless discussions with someone who commands an exceptional scientific understanding and for sharing good friendship through many dinners.

Finally, the completion of this work must be in large part credited to my supervisors Liam O'Brien and Russell Cowburn. Liam's intellectual ability to understand nature is continually astounding and his influence on both my training as a physicist and the research herein could not be overstated. I will always be especially thankful to Russell for believing in me and giving me a chance to experience "*what's in the water*" in Cambridge. Without a doubt, this has changed my life and for this opportunity, my gratitude to him knows no bounds.

# Abstract

All-metallic spintronic heterostructures have the ability to generate pure spin currents at low resistance-area products via spin-orbit coupling. Heavy metal/ferromagnet (HM/NM) bilayers are often used in this context to extract key spin-dependent parameters such as the spin Hall angle, $\theta_{SH}$, and spin diffusion length, $\lambda$, of the constituent materials. However, in the ultrathin film limit, morphology is highly sensitive to growth parameters, making consistent extraction of the spin-dependent properties challenging. Although much work has been done to study spin transport in nanodevices, a long-standing controversy in literature remains over quantifying the magnitudes of spin-dependent parameters in highly spin-orbit coupled HMs. Despite growing evidence that spin-dependent properties vary with HM resistivity, a concerted effort to understand the effect of HM microstructure morphology on spin transport in HM|FM bilayers has yet to be made.

In this thesis, we investigate the role of ultrathin HM microstructure morphology on spin transport properties within HM|FM bilayers (FM = Co, CoFeB; HM = W, Ta, Ru, Pt). By seeding HM growth with thin metallic buffer layers including Ta and Ru, we are able to tune the growth mode and so morphology of the HM layer. X-ray diffractometry and transmission electron microscopy confirm the good control of HM growth modes through film wetting, continuity, texture and roughness. The subsequently altered electronic properties mediate the coupling of HM morphology to spin transport by impacting resistance and voltage readouts in common electrical spin injection / detection schemes.

We probe spin reflection, transmission and accumulation at the HM|FM interface in three such measurement schemes with a systematic set of spin Hall magnetoresistance (SHMR), spin pumping and spin-orbit torque (SOT) effective field measurements on (un)buffered Pt|CoFeB bilayers. We experimentally demonstrate a large enhancement of generated spin currents with SHMR and spin pumping measurements in ultrathin buffered devices, which can be directly correlated to HM microstructure. After extending current magnetoelectronic circuit theory to include the seed layer, we find that spin transport in buffered Pt|CoFeB bilayers can only be well understood when considering HM film morphology through Elliot-Yafet-dominated spin relaxation and intrinsic spin scattering in the Pt layer. By modelling both SHMR and spin pumping data simultaneously following this methodology, the different dependence on $\theta_{SH}$ in the schemes allows us to estimate a single set of $\theta_{SH}$ and $\lambda$ despite drastically different spin signals in buffered Pt|CoFeB layers. We further confirm the domination of intrinsic spin scattering in Pt by measuring near-constant normalised SOT effective fields across the (un)buffered bilayers. The demonstration of the significant effect of HM microstructure morphology on spin current generation in common measurement schemes indicates this work may potentially provide resolution to the widely varying values of $\theta_{SH}$ and $\lambda$ reported across the literature.

# Table of Contents

# List of figures

# List of tables

# 1 Introduction

It would be hard to imagine everyday life without the modern day computational power and mobile telecommunications, upon which humanity has become so reliant. The very existence of the digital age emerged from the invention of conventional hard disk drive read heads with magnetoresistive sensors discovered through ‘spin electronics' research. Initially, spin electronics – or ‘spintronics' for short – research focused on the intrinsic spin rather than the charge of electrons to manipulate material properties in magnetoelectronic devices. As our understanding of electron spin transport developed, magnetic sensors have moved from moved from metallic giant magnetoresistance (GMR) effect [1] devices to a larger tunnelling magnetoresistance (TMR) effect through MgO-based magnetic tunnel junctions [2]. Therefore, it may appear that metallic spintronics has had its time. However, this cannot be less the case; there has been a recent surge of interest in metallic spintronic devices due to their inherent low resistance-area products, low-power operation and non-volatility.

In the advent of ‘Big Data’, the 7.9 Zettabytes (1 Zettabyte = $10^{21}$ bytes) of digital data created in 2015 [1] will only continually demand more energetically efficient, robust magnetoresistance devices for information storage. All-metallic spintronic devices are, once again, well positioned at the forefront in light of recently observed exotic effects [3–6] which depend on the spin-orbit interaction of normal metals when in contact with a magnetic layer. Furthermore, these effects open new technological pathways to novel hard drives, spin-based thermoelectric generators, and microwave communication and sensing devices [7–9]. These exciting opportunities will only be realised, however, once spin transport is well defined across the relevant scale of spin propagation in thin film devices: the nanoscale. Currently, there is much understanding left to be desired in spin transport research at this length scale, particularly with respect to how the bulk and interfacial material properties affect efficient spin transfer. The work herein focuses on obtaining a better understanding of spin transport in metallic devices in ultrathin nanofilms.

This chapter introduces the fundamental principles and concepts underpinning spin transport in thin films. Starting with the concept and discovery of intrinsic spin angular momentum, it reviews how spins can create stable macroscopic order and magnetic precession at room temperature in ferromagnets. The chapter outlines how electrons flowing through conductive heavy metals and ferromagnetic materials become spin polarised to create spin currents. The coupled transport of electron charge and spin gives rise to an array of spin-dependent effects in individual layers as well as in more exotic, all metallic multilayers. Important considerations in spintronics such as how electron spin accumulates about and transports through interfaces are highlighted to lend background to the detailed discussions in the following chapters.

# 1.1 Electron spin

## 1.1.1 Spin angular momentum

Niels Bohr revolutionised our physical understanding of microscopic states when he proposed that his quantum mechanical model could describe the spectral series of the hydrogen atom. Instead of radiating energy during acceleration about the nucleus, he proposed that electrons instead form a stationary orbit and may transition between these orbitals with a quantum energy jump of $h\upsilon$, where $h$ is Plank's constant and $\upsilon$ is the frequency of radiation. However, his model did not account for 'fine' splitting in the hydrogen spectrum, where the single lines were comprised of more complex multiplets. Sommerfeld expanded on Bohr's work to find the spectra was well-modelled assuming elliptical electron orbit at relativistic speeds. However, the model was left wanting, as the outer-orbit electrons were moving at relatively low, non-relativistic speeds and the model required a ½ integer quantum number to satisfy the solution [10].

To explain the fine structure correctly, two Dutch graduate students named Uhlenbeck and Goudsmit purposed the electron spins about its axis in addition to the orbital angular momentum. In due course, Pauli suggested that this theory be applied to quantum mechanics and the idea of spin intrinsic angular momentum was born. Counterintuitively, spin should not be thought of classically as a particle's rotation about its axis since that would require surface angular velocities of 10 times the speed of light [10]! Instead, it is an intrinsic, purely quantum mechanical property [11,12], which satisfies the commutation relations

$$\left[\hat{S}_i, \hat{S}_j\right] = i\hbar\epsilon_{\mathrm{ijk}}\hat{S}_{\mathrm{k}}\,, \tag{1.1}$$

where $\hat{S}_i = \pm\frac{\hbar}{2}\sigma_P$ is the quantum mechanical spin operator given by the Pauli matrices $\sigma_P$ in the $i^{\text{th}}$ direction and $\hbar = h/2\pi$ is the reduced Plank's constant. Analogous to orbital angular momentum, the eigenvalues of $\hat{S}_{\mathrm{z}}$ for any spin-$s$ particle satisfy $\mathrm{m_s} = -\hbar s, -\hbar(s+1)\ldots, \hbar s$ where $s$ is the spin quantum number. Electrons are spin fermions and must take on a half-integer spin, with $s$ = ½. In Bra-Ket notation, any spin operator acting on an electron wavefunction with one of two eigenstates $\left|\psi_{\uparrow(\downarrow)}\right\rangle$ and will give one of two eigenvalues $\left(\pm\frac{\hbar}{2}\right)$ depending on the spin orientation ↑ (up) or ↓ (down), such that

$$\hat{S}_{\mathrm{z}}\left|\psi_{\uparrow(\downarrow)}\right\rangle = \pm\frac{\hbar}{2}\left|\psi_{\uparrow(\downarrow)}\right\rangle. \tag{1.2}$$

In this way, we can conceptualise the idea of spins having one of two states for electrons; either majority (↑) or minority (↓) states.

The total angular momentum $J$ of a particle is just the vector addition $J = L + S$ of the classical orbital momentum $L$, and the quantum intrinsic spin momentum $S$. The relativistic interaction between the intrinsic spin and the angular momentum of an electron inside a potential well is essential in spintronics. This phenomenon is known as a spin-orbit

interaction or spin-orbit coupling (SOC) and can be readily understood classically by picturing the interaction between the spin of an electron and its orbit about a positively charged nucleus. SOC is crucial to quantum mechanics, where fine and hyperfine spectral splitting may only be explained by the total angular momentum $j$ as a good quantum number. Moreover, this interaction gives rise to many significant effects explored in this work such as magnetocrystalline anisotropy and the spin Hall effect.

### 1.1.2 (Ferro)Magnetism from intrinsic spin

Intrinsic spin angular momentum in electrons gives rise to microscopic magnetic moments $\boldsymbol{\mu}$ through the Bohr magneton given by

$$\boldsymbol{\mu} = -\frac{\mathrm{e}}{m\mathrm{c}}\boldsymbol{S}, \tag{1.3}$$

where - $e$ is the elementary charge, $m$ is the mass of an electron, and $\mathbf{c}$ is the velocity of light in a vacuum. Thereby, any electron stationary or otherwise carries a microscopic magnetic moment. The long-range ordering of these moments through the alignment of neighbouring electron spin creates macroscopic magnetic properties, which are dependent on the shape and filled density of electronic orbitals. Although many types of magnetic order are possible in fluid and solid systems ranging from paramagnetism and diamagnetism to ferrimagnetism and ferromagnetism, this work specifically focuses on ferromagnetism in transition metals.

Ferromagnetism is the spontaneous alignment of neighbouring magnetic moments to produce long-range magnetic order in a solid material at temperatures below its Curie temperature. Hund's first rule states that electrons are added with the same spin state before adding spins of the other direction, which maximises total spin and gives rise to magnetic order. The thermodynamic incentive for ferromagnetism is due to the exchange energy experienced between two neighbouring electrons. Electrons with the same spin state are spatially separated more on average from Pauli's exclusion principle, which lowers the Coulomb repulsion between them. A generalised version of Heisenberg's exchange principle in a lattice is given by

$$\mathcal{H} = -2\sum_{i>j} J_{ij}\,\hat{\boldsymbol{S}}_i \cdot \hat{\boldsymbol{S}}_j, \tag{1.4}$$

where the Hamiltonian $\mathcal{H}$ is summed over all pairs of neighbouring lattice sites $i$ and $j$ and $J_{ij}$ is the exchange constant (positive for ferromagnets and negative for antiferromagnets). The coupling of the *s* conduction electrons and the low-lying *d* electrons is a highly localised interaction in metals, giving rise to large $J_{ij} \sim$ 1 meV and promoting long-range ferromagnetic order [13].

However, in solid materials, the electrons hybridise with neighbouring atoms to form bands which suppress magnetic order by minimising spin polarisation and quenching any orbital component $L$ adding to the total moment. Transition metal ferromagnets like Co and Fe are particularly interesting because they have both strong exchange interactions and hybridisation. In order to remain ferromagnetic, the exchange interaction must outweigh the hybridisation effects. The most intuitive way to understand this is visually by plotting the density of states $\mathcal{D}(\varepsilon)$ for the hybridised band structure of a common ferromagnet.

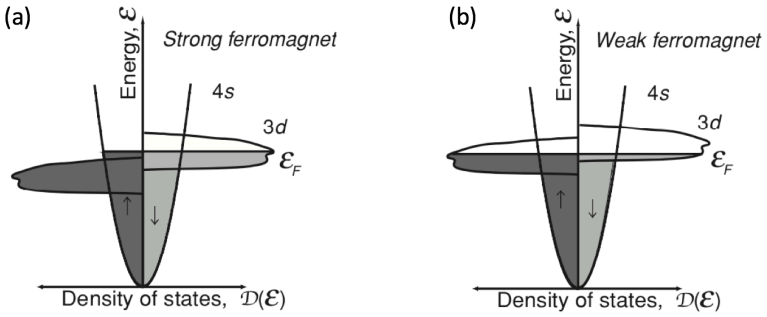


Figure 1.1 Illustration of the density of states of the majority and minority spin channel with different energy dispersion in hybridised 3*d* and 4*s* electronic orbitals in (a) strong and (b) weak ferromagnets. The stronger ferromagnet has a much larger density of states at the Fermi level than the weak ferromagnet. Reproduced from [13].

The schematic in figure 1.1 depicts the density of states $\mathcal{D}(\varepsilon)$ as a function energy $\varepsilon$ for a ferromagnet with hybridised 3*d* and 4*s* subbands in the Stoner model of ferromagnetism. If the exchange splitting between the spin up and down states is sufficient to push *d*-subband completely below the Fermi level $\varepsilon_{\mathrm{F}}$ then the metal strongly favours spin down electrons, as seen by the discrepancy in $\mathcal{D}(\varepsilon)$ between spin states at $\varepsilon_F$ in figure 1.1 (a). In weaker ferromagnetic materials depicted in figure 1.1 (b), the exchange interaction is less effective in splitting the spin states for the given hybridised metallic solid, and only a small difference in $\mathcal{D}(\varepsilon)$ at $\varepsilon_F$ arises.

### 1.1.3 Spin dynamics

As seen in the previous section, strong exchange energy can align neighbouring spins in some transition metals. Each spin with moment $\boldsymbol{\mu}$ drives a spontaneous bulk magnetic order with a net magnetisation $\boldsymbol{M}$ below the Curie temperature when thermal fluctuations are not dominant. When a magnetic film is subject to an external effective magnetic field $H_{\mathrm{eff}}$, $\boldsymbol{M}$ attempts to align with it to reduce the system Zeeman energy and a torque proportional to $\boldsymbol{M} \times \boldsymbol{H}_{\mathrm{eff}}$ arises. When a time-varying radio frequency (RF) field $H_{\mathrm{RF}}$ is applied perpendicular to the static field, $\boldsymbol{M}$ precesses about $H_{\mathrm{eff}}$ following the Landau-Lifshitz equation [14]

$$\frac{\mathrm{d}\boldsymbol{M}}{\mathrm{dt}} = -\gamma\mu_0\, \boldsymbol{M} \times \boldsymbol{H}_{\mathrm{eff}}\,, \tag{1.5}$$

where $\gamma = g|e|/2m_e$ is the gyromagnetic ratio, $g$ is the Lande g-factor whose value depends on the material (for free electrons g = 2.0023) and the permeability of free space $\mu_0 = 4\pi \times 10^{-7}$ Wb/Am. This can be visualized in Figure 1.2.

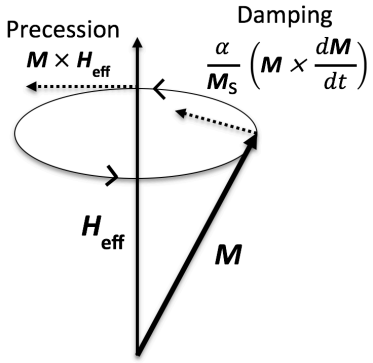


Figure 1.2 Illustration of the LLG spin dynamics. The magnetisation precesses about the effective applied field, while the Gilbert damping term tends to pull it towards the effective field, dissipating the dynamics.

The precessional motion in equation 1.5 would continue indefinitely unless energy is dissipated by Gilbert damping [15]. The following equation shows the famous Landau-Lifshitz-Gilbert (LLG) equation describing damped precession

$$\frac{\mathrm{d}M}{\mathrm{dt}} = -\gamma\mu_0 M \times H_{\mathrm{eff}} + \frac{\alpha}{M_s}\left(M \times \frac{\mathrm{d}M}{\mathrm{dt}}\right), \tag{1.6}$$

where $M_s$ is the saturation magnetisation of the magnetic film and $\alpha$ is the Gilbert damping parameter. The second term in this equation is the damping component as illustrated in figure 1.2, which retards precession by pulling $M$ towards $H_{\mathrm{eff}}$.

Following this logic, a ferromagnet may be driven into coherent precession at conditions satisfying the solution to the LLG equation [16]. This state is known as ferromagnetic resonance (FMR). The general solution for FMR precession is given by [17]

$$\left(\frac{\omega}{\gamma}\right)^2 = [H_{\mathrm{FMR}}\cos(\theta_H - \theta_M) - 4\pi M_s \cos 2\theta_M] \times [H_{\mathrm{FMR}}\cos(\theta_H - \theta_M) - 4\pi M_s \cos^2\theta_M], \tag{1.7}$$

where $H_{\mathrm{FMR}}$ the static field applied at resonance, $\omega$ is the angular frequency where $\omega = 2\pi f$ (typically with frequency $f$ in GHz), $\theta_M$ and $\theta_H$ are the angles of the magnetisation $M$ and the applied field $H$ from the film normal, respectively. Kittel [18] solved for a simplified solution to the LLG equation, which is used frequently in thin FM films when $H$ is applied in-plane $\theta_H = 0$, described by

$$\frac{\omega}{\gamma} = \sqrt{H_{\mathrm{FMR}}(H_{\mathrm{FMR}} + 4\pi M_{\mathrm{eff}})}, \tag{1.8}$$

where $4\pi M_{\mathrm{eff}} = 4\pi M_s - H_{\mathrm{k,eff}}$ is the effective magnetisation including the anisotropy field $H_{\mathrm{k,eff}}$, which acts to align $M$ in a particular crystallographic direction to reduce the magnetostatic energy.

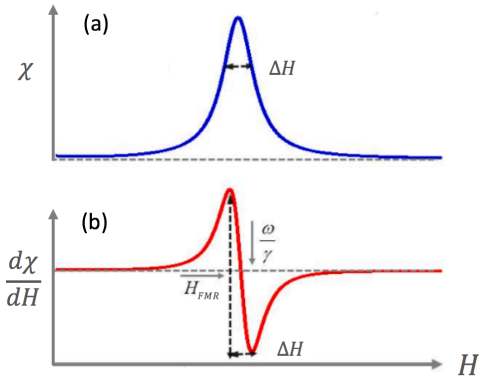


Figure 1.3 Illustrative schematic of the magnetic susceptibility a FM passing through resonance in arbitrary units. (a) Magnetic susceptibility of the FM in resonance at the peak with a linewidth defined by the FWHM ΔH. (b) The derivative of magnetic susceptibility representative of a typical absorption spectrum. Figure modified and reproduced from [16].

Typically, FMR is probed experimentally by observing the linewidth $\Delta H$ or lineshape of the magnetic susceptibility $\chi$ or the first derivative $\frac{d\chi}{dH}$ versus the applied static field $H$ as illustrated in figure 1.3 (a) and (b), respectively. Susceptibility is measured with a perpendicular $H_{RF}$ to induce precession in the FM. The full width at half maximum (FWHM) FMR linewidth can be directly related to magnetisation damping of a FM by

$$\mu_0 \Delta H = \alpha \frac{\omega}{\gamma} + \mu_0 \Delta H_0, \tag{1.9}$$

where $\Delta H_0$ is the zero-frequency linewidth offset [19–21]. The second term must be included to account for damping from inhomogeneities of the sample [22,23]. Moreover, the lineshape in figure 1.3 (a) of the microwave absorption can be represented by a symmetric and an antisymmetric Lorentzian component [24–27] following

$$L = S\frac{(\Delta H)^2}{(H - H_{FMR})^2 + (\Delta H)^2} + A\frac{-2(\Delta H)(H - H_{FMR})}{(H - H_{FMR})^2 + (\Delta H)^2}, \tag{1.10}$$

where $L$ is the absorbance lineshape, $S$ is the symmetric, and $A$ is the antisymmetric component of the Lorentzian lineshapes defined in the first and second terms, respectively. By fitting the absorbance lineshape, the linewidth, $H_{FMR}$ and the two Lorentzian components $S$ and $A$ may be extracted for a given applied microwave frequency.

### 1.1.4 Spin currents

In addition to precession about a fixed axis, intrinsic angular momenta may also be transported through materials. Analogous to a conventional current density $\boldsymbol{j}_c$, which describes the flow of electron per unit cross-sectional area, a spin current density $\boldsymbol{j}_s$ is considered to be a steady flow of angular momentum per unit cross-sectional area. Unlike charge currents though, spin currents are not a conserved quantity – even at steady-state – where spin angular momentum is transferred or lost due to spin-flip scattering events. Spin currents are readily understood with a simplified, two-current model developed by Mott in

1937 [28]. He postulated that the conductivity of each spin channel $\sigma^{\uparrow(\downarrow)}$ is different and that they are independent without inter-channel interaction. Thereby, conventional charge and quantum spin current densities are typically [29] written as

$$\boldsymbol{j}_c = -e\left(\boldsymbol{j}_c^{\uparrow} + \boldsymbol{j}_c^{\downarrow}\right) \tag{1.11}$$

$$\boldsymbol{j}_s = -\frac{\hbar}{2}\left(\boldsymbol{j}_c^{\uparrow} - \boldsymbol{j}_c^{\downarrow}\right) \tag{1.12}$$

where $\boldsymbol{j}_c^{\uparrow(\downarrow)}$ is the partial current density of the spin up(down) channel.

There are two types of conduction electron-mediated spin currents. The first is a spin-polarised charge current, which arises in magnetic metals due to exchange splitting in the conduction *s* electrons. Since $\sigma^{\uparrow} \neq \sigma^{\downarrow}$ and $\boldsymbol{j}_c^{\uparrow} \neq \boldsymbol{j}_c^{\downarrow}$, a charge current flowing through a ferromagnetic metal carries a spin-polarised component given by

$$P \equiv \frac{\sigma^{\uparrow} - \sigma^{\downarrow}}{\sigma^{\uparrow} + \sigma^{\downarrow}}. \tag{1.13}$$

The second arises in non-magnetic metals without any net $\boldsymbol{j}_c$ from spin-dependent scattering events and is, therefore, a pure electronic spin current. These spin currents are illustrated in Figure 1.4 (a) and (b), respectively.

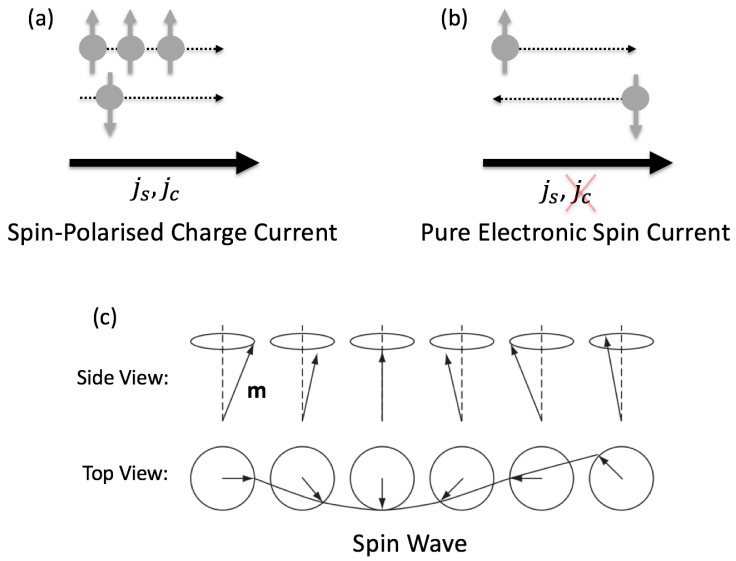


Figure 1.4 Schematic illustration of the different types of spin currents. (a) A spin-polarised charge current, where both a charge and spin current flow. (b) A pure electronic spin current where the charge current is equal in both directions resulting in a net transfer of spin only. (c) A spin-wave (magnon) excitation from the partial alignment of neighbouring, precessing spins modified and reproduced from [30].

Additionally, it was recently found that spin transport need not be mediated by electron flow, but also by spin-waves. Spin-waves transfer spin angular momenta via the collective motion of magnetic moments in a solid [31]. A spin-wave is equivalent to a massless, low-energy quasi-particle called a magnon, by particle-wave duality. Magnons have proved

particularly useful for measuring spintronic effects in insulating magnetic materials [31–33], where spin currents arising from conduction electron flow are not possible. They persist due to the same principle behind the ordering of moments in a ferromagnet: to reduce the Coulomb repulsion through exchange energy in a lattice of atoms by aligning neighbouring electron spins through Heisenberg's model, as outlined in equation 1.4. On each site, slight spin precession about an axis caused by thermal fluctuations coupled with the exchange interaction between neighbouring electrons creates a spin wave as depicted in Figure 1.4 (c). In this work, however, electron flow spin transport is paramount in the conducting ferromagnetic metals.

### 1.1.5 Hall effects and magnetoresistance

*To allow for a better understanding of the symmetries of the family of Hall effects and magnetoresistances, we outline two useful tools used to describe effects and observations in this thesis. Firstly, the term longitudinal will be used to describe the direction of the applied current* $\hat{\boldsymbol{x}}$ *and transverse will be used to describe the perpendicular direction* $\hat{\boldsymbol{y}}$*, in the plane of the metal film. Secondly, we assign a notation to the resistivity tensor* $\overleftrightarrow{\rho}_{ijk}$ *of a material, where* $i, j, k$ *are the direction of the applied current, the measured voltage and the applied magnetic field, respectively. An illustration of this is visualised in figure 1.5.*

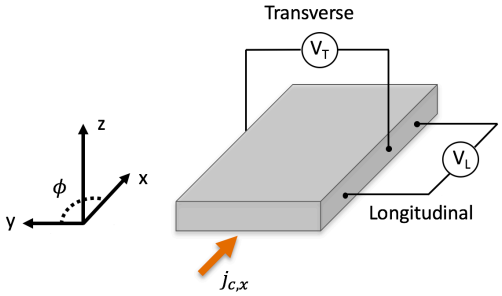


Figure 1.5 Schematic illustration of a thin metallic film and the directions of the applied current density, and resultant longitudinal and transverse voltage measurement taps used in this work.

In 1879, a young graduate student named E. H. Hall discovered an effect of an external magnetic field on electrons flowing in conductive materials [34]. Owing to the Lorentz force ($\boldsymbol{F} = e(\boldsymbol{E} + v \times \boldsymbol{B})$ , where $v$ is the velocity of electrons and $\boldsymbol{E}$ is the electric field), the mobile charge carriers are deflected perpendicular to both $v$ and $\boldsymbol{H}$ as illustrated in figure 1.6 (a). This was the first observation of magnetoresistance, i.e. the dependence of the electrical resistance of a material on its magnetic properties. This effect is now known as the ordinary Hall effect (OHE) and was the first of an entire family of effects with the similar symmetry, known as the Hall family. The symmetry of the OHE may is written $\rho_{\mathrm{xyz}}^{\mathrm{OHE}} = \mu_0 R_H H_Z$, where $R_H$ is the Hall coefficient.

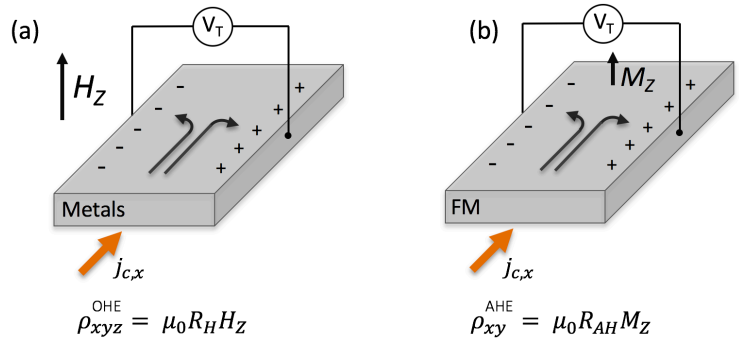


Figure 1.6 Schematic illustration of the two fundamental Hall effects. (a) The ordinary Hall effect requires an external magnetic field and is present in all conducting metals due to the Lorentz force. (b) The anomalous Hall effect is only dependent on intrinsic magnetisation in films such as FMs, where there is an inherent imbalance in spin channels at the Fermi level. The Hall symmetry is identical.

Soon after he discovered the OHE in normal metals,in 1881 he observed the same effect, but much stronger, in FM materials [35]. This is now known as the anomalous Hall effect (AHE). The AHE has the identical symmetry to the OHE but does not require an external field to drive electron deflection. Instead, electrons are transversely scattered depending on their spin state through SOC [36] due to inherent film magnetisation and therefore shows a magnetoresistance $\rho_{xy}^{AHE} = \mu_0 R_{AH} M_Z$, where $R_{AH}$ is the anomalous Hall coefficient. Since $\sigma^{\uparrow} \neq \sigma^{\downarrow}$ in a FM, an electric Hall field is established across $\hat{\boldsymbol{y}}$, as illustrated by figure 1.6 (b).

Nearly a century later, a Dyakonov and Perel [37,38] predicted a quantum, spin-dependent effect with the same Hall symmetry in systems which have large, relativistic SOC such as HMs. It was later experimentally verified by Hirsch [39]. In the so-called spin Hall effect (SHE), conduction electrons with opposite spin states achieve spatial separation by spin-dependent scattering. In this way, the charge current produces a pure, transverse spin current in open circuit conditions. The spin polarisation direction $\boldsymbol{\sigma}_s$ is perpendicular to both $\boldsymbol{j}_c$ and $\boldsymbol{j}_s$, thus satisfying Hall symmetry. The SHE can be visualised in figure 1.7 (a), where the spin accumulation is illustrated in $\hat{\boldsymbol{z}}$ instead of $\hat{\mathrm{y}}$ prefacing further discussions of spin transport.

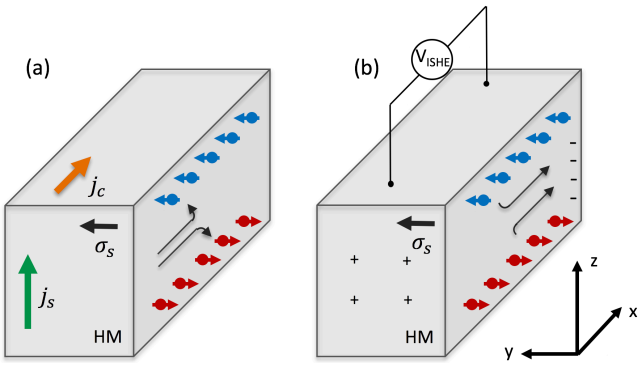


Figure 1.7 Schematic of the spin Hall family of effects. (a) The SHE produces a pure, perpendicular spin current to the applied charge current in a material with a large SOC such as a HM. (b) The ISHE is Onsager's reciprocal mechanism to the SHE, whereby a pure spin current is converted into a charge current. In open circuit conditions, this is measured as an ISHE voltage.

Moreover, Saitoh showed that the same effect, but inverted (i.e. a steady $\boldsymbol{j}_s$ produces a transverse charge current) could be used to measure spin currents and accumulation [27] electrically. The inverse spin Hall effect (ISHE) is illustrated in figure 1.7 (b). The (inverse)SHE follows Onsager's reciprocity relations [40], whereby the efficiency of charge-to-spin conversion (and back) are identical since they stem from the same physical origin. Phenomenologically,

$$\boldsymbol{j}_s^{\mathrm{SHE}} = \frac{\hbar}{2e}\theta_{\mathrm{SH}}\,(\boldsymbol{\sigma}_s \times \boldsymbol{j}_c) \tag{1.14}$$

$$\boldsymbol{j}_c^{\mathrm{ISHE}} = \frac{2e}{\hbar}\theta_{\mathrm{SH}}\,(\boldsymbol{\sigma}_s \times \boldsymbol{j}_s) \tag{1.15}$$

where, the governing parameter is the spin Hall angle $\theta_{\mathrm{SH}}$, which is a measure spin-to-charge conversion efficiency and $\boldsymbol{j}_s^{\mathrm{SHE}}$ is in units of angular momentum [J/m$^2$]. Strictly, the spin Hall angle is a ratio between the transverse spin Hall conductivity $\sigma_{xy}^{\mathrm{SH}}$ and the longitudinal charge conductivity $\theta_{\mathrm{SH}} \equiv \frac{\sigma_{xy}^{\mathrm{SH}}}{\sigma_{xx}^{\mathrm{c}}}\frac{e}{\hbar}$. Or more intuitively, the percentage of electrons that will be spin-dependently scattered by the SHE normal to the number driven by the electric gradient along $\boldsymbol{j}_c$.

Two other spin-dependent effects whose physical origins originate from SOC set by the crystal structure of FMs [41] are the anisotropic magnetoresistance (AMR) and the planar Hall effect (PHE). In contrast to the out-of-plane $\boldsymbol{H}$ ($\boldsymbol{M}$) requirement in the aforementioned Hall effects, the AMR and PHE arise from $\boldsymbol{M}$ in the sample plane. As illustrated in figure 1.8, the FM film resistivity when $\boldsymbol{M}$ is transverse to $\boldsymbol{j}_{c,x}$ ($\boldsymbol{M} \perp \boldsymbol{j}_{c,x}$) is not equal to that when they are collinear ($\boldsymbol{M} \parallel \boldsymbol{j}_{c,x}$). Thereby, depending on the angle $\phi$ between $\boldsymbol{M}$ and $\boldsymbol{j}_{c,x}$, a magnetoresistance arises. To evaluate this magnetoresistance, an external field $\boldsymbol{H}$ is applied to fix $\boldsymbol{M}$ in a given direction such that the resistivities are $\rho_{xxx}$ ($\rho_{\parallel}$) at $\boldsymbol{M} \parallel \boldsymbol{j}_{c,x}$ and $\rho_{xxy}$ ($\rho_{\perp}$) at $\boldsymbol{M} \perp \boldsymbol{j}_{c,x}$. AMR is measured as a longitudinal voltage accumulation, whereas the PHE results in a transverse voltage accumulation.

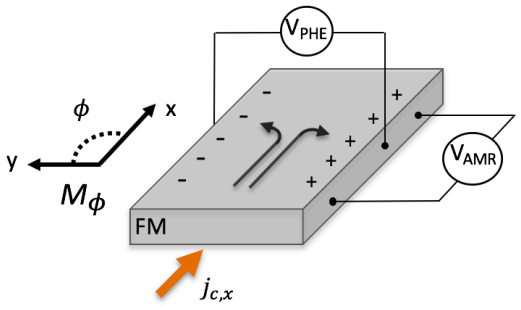


$$\rho_{xy}^{\mathrm{PHE}}(\phi) = \tfrac{1}{2}(\rho_{\parallel} - \rho_{\perp})\sin(2\phi)$$

$$\rho_{xx}^{\mathrm{AMR}} = \rho_{xx} + \tfrac{1}{2}(\rho_{\parallel} - \rho_{\perp})\cos(2\phi)$$

Figure 1.8 Schematic illustration of the magnetoresistive effects depending on the relative angle between the in-plane magnetisation $\boldsymbol{M}$ and $\boldsymbol{j}_{c,x}$. The planar Hall effect is the measured transverse to the charge current, while the anisotropic magnetoresistance is measured longitudinally. Both effects vary sinusoidally with the angle of magnetisation $\phi$.

In general, it is possible that more than one magnetoresistive effect is present when symmetries overlap. Furthermore, even slight sample misalignments may couple effects and yield spurious voltages. Therefore, to accurately measure magnetoresistance, one must be design and conduct the experiment carefully. The effects outlined above are all experimentally observed in this work but only comprise a subset of the full range of spin-dependent phenomenon now observed. For a more extensive list including the giant magnetoresistance (GMR) [1,42], the Rashba-Edelstein effects [43–50], the Nernst effect family [51,52], the quantum Hall effect [53–55] and the Seebeck effect family [56–59], please refer to the noted references.

### 1.1.6 Spin-dependent scattering

There are three separate physical origins of transverse spin-dependent scattering of electrons, which underpin the AHE and both the (I)SHE [60,61]. A simple schematic outlining these mechanisms is shown in figure 1.9 (a-c). Here they will be briefly treated in chronological order of their introduction. In 1954, Karplus and Luttinger first theoretically proposed [62] that SOC in combination with interband coherence, which is induced by the applied electric field, spontaneously results in an intrinsic, transverse velocity depending on the spin polarisation [63]. This is known as intrinsic spin scattering because the transverse velocities result from the band structure of the solid as opposed to a mechanism extrinsic to its fundamental properties. This theory has since been revisited and treated with a Berry phase [64–66] analysis to find electrons pick up transverse velocities when their Berry phase curvatures [67–69] are not compensated. The intrinsic spin scattering mechanism yields a constant $\sigma_{xy}^{SH}$ [61].

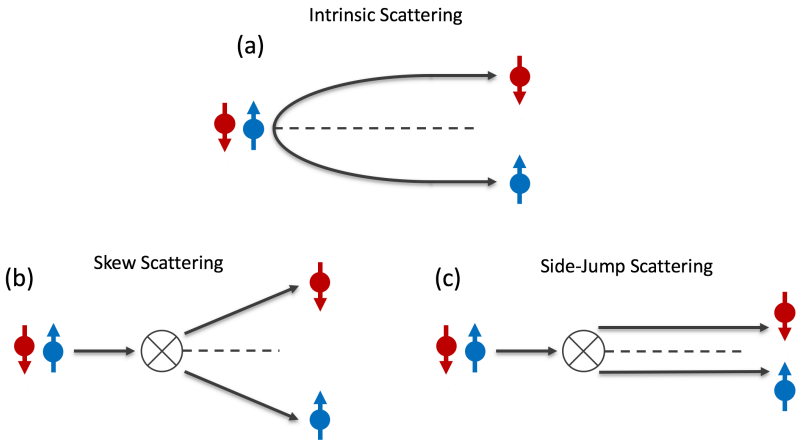


Figure 1.9 Schematic illustrations of spin-dependent scattering mechanisms. (a) Intrinsic transverse spin scattering without a scattering site due to the band structure of the material. (b) An external scattering mechanism called skew scattering, which deflects electrons from a scattering site in a spin-dependent direction. (c) Side-jump scattering is another external scattering mechanism where electrons are displaced after the scattering site depending on their spin orientation.

Soon after Karplus and Luttinger proposed the intrinsic method, Smit and Berger, focused separately on the influence of disorder in the solid causing transverse, extrinsic spin scattering. Smit proposed a mechanism known as spin-skew scattering [70], where an effective, in-plane magnetic field arises from SOC, which deflects incoming electrons at the scattering site depending on the direction of spin. The spin-skew mechanism gives a resistivity $\rho_{sk} = \rho_{xx}$ and a $\sigma_{xy}^{SH} \propto {\rho_{xx}}^{-1}$ [61]. Berger introduced an additional extrinsic mechanism called side-jump scattering [71,72], which is a strictly quantum effect resulting from a small spin-dependent transverse, 'side-jump' past the scattering sit. The side-jump mechanism yields a resistivity $\rho_{sj} = {\rho_{xx}}^2$ and typically contributes insignificantly to $\sigma_{xy}^{SH}$ for moderately dirty metals [73].

It is challenging to separate the intrinsic and extrinsic mechanisms experimentally. It can be done, though, by measuring $\rho_{xy}$ and $\rho_{xx}$ at ultralow temperatures (4 K) to where impurity scattering dominates in FM, or by varying deposition conditions to tune $\rho_{xx}$ in HMs [74]. It is now clear that in the super-clean metallic regime ($\sigma_{xx} \gtrsim 10^5$ S), extrinsic mechanisms dominate, whereas in the moderately dirty regime ($\sigma_{xx} \lesssim 10^5$ S) which is more common for sputtered metals, intrinsic spin-scattering dominates for both HMs [61,74] and FMs [61].

## 1.2 Spin transport in heterostructures

Although the AHE, AMR and PHE may be readily measured in a single FM layer, more exotic spin transport phenomenon arise in micromagnetic heterostructures comprised of multiple layers. The spin-mediated interaction between layers provides a myriad of exciting effects, which drives research interest, in no small part due to the potential technological applications. This section outlines the principles behind the transport of spin in magnetic multilayers, with a particular focus on spin-dependent effects in all-metallic heterostructures. These devices are widely studied due to their inherent low resistance-area products and non-volatility, which make them both energy efficient and robust. The prototypical all-metallic spintronic device for investigating such effects is a thin or ultrathin heavy metal (HM) | ferromagnet (FM) bilayer. The HM is a non-magnetic normal metal (NM), which is known to be effective at injecting (detecting) spin currents to (from) the FM layer since the magnitude of SOC goes as atomic number $Z^4$ [12]. Here, we outline pertinent fundamentals governing spin transport in each layer and the interaction between them.

### 1.2.1 Spin accumulation and relaxation

In conductive metallic layers, spin currents propagate due to an imbalance in the majority and minority spin populations expressed in equation 1.12. These populations are often represented as a quasi-equilibrium thermodynamic property known as the electrochemical potential $\mu_s^{\uparrow(\downarrow)}$ [75–78]. Analogous to an electric field, the gradient of $\mu_s$ is the driving force for spin transport, which equilibrates $\mu_s^{\uparrow(\downarrow)}$ of each spin population by the diffusion of spin.

The difference in chemical potentials of the two spin populations is known a spin accumulation and denoted $\mu_s = \mu_s^{\uparrow} - \mu_s^{\downarrow}$. Spin accumulations build up near the interface and drive pure spin currents across it, transporting spin between the HM and FM layers. To model the non-equilibrium spin populations in a HM or a FM, we turn to one-dimensional spin diffusion theory.

In natural units, the individual spin-dependent charge current density $\boldsymbol{j}_c^{\uparrow(\downarrow)}$ is the summation of an electric field term and a gradient of the electron density term: $\boldsymbol{j}_c^{\uparrow(\downarrow)} = \sigma^{\uparrow(\downarrow)}\boldsymbol{E} - eD^{\uparrow(\downarrow)}\nabla n^{\uparrow(\downarrow)}$, where $D^{\uparrow(\downarrow)}$ is the diffusion constant of the spin channel, $e = -|e|$ and the carrier density $n^{\uparrow(\downarrow)}$ is given by the density of states in the spin subband as $\nabla n^{\uparrow(\downarrow)} = \mathcal{D}(\varepsilon)^{\uparrow(\downarrow)}\nabla\varepsilon_F^{\uparrow(\downarrow)}$ [78]. Substituting in the spin-dependent conductivity from the Einstein relation $\sigma^{\uparrow(\downarrow)} = e^2\mathcal{D}(\varepsilon)^{\uparrow(\downarrow)}\ D^{\uparrow(\downarrow)}$, the spin-dependent charge current for each channel becomes

$$\boldsymbol{j}_c^{\uparrow(\downarrow)} = -\frac{\sigma^{\uparrow(\downarrow)}}{e}\nabla\mu_s^{\uparrow(\downarrow)}. \tag{1.16}$$

Note, the ohmic term $\sigma^{\uparrow(\downarrow)}\boldsymbol{E}$ here is included in the definition of $\mu_s^{\uparrow(\downarrow)} = \varepsilon_F^{\uparrow(\downarrow)} + eU$, where $U$ is the electric potential. Following from the definition of a spin current in equation 1.12, the continuity equation for spin at steady state follows the number proportion of spin-flips in the spin channels given by

$$\nabla\left(\boldsymbol{j}_c^{\uparrow} - \boldsymbol{j}_c^{\downarrow}\right) = -e\frac{n^{\uparrow} - \bar{n}^{\uparrow(\downarrow)}}{\tau^{\uparrow\downarrow}} + e\frac{n^{\downarrow} - \bar{n}^{\downarrow}}{\tau^{\downarrow\uparrow}} \tag{1.17}$$

where $\bar{n}^{\uparrow(\downarrow)}$is the equilibrium carrier density of each channel and $\tau^{ij}$ is the scattering time of an electron from spin state $i$ to $j$. Substituting $\boldsymbol{j}_c^{\uparrow(\downarrow)}$ from equation 1.16 into 1.17 and following a detailed balance linking the density of states in each spin subband with spin-flipping events for each channel, one obtains the spin drift-diffusion equation [75,76,78–81]

$$\nabla^2\mu_s = \frac{\mu_s}{\lambda^2}, \tag{1.18}$$

where $\lambda$ is the spin diffusion length $\lambda = \sqrt{D\tau_{sf}}$ and $\tau_{sf}$ is the spin-relaxation time following $1/\tau_{sf} = \frac{1}{2}\left(1/\tau^{\uparrow\downarrow} + 1/\tau^{\downarrow\uparrow}\right)$ [76]. The spin accumulation in an arbitrary direction $\hat{\boldsymbol{z}}$ driving spin transport in metallic metals is then given by the general solution of the drift-diffusion equation 1.18, which reads

$$\mu_s(z) = Ae^{-z/\lambda} + Be^{z/\lambda}, \tag{1.19}$$

where $A$ and $B$ are constants determined by boundary conditions of the system. Knowledge of the spin accumulation at any point in $\hat{\boldsymbol{z}}$ fully defines the spin propagation and relaxation in constituent materials. Hereby, equation 1.16 may be rewritten in terms of the total spin accumulation $\mu_s$ for diffusive spin transport in one dimension as

$$\boldsymbol{j}_s(z) = -\frac{\sigma}{2e}\partial_z\mu_s = -\frac{1}{2e\rho\lambda}\left[Ae^{-z/\lambda} - Be^{z/\lambda}\right]. \tag{1.20}$$

The spin diffusion theory applies to both HM and NM, with the only difference being the spin polarisation $P$ = 0 for HMs [76], unlike that for FMs. The characteristic spin decay length is called the spin diffusion length $\lambda$. It governs the distance over which the non-equilibrium $\mu_s$ persists in constituent layers. From equation 1.19, $\mu_s$ decays exponentially from the interface with the spin diffusion length $\lambda$ due to spin relaxation. Therefore, spin relaxation is essential in determining the propagation of spin in constituent materials [83]. Multiple mechanisms have been shown to relax spin through spin-flip scattering events. In metals, the two most common are the Elliot-Yafet mechanism and the Dyakanov-Perel mechanism, and in HMs, Elliot-Yafet spin relaxation is typically dominant [84–87].

The Elliot-Yafet mechanism was discovered independently by Elliot [88] and Yafet [89]. As conduction electrons move through the periodic potential $U(r)$ of the lattice ions, the electric and so magnetic perturbation exerts a torque on the electron spin. This type of momentum scattering event derives formally from the Dirac equation $\frac{h}{4m^2c^2}(\nabla U \times \boldsymbol{p})\cdot \boldsymbol{s}$, where $\boldsymbol{p}$ is the momentum of the electron. Through SOC, any fluctuation in $\boldsymbol{p}$ from scattering off of impurities, grain boundaries, phonons and surfaces readily exerts a torque on the spin $\boldsymbol{s}$ of conduction electrons [90]. Thereby, the spin-flip time is proportional to the momentum scattering time $\tau_p$ with a finite probability $P_{EY}$ of a spin-flipping event given by $\tau_{sf} = \tau_p / P_{EY}$.

The Dyakanov-Perel mechanism [37,38], on the other hand, arises when inversion symmetry is broken and results in spin precession de-phasing instead of spin-flip scattering. This occurs in solids without lattice inversion symmetry with electrons at interfaces and surfaces. In solids, an effective magnetic field dependent on the electron momentum arises due to SOC. Therefore, the net effect of momentum scattering events is to randomly fluctuate the Larmor frequencies and decohering the spin [90]. The spin-relaxation time in the Dyakanov-Perel mechanism is inversely proportional to $\tau_p$: $\tau_{sf} \propto {\tau_p}^{-1}$.

### 1.2.2 Transporting spin across interfaces

The transport of spin between layers in a heterostructure is, for the most part, governed by fundamental mass transfer theory. However, unlike classical mass transfer, spin is not a conserved quantity due to the multiple mechanisms explored above, which relax spin imbalances. Where the analogy is useful though, is in understanding pertinent resistances to spin transport about the interface.

In materials with short spin diffusion lengths $\lambda_i$, the imbalance in spin subband populations is quenched within a short distance of the interface. These materials are good spin sinks. However, as $\lambda_i$ increases, spin relaxation is less effective and $\mu_s$ persists further into the thickness of the layer. In the case represented in figure 1.10, $\lambda_{\mathrm{FM}} \gg \lambda_{\mathrm{NM}}$ since the exponential decay of $\mu_s^{\uparrow(\downarrow)}$ in the FM penetrates much deeper into the FM than the HM. In conducting materials, the resistance to spin sinking may be approximated by [82]

$$R_{s,i} = \frac{\rho_i \lambda_i}{(1-P_i)^2} \coth\left(\frac{d_i}{\lambda_i}\right), \tag{1.21}$$

where $\rho_i, P_i$, and $d_i$ are the resistivity, the spin polarisation ($P_{HM}$ = 0), and thickness of a constituent layer. The first portion of equation 1.21 is the bulk spin resistance in a metal. The additional hyperbolic cotangent portion derives from solving the drift-diffusion in equation 1.18 and is representative of a phenomenon known as spin backflow [91]. Spin backflow is the reflection of a spin current about the interface, which sees a spin current travelling in the opposite direction, back into the material in which it was generated.

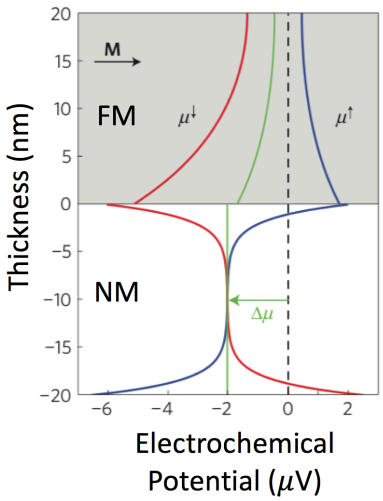


Figure 1.10 Profile of the spin-dependent electrochemical potentials about a prototypical HM|FM interface, modified and reproduced from [92]. $\mu_s^{\uparrow(\downarrow)}$ is quenched more quickly in the NM than in the FM owing to the more efficient spin relaxation. The discontinuities in $\mu_s^{\uparrow(\downarrow)}$ at the interface represent realistic interface spin-flip scattering processes, which reduce the total spin accumulation.

Spins may also experience an additional interface resistance analogous to electrical contact resistance, which may be visualised by the discontinuous jump of $\mu_s^{\uparrow(\downarrow)}$ at the interface in figure 1.10. Spin transparency at the HM|FM interface has been shown to depend on the relative direction between $\boldsymbol{M}$ in the FM and $\boldsymbol{\sigma}_s$ of the impinging spin current in the HM [93].

An itinerant spin current has spin polarisation with one collinear component (longitudinal) and one perpendicular component (transverse) to $\boldsymbol{M}$. Spin transport through the interface has been treated with magnetoelectronic circuit theory from first principles to show the spin-dependent scattering matrix contains four parameters: one for each spin-dependent conductance given by $g^{\uparrow(\downarrow)}$, and the real and imaginary part of a universal concept in spin transport known as the spin mixing conductance $g^{\uparrow\downarrow}$ [93,94]. This concept was originally proposed in 2000, but only more recently experimentally verified across multiple measurement schemes [95].

Spin transport at the HM|FM interface for longitudinal accumulations may be simply understood and is comprised of two terms, one for each spin-dependent conductance given by $g^{\uparrow(\downarrow)}$. In contrast, spin transport at the interface for transverse accumulations is governed by the spin mixing conductance, which is defined as [94,96]

$$g^{\uparrow\downarrow} = g_r + ig_i = \frac{e}{h^2}\sum_{nm}\delta_{nm} - R^{\uparrow}_{nm}\left(R^{\downarrow}_{nm}\right)^{*}, \tag{1.22}$$

where $g_r$ and $g_i$ are the real and imaginary components of the spin mixing conductance, respectively. The sum is related to the individual spin-dependent conductances since $g^{\uparrow(\downarrow)} = \frac{e}{h^2}\Sigma_{nm}\left[\delta_{nm} - \left|R^{\uparrow(\downarrow)}_{nm}\right|^2\right]$ where $R^{\uparrow(\downarrow)}_{nm}$ is the reflection coefficient for the spin up(down) channels, and $\delta_{nm}$ is the number of propagating channels from $n$ channel to $m$ channel. Generally, it can be shown that $2g_r \gg g^{\uparrow} + g^{\downarrow}$ [94,96] and $g_r \gg g_i$ for all metallic interfaces [97]. Since $g_r$ dominates spin conductance at the interface, it is common to neglect the other smaller terms. As such, from here onwards this thesis will assume $g_r \sim g^{\uparrow\downarrow}$.

In addition to spin resistance in the bulk and at the interface, spin accumulation may further relax by spin-flip processes at the interface, which is not accounted for by the concept of spin mixing conductance. This is a notable example of where the analogy to classical mass transfer breaks down; the sum of the transmission $T^{\uparrow(\downarrow)}$ and reflection $R^{\uparrow(\downarrow)}$ coefficients for each spin channel do not equate to unity. The loss of spin information across the interface has been widely observed experimentally [75,98,99] and is dubbed spin memory loss (SML). This lack of conservation of spin at the interface makes accurate extraction of electronic spin-dependent parameters and interfacial spin conductances challenging in HM|FM heterostructures.

Finally, the magnetic proximity effect (MPE) may also affect spin transport in an adjacent layer near a magnetic thin film and through the interface [100–104]. The MPE is a phenomenon which sees an induced magnetic moment in the first few monolayers of a non-magnetic material when in direct contact with a magnetic layer due to an exchange interaction [105–107]. Therefore, the MPE decays rapidly away from the interface. Induced magnetisation has observed with AMR in HMs used in this work such at Ta [108] and Pt [100,109] when in contact with an insulating ferrimagnetic (FMI) layer such as yttrium iron garnet (YIG). Indeed, in a HM|FMI layer there is no current flow in the FMI and any AMR contribution must arise from a MPE-induced signal in the HM layer. More recently, the MPE has been demonstrated to also have an effect in HM|FM bilayers whereby induced magnetic moments in Pt films have been correlated with reduced $\sigma^{SH}_{xy}$ [109]. The role of the MPE on interfacial spin transport is still under strong debate; it has been shown to enhance [104], suppress [109] or be irrelevant [110] to $g^{\uparrow\downarrow}$ [111]. As the discussion continues in the community, it is important to be mindful of the possible influence on spin transport across the interface in HM|FM systems.

### 1.2.3 Spin torque

Spin currents in HM|FM bilayers carrying intrinsic angular momenta can influence the local FM magnetisation in multiple ways. The first method was proposed by Sloncwezski and Berger [72,112] when a spin-polarised charge current flows through a FM film. If $\boldsymbol{\sigma}_s$ of the itinerant electrons is non-colinear to the local magnetic moment $\boldsymbol{M}$, angular momentum is transferred. The magnetisation exerts a torque on the conduction electrons to reorient them in a process called spin filtering. This can be visualised in figure 1.11 (a). In so doing, the spin-polarised conduction electrons exert an equal and opposite torque on $\boldsymbol{M}$, creating a phenomenon called spin transfer torque (STT).

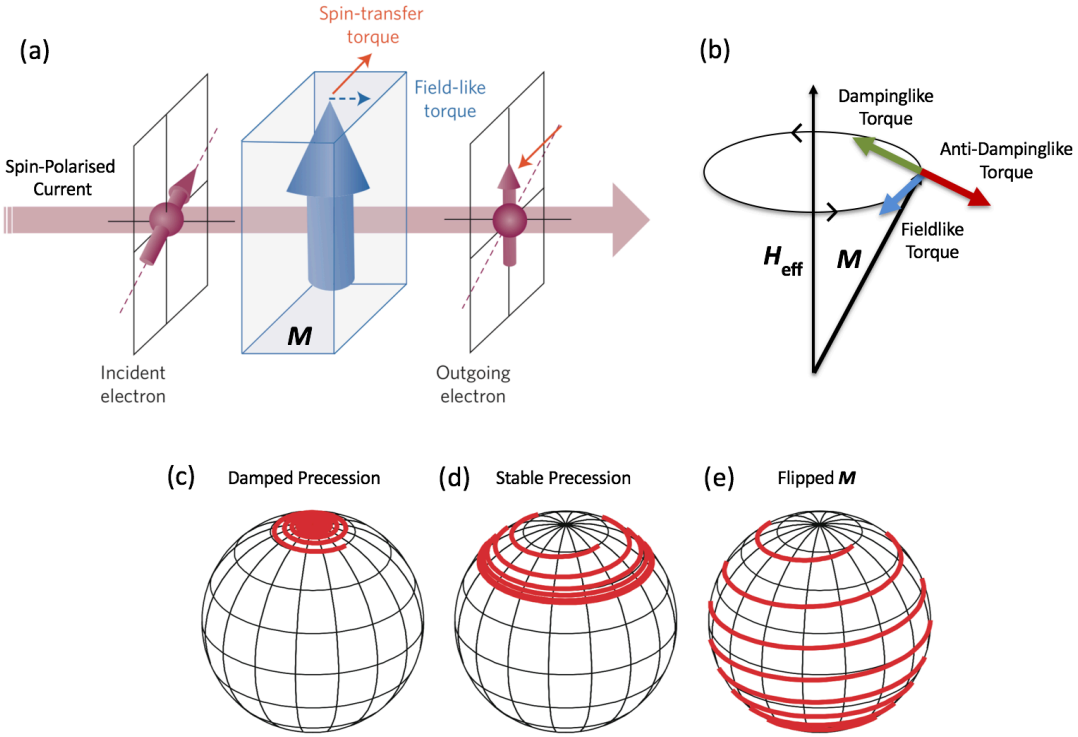


Figure 1.11 (a) Schematic of spin transfer and field-like torque exerted on low lying electrons in the FM from itinerant, conduction electron spins passing through the spin filter, reproduced from [113]. (b) An illustration of the LLG equation governing spin precession of $\boldsymbol{M}$ about an effective field. The green and red arrows represent the damping- and antidamping-like torques, which tend to move the magnetisation towards or away from the effective field. The red antidamping-like arrow arises from spin transfer torque, while the blue arrow represents a field-like torque. Trajectories of spin-torque-driven magnetisation dynamics at (c) low currents with damped precession, (d) high currents with stable precession and (e) very high currents which flip the magnetisation completely. Reproduced from [114].

Current-induced STT of a FM causes the precession of $\boldsymbol{M}$ about the effective field axis, which is governed by the fundamentals of FM spin dynamics through the LLG equation (1.6). There are two additional STT terms added to the LLG equation when $\boldsymbol{M}$ is non-colinear to $\boldsymbol{\sigma}_s$ as illustrated in figure 1.11 (b). Here, the spin state of the itinerant electrons are not eigenstates of the FM, which gives rise to the spin precession. The modified LLG the follows

$$\frac{\mathrm{d}\boldsymbol{M}}{\mathrm{dt}} = -\gamma\mu_0 \boldsymbol{M} \times [\boldsymbol{H}_{\mathrm{eff}} + a_j(\boldsymbol{M} \times \boldsymbol{\sigma}_{\mathrm{s}}) + b_j\boldsymbol{\sigma}_{\mathrm{s}}] + \frac{\alpha}{M_{\mathrm{s}}}\left(\boldsymbol{M} \times \frac{\mathrm{d}\boldsymbol{M}}{\mathrm{dt}}\right), \quad (1.23)$$

where $a_j$ and $b_j$ represent the damping-like and field-like components of STT, respectively. Depending on the sign of $a_j$, the $\boldsymbol{M} \times (\boldsymbol{M} \times \boldsymbol{\sigma}_{\mathrm{s}})$ term may act to damp precession or induce STT. The field-like component is typically very small in comparison to the damping-like term in metallic devices [113,115]. Overall, depending on the current, different types of precession arise. As shown in figure 1.11 (c-e), when the drive current is increased, $\boldsymbol{M}$ goes from damped motion (c), to stable precession (d), to precession about a switch magnetic state (e). Therefore, large spin polarised charge currents have been shown [5,116–118] to switch $\boldsymbol{M}$ lending to a new wave of spin memory applications with STT-driven magnetic random access memory (MRAM) [9,119,120].

Another way to excite spin precession and torque in a FM layer is to inject an in-plane charge current in an adjacent HM layer [43,49,121–127]. There are two physical origins of spin-orbit torque (SOT) in HM|FM bilayers. The first is a bulk effect arising from the SHE, where a current flowing through a highly spin-orbit coupled HM will induce a spin current impinging on the HM|FM interface. This spin current may diffuse into the FM and exert torque on the local moments near the interface. The bulk SHE SOT component ($a_j$) is (anti)damping-like in nature and follows the aforementioned torque formalism and symmetry. Alternatively, spin may accumulate at the interface from the Rashba-Edelstein effect [45,47,50], which torque local moments in the FM by direct exchange coupling [121,128]. This smaller, interfacial component ($b_j$) is field-like in nature and also follows the symmetry outlined in equation 1.23 [113,129].

Damping-like and field-like torques in HM|FM bilayers can be probed with new, low-current harmonic Hall voltage techniques [50,130] by electrically quantifying the slight magnetisation perturbations with magnetoresistive effects in the FM. The schematic of a typical SOT experimental setup is shown in figure 1.12.

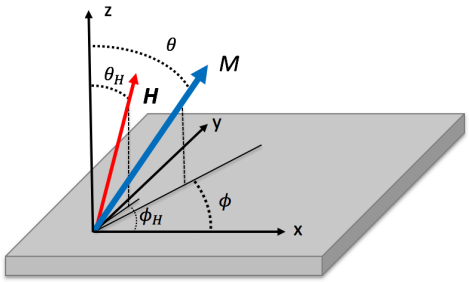


**Figure 1.12 Schematic illustration of the direction of magnetisation and applied field of a sample in a SOT experiment.**

The SOT from an in-plane $\boldsymbol{j}_c$ passing through a HM induces effective fields in an adjacent FM layer, which are both damping-like $\Delta\boldsymbol{H}_{\mathrm{DL}}$ and field-like $\Delta\boldsymbol{H}_{\mathrm{FL}}$ in nature. The SOT effective fields perturb $\boldsymbol{M}$ from equilibrium $(\theta_0, \phi_0)$, and measured voltages are related to the

modulated $\boldsymbol{M}$ amplitudes $(\Delta\theta, \Delta\phi)$ from the effective fields. Changes in transverse measured voltages arise from Hall magnetoresistances defined in section 1.1.5 and follow

$$V_{XY} = \frac{1}{2}\Delta V_{\mathrm{AHE}}\cos\theta + \frac{1}{2}\Delta V_{\mathrm{PHE}}\sin^2\theta\sin 2\phi. \tag{1.24}$$

To obtain an analytical solution for the harmonic Hall voltages in HM|FM systems, we follow the derivation completed by Hayashi *et al.* [130]. The equilibrium magnetisation direction $\boldsymbol{M}(\theta_0, \phi_0)$ is evaluated for any SOT effective field by taking the derivative of the sum of the magnetic energy components with respect to each angle $\theta$ and $\phi$. For magnetic films with $\boldsymbol{M}$ perpendicular to the surface, it is assumed that the equilibrium magnetisation does not deviate much from the film normal and there is no preferential direction of $\boldsymbol{M}$ in the film plane to simplify the solution. The harmonic Hall voltages in equation 1.24 may then be related to $\boldsymbol{M}$ and the effective fields are approximately [130]

$$\Delta H_{\mathrm{X(Y)}} = -2\frac{\left(B_{\mathrm{X(Y)}} \pm 2\xi B_{\mathrm{Y(X)}}\right)}{1 - 4\xi^2}, \tag{1.25}$$

where

$$B_{\mathrm{X(Y)}} \equiv \frac{\partial V_{2\omega}}{\partial H} \Big/ \frac{\partial^2 V_{\omega}}{\partial H^2}\Bigg|_{\boldsymbol{H}\parallel\hat{x}(\hat{y})}, \tag{1.26}$$

and $\xi = \frac{\Delta R_{\mathrm{PHE}}}{\Delta R_{\mathrm{AHE}}}$, $\Delta R_{\mathrm{PHE}}$ and $\Delta R_{\mathrm{AHE}}$ are the changes in the Hall resistances due to the PHE and the AHE, respectively. $V_{\omega}$ and $V_{2\omega}$ are the first and second harmonic voltages, respectively. In this measurement technique, the damping-like and field-like effective fields are $\Delta H_{\mathrm{DL}} = \Delta H_{\mathrm{X}}$ and $\Delta H_{\mathrm{FL}} = \Delta H_{\mathrm{Y}}$, respectively. To estimate SOT effective fields from harmonic Hall voltages, here $H_{\mathrm{Y(X)}}$ field sweeps are performed at low magnitudes to ensure the equilibrium magnetisation does not deviate significantly from the film normal.

However, to estimate the SOT effective fields from harmonic Hall voltages for magnetic films with $\boldsymbol{M}$ preferentially in the sample plane, $\boldsymbol{H}$ is swept slightly off-normal ($\theta_H \neq 0°$) at large fields, such that $\theta_0$ varies with $\boldsymbol{H}$ significantly. The effective fields can be related to SOT damping-like and field-like components $a_j$ and $b_j$ from the modified LLG equation 1.23 by measuring harmonic signals along $\hat{\boldsymbol{x}}$ ($\phi_H$ = 0° or 180°) with $(\Delta H_{\mathrm{X}}, \Delta H_{\mathrm{Y}}, \Delta H_{\mathrm{Z}}) = (-a_j\cos\theta_0, b_j, a_j\sin\theta_0\cos\phi_H)$. The SOT components $a_j$ and $b_j$ are approximated from the second harmonic voltage when $\theta_H \neq 0°$ following [130]

$$V_{2\omega} = -\frac{I_c}{2}\left[a_j\frac{\Delta R_{\mathrm{AHE}}}{2}\frac{\sin\theta_0\cos\phi_H}{H_K^{\perp}\cos 2\theta_0 + H\cos(\theta_H - \theta_0)} + b_j\Delta R_{\mathrm{PHE}}\frac{\sin^2\theta_0\cos\phi_H}{-H_K^{\parallel}\sin\theta_0 + H\sin\theta_H}\right], \tag{1.27}$$

where $I_c$ is the applied current and $H_{\mathrm{K}}^{\perp(\parallel)}$ is the perpendicular (in-plane) anisotropy field. With the PHE rotating $\boldsymbol{M}$ in-plane, and the AHE sweeping $\boldsymbol{M}$ out-of-plane, the $\Delta\boldsymbol{M}$ due to the SOT torque effective fields can be quantified and related to the magnetoresistances. In this geometry, the damping-like and field-like effective fields are $\Delta H_{\mathrm{DL}} = \Delta H_{\mathrm{Z}}$ and $\Delta H_{\mathrm{FL}} = \Delta H_{\mathrm{Y}}$, respectively.

### 1.2.4 Spin pumping

Spin pumping is Onsager's reciprocal phenomenon to spin-orbit torque in HM|FM bilayers [86,113]. A FM may be driven into resonance under particular magnetic conditions with an applied static field $\boldsymbol{H}$ and a perpendicular RF field $\boldsymbol{H}_{RF}$, governed by the Kittel equation 1.8. In metallic bilayers, the precession of a FM layer injects spin into an adjacent NM spin sink, such as a HM with good transverse spin relaxation at steady state [131]. In this way, the FM spin precession 'pumps' a DC spin current into the adjacent HM, as the name suggests. This technique is illustrated in figure 1.13.

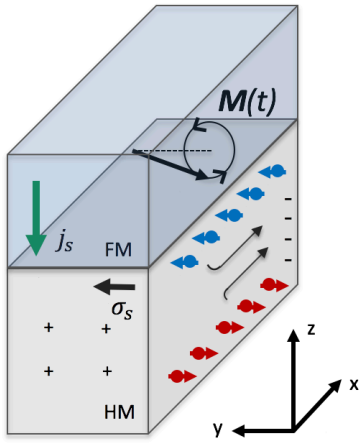


**Figure 1.13** Schematic illustration of the spin pumping technique. When the FM is driven into resonance, precession is maintained by dissipating magnetisation via a steady DC spin current passing into the HM layer. The ISHE then converts the spin current to a charge current. In open circuit conditions an electric voltage builds up along the HM bar in $\hat{\boldsymbol{x}}$.

The scattering theory of spin pumping was developed from that of adiabatic quantum pumping [96,132,133] and applies when the electronic relaxation is much faster than the variation of the scattering matrix. When $g_i$ is small, the real component of the spin-mixing conductance dominates and the spin current emitted into the HM is [132,134]

$$\boldsymbol{j}_s = g_r \frac{\hbar}{4\pi}\left(M \times \frac{dM}{dt}\right). \tag{1.28}$$

The loss of spin angular momenta from the FM layer to the HM during pumping creates magnetisation dissipation in the FM and enhances Gilbert damping [96]. This is experimentally observed by FWHM linewidth broadening [135–137], or via the change in absorption lineshape [24–27] of the RF magnetic susceptibility. The quantified linewidth broadening from additional magnetisation dissipation is directly proportional to the change in Gilbert damping $\Delta\alpha$ and the effective spin mixing conductance $g^{\uparrow\downarrow}$ [21]. Moreover, by measuring the ISHE voltage generated from the absorbed DC spin current along the HM, the absorbance lineshape is mirrored by a large voltage increase at FMR. Thereby, spin pumping is a useful technique for probing important spin-dependent parameters in the HM such as $\theta_{SH}$ and $\lambda$. Here, the magnitude of the spin current follows a different dependence on

fundamental parameters – $g_r\theta_{SH}$ – when compared to other measurement schemes. This will prove useful when decoupling HM spin-dependent parameters in the following experimental chapters.

### 1.2.5 Spin Hall magnetoresistance

The spin Hall magnetoresistance (SHMR) is a recently discovered resistive effect in a normal HM with large SOC when placed in contact directly with a magnetic layer [82,138,139]. Surprisingly, HM resistivity has been shown to depend directly on the magnetisation of the adjacent magnetic layer [3,92,140–143]. SHMR was first observed HM|FMI systems [33,139,144,145], and more recently HM|FM [3,92,140] and HM|anti-ferromagnetic (AFM) systems [146–149]. The physical origin of the SHMR can be explained by a resistivity change in the HM through the simultaneous action of the SHE and ISHE due to spin transport through, and reflection off of, the HM|magnet interface.

Owing to the SHE, when an in-plane charge current $\boldsymbol{j}_{c,x}$ is passed through a highly spin-orbit coupled HM, electrons will obtain transverse velocities due to spin-dependent scattering, as outlined in section 1.1.6. In open circuit conditions, a spin accumulation is established at the interface in $\hat{\boldsymbol{z}}$, while in closed circuit conditions when a magnetic layer is placed in direct contact with the HM, a $\boldsymbol{j}_{s,z}$ may pass through the interface. The spin polarisation direction $\boldsymbol{\sigma}_{s,y}$ of the spin current in the HM is perpendicular to both $\boldsymbol{j}_{s,z}$ and $\boldsymbol{j}_{c,x}$ following the Hall symmetry. Remember, the spin transparency at the interface will determine the magnitude of $\boldsymbol{j}_{s,z}$ and is a function of the relative angle of $\boldsymbol{M}$ in the FM and $\boldsymbol{\sigma}_s$ from section 1.2.2. Therefore, tuning the angle $\phi$ between $\boldsymbol{M}$ and $\boldsymbol{\sigma}_s$ controls how much spin is transmitted and reflected at the interface. In turn, the reduced (enhanced) spin current reflected at the interface $\boldsymbol{j}_s^R$ back into the HM, decreases (increases) conductivity of the film through the ISHE. In this way a magnetoresistance may be observed in a non-magnetic HM layer.

A HM|FMI bilayer is the most simple system in which to demonstrate SHMR since no charge current flows into the insulating layer. In this case, all the spin current injected from the SHE in the HM to the FMI has a spin polarisation $\boldsymbol{\sigma}_s$ non-collinear to $\boldsymbol{M}$, and the spin current is readily absorbed by the FM layer by virtue of a SOT. In the simplest case without electrons moving freely within the magnetic layer, there is no longitudinal spin relaxation in the FM and the spin current at the interface is given by scattering theory [82,138]

$$\boldsymbol{j}_s^{HM|FMI} = \frac{g_r}{e}\left(1 - \boldsymbol{m}_y{}^2\right)\mu_s^{HM|FMI}, \tag{1.29}$$

where it is assumed $g_r \sim g^{\uparrow\downarrow}$ and $\boldsymbol{m}_y$ is the $\boldsymbol{M}$ unit vector in $\hat{\boldsymbol{y}}$. However, in a HM|FM system where the magnetic layer is conductive, the mechanism becomes more complex. An illustration of SHMR in a HM|FM bilayer is shown in figure 1.14.

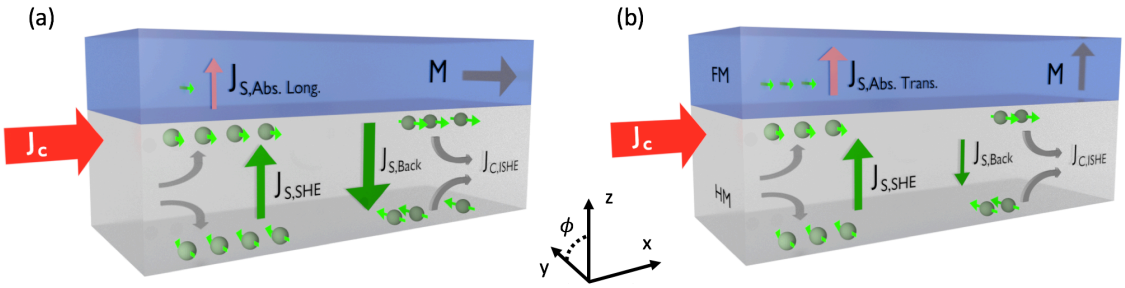


Figure 1.14 Schematic illustration of the spin Hall magnetoresistance. (a) When $\boldsymbol{M} \parallel \boldsymbol{\sigma}_s$, spins scattered through the SHE in the HM (grey) to the FM (blue) are more likely reflected at the interface than in (b) when $\boldsymbol{M} \perp \boldsymbol{\sigma}_s$, where part of the spin current is absorbed in the FM by locally torquing the magnetisation.

In figure 1.14 (a), when $\boldsymbol{M}$ in the FM is collinear (longitudinal) to $\boldsymbol{\sigma}_s$ of the conduction electrons in the HM ($\boldsymbol{M} \parallel \boldsymbol{\sigma}_s$), the spin transparency of the interface is governed by the spin-dependent conductance of each spin channel $g^{\uparrow(\downarrow)}$. However, in figure 1.14 (b) when $\boldsymbol{M}$ in the FM is non-collinear (transverse) to $\boldsymbol{\sigma}_s$ of the conduction electrons in the HM ($\boldsymbol{M} \parallel \boldsymbol{\sigma}_s$), the spin transparency of the interface is governed by the spin mixing conductance $g^{\uparrow\downarrow}$. For reference, the longitudinal spin relaxation illustrated in the schematic in figure 1.14 (a) does not occur in FMI layers, but only transverse spin relaxation occurs, as shown in panel (b). In HM|FM bilayers, longitudinal spin relaxation in (a) is less effective than transverse relaxation in (b), which creates an imbalance in $\boldsymbol{j}_s^{\mathrm{R}}$ depending on the relative angle $\phi$ between $\boldsymbol{M}$ and $\boldsymbol{\sigma}_s$, and changes $\rho_{xx}$ of the HM accordingly. The magnetoresistance is then given by

$$\frac{\Delta R_{\mathrm{XX}}^{\mathrm{SHMR}}}{R_{\mathrm{XX}}^{0}} = \frac{\Delta \rho_{xx}}{\rho_{xx,0}} = \frac{\rho_{\boldsymbol{M}\perp\boldsymbol{\sigma}_s} - \rho_{\boldsymbol{M}\parallel\boldsymbol{\sigma}_s}}{\rho_{\boldsymbol{M}\parallel\boldsymbol{\sigma}_s}}. \tag{1.30}$$

Measuring the SHMR of HM|FM bilayers is a useful way of estimating spin-dependent parameters of the constituent layers. Additionally, since the spin injection and detection follow the SHE and ISHE in the HM layer, respectively, the magnitude of the SHMR is proportional to ${\theta_{\mathrm{SH}}}^2$. Along with the interfacial spin conductivity given by $g_r$, the SHMR follows a $g_r{\theta_{\mathrm{SH}}}^2$ dependence, which is different to spin pumping and important for simultaneously estimating a unique set of values.

## 1.3 Aims of this thesis: Tuning spin transport with heavy metal microstructure

The prototypical HM|FM bilayer is a useful device for both observing a host of exciting new spin-based effects and probing the fundamental principles governing spin transport at the nanoscale. A considerable amount of research is now focused on these metallic devices for technological applications due to their low resistance-area product, low power-consumption and non-volatility. Specifically, manipulating the magnetisation orientation of a thin FM layer with the spin-orbit effects in an adjacent HM film through SOT potentiates the development of novel magnetic random access memory (MRAM) [9]. Additionally, the creation of an actionable electric voltage from the imbalance of spin gives rise to a host of magnetic sensing and energy harvesting possibilities, not least of which is that of a local, spin-based thermoelectric generator through the spin Seebeck effect (SSE) [8,150].

These exciting opportunities will only be realised, however, once the reliable control of the spin-dependent properties $\theta_{SH}$ and $\lambda$ within HM|FM bilayers is achieved. In order to engineer devices with reasonable voltage readout and large signal to noise ratios, the spin-to-charge (and back) conversion efficiency given by $\theta_{SH}$ must be maximised. Additionally, the distance over which a spin imbalance propagates – given by $\lambda$ – directly affects the desired thickness of constituent layers in a device. Evaluating and manipulating these parameters at the nanoscale is essential for good HM|FM device design. However, fabricating HM|FM bilayers by sputtering ultrathin films can yield significantly different microstructure than in the bulk, and precise morphology is highly sensitive to the particular growth parameters, including the substrate and HM surface free energies, temperature and pressure [151–154]. Specifically, electronic properties of constituent materials differ strongly in the ultrathin limit from electron surface and grain boundary scattering making a direct correlation to spin-dependent properties challenging.

Recently, it has become apparent that spin-dependent properties are, too, changing drastically in the ultrathin limit [86,87]. In fact, a long-standing controversy in literature remains over the magnitudes of spin-dependent parameters in high spin-orbit coupled HMs [61]. Table 1.1 serves to showcase the broad range of spin-dependent parameters reported at room temperature in Pt-based devices alone [57,95,155–161]. In an attempt to explain the reason behind this discrepancy, Nguyen *et al*. [87] and Sagasta *et al.* [74] have recently demonstrated that the changes of Pt resistivity in the moderately dirty regime account directly for the wide range of estimated $\lambda$ and $\theta_{SH}$ values in table 1.1 when Elliot-Yafet spin relaxation and intrinsic spin scattering dominate, respectively.

Table 1.1 A compilation of spin-dependent properties $\lambda$ and $\theta_{SH}$ in thin Pt-based devices measured with an array of different heterostructure compositions and spin transport techniques.

| Stack Composition | Measurement Technique | $\lambda$ (nm) | $\theta_{SH}$ | Reference |
|---|---|---|---|---|
| *SUB*\|$Ni_{80}Fe_{20}$(Py)-Cu-**Pt** | Non-local spin valve | - | $\approx 0.37$ | [156] |
| *$SiO_X$*\|Ta\|**Pt**\|Co\|MgO\|Ta | SOT efficiency | $4.8 \pm 0.5$ * | - | [87] |
| *$SiO_X$*\|**Pt**\|Co\|TaN | ST-FMR | $1.4 \pm 0.2$ | $0.17 \pm 0.02$ | [155] |
| *SUB*\|$Ni_{80}Fe_{20}$(Py)\|**Pt** | ST-FMR | $\approx 7$ | $\approx 0.08$ | [161] |
| Si\|$Ni_{80}Fe_{20}$(Py)\|**Pt** | Spin pumping | $3.7 \pm 0.2$ | $0.08 \pm 0.01$ | [157] |
| *GaAs*\|$Ni_{80}Fe_{20}$(Py)\|**Pt** | Spin pumping | $10 \pm 2$ | $0.013 \pm 0.002$ | [134] |
| *SUB*\|**Pt**\|Co\|$AlO_X$ | SHMR | $\approx 2.2$ | $\approx 0.28$ | [140] |
| YIG\|**Pt** | SHMR | $1.5 \pm 0.5$ | $0.11 \pm 0.08$ | [160] |
| YIG\|**Pt** | SHMR | $\approx 2.4$ | $\approx 0.04$ | [144] |
| YIG\|**Pt** | SHMR | $\approx 4$ | $\approx 0.03$ | [159] |
| YIG\|Cu\|**Pt** | Spin pumping + SSE + SHMR | $\approx 1.5$ | $\approx 0.11$ | [95] |

Although, the correlation between electronic and spin-dependent properties in HMs are becoming known, up to now there has been no complete study of the effect of HM microstructure on spin transport. In this thesis, we investigate the role of ultrathin HM microstructure morphology on spin transport properties within HM|FM bilayers (HM = W, Ta, Ru, Pt; FM = Co, CoFeB). We tune HM growth on $SiO_2$ wafers by either controlling the working pressure during HM sputtering or by seeding growth with a thin (1 nm) Ru or Ta buffer layer. An in-depth, spin transport study is undertaken to characterise microstructural changes by buffering HM growth and observing the impact on spin transmission and reflection at the HM|FM interface. With a systematic set of SHMR, spin pumping and SOT measurements on ultrathin Pt|CoFeB bilayers, we demonstrate that the HM microstructure plays an important role in spin transport in metallic HM|FM bilayers and potentially provides resolution to the widely varying values of $\theta_{SH}$ and $\lambda$ reported across the literature.

* This work demonstrated the dependence of $\lambda$ on $\rho_{Pt}$ with the Elliot-Yafet mechanism. This spin diffusion length was evaluated at $\rho_{Pt}$ = 16 μΩ cm.

# 2 Experimental Methods

This chapter highlights the sample fabrication, experimental design and techniques used to complete this work. Thin film device fabrication requires a combination of processes. First, if a specific device geometry is required, the desired the substrate is patterned and thin films are deposited with physical vapour deposition. In spintronic experimentation, sample geometry is typically set by a lithography process before depositing the thin films with DC magnetron sputtering. In this work, devices are patterned with photolithography since lateral geometric dimensions are only confined to the micrometre scale. Films are deposited in the specified pattern with DC magnetron sputtering to allow high sample throughput.

These thin metallic devices are probed with x-ray diffractometry to characterise microstructure morphology. High angle x-ray diffractometry (XRD) and low angle x-ray reflectivity (XRR) allow us to quantify crystallographic texture, thickness and roughness of ultrathin films. Furthermore, using high resolution scanning transmission electron microscopy, we can observe the growth mode of thin films directly. For magnetic thin films, we determine the magnetisation response to an externally applied field $\boldsymbol{H}$ with vibrating sample magnetometry (VSM).

To measure the magnetoresistive effects in thin films and heterostructures, we devised and constructed a versatile, low-noise electrical measurement setup. Since this was a momentous prerequisite to measuring spin transport effects, we outline the design and the capabilities of the setup in detail. In particular, important wiring methodology and instrumentation selection will be highlighted because of its direct impact on the ability to measure small nanovolt signals set by the resultant noise floor. In addition to hardware design, a modular computer application was written in Visual Basic.net (VB.net) as both an interactive experimental tool and to record data in real time during measurements.

## 2.1 Sample Preparation

The heterostructures featured in this work are composed of HM|FM bilayers. These all-metallic devices are deposited on 500 nm of thermally oxidised Si substrate to prevent current shunting during transport measurements. The 4" Si wafer may be diced either before or after photolithography depending on the number of devices required. If a large number are to be fabricated, the wafer is subject to a large, direct-write photolithography pattern immediately and cut after. Before photolithography, the surface of the $SiO_2$ is always cleaned with an acetone and then an isopropanol (IPA) rinse to remove any remaining residue. Once the sample surface has been treated, we spin coat photoresist, write the desired pattern with a laser and remove only the exposed pattern. Finally, DC magnetron sputtering deposits the thin films indiscriminately on the sample surface and the resist that remains on the

sample, which has not been exposed by photolithography, is removed in an ultrasonicated acetone bath lift-off process.

### 2.1.1 Photolithography

For sample characterisation with XRD and VSM, continuous thin films are necessary for probing structural and magnetic properties on devices with inherently low signals. However, for electrical spintronic measurements patterning thin film devices is necessary to provide a defined current direction. Furthermore, specific geometries can increase the signal to noise ratio (SNR) during electrical readout. In this work, the devices are patterned with direct-write photolithography (PL) due to their geometric variability and relatively large, micron-sized dimensions in the plane of the substrate. Instead of projecting light through a physical mask bearing the desired pattern by a method known as flood exposure, direct-write tools (or digital mask aligners) were used, which store the pattern in the software and project it onto the sample surface. Hereby, mask geometries could be varied at will to optimise the device design for each electrical measurement scheme. Other alternative methods such as focused ion beam (FIB) milling and electron beam lithography (EBL) are also common, but typically only required when higher resolution is a necessity in nanoscale devices.

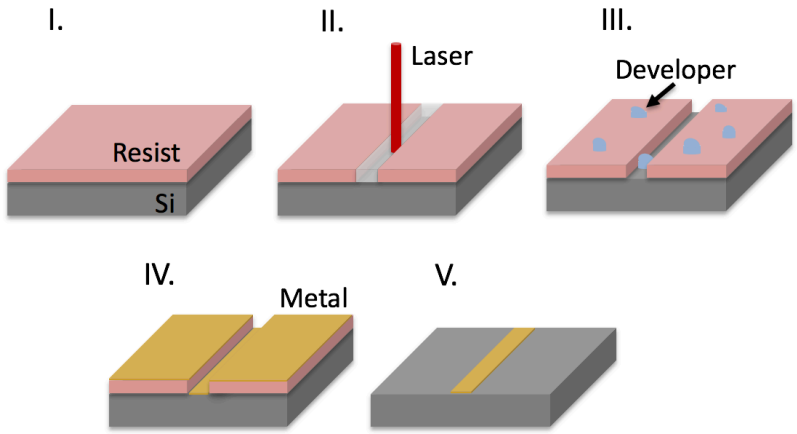


Figure 2.1. Schematic flow diagram of photolithography steps for producing thin patterned devices with a negative photoresist. See text for the full procedure.

The methodology behind photolithography is to spin coat the sample surface with a thin coating of photo-sensitive polymer (a photoresist) and expose it using a laser to write the pattern. In this work, a negative photoresist is used, which means by definition that the portion of the photoresist exposed to the laser is crossed-linked and easily removed in a developer solution. This process leaves the unexposed photoresist coating the substrate and only the desired device pattern open to atmosphere for physical vapour deposition. The process can be visualised in figure 2.1 and is fully outlined in detail for this work in the following steps:

1) The $SiO_2$ substrate surface is treated with acetone and IPA as previously mentioned.
2) The substrate is covered with ECI 3007 negative photoresist by spin coating. Spinning the wafer at 5000 rpm for 45 s produces a uniform thickness of ~600 nm for ECI 3007.
3) The sample is pre-baked on a hot plate at 90° for one minute to drive off excessive volatile resist solvents.
4) A 405 nm wavelength rastering laser exposes the sample specified sample area with a Durham Magneto-Optics Microwriter™ focused down to 0.5 µm on the sample surface. The dose (amount of energy in the columnated beam) and focus (from the top of the sample) are the two essential parameters required to achieve sharp, well-defined patterns.
5) The sample is post-baked on a hot plate at 115° for 1 minute to allow acid radicals to diffuse across the height of the resist profile. This smooths edges from interference effects written by the laser.
6) If a large number of devices are written on an entire 4" Si wafer at one time, the wafer is cut at this stage, before the development, to ensure no shards from cutting are deposited into the written pattern.
7) The sample is submerged in AZ™-326 MIF developer for 45 s to remove the exposed areas of the negative resist. The sample is then transferred into two consecutive beakers of de-ionised (DI) water for 10 s each to halt development by dilution and ensure minimal re-deposition of lifted-off resist on into the valleys. The DI water is blown off with a $N_2$ gun to ensure no $H_2O$ residue.

The device patterns were drawn up in AutoCad™ and transferred to the Microwriter™ prior to step 4. The device geometries differed for each experiment to maximise the SNR ratio and will be specified in each experimental chapter individually.

The aforementioned photolithography steps comprise what is known as a one-step process, which is sufficient only when the entire device is comprised of the same heterostructure composition. In cases where different sections of the device require different material compositions, a repeat of the PL steps was required for a two-step PL process after the first deposition is complete. This second step was necessary, for example, to grow the 20 nm Pt contact pads in the spin pumping device geometry in figure 5.4. To do so, alignment marks were pattered and deposited in the first step ensuring a ~ 5 µm overlap and good electrical connection between the two depositions at all points of contact. After the second development process, the ~ 5 µm metallic layer exposed to atmosphere at each contact was bombarded briefly (10 s at 210 V and 0.12 mA) with $Ar^+$ ions to remove any oxidised metal at the surface adding to the contact resistance and to prevent noise. This technique is known as Ar ion milling.

### 2.1.2 Sputtering in thin film deposition

All metallic thin films deposited in this work were fabricated by direct current (DC) magnetron sputtering, which is a common physical vapour deposition (PVD) technique for the growth of thin films by both industry and academia alike. Sputtering is more desirable than other PVD techniques such as thermal evaporation because it more easily deposits high melting point heavy metals. Furthermore, magnetron sputtering delivers high-purity (99.99%) films with excellent coverage for small device features, uniformly over large sample areas [162].

In sputtering PVD, an arc of ionised process gas is established between two electrodes to accelerate high-energy positive ($Ar^+$ in this case) ions at a cathode (or target) of the desired material. The bombardment of the target surface ejects surface atoms, which are isotropically deposited in the above hemisphere. A subset of the atoms then condenses on the sample surface placed at the anode. Because this PVD technique relies on line-of-site deposition, a long mean free path is vital to obtain reasonable growth rates. The mean free path is directly influenced by the altering working pressure during deposition. Unfortunately, even at high vacuum, this basic DC sputtering process still only delivers slow growth rates unless high voltages (~ 2.5 kV) are applied [163]. To increase the quality of the plasma, and hence the efficiency of the system, the cathode is subjected to alternating polarity magnets (magnetrons) to create a magnetic field and trap electrons. Primary and secondary electrons from the ionisation and bombardment processes become localised to a region directly above the cathode. Thereby, the magnetrons significantly increase the propensity of an ionising collision to sustain the arc and reduce requisite voltages to ~ 300 V.

To enable high PVD throughput, while maintaining a low base pressure (at a minimum $2 \times 10^{-8}$ mbar and $3\text{-}6 \times 10^{-8}$ mbar in a growth series) in the main chamber, a load-lock was installed to reduce the pump-down time. The chamber is equipped with six magnetrons to deposit multiple material layers without breaking vacuum and operated at a ~ $7 \times 10^{-3}$ mbar working pressure and ~ 20 °C unless specifically stated otherwise. The growth rate for each metallic target is calibrated with one of two methods. The first is by measuring the step height between the $SiO_2$ sample surface and the top of an ~ 30 nm deposited film with atomic force microscopy. A number of step heights are measured across the sample and averaged. The second is by evaluating the film thickness with x-ray reflectivity. In each case, the real measured thickness was divided by the deposition time to calculate the growth rate. For HM films used in thickness-dependent experimentation in chapters 3-6 such as Ta, W and Pt, calibration with XRR is used because of its higher precision.

# 2.2 Sample Characterisation

## 2.2.1 Vibrating sample magnetometry

Vibrating sample magnetometry was used to quantitatively characterise magnetic thin films by comparison to a reference Ni calibration sample. Magnetic properties of films such as the coercivity $H_c$, saturation magnetisation $M_S$ and hard-axis saturation field (or anisotropy field) $H_K$ were extracted from the in-plane and out-of-plane $M$ versus $H$ hysteresis loops. For each applied field $H$, the VSM measures the magnetic response of a vibrating sample.

The sample is fixed to the end of a rigid quartz rod, which is vibrated at a frequency $f_{VSM}$ between the pole pieces (mounted in $\hat{\boldsymbol{x}}$) of a large, water-cooled 1.75 T electromagnet. Pick-up coils mounted inside the pole pieces detect an alternating, induced EMF from the oscillating stray field of the vibrating magnetic sample. This EMF is directly proportional to the magnetic moment of the sample from Faraday's law of induction [164]. The induced voltage from a time-varying magnetic flux $\boldsymbol{\Phi}$ through the area of a coil is given by Faraday's Law [165]

$$V = -\frac{\delta \boldsymbol{\Phi}}{\delta t} = \frac{\delta \boldsymbol{\Phi}}{\delta x}\frac{\delta x}{\delta t} \tag{2.1}$$

and from Biot-Savart law, reciprocity states a $\boldsymbol{\Phi}$ produced by a magnetic moment $\boldsymbol{\mu}$ in a coil is equivalent of $H(r)$ from a coil carrying current $I$

$$H(r) \cdot \boldsymbol{\mu}(r) = I\Phi. \tag{2.2}$$

Applying equations 2.1 and 2.2, while assuming that sample vibration follows simple harmonic motion $\frac{dx}{dt} = A\omega\, cos(\omega t)$ with amplitude $A$ and angular frequency $\omega = 2\pi f_{VSM}$ yields an alternating voltage

$$V = \frac{d}{\partial x}\left(\frac{H(r)}{\boldsymbol{I}} \cdot \boldsymbol{\mu}(r)\right) A\omega\, cos(\omega t) = \mu Q(r) A\omega\, cos(\omega t), \tag{2.3}$$

where $Q(r)$ is called the sensitivity function as it represents the coil sensitivity in $\hat{\boldsymbol{x}}$ [166].

On the MicroSense™ EZ7 VSM used in this work, the alternating voltage is frequency locked with a Stanford Research Systems SR830 lock-in amplifier (at $f_{VSM}$ = 75 Hz in this case), yielding a room temperature (RT) noise floor of $\sim$ 1 x $10^{-6}$ emu at an average of 300. The diamagnetic response of the quartz rod was calibrated and subtracted as a background from the measured voltage when appropriate to give the accurate magnetic response of the sample.

## 2.2.2 X-ray diffractometry

XRD is an effective method of probing the sample atomic spacing and crystallinity with x-rays to provide information about lattice structure (crystalline texture), internal strain, dislocations and much more [167]. In the Bruker D8 XRD used in this work, the x-rays are generated in a cathode ray tube by heating a W filament to produce electrons, which are

accelerated towards a Cu target to dislodge inner shell electrons of the Cu. This process produces a mixture of Cu $K_{\alpha 1}, K_{\alpha 2}$ and $K_{\beta}$ x-rays, which are typically filtered by foils or crystal monochromators, collimated and fired at the sample surface. The basic principle of operation follows. X-rays penetrate the lattice planes of the thin film and are scattered in preferred directions creating distinct interference patterns. In a typical XRD scan, the sample stage (rotating at an angle $\theta$) and detector arm (rotating at an angle $2\theta$) are coupled to maintain a fixed relative angle at the specular reflection condition. When incident x-rays satisfy the Bragg's law in equation 2.4, constructive interference is achieved and a peak in the number of x-rays are collected at the position sensitive detector (PSD) results.

$$n\lambda = 2d\sin\theta \tag{2.4}$$

Where $n$ is an integer, $\lambda$ is the wavelength of x-ray (1.5418 Å for a weighted average of Cu-$K_{\alpha}$), $d$ is the distance between atomic planes and $\theta$ is the angle between the lattice plane and the incident radiation. The diffraction peaks for all materials penetrated by the incident x-rays are superimposed in the $\theta/2\theta$ scan.

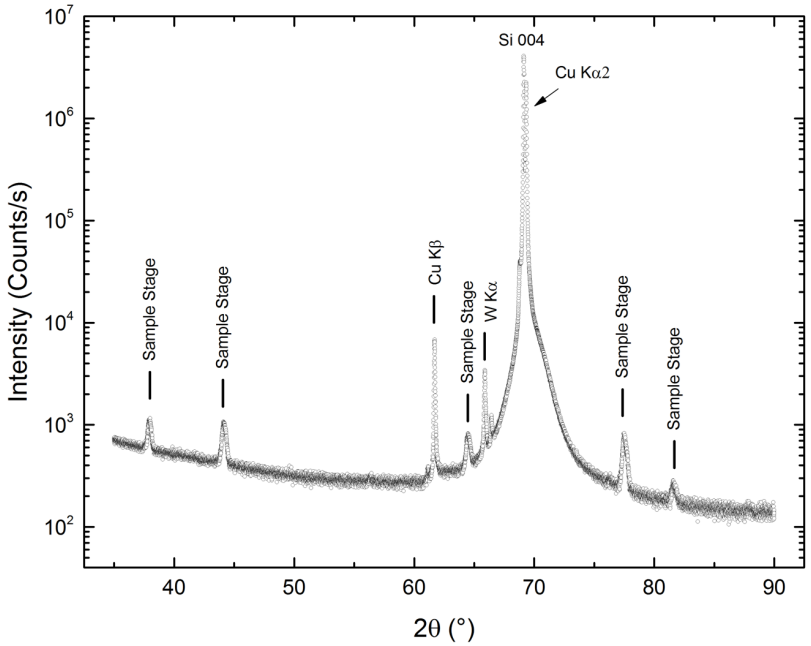


Figure 2.2. A high-angle $\theta/2\theta$ x-ray diffractometry scan recorded on a baseline $SiO_2$ thermally oxidised Si substrate with dimensions of ~ 1 x 1 $cm^2$ to reference irrelevant peaks from the sample backplate stage and spurious diffraction peaks from non-Cu-$K_{\alpha}$ radiation.

In the Bruker D8 used for this work, the cathode ray tube is driven at a filament current of 40 mA and voltage 40 kV. A typical sample (dimension ~ 1 cm x 1 cm) is stuck down onto the sample plate with a small vacuum pump. The system is re-zeroed by maximising the throughput of radiation directly into the PSD and subsequently aligned by moving the sample into the beam path to cut the incident beam in half with the cross-section of the sample. Iterating about the three angles of rotation of the sample stage while fixing the detector at $2\theta$, the radiation impinging on the PSD is maximised. Finally, the sample stage and detector are driven to the position of the Si 004 diffraction peak ($2\theta$ = 69.12928°, $\theta$ =

34.56464°) and three angles of rotation of the sample stage are iterated about to maximise counts. At this point, the slit in the cathode source is changed to 0.1 mm to minimise stray radiation on the stage backplate and open the 1-D PSD to 1 mm and set to 'auto' before running the coupled the high-angle $\theta/2\theta$ scan (typically 35° to 90°).

Since the ultrathin films used in this work yield low scattered intensities in XRD, no monochromator is used resulting in spurious diffractions peaks from Cu-$K_\beta$ and W-$K_\alpha$ radiation impinging on the sample or the backplate. Figure 2.2 shows a typical XRD $\theta/2\theta$ scan on a thermally oxidised Si substrate baseline sample without thin film deposition. These peaks fall at significantly different $2\theta$ values than the desired Pt(111) ($2\theta$ = 39.7634°) and Pt(222) ($2\theta$ = 85.7121°) peaks from Cu-$K_{\alpha 1}$ radiation and so do not interfere with the characterisation of Pt films.

### 2.2.3 X-ray reflectivity

In low angle grazing incidence XRR, x-rays are accelerated at low incident angles $\theta$ to measure the specular reflectivity from the surfaces and interfaces in a thin film heterostructure. The x-rays are generated by the same method as for XRD and impinge on the sample with incident wavenumber $k$. The radiation laterally probes the average electron density and lattice planes to quantitatively extract film thicknesses of 0.1 nm – 1000 nm, roughnesses < 2 – 3 nm and densities of constituent thin film layers. The measured radiation reflected from the sample has a non-zero component perpendicular to the surface $\hat{\boldsymbol{z}}$ with a wavevector at $q_Z = 2k\sin(\theta)$ yields a typical XRR curve displayed in figure 2.3.

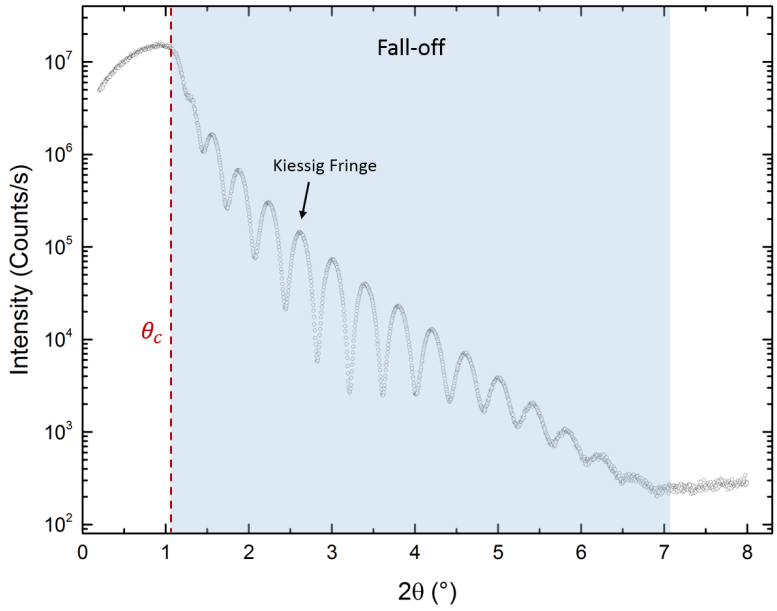


Figure 2.3 A prototypical low-angle $\theta/2\theta$ x-ray reflectivity scan from 0.2° to 8° of a ~ 21.5 nm thin Pt continuous film deposited on a thermally oxidised Si substrate.

The position of the critical angle $\theta_c$ depends on the material density ($\theta_c \sim \sqrt{\rho}$), as more x-rays are scattered at higher angles in materials with higher electron density. Above $\theta_c$, interference from the scattered x-rays reflected into the detector create Kiessig fringes of period

$$\Delta q_z = \frac{2\pi}{d}. \quad (2.5)$$

From the periodicity of the Kiessig fringes, an accurate measure of the thin film thickness $d$ can be quantified. Additionally, XRR is particularly sensitive to roughness, which manifests in a deviation from total Fresnel reflectivity due to imperfect surfaces and interfaces. Here, when reflection becomes predominantly diffuse rather than specular, the reflected intensity (the Kiessig fringes) at angles larger than $\theta_c$ is suppressed.

XRR in this work is performed on the same Bruker D8 diffractometer as XRD. When fully characterising a sample, both low angle XRR and high angle XRD are measured without re-aligning the detector or sample to the incident beam path. If only performing XRR, the alignment is consistent with that of XRD for calibrating the straight-through beam and the beam incident on the sample surface. However, during the percise final alignment stage, a prominent Kiessig fringe is used instead of aligning to a diffraction peak to maximise counts.

### 2.2.4 High angle annular dark field scanning transmission electron microscopy

Transmission electron microscopy (TEM) reveals the sub-micron, internal structure of solids and it was used in this work to probe the microstructure of ultrathin Pt films. Scanning transmission electron microscopy (STEM) differs from standard TEM by converging the bright electron beam into a fine, focused probe, which is rastered across the sample. The resolution, determined by the beam size, is set by the spherical aberration $C_S$ of the probe-forming, condenser lens [168]. In aberration-corrected systems, like the FEI Titan$^3$ used in this work, the $C_S$ coefficient can be optimised by the technician to reduce the beam tails and achieve incredible sub-angstrom beam focus.

In this system, the measured signal comes from only very few primary electrons, fired at 300 keV in our system, which are scattered by atomic nuclei in the film to high angles (~50 mrad in the Titan$^3$) incoherently through Rutherford scattering. As such, the HAADF collection process depends strongly on the thickness of the cross-sectional lamella cut by focused-ion beam (FIB) irradiation through which the electrons are impinging and the atomic number $Z$ (the contrast typically goes as $Z^{1.7}$) of the sample [168,169]. The HAADF ring-shaped detector collects a signal directly proportional to the number of incident electrons. Typically, a capping Pt layer is deposited in the FIB to protect the film surface before STEM. However, since the material of interest here is an ultrathin Pt layer, a 400 nm protective layer of thermally evaporated Al is deposited, instead, as a light metal with a small $Z$ to provide good contrast.

In a similar vein, an energy-dispersive x-ray (EDX) technique is used to detect the material composition of the ultrathin films. Here, the inelastic scattering of impinging, high energy electrons knock atomic electrons out of position. Higher-orbital atomic electrons drop down to fill the vacant holes releasing a quantum of energy (the x-ray) specific to the band structure of the material. Note, when probing the material in the constituent layers, there was a significant overlap in EDX signal from the Ta $l_\alpha$ = 8.1 keV x-ray with that of the Cu STEM grid $k_\alpha$ = 8.0 keV x-ray. Therefore, the lamella was deposited on a Mo STEM grid instead of a standard Cu grid in order to distinctly observe the presence of Ta in the film heterostructure.

## 2.3 Spin transport measurement setup

To measure magnetoresistive effects in thin film monolayers and heterostructures, we devised and constructed a compact, low-noise electrical measurement setup. This setup is designed to measure both spin (calori)tronic effects by recording spin-dependent voltages arising from electrical and thermal gradients. Probing these small, spin-mediated electronic effects with high SNRs requires specific instrumentation and wiring methodology. The instrumentation was specifically selected to not only source (measure) DC currents (voltages), but also to apply AC voltages and record resultant harmonics with phase-sensitive detection. Phase-sensitive detection is particularly useful for discerning small voltages from large backgrounds. In addition to the construction of a physical setup, a computer application was written in VB.net as both an interactive experimental tool and to record data in real time. In this section, we provide an overview of the construction and capabilities of the spin transport measurement setup.

### 2.3.1 System overview

All of the instrumentation, the electrical breakout boxes and the operating computer are rack-mounted or placed on top of the 19" rack with the operating computer as seen in figure 2.4 (a). Only the GMW 3470 electromagnet and the sample holder supporting structure securing the continuous flow MicrostatHe2 cryostat are fixed directly to the Newport ST damped optical table in figure 2.4 (b). In this way, the setup is highly mobile with the rack easily transportable, yet the stage of the sample holder is securely fixed on the optical table relative to the pole pieces of the electromagnet. Moreover, the device sits far away from the measurement instrumentation to prevent any mechanical perturbation from the rotation of the electromagnet.

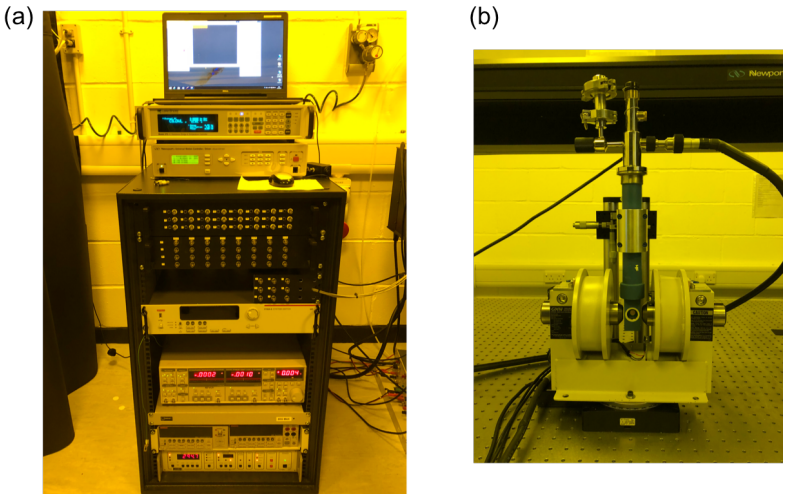


Figure 2.4. (a) An image of the spin transport setup rack with all measurement electronics, breakout boxes and the operating computer. (b) An image of the GMW 3470 electromagnet mounted on the rotational stage. The MicrostatHe2 cryostat is mounted in between the electromagnet pole pieces with optical access at the front of the cavity. The thicker, black Fischer cable on the top right of the cryostat transports the electrical signals to the cryostat breakout box.

Figure 2.5 is a schematic illustration of the system constructed and used for magnetoresistace measurements in this work. The system applies an external field *H*, which alters the magnetisation *M* of the thin film, while simultaneously aquiring electrical voltages passing from the device through the cabling and breakout boxes with the desired instrumentation. The spin transport measurement application (STMA) written in VB.net running on the operating computer controls the field magnitude and angle, current sourcing and voltage detection, data display and recording. Below we briefly describe the setup specifics to provide more insight into how the system operates.

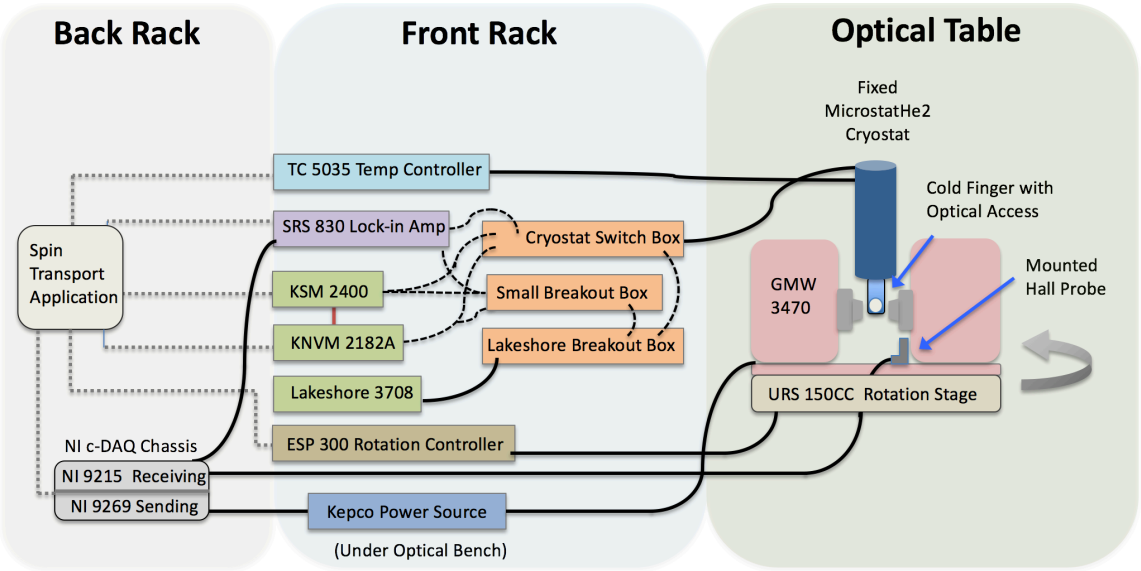


Figure 2.5 (a) Schematic illustration of the entire spin transport rig separated by physical location. All solid wires represent fixed wiring, while the dark dashed wires represent removable BNCs from the instrumentation to the breakout boxes. The light grey dashed lines illustrate connection from instrumentation to the operating computer, which runs the STMA.

The modular system was constructed with the possibility of running two general types of measurements: one at low temperature limited to low applied field $H$ and one at room temperature with larger applied fields. For low-temperature measurements, the MicrostatHe2 cryostat was modified to house the requisite wiring, chip carrier and socket with 24 available pins for sourcing and recording electric voltages. The internal wiring was connected to a robust Fischer cable at the top of the cryostat, which was, in turn, connected to the instrumentation. This is illustrated in figure 2.4 (b). A full detailed explination of the design and engineering of the retrofit is available in Appendix A. However, in low-temperature experimentation, the external field magnitude is limited to $\mu_0 H \sim 3.25$ kG due to the broad frame of the cryostat ($\sim$ 32 mm), which constrains the minimum pole spacing. In order to apply larger fields, two compact, removable sample holders were constructed from a Cu BreadBoard for experimentation at room temperature (RT). Each holder was connected to an 8-pin dip socket mounted on a brass rod as illustrated in figure 2.6, which transmits signals from the wire-bonded device to the instrumentation. In figure 2.6 (a), an illustration shows the sample holder sitting between the electromagnet, which is screwed onto a URS 150CC rotation stage. The two holder variants shown in figure 2.6 (b) and (c) allow for an out-of-plane and an in-plane $H$ rotation, respectively. With these compact holders, all three planes (XY, XZ and YZ) of rotation in the sample reference frame are possible depending on the orientation of the sample placement on the out-of-plane field holder. These narrow holders allow a minimum pole spacing of 12 mm and a resultant field of $\mu_0 H \sim 9.75$ kG.

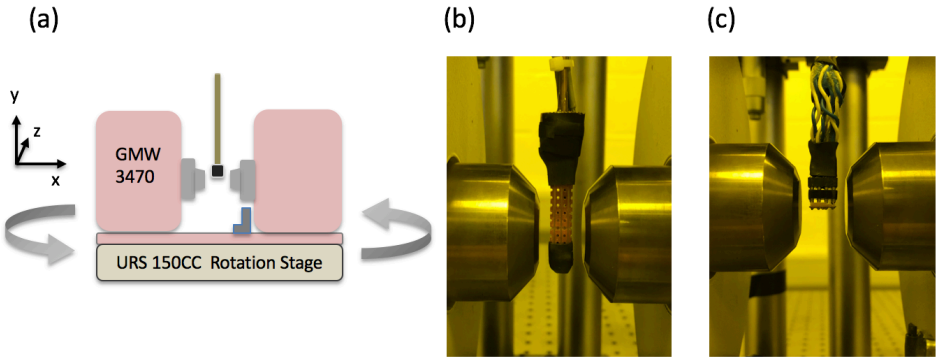


Figure 2.6 Illustration of the GMW 3470 electromagnet mounted on a rotational stage for rotating the applied magnetic field. An image of the removable, compact sample holder constructed for (b) out-of-plane (XZ and YZ) and (c) in-plane field (XY) rotation in the sample reference frame. In (c) the sample sits flush at the bottom of the holder and would be hardly visible in this image.

To be able to rotate the external field about the sample holder, holes were drilled into the GMW 3470 electromagnet base plate and it was screwed into the URS 150CC Newport rotational stage. A Newport ESP300 3-axis motor controller and driver powers the stage and provides a 1000$^{th}$ of a degree rotation resolution of the field angle. The field magnitude is driven by a Kepco Bipolar 6 A / 40 V power supply and adjusted by a voltage sourced by a National Instruments NI 9269 card. The STMA interfaces with the National Instruments cDAQ 9188XT chassis, which houses both NI 9269 card and cRIO 9215 cards to continuously source

$\pm$ 10 V and detect analogue voltages, respectively. The NI 9269 card also sources a constant 5 V, to power the Hall probe mounted on the base of the GMW 3470 electromagnet for real time field measurements. Simultaneously, the Hall voltage generated from the 3-pin, linear Allegro A1301 Hall effect sensor was calibrated to the external field and is detected by the NI cRIO 9215 card. During experimentation, these values are averaged over the measurement window to get an instantaneous value. In this way, the STMA both controls the applied field magnitude with a calibrated $V_{\text{out}}$ and the angular position in which the field was applied. In the following sections, general wiring principles and instrumentation specifications will be discussed further.

### 2.3.2 Wiring and grounding

To perform electrical spintronic measurements, thin film devices are wire bonded to a sample holder and placed within the pole pieces of the electromagnet. Since the voltages must travel to and from the instrumentation, careful cable selection, and robust sample holder and breakout box wiring was necessary for confidently measuring magnetoresistive signals with longevity. Below the methodology for reducing noise and wiring specifics are outlined.

To obtain an adequate SNR for measuring nanovolt signals, the electrical and mechanical noise must be minimised. In this system, all wires were shielded with metallic foil to reduce electromagnetic (EM) interference from external EM radiating sources. The conductive shield acts as a Faraday cage to minimise capacitive-coupled electrical noise from external sources (e.g. mobile phones and power lines) by maintaining a constant voltage across its surface. Furthermore, to minimise induced EMF voltages from time-varying magnetic fields, all cabling was wound into a twisted pair configuration.

Furthermore, the Faraday cable shielding for each current carrying line was only grounded at one end to avoid massive ‘ground loops', which act as large induction antennae for EM waves. To prevent this, a star-point connection principle was adhered to, whereby all shields connect only at one node (a star-point). This method was deployed on a large scale creating multiple small ground nodes, which cumulated at a large-node star point on the 19" rack, connecting cable shields, breakout box ground cables, and instrument grounds. Furthermore, all equipment was connected through one of two power bars to the mains. Poor mains grounding prompted the separation of the sensitive voltage source/detection equipment from the heavy equipment (the Kepco power source, the ESP 300 controller, the TC 5035 temperature controller) onto different circuits. This also made the (un)plugging much more straightforward when moving the rack.

Each sample holder is custom wired and connected to the BNC connectors of a breakout box. More specifically, the compact Cu BreadBoard sample holders are soldered to 8-pin dip sockets and wired with four twisted-pair, shielded wires to the small breakout box. The wiring and electrical retrofit of the MicrostatHe2 cryostat was far more complex due to thermoelectric considerations and spatial restrictions, and is detailed in Appendix A. The

BNC sockets located on the breakout boxes at the front of the rack may then be easily connected to any desired piece of instrumentation with BNC cables, depending on the system operator.

### 2.3.3 Measurement instrumentation

In this work, electrical voltage measurements are performed in the plane of the device either longitudinal or transverse to $\boldsymbol{j}_{c,x}$ as illustrated in figure 1.5. The voltages are sourced/detected by three electrical systems in this setup. These three systems are outlined below.

1. The Lakeshore 3708 is an AC resistance bridge designed for measuring ultra-low noise, 4-terminal AC resistance directly from a voltage. Low power AC excitation (down to 55 pA) is available at five frequencies (all under 20 Hz) and multiple measurements may be recorded simultaneously across shielded resistor leads through the eight channel scanner and pre-amplifier. Through the phase sensitive detection, small signals may be observable on large background resistances. In addition, the AC coupling at each amplifier phase allows this resistance bridge to perform with more gain and greater sensitivity that DC systems, yielding a low input noise performance of 2 n$V_{\mathrm{RMS}}/\sqrt{\mathrm{Hz}}$. This device has full-scale deflection ranges of 2 mΩ to 2 MΩ, however, the excitation current is limited in samples with large $R_{\mathrm{XX}}$, such that the $V_{\mathrm{mixer}}$ (the phase sensitive detector) does not exceed 10 V.

2. The Stanford Research Systems SRS 830 is a lock-in amplifier sourcing constant voltage, which uses phase sensitive detection to measure differential input voltages down to 6 n$V_{\mathrm{RMS}}/\sqrt{\mathrm{Hz}}$. With high a dynamic reserve (>100 dB) and up to 24 dB/oct roll-off, the SRS 830 can accurately lock-in to a narrow frequency band and measure small voltages. Unlike the Lakeshore 3708, the lock-in amplifier can source voltage at frequencies up to 256 kHz and measure *n* harmonics. The SRS 830 was operated with all filters disabled to ensure the detection of an unattenuated differential voltage and driven at frequencies larger than 500 Hz (off-multiple of 50 Hz) to reduce $1/f$ noise and mains noise. By measuring with a 300 ms time constant, averaging successfully reduces the RMS noise. The SRS 830, however, is also limited in capacity to supply large $\boldsymbol{j}_c$ in resistive devices, with a maximum $V_{\mathrm{RMS,out}}$ = 5 V sinusoidal voltage.

3. A Keithley 2400 Source Meter (KSM) (in 2-terminal mode) and a 2-terminal 2182A Nanovoltmeter (KNVM), may be used to source DC currents and measure voltages, respectively. The KSM drives large current densities, but by definition, this DC measurement type is not phase-sensitive and therefore may be afflicted by spurious voltages. However, a very low-frequency lock-in measurement may be simulated with the Keithley pair known as ‘delta mode'. By wiring a trigger cable between the

pair, an alternating current polarity sourced by the KSM is measured by the KNVM. The voltages are subtracted to remove slow background drift signals, such as thermoelectric offsets.

To measure a signal with adequate SNR, the minimum distinguishable signal size must be larger than the RMS noise of the system, which is dependent on both the load resistance of the device and the driving current. Since the RMS noise is centred about zero, it is equivalent to the standard deviation of the measured voltage. The resolution of the device is then the minimum discernible voltage over the background voltage $\left(\frac{V_{\mathrm{RMS}}}{V_0}\right)$. Figure 2.7 shows the RMS noise and resolution of each instrument quantified by measuring approximately 50 voltages on a series of three industrial resistors (short, 100 Ω and 10 kΩ) for each instrument at RT.

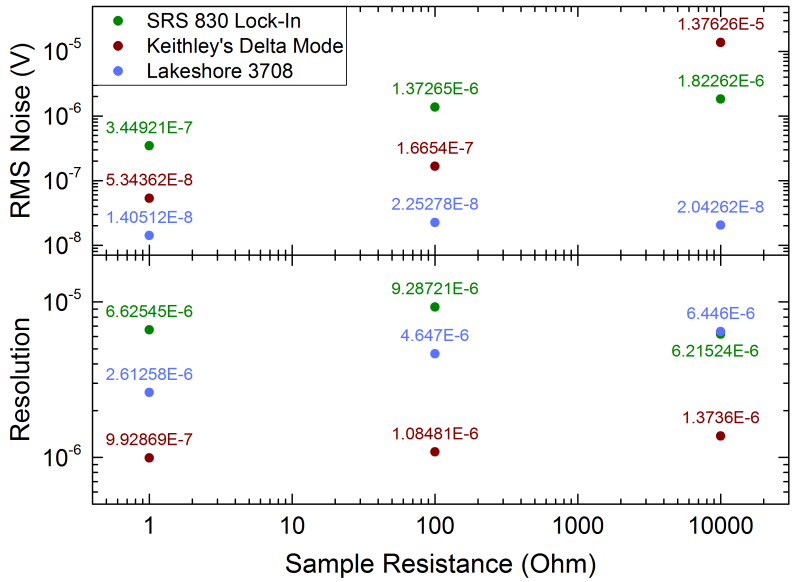


**Figure 2.7. RMS noise and resolution measurements on a series of test resistors for each instrument at 1 mA drive current. The raw resistances obtained from the Lakeshore 3708 were converted to voltages by Ohm's law and displayed in volts for comparison.**

Figure 2.7 illustrates that the Lakeshore 3708 has the lowest noise floor due to the low-noise pre-amplifier, while the two Keithleys in delta mode was (unsurprisingly) the noisiest. However, due to the larger sensitivity range on the KNVM 2182A, delta mode yielded the highest resolution (lowest value) across the entire load resistance range. The resolution of the Lakeshore 3708 was second best and the SRS 830 lock-in amplifier, the worst. The Lakeshore 3708 lacks the sensitivity range of the KNVM 2182A, and so at a given $\boldsymbol{j_c}$, the resolution is lower. Overall, when measuring small signals on a large background, which are not expected to be confounded by spurious voltages, a DC measurement with the Keithleys is optimal. When measuring small signals on smaller backgrounds, the Lakeshore 3708 is best due to its low noise floor. Finally, the SRS 830 lock-in amplifier is vital for separating in the in-phase (X, 0°) and out of phase (Y, 90°) components of an AC voltage, overcoming parasitic noise at low frequencies and measuring *n* harmonics.

### 2.3.4 Spin transport application

An extensive spin transport measurement application was written in VB.net and installed on the operating computer. VB.net is an object-oriented language written similar to C++, making it highly powerful for creating graphical and interactive user interfaces, such as laboratory applications. The hard code will not be supplied in this document, but the programming methodology and application functionality follows.

The application is written in a modular fashion and is separated into segregated ‘classes', each with their own methods and parameters. In the STMA, classes are defined for both instrument type and experiment type. Multiple of the same instrument with different operating parameters may be used with the same class, through the creation of new ‘instances'. This compartmentalisation is run-time efficient, as it only executes the code of the specified experiment, with user-selected instrumentation.

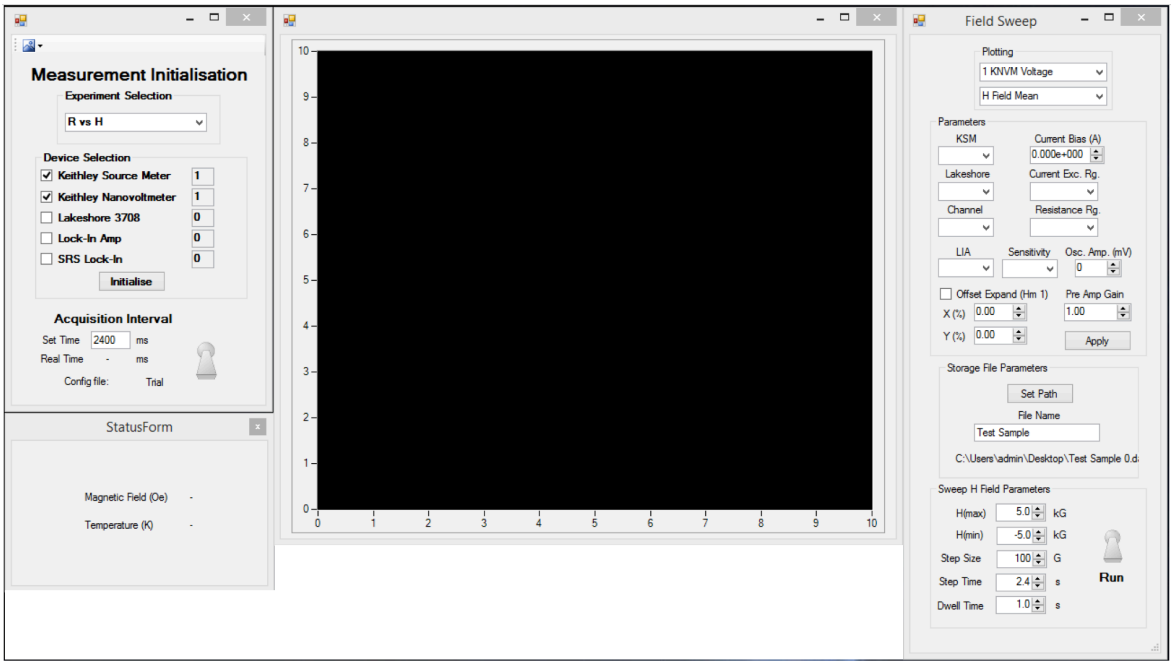


Figure 2.8. The user interface of the STMA awaiting use. On the left, the instrumentation, experiment type and acquisition interval is selected. In the middle graph, the measured signals are updated in real time during operation. On the right, the ‘Field Sweep' experiment is loaded, where the plot x and y axes are selected, specific instrument parameters are altered and the external magnetic field sweep parameters are specified.

The main functions of the application are to send commands to instrumentation with user programmed settings and to read, store and display data live, which is collected during experimentation. It retrieves and loads set parameters (or those last used), from a config file, and sends setup commands to instrumentation via serial RS-232 connections. In figure 2.8, the left-most pane of the STMA shows the experiment and instrumentation selected. The instrument parameters can be amended while the application is open before the measurement in the ‘Advanced Parameters' window (not shown in figure 2.8), or between

acquisitions in the right-most pane of figure 2.8. This gives the user simple access to a clean interface, without having to delve into the code itself to change settings. Hard-coding in parameters was completely avoided and instead the user is prompted to input parameters they deem appropriate.

Once the desired parameters are selected, the program is 'initialised', to create instances of each instrument class, that of the experiment class and send the set of start-up command to each instrument. At this juncture, the software and instrumentation are ready to acquire data. Once the measurement is started, the system queries most instruments via RS-232 at a periodic interval set by the user to acquire, store and graph the data. Only the Hall probe and the SRS 830 are not queried but continuously acquired by the NI cRIO 9215 card, as mentioned above. Measurements are always acquired when the field dwells in between field steps to avoid EMFs. The dwell time was set empirically to eliminate these induced voltages from changing the field magnitude.

To perform the experiments conducted in chapters 3,4 and 6, multiple experiment classes were written. Each of these measurements may be conducted with any of the specified instrumentation. The '*No Field*' class measures voltage at a fixed interval without field or rotation, which proves useful for checking noise and observing the thermal drift in background voltages over time. The '*R vs H*' experiment class is used for field sweep measurements at fixed field position. It measures a voltage by sweeping the field within a selected field magnitude window and steps at a selected interval. The '*Rotation*' class is used to rotate the field by encoding the ESP300 rotation controller with a user-defined rotation window (typically from -12° deg to 372°) and speed, at a fixed $\boldsymbol{H}$. The '*VSM Rotation*' class functions the same way, yet sends a list of alternate commands to the rotation motor controller when using the VSM magnet for 1. 7 T rotation measurements. Finally, the '*V vs I*' class steps the current applied by the KSM 2400 source meter, dwells and records the resultant voltage with the KNVM 2182A, at a specified current step size within a current window.

## 2.4 Summary

In this chapter, we outlined the processes to fabricate and measure patterned and continuous thin film spintronic devices. The thin metallic films grown by DC magnetron sputtering may be deposited on an entire $SiO_2$ chip, or only within a specific pattern defined by photolithography. Film characterisation is performed on thin continuous films, but for electronic spin-mediated measurements, a patterned device is always preferable to direct current flow and voltage direction and increase the SNR.

Characterisation techniques such as high angle x-ray diffractometry and low angle reflectivity were explored, which allow us to quantify crystallographic texture, thickness and roughness of ultrathin films. In addition, the principles behind high angle annular dark field scanning electron microscopy were outlined, which make it possible to observe growth mode and microstructure morphology of ultrathin films directly. Finally, the vibrating sample magnetometer technique was described, whereby the magnetic response of thin ferromagnetic films under external magnetic fields is probed.

To perform the spin transport measurements shown in this thesis, we devised and constructed a robust, low-noise electrical measurement setup. We outlined the design, wiring methodology, instrumentation specifications and noise floor testing to show the capabilities of the system. In short, experiments may be conducted at room or low temperature with AC or DC voltages across a range of instruments, which prove useful under different measurement conditions for probing spin(calori)tronic effects. A wide variety of experimentation, including current and field sweeps, and angular field rotations may be easily performed with help of the full STMA computer application developed in VB.net.

# 3 Characterisation of ultrathin metallic films

## 3.1 Introduction

In this chapter, we characterise the structural, electronic and magnetic properties of HM and FM constituent materials used in this work. Much of the experimentation in spin transport is conducted on ultrathin metallic films less than 10 nm in thickness, where exotic material properties are far different than those where bulk-like behaviour dominates. At this length scale, precise microstructure morphology of sputtered metallic films is highly sensitive to particular growth conditions, including substrate and material surface free energies, temperature and pressure. Consequently, the electronic properties of the materials may differ dramatically due to electron confinement [170], reduced grain size [171] and surface scattering [172,173] from inversion symmetry-breaking at the interface, making a direct correlation to spin-dependent properties with electrical measurements challenging.

To correlate changes in spin-dependent properties of HM layers to microstructure morphology, we first determine the most effective method for tuning morphology in the ultrathin limit. Altering the chamber working pressure during HM growth [174,175] and seeding HM growth with high-melting-point buffers [87,176,177] have been found to be effective methods and are explored in this work. Changes in texture and surface roughness in ultrathin HM microstructures are quantified with x-ray diffractometry and reflectivity. Additionally, films are probed with energy-dispersive x-ray spectroscopy to determine constituent material compositions and are optically observed with high resolution, aberration-corrected scanning transmission electron microscopy.

Of particular importance to electrical spin transport measurements are the conduction properties of thin metallic films. In all-metallic devices, each constituent layer contributes to electron flow, and the resistivity of each may be estimated from stack sheet resistances. However, polycrystalline films such as Pt have been shown [171–173,178–184] to have a strong thickness-dependent resistivity in the ultrathin limit, thus requiring careful attention. The increase in resistivity at low thicknesses is well-predicted in thin films by surface scattering (following the Fuchs-Sondheimer model [172,183]) and grain boundary scattering (following the Mayadas- Shatzkes model [171,184]).

The first exact solution to describe thin film resistivity increases was developed Fuchs-Sondheimer, which relates the increased electron scattering to inversion symmetry-breaking limiting the mean free path $l_0$ of electron flow. The full form follows

$$\rho_{FS} = \rho_{\text{bulk}}\left[1 + \frac{3}{2\,k}\int_1^{\infty}\left(\frac{1}{x^3} - \frac{1}{x^5}\right)\left(\frac{1 - e^{-kx}}{1 - p\,e^{-kx}}\right)dx\right], \tag{3.1}$$

where $\rho_{\text{bulk}}$ is the bulk resistivity, $p$ is a parameter describing the specular component of electron reflection ($p = 0$: diffuse reflection, $p = 1$: specular reflection) and $k = {}^{t}/_{l_0}$. Later Mayadas and Shatzkes postulated that the resistivity increase may also be due to grain boundary scattering. In their mode, grain boundaries are represented as parallel, partially-reflecting planes, which are perpendicular to both $\boldsymbol{j}_c$ and the plane of the film. The interaction between grains and conduction electrons may result in either reflection or transmission, but the frequency of scattering sites is drastically increased at low film thickness as grain boundaries reduce in size. The Mayadas-Shatzkes has the function form

$$\rho_{MS} = \frac{\rho_{\text{bulk}}}{1 - \frac{3}{2}\eta + 3\eta^2 - 3\eta^3 \text{Log}\left[1+\frac{1}{\eta}\right]}, \tag{3.2}$$

where $\eta = \frac{l_0}{D}\frac{R}{1-R}$, $R$ is the reflection coefficient indicating the reflection probability at each grain boundary ($R = 0$: full transmission, $R = 1$: full reflection), and $D$ is the distance between grain boundaries.

Here, we extract thickness-dependent resistivities in (un)buffered Pt films, fit the discrete device data to a continuous $\rho(t)$ function and correlate the electronic properties of each series to HM microstructure. Additionally, the resistivity of each (un)buffered Pt series is fit with Fuchs-Sondheimer and Mayadas-Shatzkes simultaneously to better understand the scattering mechanism dominating in the ultrathin limit and gain insight into the effect on transverse spin-dependent scattering.

In order to conduct a meaningful test of HM microstructure morphology on spin transport with all-metallic bilayers, the electronic and magnetic properties of the ultrathin FM layer must remain consistent across the (un)buffered Pt series deposited underneath. The magnetic properties of thin FM films are probed with VSM magnetometry, and the saturation magnetisation is used as a figure of merit to determine the magnetic quality of the FM film. Additionally, to protect the FM layer, which is otherwise exposed to atmosphere, thin capping layers are explored to ensure a robust heterostructure, well-protected from stack oxidation.

## 3.2 Tuning the HM microstructure in ultrathin films

There are multiple methods to control microstructure morphology of ultrathin DC sputtered films. In this work, the structural properties of sputtered HM (Pt) films are altered with the $Ar^+$ flowrate (and thereby the working pressure) in the sputter chamber during growth and by seeding growth on $SiO_2$. Although post-deposition annealing is also frequently used to alter HM structure [185,186], there is no heating stage for high-temperature (> 150 °C) annealing inside the magnetron sputter chamber for restructuring in an $O_2$-free environment. Indeed, this would also cause an unwanted intermixing of atoms between the constituent layers [187].

In this section, we characterise microstructural properties of thin sputtered Pt films by altering growth conditions directly. Thin Pt films are commonly sputtered in spintronics applications [3,74,87,155,188] in the moderately dirty regime [74] similar to this work. The expected crystal structure of thin Pt from physical vapour deposition is FCC (111) [179,189].

### 3.2.1 Working pressure during DC sputtering

In DC sputtering at ultrahigh vacuum, metal ions of the desired material are impacted by $Ar^+$ ions on the surface of the target. If the impact energy is sufficient, the ions are ejected and travel ballistically, and deposit on the substrate and chamber walls alike. However, when the working pressure is increased (by increasing the $Ar_2$ flowrate during growth), the likelihood of a metal ion striking argon is greater. At high pressures the metal ions move more diffusively, reaching the substrate surface by random walk. Therefore, by altering the working pressure, we can tune the impacting energy of the metal ion on the substrate surface and so the film microstructure. Here, we incrementally vary the working pressure within a narrow range (from the 7.3 to ~ 10.4 x $10^{-3}$ mBar) to gain precise control over Pt texture and roughness, while maintaining a nearly constant growth rate.

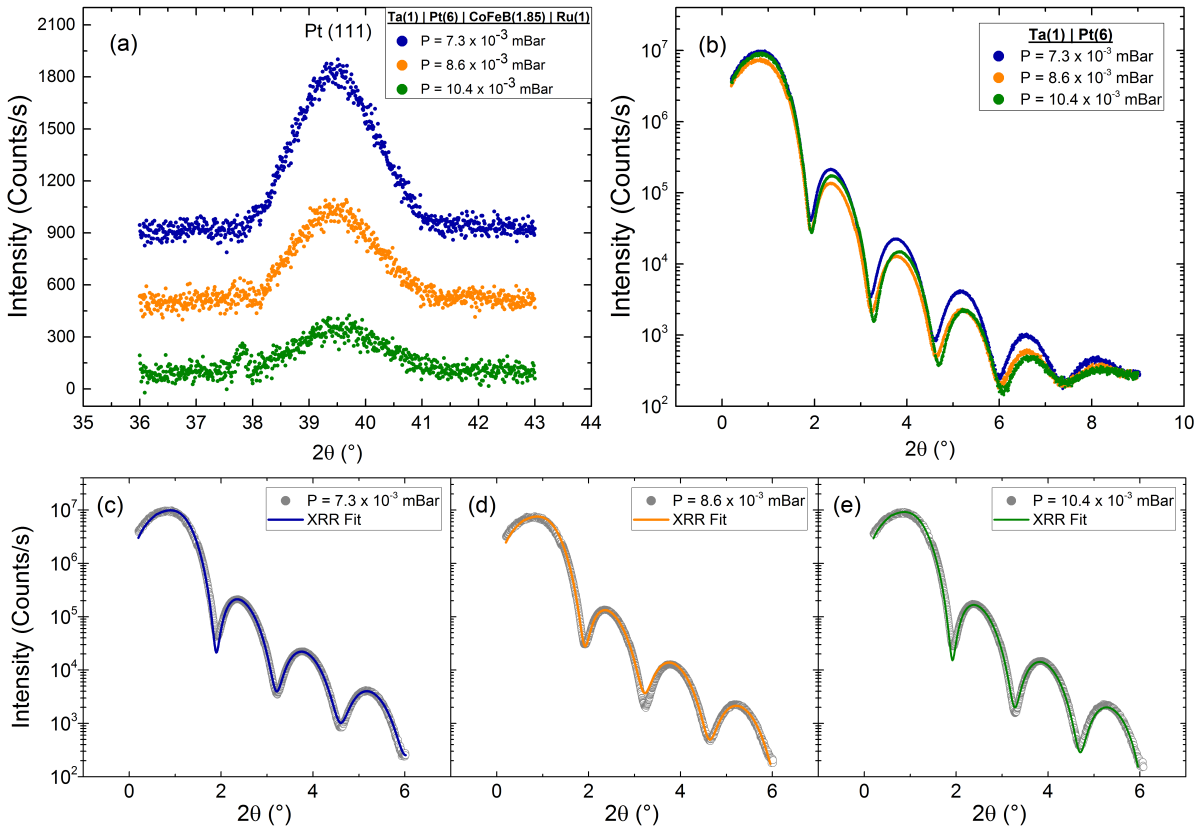


Figure 3.1 X-ray diffractometry $\theta$ /$2\theta$ scans with Pt deposited under different chamber working pressures. (a) Excerpts from high-angle, full $\theta/2\theta$ XRD scans about the Pt(111) diffraction peak for a series of Ta(1)|Pt(6)|CoFeB(1.85)|Ru(1). For improved visualisation the peaks are shifted by 100, 500, 900 counts/s for the devices with Pt grown at P = 10.4, 8.6 and 7.3 x $10^{-3}$ mBar, respectively. (b) Low-angle XRR $\theta/2\theta$ scans on Ta(1)|Pt(6) bilayers. (c-e) Individual XRR $\theta/2\theta$ scans reproduced from (b) and fit with GenX™ to extract roughness and thickness values.

Figure 3.1 shows x-ray diffractometry measurements performed on Ta(1)|Pt(6) continuous films to highlight Pt microstructure changes in the ultrathin limit. It is challenging to extract accurate thickness and roughness values below a Pt thickness $t \sim 6$ nm in XRR because there is an insufficient number of Keissig fringes to fit accurately. To isolate the effect of working pressure on HM microstructure, we fabricate all constituent layers at the normal operating pressure for our chamber (P = 7.3 x $10^{-3}$ mBar) except for the pressure during Pt growth, which is varied. To ensure each of the constituent layers is deposited at a desired chamber pressure, we dwell for 20 s before (after) the Pt film is deposited without striking the target of the previous (next) layer in the stack to allow the pressure to equilibrate.

Panel (a) shows a portion of the full $\theta/2\theta$ XRD scan from 35° to 90° (available in full in figure B.1 of Appendix B) about the Pt(111) peak at $2\theta \sim 39.7634°$ where the crystalline texture is most apparent. The full $\theta/2\theta$ XRD scans (in figure B.1) show nearly identical substrate peaks for all samples, which allows the counts obtained in both XRD and XRR to be directly compared. Note, a small background slope was subtracted here. We observe a significant reduction in the peak at $2\theta \sim 39.7634°$ as the working pressure is increased. In panel (b), the low-angle XRR scan shows suppression of the Keissig fringes as the working pressure is increased from the blue data points where Pt is fabricated at P = 7.3 x $10^{-3}$ mBar to the green data points where Pt is fabricated at P $\sim$ 10.4 x $10^{-3}$ mBar.

Table 3.1 Pt film thickness and roughness data extracted from GenX™ fitting of the XRR data displayed in figure 3.1 for different sputter chamber working pressures.

| Chamber Pressure (mBar) | Thickness (nm) | Roughness (Å) |
|---|---|---|
| 7.3 x $10^{-3}$ | $5.0 \pm 0.4$ | $2.36 \pm 0.08$ |
| 8.6 x $10^{-3}$ | $4.8 \pm 0.2$ | $2.81 \pm 0.08$ |
| $\sim$ 10.4 x $10^{-3}$ | $4.9 \pm 0.5$ | $3.24 \pm 0.05$ |

An increase in Pt film roughness explains this suppression and GenX™ confirms that fitting the XRR data in panels (c-e) yields a trend of increasing roughness with chamber pressure in table 3.1. This is in direct agreement with recent film characterisation work [174,175]. Notice, only a slight shift in the periodicity of the Keissig fringes between samples in figure 3.1 (b), amounting to an insignificant difference in Pt thickness between the P = 7.3 and 10.4 x $10^{-3}$ mBar samples. This is evidenced by the values in table 3.1, which shows the film thickness data extracted with GenX™ to not change appreciably with the small variation in chamber pressure at the resolution offered in these samples. Therefore, we conclude that by varying the chamber working pressure during Pt growth within a narrow window, we can obtain small, yet well-controlled changes in Pt(111) texture and surface roughness.

### 3.2.2 Buffered HM growth with a seed layer

Another method for altering growth conditions of HM bilayers is by depositing a seed (or buffer) layer, which acts as a buffer between the HM and the substrate. Sputtered deposition directly on an oxide layer such as $SiO_2$ is thermodynamically unfavourable for HMs due to large free energies of thin film formation. Therefore, metals which deposit in a crystalline manner such as Pt do not entirely wet the surface in the ultrathin limit, but instead, form percolated grains to reduce the $SiO_2$|HM interface area. This Volmer-Weber (VW), 3-D type growth mode produces columnar Pt grains [190–192], characterised by reduced texture and increased roughness. To reduce the surface free energy of formation of Pt on the oxide layer, a thin 1 nm, high melting-point metal buffer (such as Ru or Ta in this work) is deposited first to promote wetting. Under these thermodynamically favourable conditions, Pt conforms to the substrate with layer-by-layer deposition and a smooth, continuous 2-D film is formed following Frank van der Merwe (VDM) type growth [153,192].

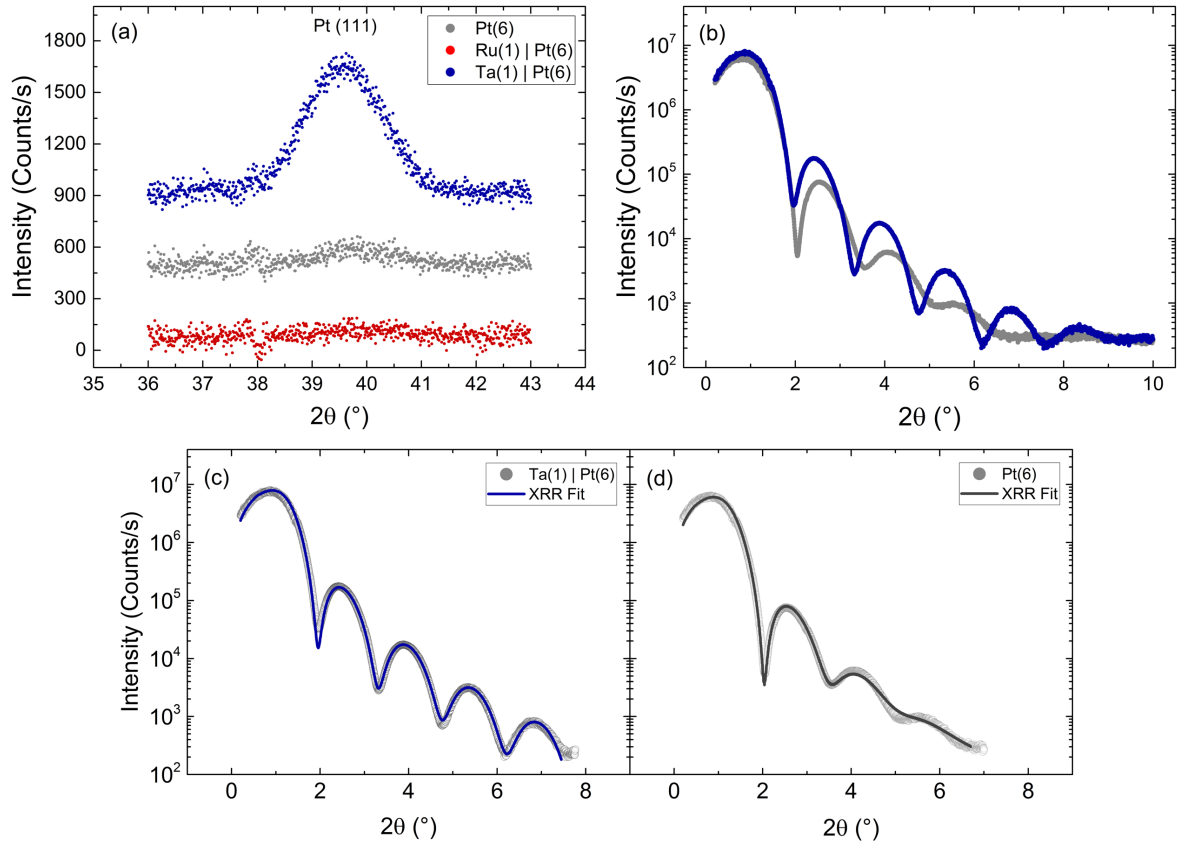


Figure 3.2 X-ray diffractometry $\theta$ /$2\theta$ scans with Pt deposited on different seed layers. (a) Excerpts from high-angle, full $\theta/2\theta$ XRD scans about the Pt(111) diffraction peak for a series of (un)buffered Pt(6) films in arbitrary units. For improved visualisation the peaks are shifted by 100, 500, 900 counts/s for the Ru-, un- and Ta- buffered Pt devices, respectively. (b) Low-angle XRR $\theta/2\theta$ scans on (un)buffered Pt(6) films. (c-d) Individual XRR $\theta/2\theta$ scans reproduced from (b) and fit with GenX™ to extract roughness and thickness values.

Figure 3.2 shows x-ray diffractometry measurements performed on (un)buffered Pt(6) continuous films to probe the Pt microstructure in the ultrathin limit. Again, panel (a) shows a portion of the full $\theta/2\theta$ XRD scan from 35° to 90° (available in full in figure B.2 of Appendix B) about the Pt(111) peak at $2\theta \sim 39.7634°$ where the Pt crystalline texture is most apparent. The full $\theta/2\theta$ XRD scans (in figure B.2) show nearly identical substrate peaks for all samples, which allows the counts obtained in both XRD and XRR to be directly compared. Note, a small background slope was subtracted here. We observe only a slight Pt(111) peak in unseeded thin film deposition, whereas there is a stark increase in texturing when buffered by a 1 nm amorphous Ta layer. In contrast to Ta buffering, we observe a thin 1 nm Ru seed layer to suppress Pt(111) texturing completely. In panel (b), the low-angle XRR scan shows the unbuffered Pt(6) layer with highly suppressed Keissig fringes when compared to the Ta-buffered Pt(6) film, indicated a rougher film. In panels (c-d), the GenX™ XRR fitting compiled in table 3.2 confirms that the unbuffered Pt(6) layer has triple the roughness of the Ta-buffered Pt layer. The fitting parameters displayed in table 3.2 also demonstrates that the accurate Pt thickness for the unbuffered film is $5.2 \pm 0.3$ nm (not a nominal 6 nm as expected from calibration[2]) and is larger than for the Ta-buffered film ($4.78 \pm 0.07$ nm). The combination of increased roughness and thickness of the unbuffered Pt film suggests 3-D Volmer-Weber-type growth, with percolated grains.

Table 3.2 Pt film thickness and roughness data extracted from GenX™ fitting of the XRR data displayed in figure 3.2 for varying buffer conditions.

| Buffer | Thickness (nm) | Roughness (Å) |
|---|---|---|
| – | $5.2 \pm 0.3$ | $6.7 \pm 0.3$ |
| Ta(1) | $4.78 \pm 0.07$ | $2.09 \pm 0.04$ |

Since seed layers are extensively used in spintronics applications [177,193,194] and are more effective at tuning HM microstructure than altering working pressures, we focus on buffering HMs from here onwards and explore the resultant effects on spin transport in metallic bilayers through chapters 4-6. To better characterise the HM microstructure at different seed conditions, x-ray diffractometry data is augmented with optical STEM microscopy and EDX to probe constituent materials. Here, we explore un-, Ru- and Ta-buffered Pt layers with electron microscopy in the ultrathin limit to directly observe microstructure changes. This data was collected with Dr Giorgio Divitini, a TEM technician in the Department of Material Science.

In Figure 3.3 we probe the cross section of a thin lamella of ultrathin (un)buffered Pt(1.6) continuous films with in-situ EDX to confirm the material composition is as expected. In panel (a), a low-resolution, high angle annular dark field scanning transmission electron microscopy (HAADF-STEM) shows the full lamella prepared with a $Ga^+$ ion FIB from a

[2] Here the nominal stated Pt thickness is larger than the true thickness due to the imprecision of Pt growth rate calibration with thick 30 nm samples. For films used in chapters 4-6, we confirm that the nominal thickness is only a maximum of 10% larger than the true thickness.

continuous (un)buffered Pt(1.6) film. The lamella structure shows Si underneath an ~ 500 nm layer of $SiO_2$. The thin film is deposited directly on the $SiO_2$, capped by a protective 400 nm of thermally-evaporated Al and stuck to the Mo grid with FIB-deposited Pt. Typically, Pt is deposited in-situ as a protective capping layer when preparing the lamella, however, since Pt is the element of interest, it was necessary to ex-situ deposit a light metal (Al) for good contrast. Figure 3.3 (a-c) shows the resultant colour-coded counts from the EDX spectra for the (un)buffered Pt(1.6) films on the right-hand side (RHS) of the figure taken from the STEM on the left-hand side (LHS). Note, the STEM images here are in low-resolution and drifting; they are only shown to guide the reader for the EDX spectroscopy displayed on the RHS of figure 3.3. Higher resolution TEM microscopy follows in Figure 3.4.

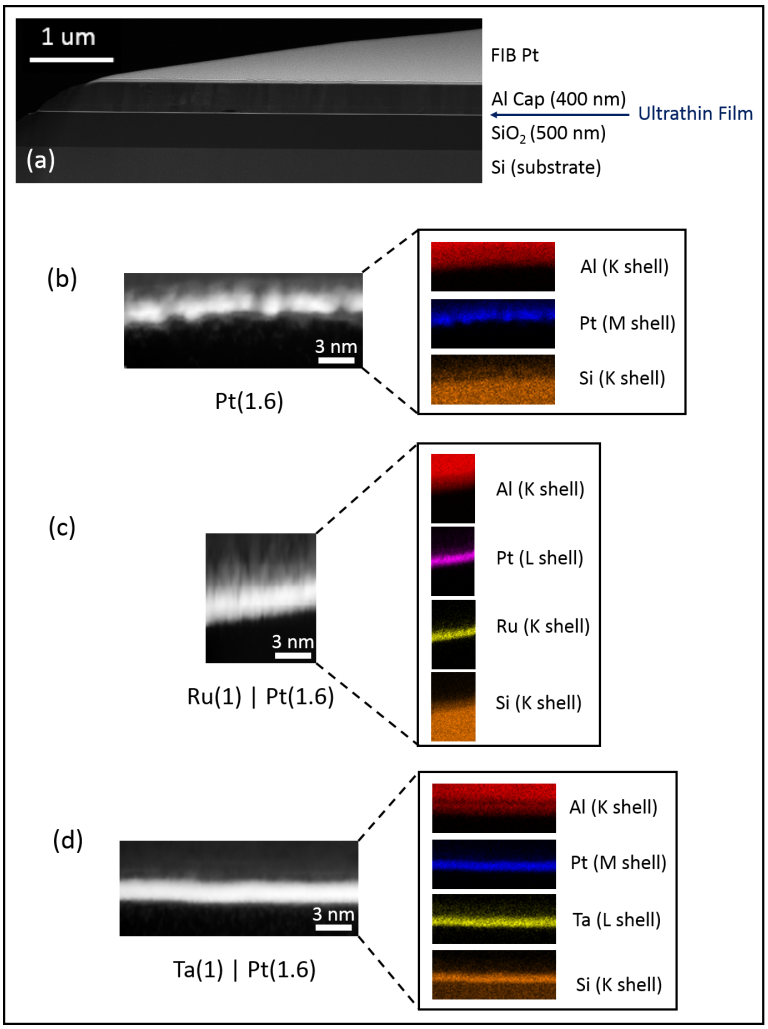


Figure 3.3 (a) Scanning electron microscopy cross-sectional image from a lamella extracted of an ultrathin film deposited on a thermally oxidised silicon substrate. Low-resolution HAADF-STEM images of (b) unbuffered, (c) Ru-buffered and (d) Ta-Buffered 1.6 nm Pt films and respective colour-coded EDX counts measuring x-ray emission from Auger transitions of the noted electronic orbitals.

With EDX spectroscopy, we observe the colour-coded counts for each constituent layer are as expected. The colours represent the number of counts recorded for each the x-ray emission specific to the Auger transition from a higher shell electron dropping down to a lower orbital, based on the band structure of the constituent material. For example, on the right-hand side of panel (b), the red density count at the top of the film shows the counts of the K-shell electrons Auger transitions in the capping Al layer. Similarly, the M-shell transitions from the Pt are accounted for by the blue density counts and the K-Shell transitions from the Si substrate are depicted by the orange density counts. The same applies for panels (c-d), where we find the constituent layers are grown as expected. At this resolution and with substantial thermal drift, it would be challenging to make claims about any intermixing between layers.

In figure 3.4, we show the results of the high resolution, cross-sectional, aberration-corrected HAADF-STEM images collected of the (un)buffered Pt($t$) films deposited directly on $SiO_2$. The left-most column (panels a,c,e) are images of the thinnest Pt(1.6) films, while the right-most column (panels b,d,f) depict thin Pt(3) nm films. These (un)buffered Pt films are imaged to directly observe how HM morphology microstructure is affected by 1 nm HM seed layers without inference through electronic property measurements such as film conductivity.

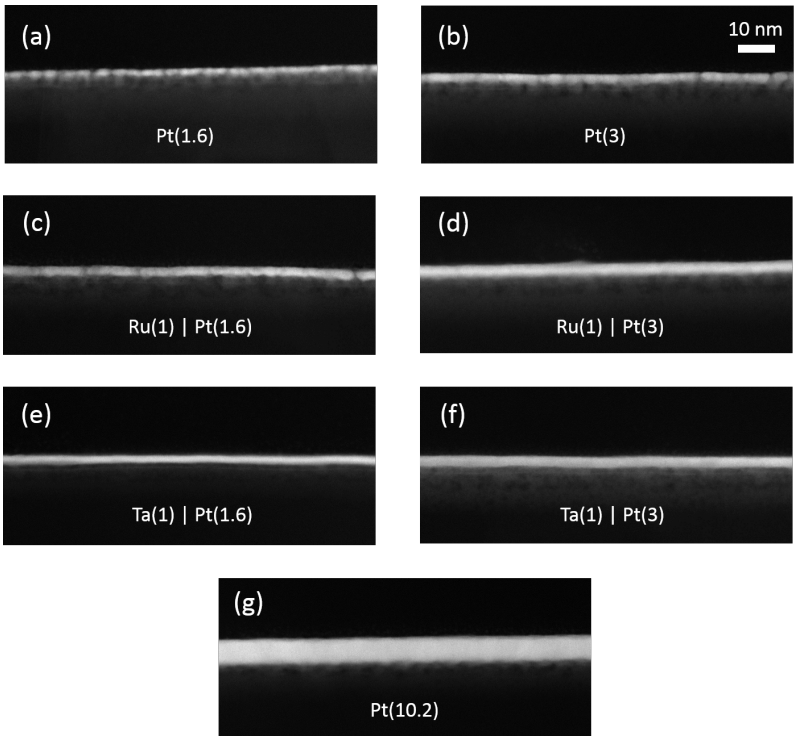


Figure 3.4 Aberration-corrected HAADF-STEM images of (un)buffered ultrathin Pt films taken on an FEI Titan$^3$ at 300 kV. The composition of each film is annotated on each image.

It is evident from the clustered grains and island-like growth in figure 3.4 (a-b) that deposition of ultrathin Pt directly on the oxide surface is thermodynamically unfavourable. Under these conditions, Pt is following 3-D, VW type growth instead of thoroughly wetting the substrate surface. In panels (c-d), the Ru buffer makes a noticeable impact on film growth by increasing film continuity and promoting wetting. In the Ru(1)|Pt(1.6) nm case in panel (c), there are still noticeable grains, but by 3 nm of Pt growth (panel d) a seemingly continuous film forms. In panels (e-f), the Ta buffer does well to decrease the surface free energy of formation for the ultrathin Pt film, and both 1.6 and 3 nm films experience favourable growth conditions. A well-wet layer Pt layer results from layer-by-layer deposition following VDM-type growth. These results are unique to the ultrathin limit, where continuity also improves from island growth as the volume of Pt is increased in thicker films. This is directly apparent in both the unbuffered and Ru-buffered films and further evidenced by the fully continuous unbuffered, thick Pt(10) film.

## 3.3 Conductivity of ultrathin films

Since mobile conduction electrons mediate spin angular momentum transport in metallic systems, the electrical properties of the heterostructure strongly affect spintronic measurements. In metallic multilayers, film conductivity is particularly significant, since each of the constituent layers contributes to electron flow adding complexity to spin-based measurements, unlike well-studied systems that are comprised of insulating ferrimagnets. In (un)buffered HM bilayers, it is necessary to quantify the conductivity of each layer to understand the current distribution through the heterostructure, tailor spin systems to maximise signal and electrically measure spin (polarised) currents in the presence of current-shunting. This is of particular importance to the work presented in chapters 4-6, where we electrically probe HM bilayers with ultrathin constituent layers, whose resistivities deviate significantly from bulk values from finite thickness effects. Here, we quantify resistivities of the thin, sputtered metal constituent layers by measuring stack conductances and, in so doing, gain insight into scattering mechanisms influencing conduction of the ultrathin films.

### 3.3.1 Extracting electronic properties of constituent materials

To evaluate the resistivity of the constituent layers in all metallic heterostructures, we constrain current flow from the Keithley Sourcemeter 2400 in $\hat{\boldsymbol{x}}$ and record longitudinal voltage in the Keithley Nanovoltmeter 2182A in $\hat{\boldsymbol{x}}$ with a 4-terminal electrical measurement a patterend device known as a Hall bar.

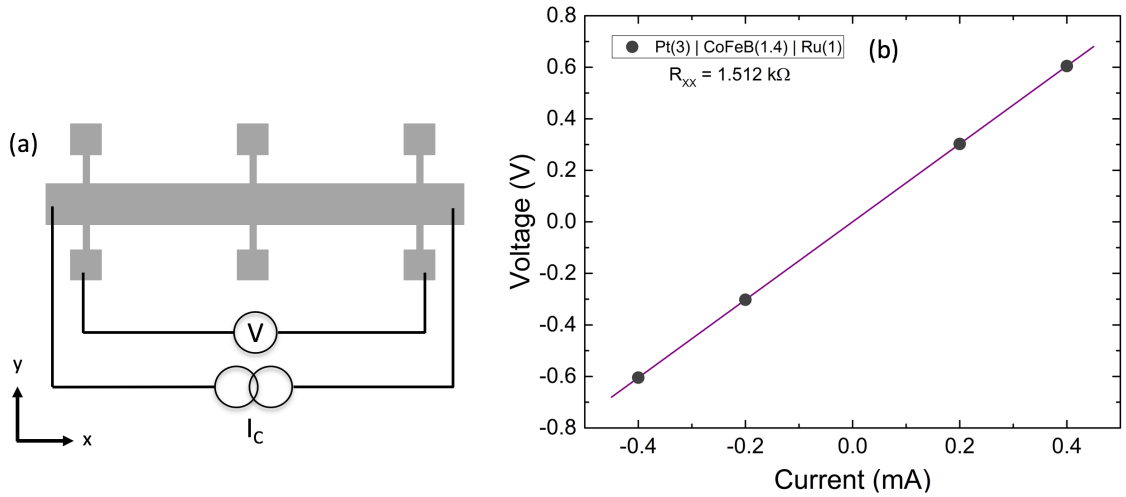


**Figure 3.5 (a) Schematic illustration of a prototypical Hall bar during a longitudinal $R_{XX}$ measurement. (b) Longitudinal voltage measurement across a Pt(3)|CoFeB(1.4)|Ru(1) Hall bar versus applied current to check Ohmic behaviour and evaluate $R_{XX}$.**

An illustration of a prototypical Hall bar is displayed in figure 3.5 (a). In figure 3.5 (b), the longitudinal voltages are acquired across a Pt(3)|CoFeB(1.4)|Ru(1) Hall bar – typical of a HM bilayer stack evaluated in this work – versus an applied current $I$. Instead of performing a single-shot measurement, voltages are recorded across a range of currents to check for Ohmic behaviour in the metallic multilayers. We observe a linear response in longitudinal voltage from varying the applied current amplitude in this course test. The stack resistance, $R_{XX}$ = 1.512 kΩ in this case, is evaluated from the slope following Ohm's law. This simple methodology is used to determine $R_{XX}$ for each device below.

To elucidate the resistivity of individual layers from the overall stack resistance, we perform a series of $R_{XX}$ measurement versus thickness ($t$) of the material of interest. This common method for determining resistivity [3,141] entails plotting stack conductance $G_{XX}$ versus constituent thickness. This method is particularly useful when evaluating the resistivity of constituent layers in heterostructures. In multilayer stacks, the film microstructure and so electronic properties depend on its position in the stack. The resistivity of a constituent layer is especially sensitive to the material and growth mode of the films underneath. Similarly, when a material is particularly prone to oxidation (such as CoFeB, Ta, Ru in this work), a capping layer may be used to protect the film from the atmosphere to determine the proper, native thin film resistivity.

Figure 3.6 shows stack conductance $G_{XX}$ ($^1/_{R_{XX}}$) measurements versus the thickness of constituent materials used in this work. Materials of interest include Ta, Pt, Ru, W and CoFeB. Ta, Pt, Ru and W are important HMs used in this work, which act as either the active SOC material in HM bilayers or the seed layer under the active HM layer, while CoFeB is the active FM layer. Each series of metallic multilayers is fabricated to replicate the stack structure (specifically the placement of the layer of interest within the stack) of the devices. In this way, the structure and oxidation levels are representative of the devices used in chapters 4-

6 and $\rho$ estimation is more accurate. It is expected that $G_{XX}$ is proportional to $t$, so each data set is fit to a straight line. The slope of this line reveals conductivity $\sigma$ information of the thickness-dependent layer of interest, while the y-intercept represents the total conductance of the remainder of the stack $G_0$ without the layer of interest present (at $t$ = 0). The resistivity of this layer of intrest is estimated $\rho \sim \frac{1}{m}\frac{w}{l}$, where $m$ is the slope extracted from the straight line fit and $w$ and $l$ are the width and length of the Hall bar, respectively. The resistivity estimated by this method is inset in each panel.

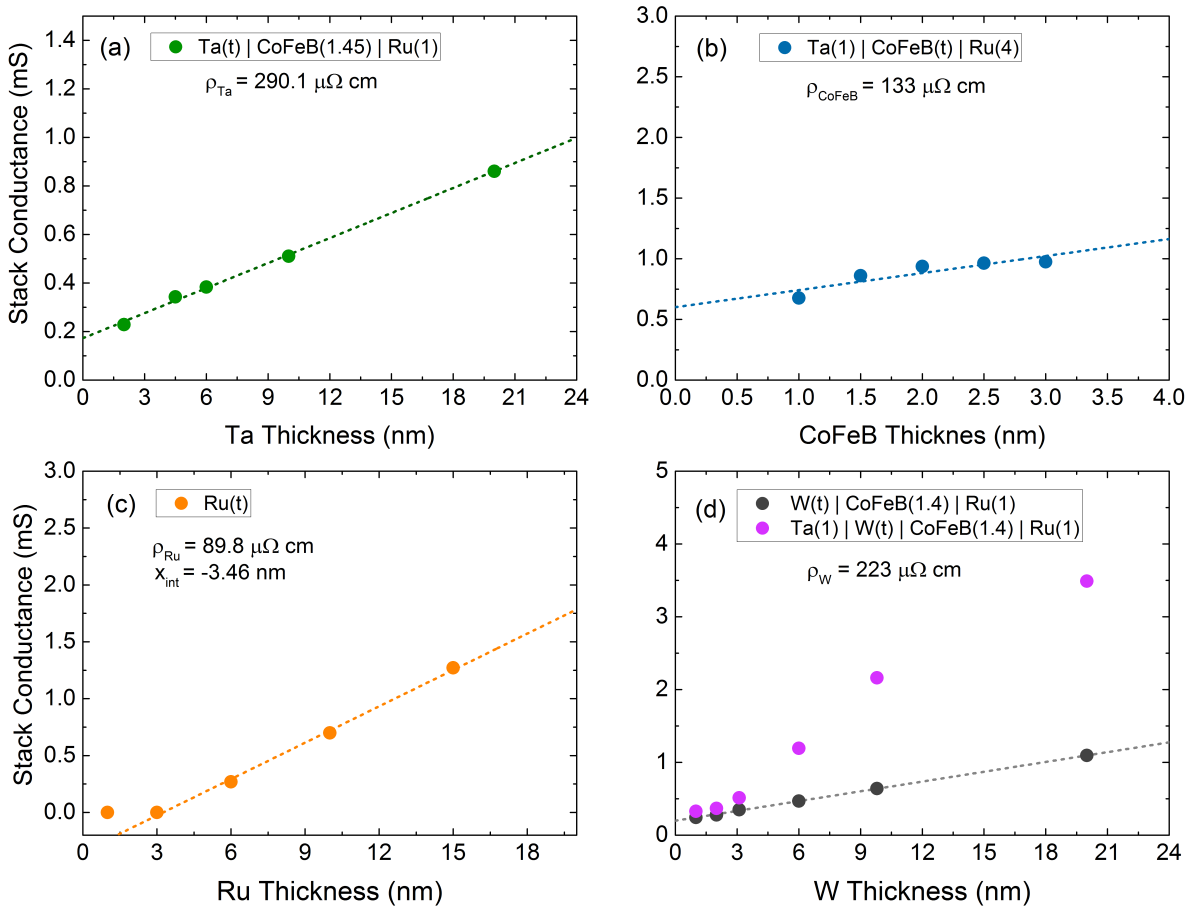


Figure 3.6 Stack conductance $G_{XX}$ as a function of constituent layer thickness for (a) Ta, (b) CoFeB, (c) Ru and (d) W. A linear fit is applied to the data to extract resistivity following the methodology in [3,141].

Figure 3.6 (a-b) show the resistance data at varying Ta and CoFeB thicknesses, respectively. Both of these materials deposit amorphously in the ultrathin limit (defined here as less than 6 nm), which explains the large listed resistivity in the inset of the panels. In panel (c), $G_{XX}$ at low Ru thickness flatlines with negligable conductivity at finite thickness, indicating the presence of an electrical dead layer (a layer which does not conduct current). A dead layer may be caused by poor film growth on the substrate or oxidation if unprotected and exposed to the atmosphere. These Ru Hall bars are uncapped, which suggests oxidation is the primary reason for poor conductivity. Moreover, this series of Ru monolayers was fabricated purposefully without capping to determine the dead layer thickness, which is given by the x-intercept and displayed inset. The 3.46 nm dead layer indicates that a thin Ru film may be

deposited on top of a heterostructure to protect the device without itself conducting any current in electrical spin transport measurements. Further discussion on the applicability of Ru cap from an $O_2$ permeability standpoint follows in section 3.4.3. Notice, all the series of Hall bars in Figure 3.6 are capped with at least 1 nm of Ru to protect rapid oxidation of the top layer.

In figure 3.6 (d) the stack conductance of films with a W constituent layer is assessed. Here, we show a series of unbuffered W stacks depicted with dark grey data points fit to extract the resistivity $\rho_W$ = 223 μΩ cm, which is typical of $\beta$-W [195–199]. However, seeding W growth with a 1 nm Ta buffer (represented by the pink data points) promotes a rapid decrease in $\rho_W$ above ~ 3 nm as shown by the stark increase in $G_{XX}$, indicating a phase change to $\alpha$-W. Recent work [3] corroborates the observation of a phase change of W at 3-4 nm and showed this had a direct impact on spin-dependent parameters. Therefore, the inability to precisely control microstructure and electronic properties do not make W an ideal HM film for this study.

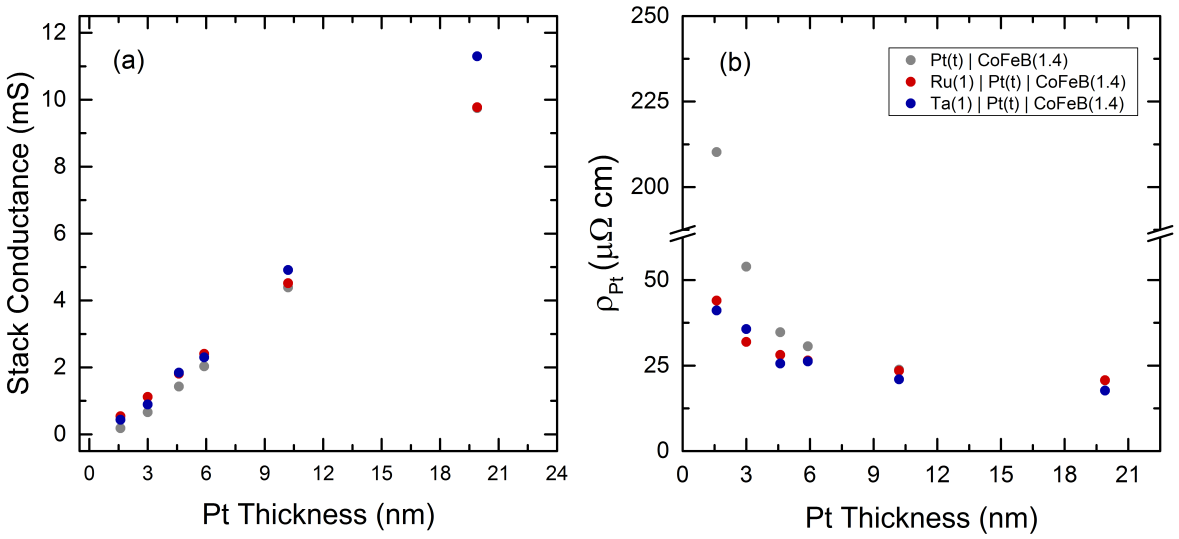


Figure 3.7 Resistance considerations of (un)buffered Pt(t)|CoFeB(1.4) stacks. (a) stack conductance versus Pt thickness. (b) Pt resistivity extracted with Matthiessen's rule versus thickness.

Pt is another high SOC HM which has been extensively studied for spin transport systems, in large part due to significant measured $\theta_{SH}$ values [61] and reduced energy requirements from inherently low resistivity. Figure 3.7 (a) shows (un)buffered Pt thickness-dependent stack conductance. Unlike the buffered W films, there is no apparent jump in stack conductivity across between $t$ = 1.6 and 20 nm, indicating a consistent Pt phase across all seeding conditions. However, if Matthiessen's rule is applied, since the current passing through a parallel circuit, to isolate $\rho_{Pt}$ from the measured $R_{XX}$ data with

$$\rho_{Pt} = \frac{t}{\frac{l}{wR_{XX}} - \frac{d_{CoFeB}}{\rho_{CoFeB}} - \frac{d_{buf}}{\rho_{buf}}}, \tag{3.3}$$

we observe a significant increase in $\rho_{Pt}$ in the ultrathin limit. Figure 3.7 (b) shows the enhancement in $\rho_{Pt}$ for all (un)buffered Pt|CoFeB series in this limit, yet especially so for the

unbuffered series at $t \leq 6$ nm. These results are consistent with microstructure film quality observed by HAADF-STEM in Figure 3.4 (a-b), where the unbuffered Pt films were observed to follow island-like, 3-D Volmer-Weber type growth. Moreover, the abrupt increase in resistivity of the thinnest unbuffered Pt multilayers suggests that segregated islands exist and the Pt film is below the percolation threshold. In contrast, both Ru- and Ta-buffered multilayers show less increase in $\rho_{Pt}$ at ultra-low $t$, which is to be expected with preferential thermodynamic substrate wetting conditions induced by the seed layers as observed in figure 3.4 (c-f).

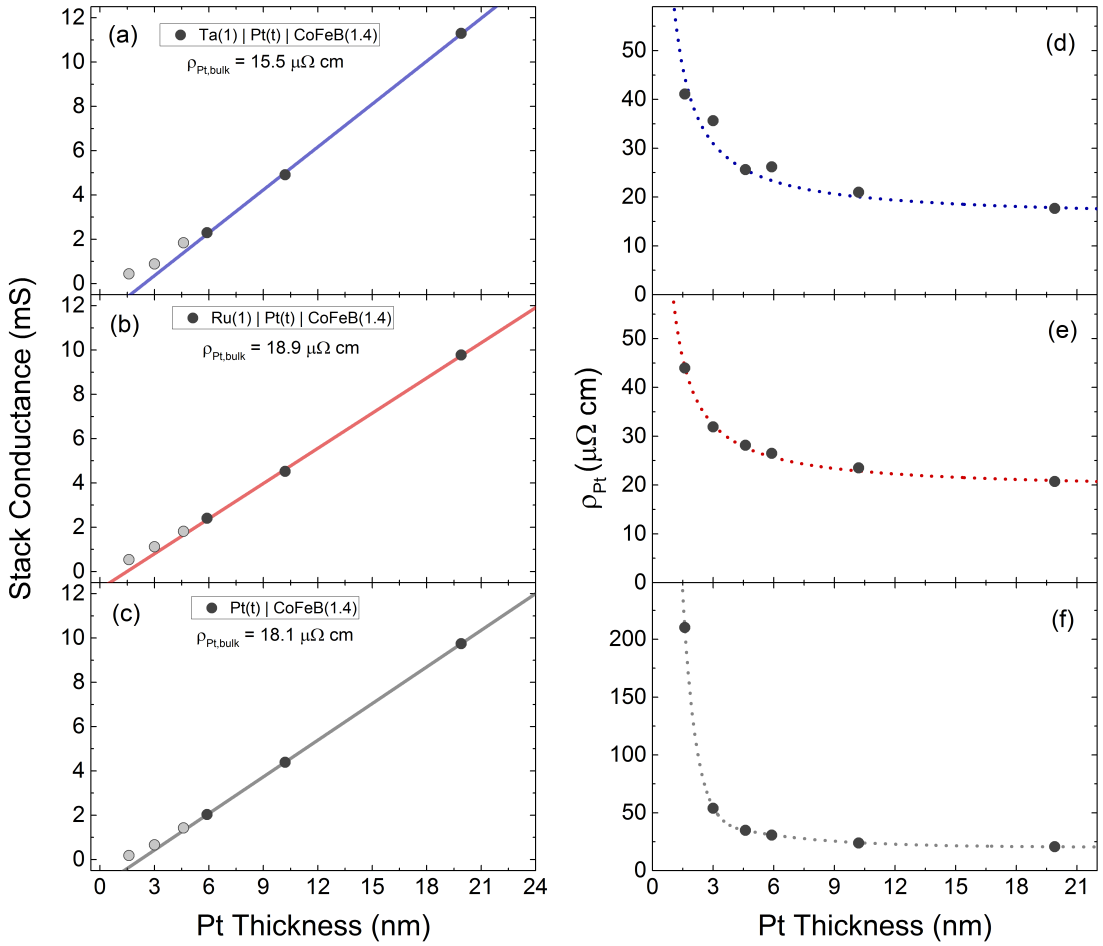


Figure 3.8 Resistivity of thin Pt films in (un)buffered Pt(t)|CoFeB(1.4) stacks. (a-c) Stack conductance versus Pt thickness. Linear fitting the dark data points down to the ultrathin limit (6 nm) are used for bulk resistivity estimation. (d-f) Discrete resistivity values extracted from Matthiessen's rule from stack conductances as a function of Pt thickness fit to Fuchs-Sondheimer function to obtain continuous $\rho(t)$ for each (un)buffered series. Note, at $t \leq 4.5$ nm in (f) the resistivity deviated significantly from the Fuchs-Sondheimer prediction and a exponential decay function was employed piecewise.

Instead of assuming a constant $\rho_{Pt}$ across the entire thickness range, which is ignorant to the sharp upturn in the ultrathin limit, in figure 3.8 (a-c) we only fit the line to $R_{XX}$ data down to $t \sim 6$ nm to extract a bulk resistivity $\rho_{bulk}$ for each of the (un)buffered bilayers. Only the solid dark grey data points are fit to estimate $\rho_{bulk}$ for each case, which are dependent on Pt microstructure. The negative intercepts in panels (a-c) may be explained by multiple compounding factors. Firstly, this suggests that Pt at $t < 1.5$ nm are forming a non-continuous layer with significant void space regardless of buffer. In addition, the growth regime here is significantly different than in those of thicker samples under 2-D, VDM-type growth; the mass flux during sputtering is equivalent, but the growth rate calibration is not expected to be the same in this limit. Here, the linear the extrapolation of the growth rate from the calibraiton thicker samples may well be inaccurate and the true film thickness will deviate from that expected.

In panels (d-f), the thickness-dependent $\rho_{Pt}$ values extracted from Matthiessen's rule for the (un)buffered Pt|CoFeB bilayers are each fit to the Fuchs-Sondheimer function represented by the dashed lines to obtain a continuous $\rho(t)$ for each series using the extracted $\rho_{bulk}$ values from panels (a-c) and assuming surface scattering is completely diffuse ($p$ = 0). The one parameter fitting yields the mean free path $l_0 \sim$ 11 nm, 5.7 nm and 8 nm for un-, Ru- and Ta-buffered Pt seires, respectively. Note at ultralow thicknesses $t \leq 4.5$ nm in the unbuffered series, the resistivity deviated significantly from the Fuchs-Sondheimer prediction and an exponential decay function was employed here piecewise to fit the data and for a representative $\rho(t)$ function. These functions are instrumental in the analysis of all spin transport measurements in chapters 4-6.

### 3.3.2 Scattering mechanisms in the ultrathin limit

To better understand the physical mechanisms behind the thickness-dependent $\rho_{Pt}$ in the ultrathin limit and the resultant effect on spin dependent-scattering, we compare the functional forms of Fuchs-Sondheimer diffuse surface scattering and Mayadas-Shatzkes grain boundary scattering models to the resistivity data. To determine the physical origin of the enhanced electron scattering at low thickness, we fit each series with a combination of Fuchs-Sondheimer surface and Mayadas-Shatzkes grain boundary scattering models from equations 3.1 and 3.2, simultaneously. In the Mayadas-Shatzkes grain boundary scattering model, we use approximate $D(t)$ from the observed lateral grain sizes from HAADF-STEM images, calculated from the equation B.1 in Appendix B. For this analysis, we now fit the resistivity data displayed in figure 3.8 with a fixed mean free path of 11 nm [170,200] for both models to reduce the number of free parameters and determine the dominance of each scattering mechanism. We also assume that grain boundary scattering is both elastic and inelastic in equal weight ($R$ = 0.5) and that surface scattering is completely diffuse ($p$ = 0) in the Fuchs-Sondheimer model. By setting the scaling factor $R$ = 0.5, we do not bias the Fuchs-Schondheimer model to better test the dominance of each term.

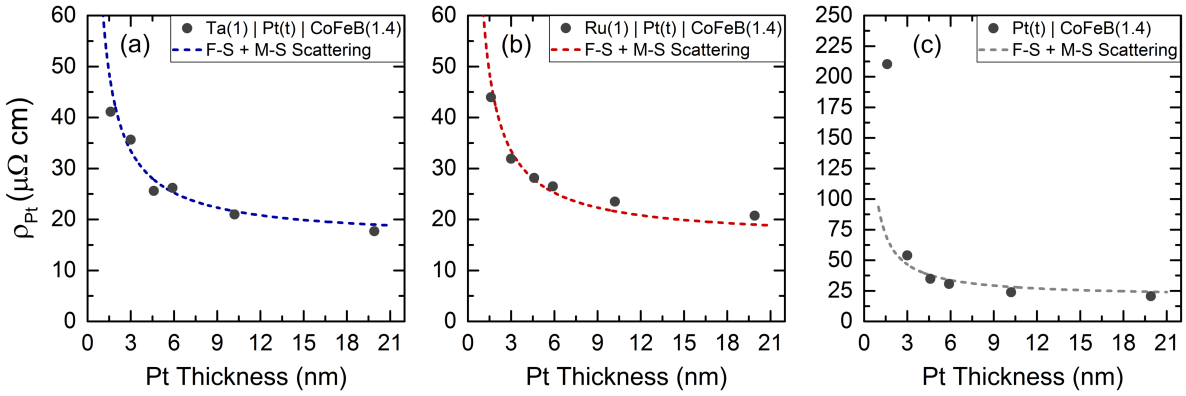


**Figure 3.9 Fitting Pt resistivity data down to the ultrathin limit of (un)buffered Pt with a combination of Fuchs-Sondheimer and Mayadas-Shatzkes models to determine the dominant physical origin responsible for the enhancement at low Pt thickness.**

The contribution of each scattering mechanism was evaluated by weighting the individual models with a pre-factor of unknown value and performing a residual analysis to find the set of factors to minimise the error between the resultant fitting function and the experimental data in figure 3.9. For ultrathin Pt films, we demonstrate that we cannot quantitatively distinguish between the two from the residual analysis; the minimum residual values are found across the near diagonal of the colour map displayed in figure B.3 of Appendix B. Indeed, these two scattering mechanisms are indistinguishable for thin Pt films when grain size scales with thickness [201]. Therefore, the fitting functions in figure 3.9 are comprised of an equal weighting (50 %) of each model and predict the resistivity well for the (un)buffered Pt films. This suggests that in these Pt|CoFeB bilayers, both grain boundary and diffuse surface scattering account for the enhanced $\rho_{Pt}$ in the ultrathin limit, and it is not possible to state quantitatively that one mechanism is more dominant.

Furthermore, in figure 3.9 (a) and (b), we observe a simple addition of both the Fuchs-Sondheimer and Mayadas-Shatzkes models fit the data well for both the Ta- and Ru-buffered series. The increased resistivity in ultrathin Ta-buffered Pt films, which were found to deposit following a VDM-type growth mode from STEM imaging in figure 3.4, suggests that the enhanced $\rho_{Pt}$ at low thickness is not due to percolation in ultra-low thicknesses, but instead from the aforementioned scattering mechanisms. However, the unbuffered Pt films in the ultrathin limit experience a drastic enhancement in $\rho_{Pt}$ as seen in figure 3.9 (c), which cannot be accurately predicted by grain boundary or surface scattering theory. Additionally, these unbuffered films were found to grow in islands with VW-type growth from the STEM images in figure 3.4. The combination of this evidence strongly suggests that these poorly-wet films are underneath the percolation threshold.

# 3.4 Magnetometry

To understand how $\boldsymbol{M}$ moves under an applied field $\boldsymbol{H}$ during spin transport measurements in chapters 4-6, we discuss the relevant forces competing to reduce the system energy and conduct preliminary magnetometry on thin FM films in metallic bilayers. Since the FM films in this work are deposited on top of the (buffer)|HM layer(s) where the discrepancy in microstructure is vast, we test the consistency of macroscopic magnetic properties with VSM measurements in the various of (un)buffered HM|FM bilayers. Hereby, the essential magnetic properties governing the magnitude and preferential direction of alignment of the FM thin films are ascertained.

## 3.4.1 Magnetometry on HM|FM bilayers

The magnetisation $\boldsymbol{M}$ of the FM film is set by an energy equation comprising two competing terms in the Stoner-Wolfrath[3] model [202]: the uniaxial anisotropy (aligning the magnetic moment to reduce magnetostatic energy) and the Zeeman energy (aligning the moment to an external magnetic field) define the overall direction of $\boldsymbol{M}$ in the FM. In typical thin FM films, the demagnetising field of $H_D = -4\pi M_s$ sets the preferred direction of the moment – the easy-axis – in the plane of the sample. $M_s$ is the saturation magnetisation in a FM film. The shape anisotropy of the thin FM film devices with lateral patterned dimensions up to $10^6$ times larger than the ultrathin thickness of the FM (on the order of 1 nm) also promotes in-plane anisotropy. Although the thin film geometry favours an easy-axis in-plane in the bulk of FM films, at ultralow thicknesses, interfacial effects become increasingly dominant. Therefore, at these thicknesses, $\boldsymbol{M}$ may preferentially point out of the film plane despite the extreme energetic unfavorability in the bulk due to demagnetisation. Perpendicular magnetic anisotropy (PMA) $K_\perp$ is the interfacial anisotropy term which promotes this easy-axis out-of-plane magnetisation. Therefore, when shape anisotropy is small, the effective anisotropy of a thin film is $K_{eff} = K_\perp - 2\pi M_s^2$, where the last term is the magnetostatic contribution pulling the FM in-plane.

The point at which the FM switches energetic favourability between an easy-axis in-plane to one out-of-plane is known as the spin reorientation transition (SRT) position and is governed by the thickness in ultrathin FM metals. Because PMA is an interface effect, it drops off at $d_{FM}^{-1}$. Further decreasing the FM thickness below the SRT (less than 2 nm for both Co and $Co_{60}Fe_{20}B_{20}$), allows for PMA to dominate over bulk demagnetisation effects, making it energetically favourable for $\boldsymbol{M}$ to sit perpendicular to the film surface. In this way, we may tune the FM anisotropy with $d_{FM}$ to satisfy different experimental requirements.

[3] The Stoner-Wohlfarth model is a macrospin approach (one that assumes the alignment of all electron spins) to the response of a single-domain ferromagnet under the application of an external field $\boldsymbol{H}$.

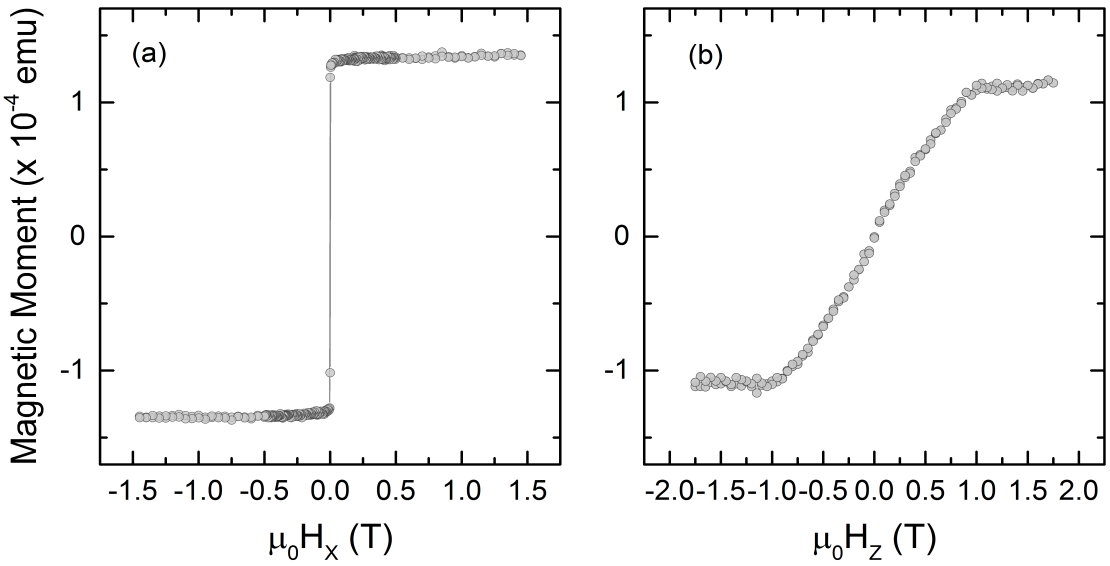


Figure 3.10 VSM hysteresis loops of a continuous thin Ta(1)|Pt(3)|CoFeB(5) film with an easy axis in the plane of the film. Prototypical (a) easy-axis and (b) hard-axis magnetisation switching of ***M*** from an in-plane and a perpendicular-to-plane applied field, respectively.

Important magnetic properties may be elucidated from prototypical ***M*** versus ***H*** easy-axis and hard-axis hysteresis loops of a Ta(1)|Pt(3)|CoFeB(5) continuous film in Figure 3.10 (a) and (b), respectively. At $d_{\mathrm{CoFeB}}$ = 5 nm, the FM is well above the SRT and the film is pulled strongly in-plane by the magnetostatic energy contribution. Panel (a) shows the film switching magnetisation in-plane at low field, typical of ***M*** when an ***H*** is swept along the easy-axis of the film. At this scale, is not possible to see the hysteretic coercivity common of easy-axis switching. The extrinsic property $M_s$ may be quantified from the plateau of the ***M*** at $\pm H$ by dividing the magnetic moment in figure 3.10 by the volume of magnetic material. Panel (b) shows the ***M*** pulled through a hard-axis by $H_Z$ and only switching above the anisotropy field $H_K^{\perp} = \frac{2K_{\perp}}{M_s} \sim 1$ T, where ***M*** plateaus from saturation. With both an in-plane and out-of-plane VSM measurement, we can fully characterise the FM macrospin properties of the Co(FeB) thin films. The difference in the measured moment between the two hysteresis loops may be explained by the filling factor (the ratio of the sample volume to the effective pickup coil volume) in our VSM system [203].

### 3.4.2 Protecting the ultrathin HM|FM bilayers

To protect the HM|FM bilayer from surface contamination and oxidation, a thin film capping layer is deposited on top of the heterostructure. The FM is the most susceptible layer in the (un)buffered bilayer as it is deposited on top of the stack. If the protective, capping layer is insufficient, the diffusive effects of oxidation from interstitial $O_2$ atoms dispersed in the FM layer can strongly alter the microstructure, directly affecting the conductive and magnetic properties. A course way of measuring the effects of oxidation in the FM layer is to quantify $M_s$ for various capping materials and thicknesses. Figure 3.11 shows the $M_s$ values for ultrathin CoFeB films measured on the VSM to determine an appropriate protective layer for

the metallic multilayers studied in this work. Using the dashed line as a reference value for thin film CoFeB $M_S$, we compare the effectiveness of the capping layers by observing which layer limits oxidation (quantified by reduced $M_S$) of the FM layer.

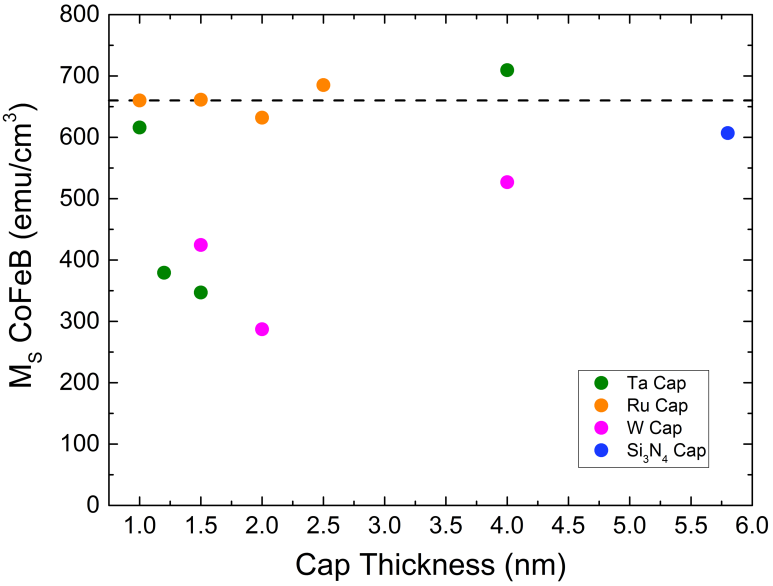


**Figure 3.11 Saturation magnetisation of ultrathin CoFeB films with different protective capping materials to prevent oxidisation.**

Ultrathin CoFeB films deposited in our laboratory have been found to have lower $M_S$ than films with bulk-like magnetic properties on occasion [204]. The dashed line in figure 3.11 representing the thin film CoFeB $M_S$ measured in these 1.5 nm samples is, indeed, much lower than bulk CoFeB film values presented in literature [205] as $M_S \sim 1100$ emu/cm$^3$. However, recent measurements show values similar to bulk $M_S$ on $(Pt|CoFeB)_2$ heterostructures. Therefore, we attribute these low values to a poor magnetic order in this specific target; this target was purchased from Lesker, which had recently changed their method of fabrication and thus its precise formulation. These low measured $M_S$ values do not impact the spin transport measurements presented in chapters 4-6.

All the tested metals oxidise substantially when exposed to atmosphere, however when capping with thin Ta and W, $M_S$ of the ultrathin 1.5 nm CoFeB continuous film is reduced significantly. Only when thicker Ta $\sim$ 4 nm is deposited does the $M_S$ recover to the thin film maximum. A thick insulating layer such as $Si_3N_4$ provides an acceptable protective layer, however, RF sputtering required to grow the insulator proved slow and inconvenient due to the limited number of magnetrons in the chamber. Ru is the only material to provide good protection in the ultrathin limit down to 1 nm as evidenced by $M_S$ in figure 3.11.

Furthermore, to limit current shunting in the HM bilayers, ultrathin, highly resistive materials are desirable. In the conductance measurements shown in figure 3.6 (c), we found that Ru is strongly oxidised, negating current flow. Additionally, the Ru deposited in this work has a negligible $\theta_{SH}$, which makes it an ideal, non-interactive, protective capping layer. All

multilayers used in the following chapters for spin transport measurements are protected with a 1 nm of Ru.

### 3.4.3 Consistency of magnetic properties in (un)buffered Pt|CoFeB bilayers

The thin films in this work used to probe the spin transport phenomenon in chapters 4-6 are predominantly Pt|Co(FeB) bilayers. In ultrathin FM samples, symmetry breaking at the interface in Co(FeB) creates PMA from unquenched in-plane electronic orbitals [206]. Additionally, PMA is strongly enhanced by depositing Pt under the Co(FeB) film through the hybridisation of the large SOC in Pt 5*d* orbital with the 3*d* orbital in Co [207,208]. Specifically, textured Pt underlayers have been attributed to larger PMA [209], with thicker Pt layers introducing more PMA [210]. Because we found that buffering Pt films increases Pt(111) texturing (Figure 3.2 (a)), and we perform Pt thickness-dependent measurements in chapters 4-5 grown on various seed layers, the contribution of $K_{\perp}$ to $K_{eff}$ will vary significantly. Specific methodology to control the magnetic properties of the (un)buffered HM|FM bilayers for each measurement will be outlined in the respective spin transport measurement chapters.

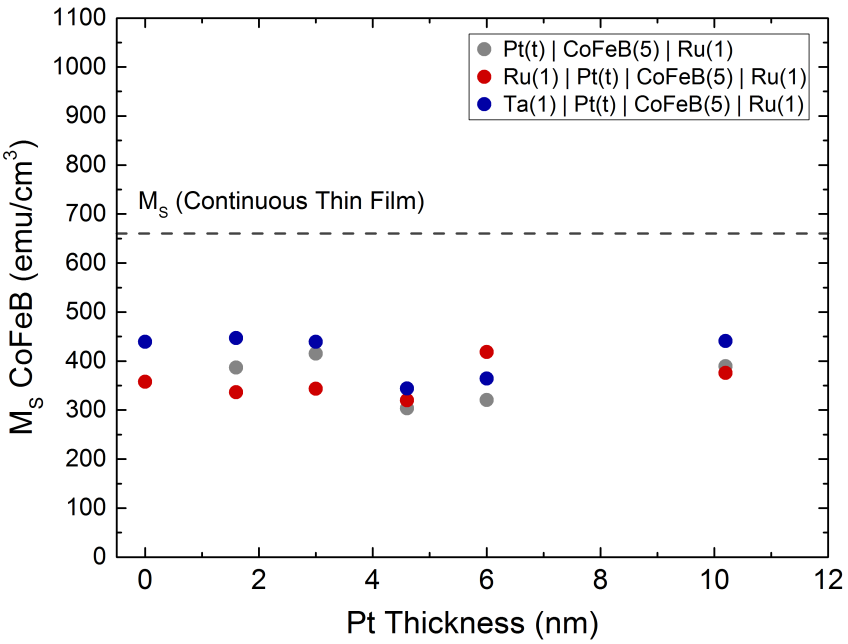


Figure 3.12 Saturation magnetisation of ultrathin 5 nm, 1.2 mm x 3 mm CoFeB bars deposited (un)buffered on $SiO_2$ versus underlayer Pt thickness.

With the FM deposited on top of the (buffer)|HM layer, it is possible that the microstructural changes with buffer and thickness of the underlayer HM may introduce similar variation in the FM. To check the effect of underlayer microstructural variations on $M_s$, we measure the easy-axis in-plane $M$ versus $H$ loops of ultrathin (un)buffered Pt(t)|CoFeB(5) bilayer rectangular bars ($l$ = 1.2 mm & $w$ = 3 mm). The tabulated results are displayed in Figure 3.12. There is no indication that $M_s$ is reduced on thin, unbuffered Pt films, which would indicate poor HM microstructure has an appreciable effect on the total moment $M$. Instead, $M_s$ is found to be relatively constant across all the (un)buffered HM thicknesses measured. This suggests that underlayer microstructure doesn't play an important role in altering the total

moment $\boldsymbol{M}$ of the FM, which is likely moderated by the amorphous growth of the CoFeB layer. Notice the $\boldsymbol{M}_S$ of these small, patterned bars are lower than that of a 5 mm x 5 mm continuous thin film (shown by the dashed line). There are multiple confounding effects, which we expect to explain this low $\boldsymbol{M}_S$ value. First, deposition with a sputtering target non-normal onto a sample with patterned resist creates a shadowing effect at the side of the bars. Here, less magnetic material is depsoited than expected, which artificially reduces $\boldsymbol{M}_S$. However, due to the thin ~ 0.6 μm resist layer and the large feature sizes of the patterned bars, this is not likely the dominant effect. The organic resist degassing oxygen and water vapour in the ultralow vaccuum chamber during growth is a more reasonable explination for the low reported $\boldsymbol{M}_S$ value. Again, this has no bearing on the comparative analysis of the effects of HM microstructure on spin transport.

## 3.5 Conclusions

In this chapter, we characterised ultrathin film HM and FM layers in preparation for all subsequent spin transport measurements discussed in chapter 4-6. Ultrathin HM films are strongly sensitive to growth conditions, allowing us to tune HM microstructure by both adjusting the working pressure in the sputter chamber during deposition and by seeding HM growth with high melting-point metals. X-ray diffractometry and reflectivity measurements proved that an increase in the chamber working pressure reduced Pt film deposition energy on the substrate, which resulted in a less crystalline Pt(111) texture and a larger roughness. Deposition of a buffer layer showed more significant changes in Pt microstructure than by changing the working pressure during HM growth. Pt(111) texture was strongly enhanced (completely suppressed) with a 1 nm Ta buffer (Ru buffer). A significant roughness and thickness reduction in Ta-buffered Pt suggest an additional control of the growth mode in the ultrathin limit depending on seed conditions. This is confirmed by aberration-corrected HAADF-STEM microscopy, which shows superior wetting from unbuffered, to Ru-buffered to Ta-buffered ultrathin Pt films. Since buffering Pt growth showed more texture and roughness tunability than through changing the chamber working presure, it was chosen as the most effective method to study the effects of Pt microstructure morphology to spin transport in HM|FM bilayers.

Thin film resistivities were characterised for the constituent materials deposited in this work. Quantifying resistivity from thickness-dependent measurements was useful for some materials, but insufficient for understanding electronic properties of crystalline materials in the ultrathin limit. For thin Pt films, resistivity was instead extracted with Matthiessen's rule, and the sharp rise at ultralow thickness was fit by Fuchs-Sondheimer and Mayadas-Shatzkes theories, simultaneously. The upturn in Pt resistivity in the ultrathin limit was attributable to both grain boundary scattering and diffuse surface scattering.

The magnetic properties of the widely used FM in this work, CoFeB, were probed across a range of (un)buffered Pt(t)|CoFeB bilayers to analyse the uniformity of the FM film in chapter 4-6 devices. However, a constant $M_s$ was recorded in the ultrathin CoFeB films, likely due to its amorphous structure, which suggests consistent magnetic properties. The 1 nm Ru cap was found to be optimal in protecting the CoFeB against oxidisation with $M_s$ measurements while hindering current shunting. It is used to cap all fabricated devices in the following chapters.

# 4 Spin current reflection in the ultrathin limit: Spin Hall magnetoresistance

## 4.1 Introduction

Quantifying the spin Hall magnetoresistance in metallic thin films is becoming increasingly common to probe spin-dependent properties. As outlined in section 1.2.5, SHMR sees the resistivity of a HM layer directly affected by magnetisation of the adjacent magnetic layer [3,92,140–143]. Through the simultaneous action of the SHE and the ISHE, the interfacial spin transparency and the amount of spin absorption in the FM depend on the relative angle of $\boldsymbol{M}$ in the FM and $\boldsymbol{\sigma}_s$ of the conduction electrons in the HM. The proportion of spin transmission through and reflection at the interface determines the magnitude of ISHE in the HM acting to increase film conductivity. Therefore, by controlling the relative direction between $\boldsymbol{M}$ and $\boldsymbol{\sigma}_s$ with an externally applied field $\boldsymbol{H}$, a change in HM resistivity is observed through the (I)SHE.

HM thickness-dependent SHMR measurements have been shown to be an effective way of observing spin-to-charge conversion and spin relaxation through a change in film resistivity [3,92,140,188]. The imbalance of spin subband populations about the interface in the HM is strongly depth-dependent and decays quickly with spin-flip scattering as spins relax into the layer. So, the spin Hall magnetoresistance of a bilayer given by equation 1.30, changes with HM thickness too, regardless of the relative direction of $\boldsymbol{M}$ and $\boldsymbol{\sigma}_s$. Thereby, the SHMR signal propagation into the HM depth is determined by its spin-dependent parameters: the spin $\lambda$ diffusion length and the magnitude of the signal by the spin-to-charge conversion efficiency $\theta_{\mathrm{SH}}$.

However, as it turns out, this method of estimating spin-dependent parameters has limitations which prevent an accurate estimate thereof. In particular, growth modes and microstructure of ultrathin HM films change over the thickness range, as shown in the previous chapter. Electrical measurements are particularly challenging in this limit due to inherent changes in film resistivity from grain boundary and diffuse surface scattering. Therefore, extracting spin-dependent parameters from the spin Hall magnetoresistance in ultrathin textured films such as Pt, which have notable changes in resistivity (as shown in section 3.3.1), must be done cautiously. In this light, Yin *et al*. [140] have recently accounted for the change in $\rho_{\mathrm{Pt}}$ across the Pt thickness range to more precisely model SHMR in the Pt|Co system. However, building evidence shows that spin transport in Pt is governed by Elliot-Yafet spin relaxation [84–87] and intrinsic spin scattering [67,68,74,87,143,211], which should additionally prompt the effective $\lambda$ and $\theta_{\mathrm{SH}}$ values to vary with Pt resistivity across the thickness range.

In this chapter, we revisit the methodology behind varying HM thickness to extract spin-dependent parameters in SHMR measurements. Although observing SHMR in bilayers is powerful for extracting spin-dependent parameters such as $\lambda$ and $\theta_{SH}$ in HMs, we prove it is more challenging than currently expected in the ultrathin limit. To do so, we fabricate multiple series of all metallic bilayer devices comprised of commonly studied constituent materials (HM: Ta, W, Pt and FM: Co, CoFeB) and measure HM thickness dependent SHMR. Furthermore, we demonstrate the vital influence of HM microstructure on spin transport in the ultrathin limit on a series of (un)buffered Pt|CoFeB bilayers. To estimate spin-dependent parameters, we extend the current HM|FM bilayer magnetoelectronic circuit theory to include the buffer layer. We show that buffered bilayers can only be accurately modelled when varying Pt resistivity across the thickness range, as well as $\lambda$ and $\theta_{SH}$ due to Elliot-Yaffet spin relaxation and intrinsic spin scattering in the Pt. We demonstrate that this approach is successful in its prediction of SHMR measurements despite vastly different magnitudes observed in HM|FM bilayers due to changing HM microstructure.

## 4.2 Experimental setup

In this chapter we measure SHMR in metallic HM|FM bilayers of commonly studied constituent materials (HM: Ta, W, Pt and FM: Co, CoFeB). Angular magnetoresistance measurements are performed with the spin transport rig to probe both AMR and SHMR in (un)buffered HM|FM bilayers. The bilayers deposited in a Hall bar geometry depicted in figure 4.4 are temporarily fixed directly on one of the compact samples holders with Rubber Cement™ and wire bonded. The ends of the Hall bars are contacted as current leads, while the two outermost voltage taps are used to increase the spin signal size. If the voltage taps are connected on opposite sides of the Hall bar, a spurious AHE signal will arise from an out-of-plane $\boldsymbol{M}$ component. To avoid this parasitic signal in SHMR measurements, we always contact the same side of the Hall bar as illustrated in figure 4.4.

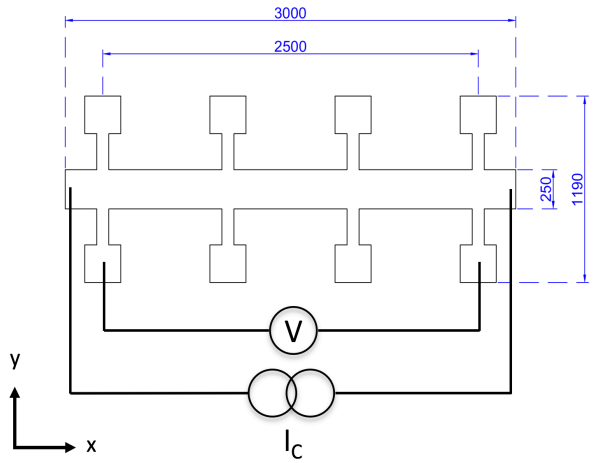


Figure 4.1. CAD illustration of the (un)buffered HM|FM Hall bar used in SHMR measurements. A schematic is displayed of the voltage and current taps connecting instrumentation to the Hall bar through wire bonding. The dimensions are displayed in µm.

All experiments are conducted at room temperature with the Keithleys in delta mode by sourcing 1 mA current from the KSM 2400 and recording a voltage reading every 2.4 s. This is the minimum acquisition time possible for delta mode due to a combination of both the code's run-time and the slow, differential voltage delta mode measurement. While the STMA measures voltage, a constant applied field ***H*** is rotated about the sample plane at a 1.67°/s in one of the three planes (XY, XZ or YZ) as outlined in figure 4.6 (a). The angular velocity is chosen to minimise thermal drift, yet still provide a sufficient set of data points to observe the sinusoidal dependence of the magnetoresistance with rotation. This methodology is applied to all angular magnetoresistance measurements on HM|FM bilayers to ascertain the anomalous and spin Hall components depending on the plane of ***H*** rotation.

Experimentation at RT permits the use of the compact sample holders instead of the cryostat, allowing us to apply larger saturating fields to decouple the AMR from SHMR with the GMW 3470. The field magnitude is of particular importance since ***M*** must saturate and follow ***H*** in all angular measurements. To avoid non-uniform radiative heating from the pole pieces during rotation when driving the electromagnet to $\pm$6 V, the sample was shielded with a bored Al cylinder to redistribute the radiation and to eliminate parasitic voltages at the same period as the field rotation. Although the differential acquisition in delta mode reduces background offsets such as thermoelectric drift, small thermal backgrounds (maximum $\sim$ 10 % of the initial voltage $V_0$) persist across the measurement window ($\sim$ 3m40s) arising from changes in resistivity with temperature. To quantify this change, we calibrated the change in $R^0_{XX,Pt}$ of a Pt Hall bar as a function of ambient room temperature (see figure A.1 Appendix A). The 3 nm thick Pt Hall bar resistance is found to change at a rate of 0.088 %/K at most, indicated the observed drift in SHMR measurements may be sensibly attributed to heating from the GMW 3470 pole pieces. Therefore, during each magnetoresistance measurement, we simultaneously acquire the resistance change of a patterned Pt thermometer on-chip to linearly correct any thermal drift.

For low anisotropy samples, ***H*** of the GMW 3470 electromagnet at narrow pole spacings is sufficient to saturate ***M*** in the hard-axis. The SHMR devices are designed to lie close to the SRT, and so minimise the anisotropy field. However, for series with larger anisotropy, the transport setup rack was moved to a larger 1.75 T electromagnet to ensure ***M*** saturation. In this system, the electromagnet is large and remains fixed, while the sample holder rotates. A new compact sample holder was fabricated from a Cu BreadBoard for these measurements in the same way as in section 2.3.1, with a longer brass rod, flexible wires and good secure solder contacts to minimise noise.

## 4.3 Modelling SHMR in (un)buffered HM|FM bilayers

### 4.3.1 Current HM|FM bilayer SHMR model

SHMR was first theoretically explained in a simply HM|FMI bilayer [82,138], where the magnetoresistance arises only from absorbed SOT in the FMI, and no $\boldsymbol{j}_c$ flows through the insulating ferrimagnetic layer. In this system, the majority and minority spin populations are modelled with spin electrochemical potential as outlined in section 1.2.1. The drift-diffusion equation (1.18) is solved to find an exponential decay of the spin accumulation over the spin diffusion length $\lambda$ from equation 1.19. For normal metals, this results in a spin accumulation in equation 1.20, but for layers with high SOC, like those of HMs, a significant amount spin angular momentum is separated by the SHE with an applied $\boldsymbol{j}_c$. Therefore in these layers, the spin current can be seen to follow

$$\boldsymbol{j}_{s,i} = -\frac{1}{2e\rho_i\lambda_i}\left[Ae^{-z/\lambda_i} - Be^{z/\lambda_i}\right] - \boldsymbol{j}_{\mathrm{SHE},i}. \tag{4.1}$$

The HM|FMI system is illustrated in figure 4.2. Here the boundary conditions state that the spin current is continuous across the interface $\boldsymbol{j}_s(z=0) = \boldsymbol{j}_s^{\mathrm{HM|FMI}}$ and at the top of the NM, the spin current is nil when in contact with atmosphere $\boldsymbol{j}_s(z=t) = 0$. The purely transverse spin current transmitted across the interface depends on the relative orientation of $\boldsymbol{M}$ and $\boldsymbol{\sigma}_s$ as given by [93]

$$\boldsymbol{j}_s^{\mathrm{HM|FMI}} = g_r\, \boldsymbol{M}\times(\boldsymbol{M}\times\boldsymbol{\sigma}_s) + g_i(\boldsymbol{M}\times\boldsymbol{\sigma}_s). \tag{4.2}$$

By solving for $\boldsymbol{j}_s$ in the HM layer when $\boldsymbol{M} \parallel \boldsymbol{\sigma}_s$ and $\boldsymbol{M} \perp \boldsymbol{\sigma}_s$, assuming $g_r \gg g_i$ and converting the total (integrated) $\boldsymbol{j}_s$ to a $\boldsymbol{j}_c$ with the ISHE from equation 1.15, the SHMR is given by [138]

$$\frac{\Delta R_{XX}^{\mathrm{SHMR}}}{R_{XX}^{0}} = \theta_{\mathrm{SH}}{}^2\frac{\lambda}{t}\frac{2\lambda g_r\tanh^2(t/2\lambda)}{\sigma + 2\lambda g_r\coth(t/2\lambda)}, \tag{4.3}$$

where all relevant parameters are of the HM layer. Notice the exponential functions from the spin accumulation are represented in the hyperbolic tangent and cotangent terms. Here, we observe the SHMR signal magnitude is dependent directly on $\theta_{\mathrm{SH}}{}^2$ from both the SHE and ISHE and the real component of the spin mixing conductance $g_r$. This theory assumes, of course, that there is no induced magnetic proximity effect in the few monolayers of HM near the interface, nor any additional interfacial spin relaxation due to SML.

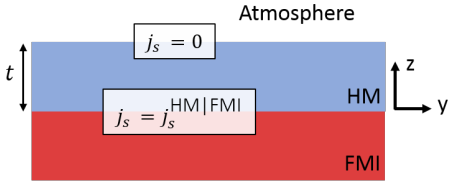


Figure 4.2 Cross-sectional illustration of a HM|FMI bilayer with the boundary conditions denoted at their respective position in the heterostructure. These conditions were used to solve the magnetoelectronic circuit theory model for predicting SHMR.

Recently, SHMR theory was extended to the more complex HM|FM system [3]. Unlike in the case of insulating ferrimagnets, the FM is electrically conductive, which results in resistance changes from parasitic AMR signals and additional current shunting. Moreover, a charge-mediated spin current can travel across the HM|FM into the conducting FM layer and longitudinally relax the spin polarisation when $\boldsymbol{M}$ is collinear to $\boldsymbol{\sigma}_s$. This is in addition to the transverse spin relaxation due to local torque exerted on the magnetisation, which is the mechanism behind the SHMR signal of interest as outlined in section 1.2.5. Here Kim *et al.* [3] redefined SHMR for HM|FM bilayers by adding another term onto equation 4.3 to account for this longitudinal spin-flip relaxation

$$\frac{\Delta R_{XX}^{SHMR}}{R_{XX}^{0}} = {\theta_{SH}}^2 \frac{\lambda_{HM}}{t} \frac{\tanh^2(t/2\lambda_{HM})}{1+\xi} \left[ \frac{g_1}{1+g_1 \coth(t/\lambda_{HM})} - \frac{g_2}{1+g_2 \coth(t/\lambda_{HM})} \right], \tag{4.4}$$

$$g_1 \equiv 2\rho_{HM}\lambda_{HM} g_r, \tag{4.5}$$

$$g_2 \equiv \frac{(1-P_{FM})^2}{\rho_{FM}\lambda_{FM} \coth\left({d_{FM}}/{\lambda_{FM}}\right)}. \tag{4.6}$$

Where $\xi = \frac{d_{FM}\,\rho_{HM}}{t\,\rho_{FM}}$ accounts for the current shunting through the conductive FM. This is the identical form to equation 4.3, except for the second term in the square brackets which denotes the longitudinal spin-flip scattering in the FM. Notice, $g_2$ in equation 4.6 is the spin resistance including spin backflow in the FM as outlined previously in equation 1.21. This model will be used to fit unbuffered HM|FM bilayer experimental data in this chapter.

### 4.3.2 Buffered HM|FM bilayer SHMR model

The unbuffered HM|FM model is not suitable to be applied to buffered devices for two important reasons. Firstly, unlike the case where a bilayer is deposited directly on a completely spin reflective $SiO_2$ substrate, the buffer has a non-zero spin resistance and a finite $\mu_s$. The effects of spin sinking in the seed layer propagates through the stack, altering $\mu_s$ for each constituent layer from those in the standard model. Secondly, $\mu_s$ gives rise to an appreciable ISHE signal when $\theta_{SH,buf}$ is finite. Therefore, we developed an extended SHMR magnetoelectronic circuit theory model to fit buffered bilayers (BUF|HM|FM) and model $\mu_s$, $\boldsymbol{j}_s$ of the non-magnetic layers. Similar to section 4.2.1, SHMR signals are predicted directly from converting the spin population imbalance to a $\boldsymbol{j}_c$ from the ISHE.

Both the buffer and the HM are potentially significant SOC layers adding to the SHMR signal. The spin accumulation and currents of these layers are defined

$$\mu_{s,\text{buf}} = Ae^{-z/\lambda_{\text{buf}}} + Be^{z/\lambda_{\text{buf}}}, \tag{4.7}$$

$$\mu_{s,\text{HM}} = Ce^{-z/\lambda_{\text{HM}}} + De^{z/\lambda_{\text{HM}}}, \tag{4.8}$$

$$\boldsymbol{j}_{s,\text{buf}} = -\Psi_{\text{buf}}\left[Ae^{-z/\lambda_{\text{buf}}} - Be^{z/\lambda_{\text{buf}}}\right] - j_{\text{s,buf}}^{\text{SHE}}, \tag{4.9}$$

$$\boldsymbol{j}_{s,\text{HM}} = -\Psi_{\text{HM}}\left[Ce^{-z/\lambda_{\text{HM}}} - De^{z/\lambda_{\text{HM}}}\right] - j_{\text{s,HM}}^{\text{SHE}}, \tag{4.10}$$

where we set $\Psi_i \equiv \frac{1}{2e\rho_i\lambda_i}$. To solve for the four unknowns $(A, B, C, D)$ of the system of equations 4.7 - 4.10, the boundary conditions from original magnetoelectronic circuit theory work are extended to a buffered HM|FM system as illustrated in figure 4.3.

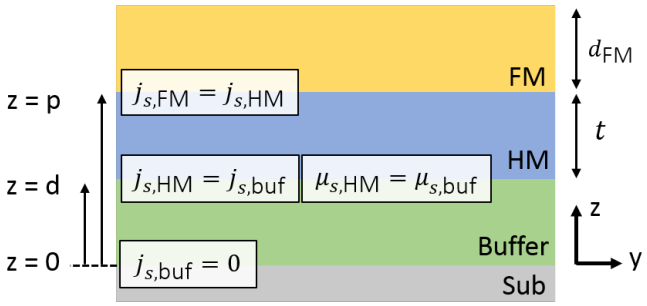


Figure 4.3. Cross-sectional illustration of a buffered HM|FM bilayer with the boundary conditions denoted at their respective position in the heterostructure. These conditions were used to solve the magnetoelectronic circuit theory model for predicting SHMR.

These boundary conditions are:

The spin current passing through the SUB|BUF interface is nil ($j_{s,\text{buf}} = 0$) at z = 0:

$$\boldsymbol{j}_{\text{s,buf}}^{\text{SHE}} = \Psi_{\text{buf}}[B - A] \tag{4.11}$$

The spin current passing through the BUF|HM interface is equal ($\boldsymbol{j}_{s,\text{buf}} = \boldsymbol{j}_{s,\text{HM}}$) at z = $d$:

$$\Psi_{\text{buf}}\left[-Ae^{-d/\lambda_{\text{buf}}} + Be^{d/\lambda_{\text{buf}}}\right] - \boldsymbol{j}_{\text{s,buf}}^{\text{SHE}} = \Psi_{\text{HM}}\left[-Ce^{-d/\lambda_{\text{HM}}} + De^{d/\lambda_{\text{HM}}}\right] - \boldsymbol{j}_{\text{s,HM}}^{\text{SHE}} \tag{4.12}$$

The spin accumulation at the BUF|HM interface is equal ($\mu_{s,\text{buf}} = \mu_{s,\text{HM}}$) at z = $d$:

$$Ae^{-d/\lambda_{\text{buf}}} + Be^{d/\lambda_{\text{buf}}} = Ce^{-d/\lambda_{\text{HM}}} + De^{d/\lambda_{\text{HM}}} \tag{4.13}$$

Note, in equation 4.13, equating $\mu_{s,\text{buf}} = \mu_{s,\text{HM}}$ assums no spin interface resistance, however a term may be added here to introduce a discontinuous jump in $\mu_s$ across the BUF|HM interface.

The spin current passing through the HM|FM interface is equal ($\boldsymbol{j}_{s,\text{HM}} = \boldsymbol{j}_{s,\text{FM}}$) at z = $p$:

$$\Psi_{\text{HM}}\left[-Ce^{-p/\lambda_{\text{HM}}} + De^{p/\lambda_{\text{HM}}}\right] - \boldsymbol{j}_{\text{s,HM}}^{\text{SHE}} = \frac{\Pi_{\text{sink}}}{e}\mu_s^{\text{HM|FM}} \tag{4.14}$$

Where $\mu_s^{\mathrm{HM|FM}} = \left[Ce^{-p/\lambda_{\mathrm{HM}}} + De^{p/\lambda_{\mathrm{HM}}}\right]$ due to the continuity of $\mu_s$ across the HM|FM interface. In HM|FM bilayers, the FM conduction allows longitudinal spin relaxation from spin-flip scattering regardless of the relative orientation of $\boldsymbol{M}$ and $\boldsymbol{\sigma}_s$. Therefore, $\boldsymbol{j}_s^{\mathrm{HM|FM}} \neq 0$ when $\boldsymbol{M} \parallel \boldsymbol{\sigma}_s$, which requires us to revisit the spin sinking term outlined in equation 1.29. Instead, the spin relaxation at $\boldsymbol{M} \parallel \boldsymbol{\sigma}_s$ is defined by the spin resistance of the FM, as defined in equation 1.21. Here, $\Pi_{\mathrm{sink}} \rightarrow R_{s,\mathrm{FM}}/2$ at $\boldsymbol{M} \parallel \boldsymbol{\sigma}_s$ and $\Pi_{\mathrm{sink}} \rightarrow g_r$ at $\boldsymbol{M} \perp \boldsymbol{\sigma}_s$ to align with current magnetoelectronic circuit theory.

We use Mathematica to solve the system of four equations simultaneously to predict $\mu_s$, $\boldsymbol{j}_s$ in both the buffer and the HM layer. In figure 4.4 (a) and (b), an example of $\mu_s$, $\boldsymbol{j}_s$ in a Ta(1)|Pt(3)|CoFeB(1.4) heterostructure is plotted, respectively, for each case where $\boldsymbol{M} \parallel \boldsymbol{\sigma}_s$ and $\boldsymbol{M} \perp \boldsymbol{\sigma}_s$ in both the Ta-buffer and the Pt layer. Notice, the model follows the boundary conditions outlined in equations 4.11 – 4.13: $\mu_s$ and $\boldsymbol{j}_s$ are continuous at the Ta|Pt interface and $\boldsymbol{j}_s$ = 0 at the SUB|Ta interface. In figure 4.4 (a) the spin accumulation $\mu_s$ is zero when $\boldsymbol{M} \parallel \boldsymbol{\sigma}_s$ at approximately halfway through the Pt layer (z ~ 1.5 nm) as expected. The area between $\boldsymbol{j}_s$ at $\boldsymbol{M} \perp \boldsymbol{\sigma}_s$ and $\boldsymbol{M} \parallel \boldsymbol{\sigma}_s$ shaded in blue in figure 4.4 (b) shows the amount of spin current in the Ta-buffer and Pt layers which is converted to a $\boldsymbol{j}_c$ with the ISHE as illustrated in equation 4.15.

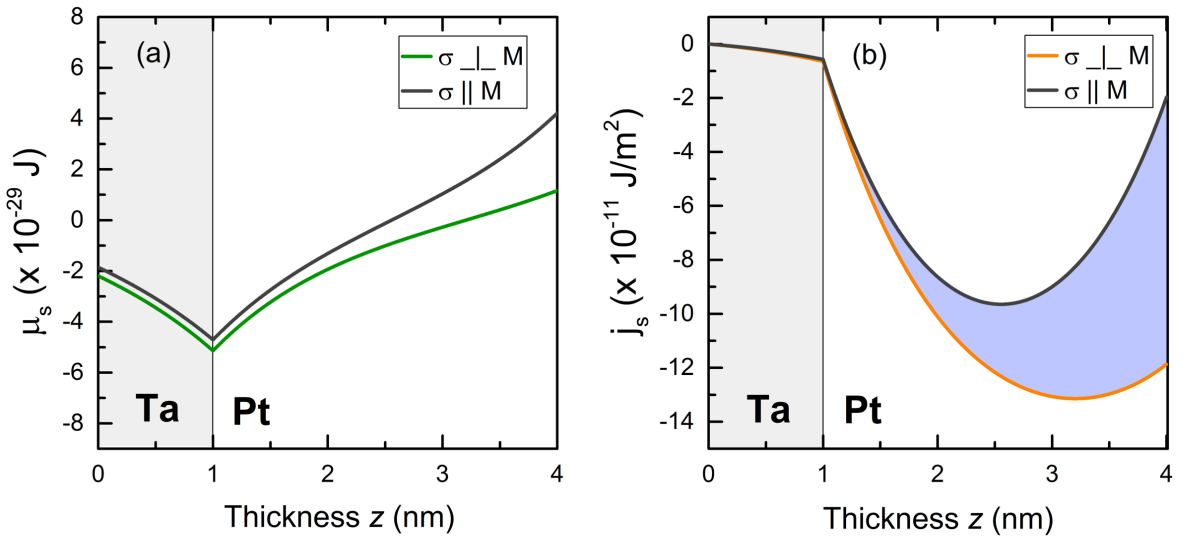


Figure 4.4. Modelled (a) spin accumulations and (b) spin currents in a Ta(1)|Pt(3)|CoFeB(1.4) sample for reasonable spin-dependent values $\theta_{\mathrm{SH,Pt}}$ = 0.086 and $\lambda_{\mathrm{Pt}}$ = 2 nm, $g_r$ = 5 x $10^{15}$ $\Omega^{-1}m^{-2}$ at different relevant orientations of $\boldsymbol{M}$ and $\boldsymbol{\sigma}_s$.

Once $\mu_s$, $\boldsymbol{j}_s$ are known for both buffer and HM layers, the entire spin system is defined for the spin Hall effect materials. As outlined in section 1.2.5, any $\boldsymbol{j}_s$ reflection at the HM|FM interface generates a $\boldsymbol{j}_s^R(z)$, which adds to film conductivity with an ISHE component defined $\boldsymbol{j}_{c,i}^{\mathrm{ISHE}}$. This component is dependent on the relative orientation of $\boldsymbol{M}$ and $\boldsymbol{\sigma}_s$ and evaluated by integrating $\boldsymbol{j}_s$ across the layer thickness for the cases where $\boldsymbol{M} \perp \boldsymbol{\sigma}_s$ and $\boldsymbol{M} \parallel \boldsymbol{\sigma}_s$ following

$$\boldsymbol{j}_{c,i}^{\mathrm{ISHE}} = \theta_{\mathrm{SH},i} \int \boldsymbol{j}_{s,i}\, dz. \tag{4.15}$$

The conductivity of the stack without any additional SHE component is the sum of the conductivities of the layers in parallel:

$$\sigma_0 = \frac{d}{\rho_{\text{buf}}} + \frac{t}{\rho_{\text{HM}}} + \frac{d_{\text{FM}}}{\rho_{\text{FM}}} \tag{4.16}$$

Therefore, the stack resistance $R_{\text{XX}}$ is given by the inverse summation of the two components:

$$R_{\text{XX}} = \frac{l}{A_c}\left(\frac{\boldsymbol{j}_{c,\text{buf}}^{\text{ISHE}} + \boldsymbol{j}_{c,\text{HM}}^{\text{ISHE}}}{\boldsymbol{E}_{\text{X}}} + \sigma_0\right)^{-1} \tag{4.17}$$

where $l$ is the length and $A_c$ is the cross-sectional area of the Hall bar, $\boldsymbol{E}_{\text{X}}$ is the applied electric field in plane and $\boldsymbol{j}_{c,i}^{\text{ISHE}}$ dependent on the relative orientation of $\boldsymbol{M}$ and $\boldsymbol{\sigma}_s$. Restating equation 1.30 for readability, the SHMR is the difference in signal follows directly from

$$\frac{\Delta R_{\text{XX}}^{\text{SHMR}}}{R_{\text{XX}}^{0}} = = \frac{R_{\boldsymbol{M}\perp\boldsymbol{\sigma}_s} - R_{\boldsymbol{M}\parallel\boldsymbol{\sigma}_s}}{R_{\boldsymbol{M}\parallel\boldsymbol{\sigma}_s}}. \tag{4.18}$$

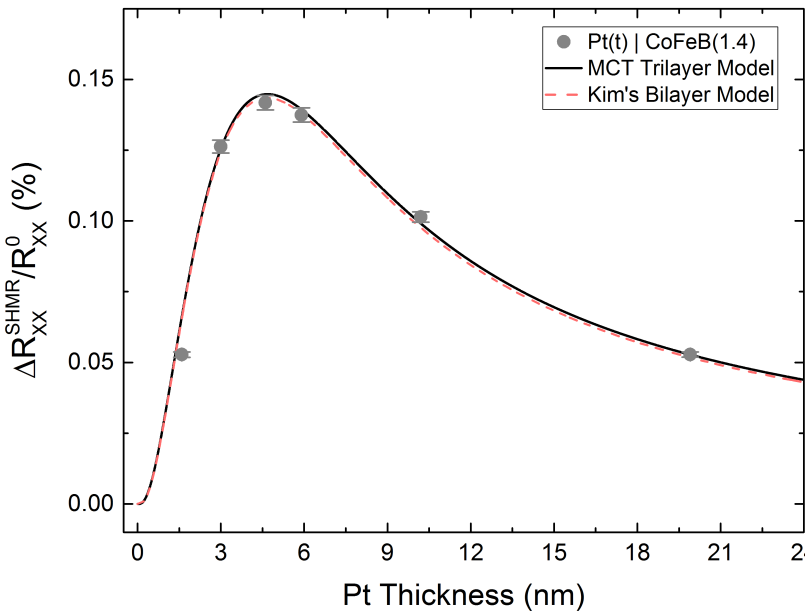


Figure 4.5 Kim's bilayer model outlined in equation 4.4 and the developed buffer model with a prototypical set of SHMR values at varying $t$. The buffer layer is set to have identical parameters as the HM Pt layer ($\theta_{\text{SH,Pt}}$ = 0.154 and $\lambda_{\text{Pt}}$ = 2 nm) and $g_r$ = $10^{15}$ $\Omega^{-1}\text{m}^{-2}$.

To show consistency between Kim's bilayer model in equation 4.4 and the developed buffered model, we plot them both together in figure 4.5. Here, the spin ($\lambda$ and $\theta_{\text{SH}}$) and electrical ($\rho$) parameters of the buffer layer are set to the same as the Pt, HM layer to directly compare the models. They show good agreement, indicating the validity of the extended BUF|HM|FM model developed in this section.

# 4.4 Spin Hall magnetoresistance in HM|FM bilayers

In this section, we highlight experimental findings of angular $\frac{\Delta R_{XX}^{SHMR}}{R_{XX}^{0}}$ measurements on HM|FM bilayers as a function of HM thickness to estimate properties such as $\theta_{SH}$ and $\lambda$. We examine an array of metallic HM|FM bilayers (HM: Ta, W, Pt, Ru; FM: CoFeB, Co) first to quantify spin-dependent properties and discern the optimal bilayer to observe the effect of changing HM microstructure morphology on spin Hall magnetoresistance. We find that bilayer to be Pt|CoFeB and seed HM growth with ultrathin, 1 nm Ta and Ru layers to tune the Pt growth mode. We apply our extension of the existing SHMR magnetoelectronic circuit theory to the model developed in the previous section to fit the experimental data. To facilitate the comparison between measurements, we depict Ta-, Ru- and (un) buffered Pt|CoFeB bilayer with their respective colour schemes as in Chapters 3.

## 4.4.1 The angular SHMR measurement

In HM|FM bilayers, SHMR signals are convoluted by parasitic AMR effects from a $\boldsymbol{j}_c$ flowing through the FM layer, unlike the less complex HM|FMI system. To disentangle the SHMR from AMR, we take advantage of the difference in angular dependence. Both magnetoresistances follow a $\cos 2\Theta$ dependence, but the relevant angle differs. As noted in section 1.1.5, AMR depends on the relative angle between $\boldsymbol{M}$ and $\boldsymbol{j}_{c,x}$. In contrast, SHMR depends on the relative angle between $\boldsymbol{M}$ and $\boldsymbol{\sigma}_s$. We evaluate the contribution of each magnetoresistance by rotating $\boldsymbol{H}$ at the maximum available field ($\mu_0 H \sim 1$ T for the 12 mm pole spacing of the GMW 3470 electromagnet and 1.7 T for the larger electromagnet) in three perpendicular planes. Figure 4.6 is a schematic for the angular measurement visualisation.

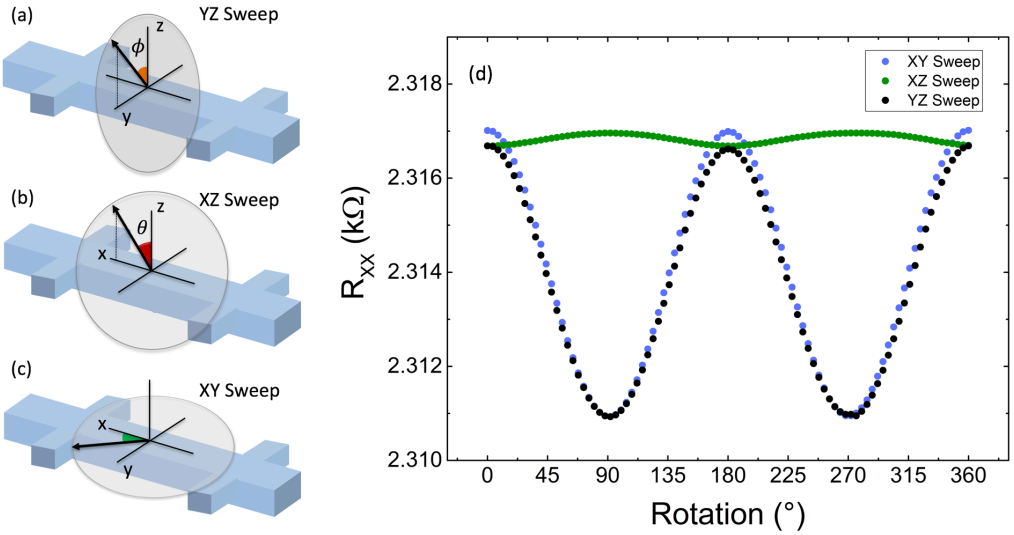


Figure 4.6. (a-c) Schematic illustrations of H field sweeps in the YZ, XZ and XY planes about a Hall bar, respectively. (d) The corresponding angular $R_{XX}$ measurements on a Ta(1)|Pt(1.6)|CoFeB(1.4) Hall bar in the three field sweep planes.

Figure 4.6 (a)-(c) illustrate the three possible planes of $\boldsymbol{H}$ rotation about a Hall bar. Panel (a) shows in the YZ plane, the relative angle $\theta$ = 0° between $\boldsymbol{M}$ and $\boldsymbol{j}_{c,x}$ is fixed, eliminating the AMR component leaving only a SHMR. Similarly, in panel (b), rotation in the XZ plane fixes the relative angle $\phi$ = 0° between $\boldsymbol{\sigma}_{s,Y}$ and $\boldsymbol{M}$, such there is a constant reflected spin current at the HM|FM interface, eliminating SHMR angular dependence and leaving only an AMR signal. The final plane of rotation XY in panel (c), holds neither the relative angles $\theta$ nor $\phi$ constant, such that both SHMR and AMR are present. So, by rotating $\boldsymbol{M}$ in the three planes, the magnetoresistive effects may be completely decoupled. Figure 4.6 (d) shows purely anomalous and spin Hall magnetoresistance by rotation H in the XZ and YZ planes, respectively, around a Ta(1)|Pt(1.6)|CoFeB(1.4) Hall bar. It is apparent that the individual magnetoresistance signals add to the total, coupled signal from the XY field sweep. Hereby, we proceed in this chapter to measure SHMR by rotating $\boldsymbol{H}$ and so $\boldsymbol{M}$ in the YZ plane. Remember, $\frac{\Delta R_{XX}^{SHMR}}{R_{XX}^{0}}$ is defined as the difference in resistance when $\boldsymbol{M} \perp \boldsymbol{\sigma}_{s,Y}$ ($\phi$ = 0°, 180°, 360°) and when $\boldsymbol{M} \parallel \boldsymbol{\sigma}_{s,Y}$ ($\phi$ = 90°, 270°).

Any slight misalignment in the relative angles of the sample and the applied field will give rise to systematic errors in the angular SHMR measurement. Sample loading misalignment errors introduce only a small sinusoidal-dependent AMR contribution set by the deviation about the misalignment angle $\theta$. This error $\epsilon \sim 1$ %. Additionally, changes in device resistance due to thermal drift during the measurement may add a small error $\epsilon \sim 0.8$ % after the linear background subtraction. The total systematic error is the summation of these two sources, which remains small, proving the precision of a SHMR measurement.

### 4.4.2 Spin Hall magnetoresistance in HM|FM bilayers

We conduct a series of HM thickness-dependent spin Hall magnetoresistance measurements on HM|FM bilayers similar to recent work [3,92,140,141] to estimate spin-dependent HM properties such as $\theta_{SH}$ and $\lambda$. Each device is measured with an angular YZ plane $\boldsymbol{H}$ rotation to extract a purely spin Hall-like resistance. To extract spin-dependent parameters from constituent materials in this work, we examine different metallic HM|FM bilayers (HM: Ta, W, Pt, Ru; FM: CoFeB, Co) in figure 4.7. Each series of devices is fit to the HM|FM bilayer model equation 4.3 developed in [3] to extract $\theta_{SH}$ and $\lambda$ at constant $g_r$ = 0.78 x $10^{15}$ $\Omega^{-1}m^{-2}$ (1 x $10^{19}$ $m^{-2}$). Constant fitting parameters for the FM layer are estimated from literature are $P_{Co}$=0.4 [212], $\lambda_{Co} \sim \lambda_{CoFeB} \sim 1$ nm [213,214], $P_{CoFeB}$= 0.6 [100] and measured $\rho_{Co}$=17 μΩ cm, $\rho_{CoFeB}$= 130 μΩ cm. Given the low $\boldsymbol{M}_s$ values, bulk $P$ and $\lambda_{FM}$ parameters may not be accurate but are applied as an order of magnitude approximation to compare between buffered HM|FM bilayers across which $\boldsymbol{M}_s$ remains nearly constant. Here, all thin film heterostructures are capped with 1 nm Ru for protection as outlined in section 3.4.3.

Firstly, in figure 4.7 (a), it is clear that unlike figure 4.6 (d) there is no appreciable $\cos 2\phi$ magnetoresistance for a Ru(3)|CoFeB(1.45) bilayer. This suggests that Ru deposited in this work has a negligible $\theta_{SH}$. The other panels show HM thickness-dependent spin SHMR

signals. In figure 4.7 (b), thin Ta($t$)|CoFeB(1.45) bilayers are fit well with Kim's bilayer model, but in thicker samples the observed SHMR signal is much lower than predicted and so are excluded from the fit (depicted by light grey points). This is consistent with a previously observed phase change in Ta from amorphous deposition to $\beta$-Ta around 6 nm in our laboratory. Panel (c) shows the W($t$)|CoFeB(1.4) bilayers fit well at ultra-low thickness similar to the Ta series, however at $t_W \sim 20$ nm, the experimental SHMR is lower than expected. This observation will be explored further as the chapter progresses. Figure 4.7 (d) and (e) show Pt|Co(FeB) series observe good agreement with Kim's metallic bilayer theory.

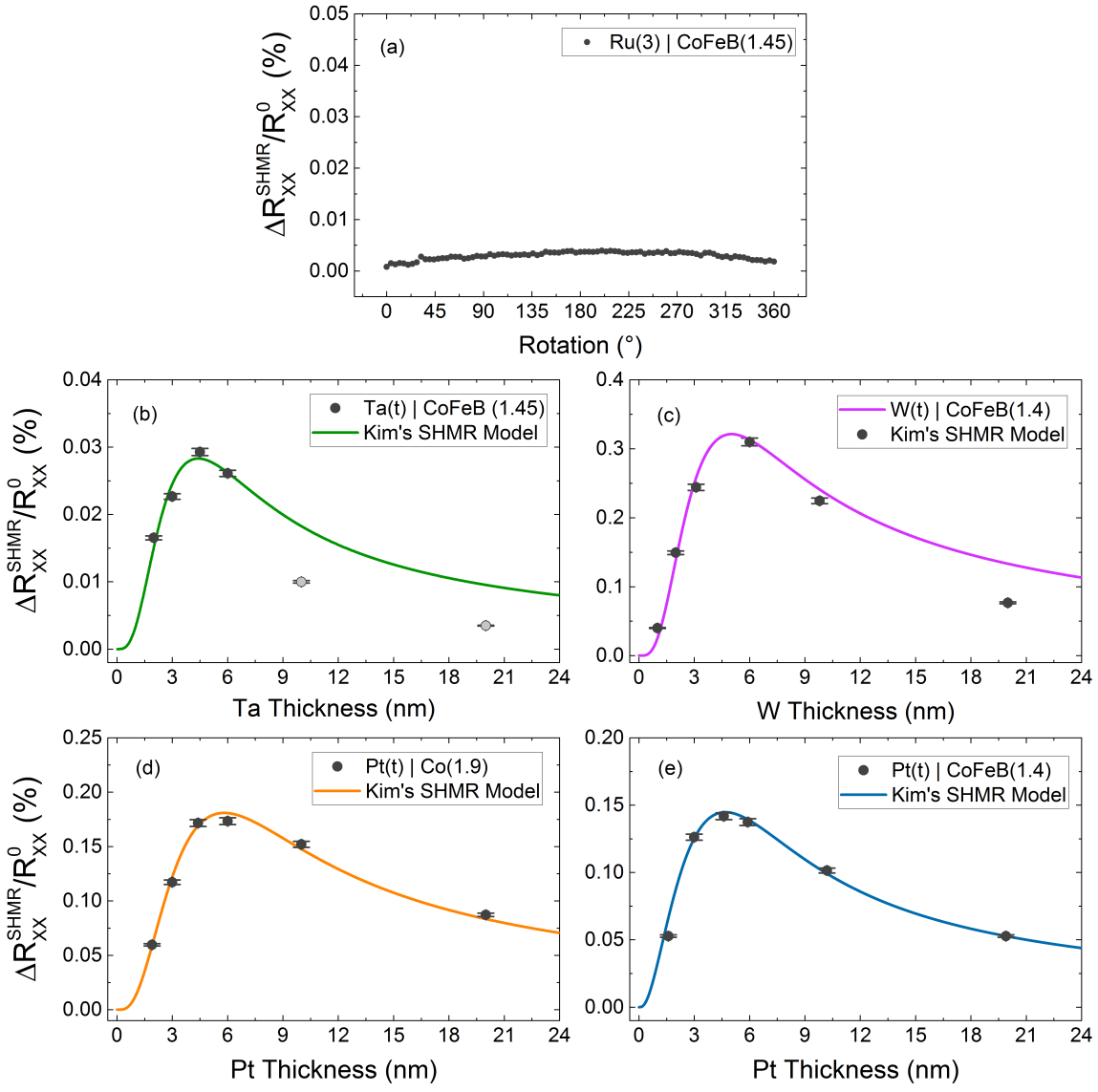


Figure 4.7 Spin Hall magnetoresistance measurements on HM|FM bilayers. (a) SHMR $R_{XX}$ measurement as a function of $\phi$ from an YZ field rotation on a Ru(3)|CoFeB(1.45) device. HM thickness-dependent SHMR values compiled from angular $\phi$ rotation $R_{XX}$ measurements for unbuffered (b) Ta|CoFeB, (c) W|CoFeB, (d) Pt|Co and (e) Pt|CoFeB bilayers. Each series is fit with Kim's bilayer model [3] to find $\theta_{SH,HM}$ and $\lambda_{HM}$ with constant parameters $P_{Co}$=0.4, $P_{CoFeB}$= 0.6, $\rho_{Co}$=17 μΩ cm, $\rho_{CoFeB}$= 130 μΩ cm, $\lambda_{Co}$ = 1 nm and $\lambda_{CoFeB}$ = 1 nm at $g_r$ = 0.78 x $10^{15}$ $\Omega^{-1}m^{-2}$.

Table 4.1 A summation of measured $\rho_{HM}$ and the estimated spin-dependent parameters evaluated from fitting unbuffered HM|FM bilayers with Kim's model in figure 4.7.

| Material | $\rho$ (μΩ cm) | λ (nm) | $\lvert\theta_{SH}\rvert$ |
|---|---|---|---|
| Ru | 89.8 | - | 0 |
| Ta | 290.1 | 1.393 | 0.0675 |
| W | 223 | 1.7 | 0.265 |
| Pt (\|Co) | 18.1 | 2.1 | 0.18 |
| Pt (\|CoFeB) | 18.1 | 2.0 | 0.154 |

The electronic and spin-dependent parameters used in and extracted from the SHMR fitting in figure 4.7 are summarised in table 4.1. The estimated values are in reasonable agreement with the literature [61]. Note, since the SHMR depends on $\theta_{SH}{}^2$, it is not possible to determine the sign, however, it is known that Ta and W have a negative $\theta_{SH}$, opposite to that of Pt. Furthermore, we extract different spin-dependent Pt parameters depending on the FM material. This is likely due to an inaccurate characterisation of FM thickness[4], which has been recently shown to strongly affect the SHMR signal [97], an inaccurate estimation of $\lambda_{FM}$ or $P_{FM}$, a more exotic interface effect like SML, or a combination thereof. A more precise estimation of bulk Pt spin-dependent parameters is demonstrated later in this chapter.

At this juncture, we evaluate the optimal HM|FM bilayer to study the effect of changing HM microstructure morphology on spin transport in the ultrathin limit. CoFeB is chosen as the primary FM material in this work for three reasons. Due to the amorphous nature of deposited CoFeB as opposed to crystalline Co, $\rho_{CoFeB} > \rho_{Co}$ by more than one order of magnitude. Therefore, CoFeB shunts less current than Co, increasing current driven in the SHE active HM layer. Moreover, the amorphous deposition of CoFeB promotes magnetic consistency across varying underlayer conditions. Finally, CoFeB has a significantly lower $K_{\perp}$, allowing $M$ to follow $H$ more readily at lower fields in angular SHMR measurements.

Similarly, Pt is chosen as the HM of particular interest for a number of reasons. Firstly, it is an important, well-studied material in spintronics [11,17,172–179,18,26,68,88,93,110,120]. Moreover, it has an order of magnitude lower resistivity than other HMs with high SOC, which drives current through the active SHE layer and increases spin-dependent signal sizes in measurement schemes like that of SHMR. Most significantly, Pt microstructure is highly tunable as outlined in chapter 3. In contrast, Ta is not well suited for this study due to the phase change readily observable in figure 4.7 (b) with the sudden drop in measured SHMR at $t \sim 10$ nm. Similarly, although W shows a large $\theta_{SH}$, a phase change is observed in figure 3.6 (d) for stacks at $t > 6$ nm (apparent by a significant decrease in $\rho_W$) in well-seeded, Ta-buffered conditions only. Thereby, only Pt allows for the maximum control of HM microstructure throughout buffered conditions and is electronically superior to the other HMs for this study.

[4] The true FM thickness should only deviate by 10 % from the expected value at a maximum yet would still contribute a non-negligible component to the change in SHMR measured in Pt|Co and Pt|CoFeB bilayers.

In addition, a long-standing controversy in literature continues over the magnitude of spin-dependent parameters in Pt [17,95,134,139,160,161,211,221–223] evaluated with different spin transport schemes. Considering Pt is one of the most well-studied HMs, this is a particularly pertinent indication that much understanding of spin transport in HM|FM bilayers at the nanoscale is left to be desired. In this chapter, we attempt to shed light on this origin of these discrepancies noted across literature.

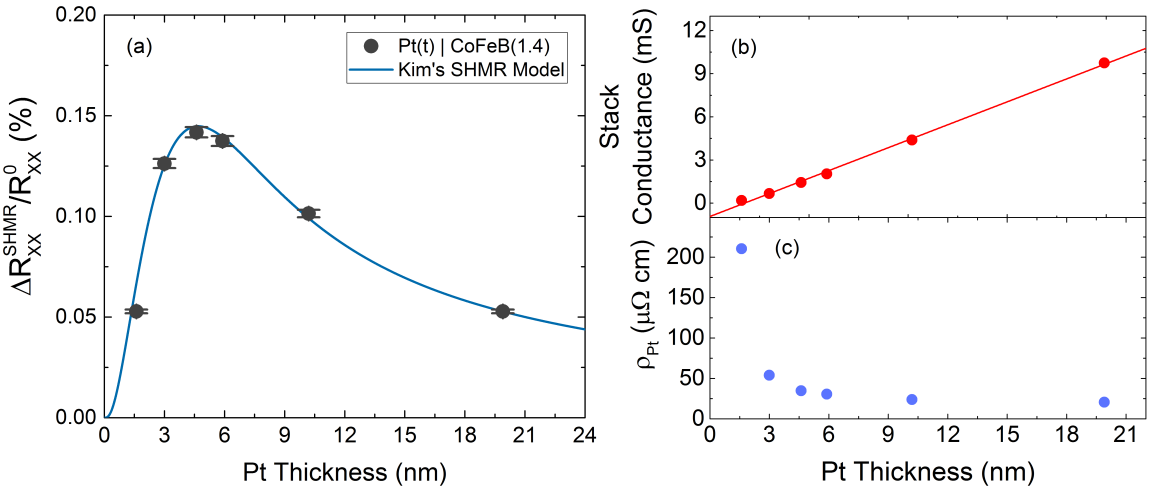


**Figure 4.8 (a) HM thickness dependent SHMR redisplayed from figure 4.7 (e). (b) The stack conductance for each HM|FM bilayer in (a) and (c) $\rho_{Pt}$ evaluated from Matthiessen's rule for an in-plane current flowing in parallel in section 3.3.1.**

Now that an optimal HM|FM bilayer has been selected, we probe the relationship between the electronic and spin-dependent behaviour of Pt|CoFeB bilayers. In figure 4.8, we note a significant pitfall when estimating spin-dependent parameters from Kim's fit in panel (a) to the experimental SHMR data of a Pt|CoFeB system. Namely, extracting consistent Pt resistivity from linearly fitting the stack conductance as outlined in section 3.3.1, is challenging in the ultrathin limit. Although the linear fit in panel (b) has an $R^2 > 0.998$, $\rho_{Pt}$ was found to increase drastically in this limit due to grain boundary and diffuse surface scattering in section 3.3.2 as well as film percolation. This is reproduced in figure 4.8 (c). Therefore, the total resistance change across the Pt thickness range is not only due to SHMR, but also the changing electronic properties, which we observed to be directly dependent on microstructure morphology in section 3.2.2. It is deceptive then, that Kim's bilayer model at fixed $\rho_{Pt}$ fits the Pt|CoFeB experimental data well. Indeed, caution should be taken when fitting any bilayers where the resistivity of constituent layer diverges in the ultrathin limit. In the following section, we propose a method more accurately fitting the SHMR data, accounting for varying $\rho_{Pt}$ across the thickness range.

### 4.4.3 Spin Hall magnetoresistance in buffered HM|FM bilayers

In order to discern the effect of HM microstructure on spin transport, we fabricate and measure three series of Pt($t$)|CoFeB(1.4) bilayers. In section 3.2.2, we found that by leaving Pt unbuffered or by buffering with 1 nm of Ru or Ta, the growth mode and electronic properties of ultrathin Pt films could be tuned controllably. Here, these same seed conditions are used to test the effect of Pt microstructure on the spin Hall magnetoresistance. The series of un-, Ru- and Ta-buffered Pt($t$)|CoFeB(1.4) probed with angular $\phi$ measurements at 1.7 T are displayed in figure 4.9.

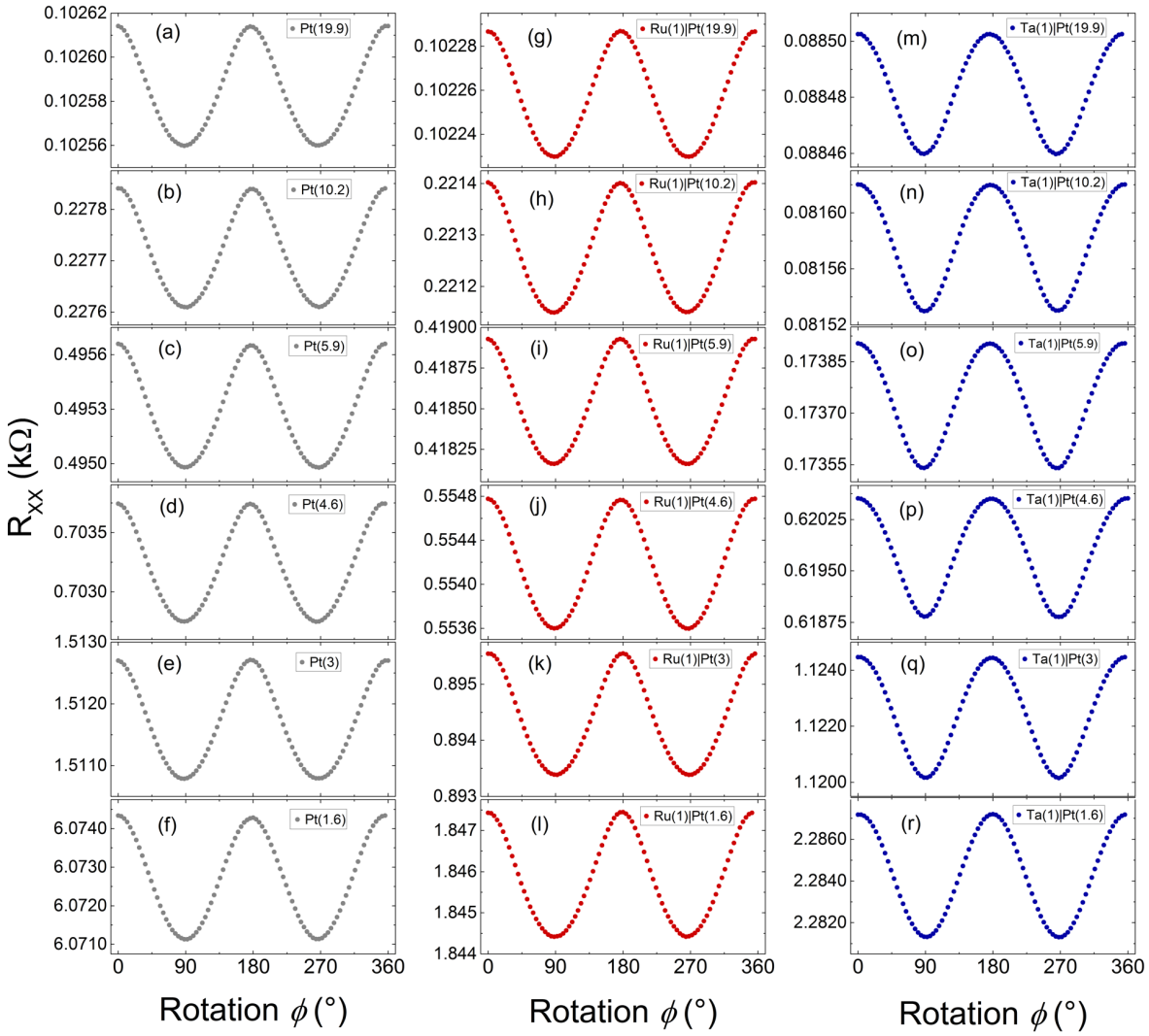


**Figure 4.9 Angular $R_{XX}$ SHMR measurements on a series of (a-f) unbuffered, (g-l) Ru-buffered and (m-r) Ta-buffered Pt(t)|CoFeB(1.4) Hall bars in $\phi$ about the ZY plane.**

Figure 4.9 (a)-(f), (g)-(l) and (m)-(r) show purely SHMR for un-, Ru- and Ta-buffered Pt(t)|CoFeB(1.4) devices as a function of $\phi$ rotation, respectively. We observe slight differences in SHMR $\cos 2\phi$ dependence for each series depending on $K_{\text{eff}}$. In section 3.2.2, Ru seeding was found to completely suppress Pt(111) texture, while Ta seeding was found to enhance it. The direct effect of Pt(111) texturing on $K_{\perp}$ is noticeable in the angular measurements in figure 4.9. The Ru-buffered bilayers, with low PMA, show a more rounded

magnetoresistance at $\phi$ = 90° and 270°, where $\boldsymbol{M}$ is in-plane than at $\phi$ = 180°, where $\boldsymbol{M}$ is pulled out-of-plane. In contrast, when PMA is enhanced in the Ta-buffered series, a more rounded magnetoresistance is observed at $\phi$ = 180°, where $\boldsymbol{M}$ is out-of-plane than at $\phi$ = 90° and 270°, where $\boldsymbol{M}$ is in-plane. Regardless of the slight difference of the SHMR angular dependence depending on $K_{\perp}$, the CoFeB is fully saturated by $\mu_0 H$ = 1.7 T in these measurements and so it is possible to extract an accurate $\frac{\Delta R_{XX}^{SHMR}}{R_{XX}^{0}}$ value. These values are tabulated and displayed in figure 4.10 (a) as a function of Pt thickness.

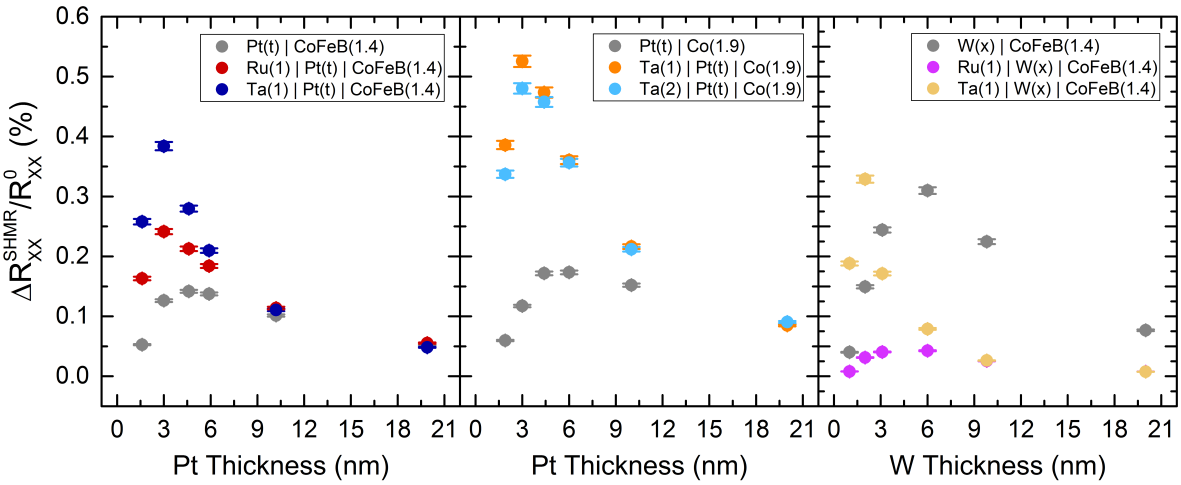


Figure 4.10 HM thickness dependent SHMR for a series of un-, Ru-, and Ta- buffered (a) Pt($t$)|CoFeB(1.4), (b) Pt($t$)|Co (1.9), and (c) W($t$)|CoFeB(1.4) Hall bars.

Figure 4.10 is a summation of SHMR data observed for different buffered HM|FM bilayers. HM thickness-dependent SHMR follows a similar trend for each HM|FM series: a maximum magnitude at an ultra-low HM thickness and a fall-off in thicker samples. This is a direct result of the exponential decay of $\mu_s$ away from the interface, given by equation 1.19. At $t < 2\lambda_{HM}$, $\mu_s$ persists across the entire HM film, whereas above $2\lambda_{HM}$ nearly all of the spin imbalance have been relaxed within the film. It is this $\mu_s$ which drives $\boldsymbol{j}_s$ in the HM adds to the conductivity of the film through the ISHE. Therefore, when $t > 2\lambda_{HM}$ there is no additional $\boldsymbol{j}_{c,HM}^{ISHE}$, but instead, the measured resistance decreases due to applied current shunting. All HM thickness-dependent electrical spin transport measurements relying on the ISHE in this (and the following) chapter will take this form.

Moreover, in figure 4.10 we demonstrate that seeding HM growth drastically alters SHMR signal size across a range of HM and FM constituent materials and is not limited to Pt|CoFeB bilayers. In panels (a) and (b), we observe significantly enhanced SHMR in buffered ultrathin Pt|FM bilayers with both CoFeB and Co as the FM layer. In panel (c), it is apparent buffering ultrathin W also strongly impacts SHMR. However, since control of W microstructure proved challenging in section 3.3.1 – due to an undesirable changing of W phase in the Ta-buffered series – it would be difficult to make claims about the influence of W morphology on spin transport.

In contrast, Pt microstructure morphology shows good tunability in the ultrathin limit, which allows for correlation with the varied SHMR observed in figure 4.9 (a) and (b). In both cases, Ta-buffered stacks are approximately three times as large as unbuffered stacks at the peak ($t \sim 3$ nm) and fall off precipitously at larger $t$. Additionally, the Ru-buffered Pt|CoFeB series are observed to be approximately twice as large as the unbuffered series at $t \sim 3$ nm. At thickness above $t \sim 10$ nm, however, SHMR is seen to drop off, and all the Pt|CoFeB series converge to a similar value resulting. The Pt|Co series also do so for slightly larger $t$. This results in a peaked HM thickness-dependent SHMR in buffered Pt|FM bilayers in contrast to the smoother HM-dependence observed in the unbuffered series of figure 4.10 (a) and (b).

For two reasons, we believe the observed change in SHMR is due to the quality of the Pt film. Firstly, by consulting the modelled spin current figure 4.4 (b), it is clear that the buffer does not contribute appreciably to the ISHE. There is a negligible difference in $\boldsymbol{j}_s$ when $\boldsymbol{M} \parallel \boldsymbol{\sigma}_s$ versus when $\boldsymbol{M} \perp \boldsymbol{\sigma}_s$, which suggests there is no significant contribution of spin accumulation in the buffer adding to the SHMR signal. This is further evidenced by a negligible change in the predicted signal size with large variations in the electronic and spin-dependent parameters of the buffer layer. Secondly and more importantly, there is a distinct correlation of the SHMR signal size to the quality of the Pt microstructure observed with HAADF-STEM in figure 3.4.

### 4.4.4 Estimating spin-dependent parameters from buffered HM|FM bilayers

We model the experimental SHMR data this section with measured spin-dependent parameters of the HM buffers, $\theta_{Ru} \sim 0$, $\lambda_{Ru} \sim 2$ nm, $\theta_{Ta} \sim -0.0675$, $\lambda_{Ta} \sim 1.39$ nm from section 4.4.2 and estimated parameters from literature $P_{CoFeB} \sim 0.6$ [100], $\lambda_{CoFeB} \sim 1$ nm [213,214]. The enhanced SHMR in ultrathin Pt observed for the buffered Pt|CoFeB bilayers is fit with the extended magnetoelectronic circuit theory model developed previously and displayed in figure 4.11.

Despite the larger SHMR in ultrathin Ru-buffered Pt|CoFeB than in the unbuffered series, the model still fits the data experimental data well with $\theta_{SH} = 0.126$ and $\lambda = 1.2$ nm in figure 4.11. The developed model here is evaluated at constant $g_r = 5 \times 10^{15}\ \Omega^{-1}m^{-2}$ and $\rho_{Pt}$ across the Pt thickness. However, in section 3.3.2, $\rho_{Pt}$ was found to be larger in the ultrathin limit due to the diffuse surface and grain boundary scattering for both Ru- and Ta-buffered Pt films, which makes this fit unphysical. Furthermore, Ta-buffered Pt films fit only poorly with $\theta_{SH} = 0.145$ and $\lambda = 1.2$ nm, where the enhanced SHMR at low thickness and fast fall-off over $t$ yields a peaked SHMR HM thickness dependence. Note, the same dependence was observed in figure 4.10 (b) in Ta-buffered Pt|Co bilayers. In an attempt to accurately model this behaviour, we take into account the variation of $\rho_{Pt}$ and the effect of a potential spin resistance at the BUF|HM interface, which may be seen in figure 4.12.

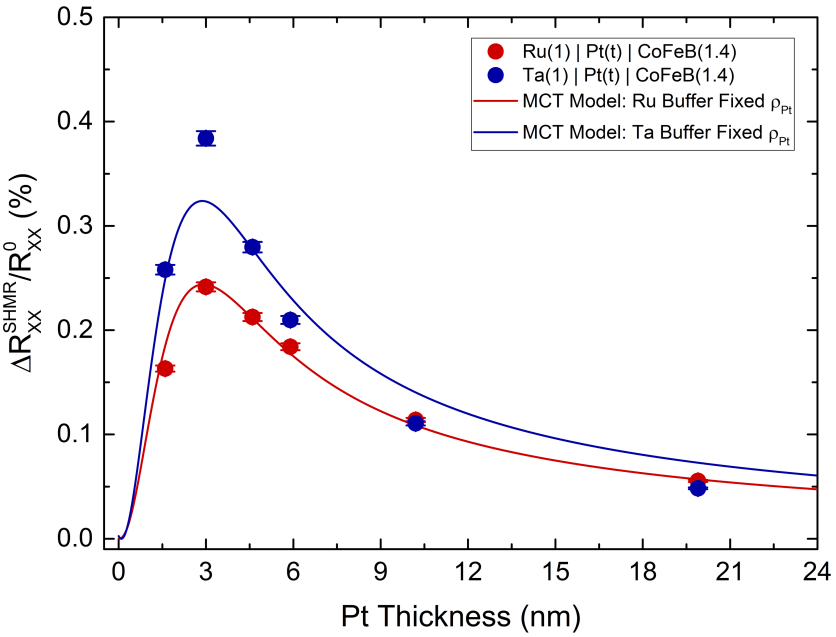


Figure 4.11 Experimental SHMR data of buffered Pt|CoFeB fit with the developed model at constant $g_r$ = 5 x $10^{15}$ $\Omega^{-1}m^{-2}$ and $\rho_{Pt}$ across the Pt thickness. Ru-buffered, bulk Pt parameters: $\rho_{Pt}$ = 18.9 μΩ cm, $\theta_{SH}$ = 0.126 and $\lambda$ = 1.2 nm. Ta-buffered, bulk Pt parameters: $\rho_{Pt}$ = 15.5 μΩ cm, $\theta_{SH}$ = 0.145 and $\lambda$ = 1.2 nm.

Figure 4.12 (a) shows the attempted fits of the developed model to Ta-buffered films for $\theta_{SH}$ = 0.145 and $\lambda$ = 1.2 nm. The continuous $\rho_{Pt}(t)$ function used in the varying $\rho_{Pt}$ model, represented by the blue dashed line in panel (a), arises from discrete, measured $R^0_{XX}$ values across the Hall bars in section 3.3.1. It is clear that the enhancement of $\rho_{Pt}$ cannot explain the thickness-dependent SHMR observed in the ultrathin limit. Another possible explanation for the enhanced SHMR at low thickness is a large spin resistance at the Ta|Pt interface. This can be visualised in figure 4.12 (b). A BUF|HM interface resistance can act to limit the relaxation of spin imbalance in the buffer layer, which promotes a larger $\mu_s$ in the HM layer and so drive larger SHMR. However, when accounting for the finite spin resistance shown in figure 4.12 (b), there was only a negligible effect on the predicted SHMR shown in panel (a). Further increasing the interfacial spin resistance only slightly reduces the expected signal size in the thin limit. Thereby, we conclude that no set of spin-dependent parameters or interface resistance arguments can adequately explain the observed SHMR data.

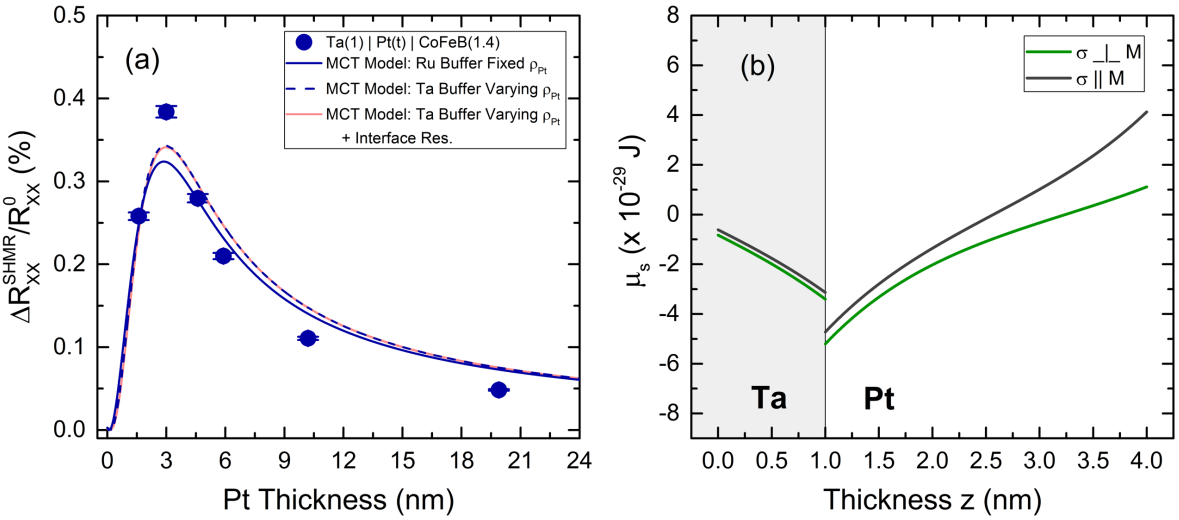


Figure 4.12 (a) Experimental SHMR data of Ta-buffered Pt|CoFeB fit with the developed model at constant $g_r$ = 5 x $10^{15}$ $\Omega^{-1}m^{-2}$ across the Pt thickness. The model at constant $\rho_{Pt,Bulk}$ = 15.5 μΩ cm, varying $\rho_{Pt}$ (with a continuous function obtained for measured values in section 3.3.1) and with an added Ta|Pt interfacial spin resistance attempting to fit the experimental SHMR data. The bulk Pt spin-dependent parameters are $\theta_{SH}$ = 0.145 and $\lambda$ = 1.2 nm. (b) Modelled Ta(1)|Pt(3)|CoFeB(1.4) spin accumulation with Ta|Pt interfacial spin resistance.

We finally attempt to model the buffered Pt|CoFeB by considering the growing evidence that Pt is dominated by intrinsic spin scattering [67,68,74,87,143,211] and Elliot-Yafet spin relxation [84–87]. Experimental SHMR data has not yet been modelled under these assumptions. Phenomenologically, this equates to a constant $\sigma_{xy}^{SH}\left(\frac{\theta_{SH}}{\rho_{Pt}}\right)$ and $\lambda\,\rho_{Pt}$ across the HM layer from intrinsic spin scattering and the Elliot-Yafet mechanism, respectively. To account for this, the model deploys $\lambda(t) = \lambda_{bulk}\frac{\rho_{Pt,bulk}}{\rho_{Pt}(t)}$ and $\theta_{SH}(t) = \theta_{SH,bulk}\frac{\rho_{Pt}(t)}{\rho_{Pt,bulk}}$ from $\rho_{Pt}(t)$ at each thickness to extract one set of bulk $\lambda$ and $\theta_{SH}$ values. Each (un)buffered Pt|CoFeB thickness-dependent SHMR series is fit under these assumptions in figure 4.13.

Figure 4.13 (a) shows that the buffered Pt|CoFeB SHMR series may be reasonably well modelled down to $t \sim 3$ nm when Pt is dominated by intrinsic spin scattering and Elliot-Yafet spin relaxation. This is in agreement with the recent observation that the Elliot-Yafet mechanism dominates in Pt|YIG devices when measuring a temperature-dependent SHMR [224]. Moreover, single set of bulk spin-dependent parameters $\lambda$ = 2 nm and $\theta_{SH}$ = 0.086 is found to model both buffered bilayers despite significantly different SHMR in the ultrathin limit. Although Pt morphology was found to differ from HAADF-STEM microscopy for the buffered Pt samples in figure 3.4, we surprisingly find consistent bulk spin-dependent parameters. Therefore, it can be seen that without adequately accounting for the change in $\lambda$ and $\theta_{SH}$ across $t$, accurately evaluating bulk spin-dependent parameters with SHMR can be challenging in the ultrathin limit due to a change in HM microstructure.

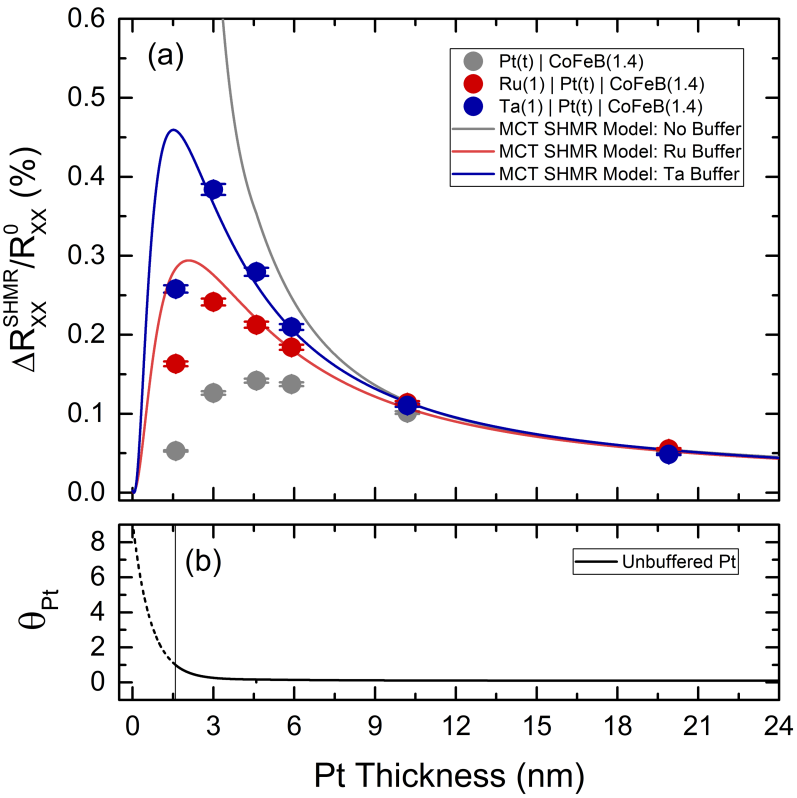


Figure 4.13 Experimental SHMR data of (un)buffered Pt|CoFeB fit with the developed model at constant $g_r$ = 5 x $10^{15}$ $\Omega^{-1}m^{-2}$ accounting for changing $\rho_{Pt}$ and so $\theta_{SH}$ and $\lambda$ across the Pt thickness assuming intrinsic spin scattering and Elliot-Yafet spin relaxation dominate. The bulk Pt spin-dependent parameters estimated are $\theta_{SH}$ = 0.086 and $\lambda$ = 2 nm. (b) $\theta_{SH}$ deployed in the model as a function of Pt thickness for unbuffered Pt diverging in the ultrathin limit.

In contrast, the SHMR in the unbuffered Pt|CoFeB bilayer series is not expected to be well modelled assuming intrinsic spin scattering and Elliot-Yafet spin relaxation in ultrathin films. In this limit, Volmer-Weber 3D growth dominates and films form clustered islands. Discontinuous current paths cause a large divergence of $\rho_{Pt}$ in ultrathin films as seen in figure 4.8 (c), which sets an arbitrarily short $\lambda$ and a massive $\theta_{SH}$ in this model. The divergence of $\theta_{SH}$ observed in figure 4.13 (b) can be attributed to heightened $\rho_{Pt}$ in the ultrathin limit. For example, at $t$ < 1.59 nm it can be seen that $\theta_{SH} > 1$, which is unphysical, and the unbuffered Pt|CoFeB SHMR model is not displayed. However, at $t$ > 10 nm, we observed the continuous deposition of Pt on the $SiO_2$ surface to effectively self-buffer in figure 3.4, resulting in 2D growth and a more continuous Pt film. At these thicknesses, the Pt film microstructure is convergent and the measured SHMR is well predicted in all series, including that of the unbuffered Pt|CoFeB series.

To determine the cause of the suppression of the experimental SHMR measurements at low thickness compared to the model for buffered Pt|CoFeB bilayers, we explore a number of possibilities. Because SHMR relies on spin-dependent scattering in the buffer and the HM, spin transport across interfaces and SOT acting on the FM layer, both constituent material parameters and interface conditions may provide potential insight.

At ultra-low Pt thicknesses, a significant $\mu_{s,\mathrm{buf}}$ is established in the buffer layer and more current flows through the buffer, such that it plays a more significant role in determining SHMR. Poor characterisation of spin-dependent parameters for Ru or Ta could result in a lower, modelled contribution to spin scattering than experimentally observed. However, the model is fit using a negligible Ru $\theta_{\mathrm{SH}}$ = 0, observed in figure 4.7 (a), and so cannot be less effective at contributing to SHMR. Therefore, since both buffered Pt|CoFeB models overestimate the expected SHMR, this explanation seems unlikely. In the HM, enhanced $\rho$ in ultrathin samples ($t \sim 2$ nm) may be due to film percolation and not contribute equally to transverse spin scattering. Although HAADF-STEM microscopy of Ru(1)|Pt(1.6) in figure 3.4 showed a semi-granular film, Ta(1)|Pt(1.6) appears to be well wet, which disproves this possibility. A more likely explanation is that $\sigma_{xy}^{\mathrm{SH}}$ and so $\theta_{\mathrm{SH}}$ is found to slightly decrease as a function of $\sigma$ in moderately dirty HMs [61] instead of being perfectly constant. This would decrease the magnitude of the fitting function.

Changes in microstructure and spin-dependent parameters of the ferromagnetic CoFeB layer may also play a significant role in ultrathin ($t \sim 2$ nm) samples. However, in the previous chapter, the CoFeB was found to have consistent bulk $M_{\mathrm{s}}$ values across the (un)buffered, bilayer series. Moreover, the thin CoFeB is deposited amorphously and so the structural and electrical properties are expected to change minimally. Indeed, $\rho_{\mathrm{CoFeB}} \gg \rho_{\mathrm{Pt}}$ so changes in the conductivity of CoFeB have only a small impact on the total current distribution since it is mostly flowing in the Pt underlayer.

Spin transport across the HM|FM interface may also be the cause the reduced SHMR observed in ultrathin Pt. One explanation may lie within an exotic spin-dependent interfacial effect like the Rashba-Edelstein effect or spin memory loss. The Rashba-Edelstein effect creates spin polarisation at the interface with broken inversion symmetry. However, it should introduce an additional SOT contribution to the bulk-like SHE contribution, and increase the observed signal size. In contrast, interfacial spin-flip scattering through SML may play an important role, but must be thickness dependent to follow the observations from figure 4.13. Again HAADF-STEM microscopy of Ta(1)|Pt(1.6) in figure 3.4, showed continuous, smooth film surfaces down to 1.6 nm, which makes such a significant change in SML unlikely.

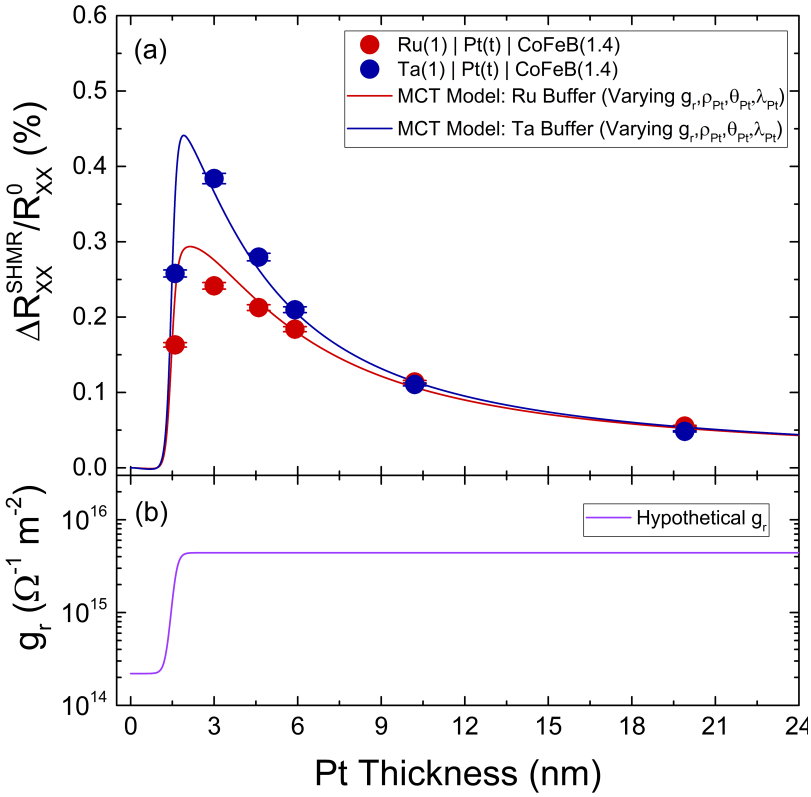


Figure 4.14 (a) Experimental SHMR data of buffered Pt|CoFeB fit with the developed model when with varying $\rho_{Pt}$ and so $\theta_{SH}$ and $\lambda$ across the Pt thickness assuming intrinsic spin scattering and Elliot-Yafet spin relaxation dominate. The bulk Pt spin-dependent parameters estimated are $\theta_{SH}$ = 0.086 and $\lambda$ = 2 nm. (b) $g_r$ deployed in the model is reduced from $g_r$ = 5 x $10^{15}$ $\Omega^{-1}m^{-2}$ in the ultrathin limit.

The final potential explanation explored here is the decrease in interfacial spin transparency at $t \sim 2$ nm due to subtle microstructure changes of the metal films. In figure 4.14, we use the model which predicts the observed SHMR down to these ultra-low thicknesses in figure 4.13, but now vary $g_r$ to determine if interfacial spin transparency can accurately account for the observed behaviour. Indeed, by reducing $g_r$ at $t \sim 2$ nm by an order of magnitude, as illustrated in figure 4.14 (b), the model now fits the observed SHMR in buffered Pt|CoFeB bilayers across the entire thickness range. This drop in $g_r$ is not unreasonable since it is often found to deviate in ultrathin films across orders of magnitude [95], which suggests that a reasonable change of $g_r$ at $t \sim 2$ nm can accurately account for discrepancy observed in the ultrathin limit.

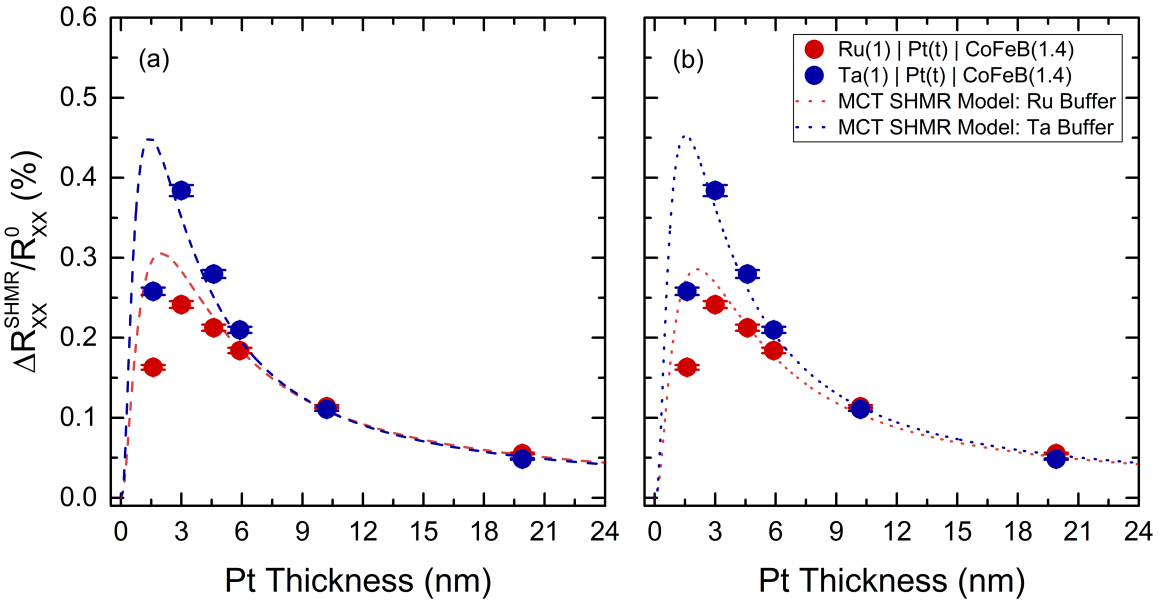


Figure 4.15 (a) Experimental SHMR data of buffered Pt|CoFeB fit with the developed model when with varying $\rho_{Pt}$ and so $\theta_{SH}$ and $\lambda$ across the Pt thickness assuming intrinsic spin scattering and Elliot-Yafet spin relaxation dominate. The bulk Pt spin diffusion length $\lambda$ = 2 nm from figure 4.13 fitting. Fitting gives an nonunique solution. (a) $g_r$ = 1 x $10^{15}$ $\Omega^{-1}m^{-2}$ and the bulk $\theta_{SH}$ = 0.13, while in (b) $g_r$ = 9 x $10^{15}$ $\Omega^{-1}m^{-2}$ and the bulk $\theta_{SH}$ = 0.08.

The magnitude of the magnetoelectronic circuit theory model depends directly on the spin mixing conductance in addition to $\theta_{SH}{}^2$ as observed in equation 4.3 and so both $g_r$ and $\theta_{SH}$ cannot be uniquely evaluated with thickness-dependent SHMR fitting. In figure 4.15 (a) and (b), the spin mixing conductance is set to 1 x $10^{15}$ $\Omega^{-1}m^{-2}$ and 9 x $10^{15}$ $\Omega^{-1}m^{-2}$, respectively. Although both series of buffered Pt|CoFeB fit the data well, drastically different $\theta_{SH}$ = 0.115 and 0.075 values are extracted from modelling in panels (a) and (b), respectively. Therefore, to accurately evaluate the magnitude of $\theta_{SH}$, another measurement scheme must be used with buffered bilayers grown under the same sputtering conditions. In the next chapter, spin pumping in similar (un)buffered Pt|CoFeB bilayers is evaluated as an alternative measurement technique to extract accurate values of $g_r$, $\theta_{SH}$ and $\lambda$.

## 4.5 Conclusions

In this chapter, we performed HM-thickness dependent, angular spin Hall magnetoresistance measurements to determine the bulk spin-dependent parameters of constituent HM materials. The SHMR in metallic HM|FM bilayers for a host of constituent material contributions (HM: Ta, W, Pt, Ru; FM: CoFeB, Co) were evaluated. For some HMs such as Ta, which are deposited amorphously and don't have strongly varying electronic properties, this is may sufficient for estimating $\theta_{SH}$ and $\lambda$. However, for crystalline HMs such as Pt in the ultrathin limit, we found good reason to be cautious when extracting film parameters. Although the standard magnetoelectronic circuit theory modelled unbuffered Pt|Co(FeB) well, it did so at fixed $\rho_{Pt}$, which was shown to be unphysical due to enhanced grain boundary and diffuse surface scattering in the ultrathin limit from section 3.2.2.

To further probe the effect of these variable electrical properties due to HM microstructure morphology in the ultrathin limit on spin transport, we fabricated and measured spin Hall magnetoresistance on a series of (un)buffered HM|FM bilayers. Across an array of (un)buffered Pt|Co(FeB) and W|CoFeB bilayers, SHMR was found change drastically when seeding HM growth with Ru or Ta in the ultrathin limit. The largest SHMR signal was observed at $t \sim 3$ nm in each series and was more enhanced for Ta-buffered stacks, followed by Ru-buffered than for unbuffered stacks. This trend directly follows the quality of Pt film deposition characterised by HAADF-STEM and XRR in chapter 3. This suggests that the spin-to-charge conversion of the ISHE is directly affected by HM microstructure.

To correlate changes in spin transport through spin-dependent properties with HM microstructure, current magnetoelectronic circuit theory was employed to created a BUF|HM|FM model and fit the experimental SHMR data. It was not possible to fit the Ta-buffered Pt|CoFeB devices well in both ultrathin and thicker ($t \sim 20$ nm) samples with a constant $\theta_{SH}$ and $\lambda$, even if $\rho_{Pt}$ was varied to model the electronic properties of the devices accurately. Moreover, a discontinuous drop in spin accumulation at the Ta|Pt interface could not account for the enhanced SHMR signals in the ultrathin limit. However, in light of growing evidence that Pt is dominated by Elliot-Yafet spin relaxation and intrinsic spin scattering, we demonstrated that the experimental data could be accurately modelled varying $\theta_{SH}$ and $\lambda$ in accordance with these mechanisms down to $t \sim 3$ nm. This confirms that spin-dependent scattering and relaxation is directly correlated to HM microstructure morphology. Furthermore, we evaluated a list of possible explanations why the model predicts a larger SHMR than observed by experiment at $t \sim 1.6$ nm to find a slight decrease in $\sigma_{xy}^{SH}$ or $g_r$ were two of most probable. Additionally, it proved challenging to accurately evaluate $g_r$ and $\theta_{SH}$ with SHMR measurements alone since both influence magnitude recorded. Instead, they were fit simultaneously with spin pumping results in the next chapter to extract bulk spin-dependent parameters $g_r$ = 5 x $10^{15}$ $\Omega^{-1}m^{-2}$, $\lambda$ = 2 nm and $\theta_{SH}$ = 0.086.

# 5 Spin current injection in the ultrathin limit: Spin pumping

## 5.1 Introduction

Spin pumping has been theorised [225] and extensively measured [17,216,222,223,226–228] in HM|FM systems. Unlike other spin transport measurement schemes, which drive an in-plane charge current to create a spin accumulation at the HM|FM interface, spin pumping excites resonance in thin FM films at conditions governed by the Kittel equation, instead. At a steady resonant state, macroscopic spin precession in the FM must dissipate additional magnetisation dynamics. The adjacent HM layer acts as a good spin sink – quickly quenching the dissipated magnetisation through transverse spin relaxation – and a DC $\boldsymbol{j}_s$ arises at the interface, thereby damping precession. Conveniently, the effective spin-dependent scattering in the HM also acts to generate a charge current at resonance from the ISHE, which can be recorded as a voltage across the bilayer.

In the last decade, spin pumping has become a commonly used method in spintronics to quantify $g_r$ at the HM|FM interface, as well as $\lambda$ and $\theta_{SH}$ in the HM layer. However, as it becomes better understood as a measurement scheme, estimating spin-dependent parameters appears more challenging than once thought. For example, capacitive coupling between the stripline on a coplanar waveguide and the FM give rise to additional magnetic effects such as AMR and the AHE [25,26,215,227,229,230], which have non-zero contributions to both the symmetric and antisymmetric components of the Lorentzian voltage lineshape. Figure 5.1, illustrates the angular dependence of these possible voltages. Moreover, ISHE lineshape measurements have also been shown to suffer from SML [86,110] through additional, elusive spin-flip scattering at the interface, which makes the correct extraction of $\theta_{SH}$ difficult.

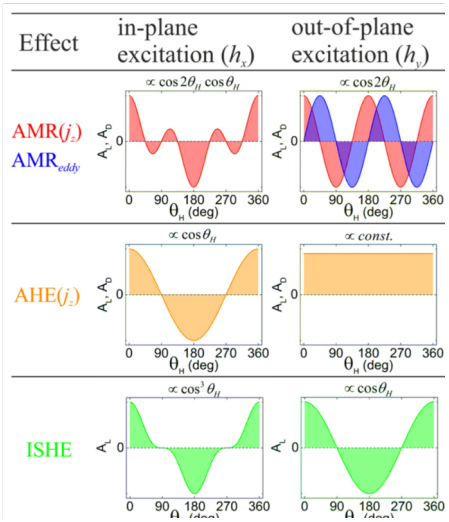


Figure 5.1 An illustration of the angular dependence of the parasitic SR signals (AHE, AMR) as well as the ISHE voltage in spin pumping experiments. Reproduced from [26].

Despite the need to overcome these experimental issues, a careful measurement of the ISHE voltage $V_{ISHE}$ with spin pumping allows an accurate estimation of spin-dependent parameters in the HM layer, especially when performed in conjunction with other measurement schemes, as is done in this work.

In this chapter, we perform HM thickness-dependent, spin pumping measurements across the series of (un)buffered HM|FM bilayers. Spurious SR components in the rectified diode voltage are tested and concluded insignificant in these $V_{ISHE}$ lineshape experiments. Moreover, the Kittel equation is demonstrated to fit experimental spin pumping data for power-dependent and frequency-dependent lineshape measurements, indicating the $V_{ISHE}$ is a direct result of FMR. In parallel, we develop a novel spin pumping trilayer model to fit the experimental data. Without accounting for variations in the $\lambda$ across the changing HM thickness due to the domination of Elliot-Yafet spin relaxation and intrinsic spin scattering in ultrathin Pt films, previous experimental values [91] are not well predicted by magnetoelectronic circuit theory models. The $V_{ISHE}$ signals are too large at $t \sim 2\lambda$ and fall-off at larger $t$ too quickly. In this vein, Roy [86] proposed that thickness-dependent Pt|FM spin pumping should be treated with the Elliot-Yafet mechanism to address these discrepancies between experiment and theory. Here, we use the extended spin pumping trilayer model with both Elliot-Yafet spin relaxation and intrinsic spin scattering dominating to accurately fit the buffered Pt|CoFeB bilayers. In addition, owing to the different dependencies of the spin pumping and SHMR magnitudes on $g_r$ and $\theta_{SH}$, we decouple the parameters by simultaneously fitting the two thickness-dependent sets of data.

## 5.2 Experimental setup

All spin pumping experiments in this chapter are performed on a specialised spin-dynamics rig constructed by Angela Wittmann who also helped with preliminary measurements. The system is designed to induce FMR in nanodevices to measure microwave absorption and small voltages generated from the ISHE. The setup is outlined in figure 5.2.

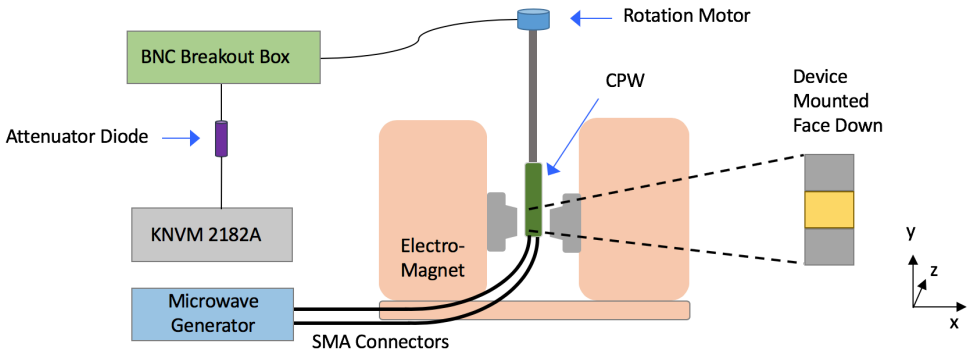


Figure 5.2 Schematic illustration of the setup designed and constructed by Angela Wittmann to induce FM resonance in the device mounted on the coplanar waveguide and measure the DC $V_{ISHE}$ on the Keithley Nanovoltmeter 2182A.

A common method for microwave excitation is utilising the well-defined field distribution of a coplanar waveguide (CPW). To create FMR, the sample is fixed to a CPW and subjected to one dynamic and one static magnetic field. Here, a gigahertz microwave generator drives an AC current through a stripline between two ground planes in a CPW to create an in-plane, RF Oersted field $H_{RF}$. The CPW was designed to fit inside the pole pieces of the GMW

electromagnet, which applies the static field $H_X$ used to excite FM magnetisation dynamics defined by the FMR conditions. In order to achieve the requisite $H_X$, the SubMiniature version A (SMA) connectors were edge-mounted at the bottom of the CPW to minimise the pole spacing. The customised design schematics are presented in Figure 5-3 (a)-(b) and the final FR-4 CPW is visualised as in Figure 5-3 (c).

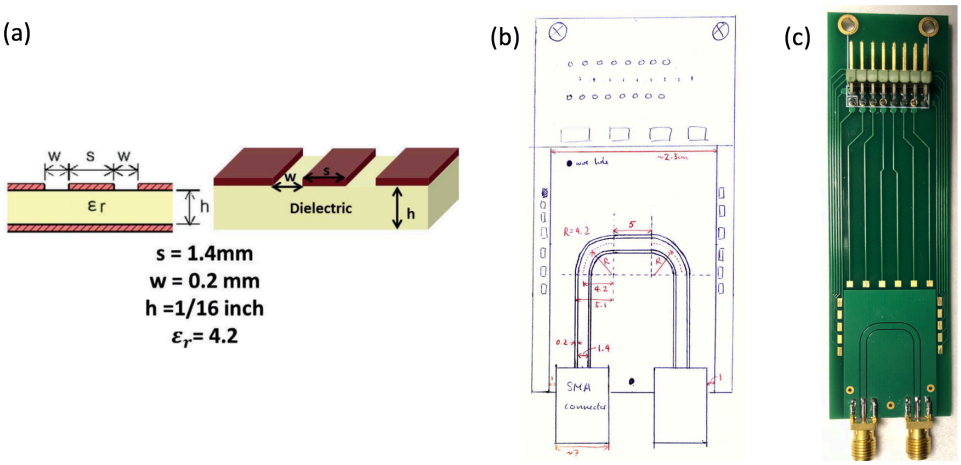


Figure 5.3 (a) Schematic of the CPW design (reproduced from [231]). (b) Wittmann's design of a PCB with the integrated angular stripline CPW with dimensions from (a). All dimensions are in mm unless otherwise annotated. (c) The CPW with 16 gold pads, which allow for easy electrical top contacting via wire bonds. The SMA connectors are edge-mounted at the bottom of the PCB board.

The electrical engineering behind the transmission of microwaves is nontrivial; both the cabling selection and CPW design were carefully considered to reduce loses. Special SMA cables are employed to transport signals both to and from the CPW. Any transmitted microwaves may be used to detect absorption from FMR in the sample. However, absorption in the HM|FM bilayers on-chip did not produce measurable signals in this work. To minimise reflection on the CPW itself, the characteristic impedance was designed to match the output impedance of the microwave source at ~ 50 Ω to obtain consistent transmission across the entire bandwidth of the CPW, from 2 to 18 GHz.

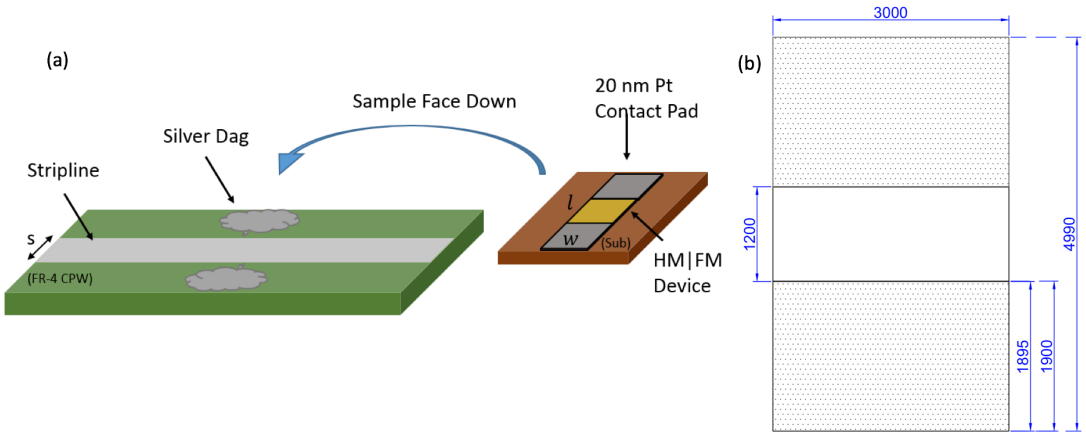


Figure 5.4 (a) A schematic of a bilayer sample mounted face-down on the CPW and electrically contacted with silver dag to the 20 nm Pt contact pads. (b) CAD illustration of the (un)buffered HM|FM Hall bar used in all spin pumping measurements with dimensions in µm. The hashed portion represents 20 nm Pt contacts and the unhashed portion is the (un)buffered Pt|CoFeB bilayer.

To quantify the steady DC $\boldsymbol{j}_s$ injected from spin pumping at FMR, we measure an attenuated DC voltage $V_{\text{ISHE}}$ established across the length of the device through a breakout box with a Keithley 2182A nanovoltmeter. Although it was initially intended to wire bond the device to the 16-contact CPW, we found the coupling between the stripline and the device fabricated on 500 µm Si chips was insufficient to induce FMR with devices mounted face-up. Therefore, the samples are mounted face-down on the CPW to maximise the $\boldsymbol{H}_{\text{RF}}$ experienced by the sample, and electrically contacted with silver dag paste as visualised in figure 5-4 (a). To further increase signal and reduce noise, the HM|FM bar design was also iterated multiple times to its final specifications, which are shown in figure 5-4 (b). To increase $V_{\text{ISHE}}$, a long bar is beneficial, but it must remain within a region of the uniform, well-defined, in-plane $\boldsymbol{H}_{\text{RF}}$ set by the stripline dimensions. A length $\boldsymbol{l}$ = 1.2 mm less than a stripline width $\boldsymbol{s}$ = 1.4 mm was found to be optimal. To reduce noise, wide width $\boldsymbol{w}$ = 3 mm bars were fabricated with thick 20 nm Pt contact pads. The bar was $Ar^+$ ion milled briefly (see section 2.1.1 for more details) before depositing the thick Pt contact pads between lithography steps to reduce electrical noise from contacting through the resistive, oxidised 1 nm Ru cap.

## 5.3 Modelling buffered HM|FM bilayers in spin pumping systems

The magnetoelectronic circuit theory model developed in this chapter owes much of its fundamental physics to that derived in the previous one for the SHMR in buffered bilayers. Since the heterostructure composition is identical to that in Chapter 4, previous models from literature, again, fail to accurately represent $\mu_s$ in these buffered (BUF|HM|FM) stacks. Therefore, an extended model was developed for these devices to quantify $\mu_s$, $\boldsymbol{j}_s$ of the buffer and HM layers when the FM is in resonance to predict $V_{\text{ISHE}}$ results and fit these models to experimental data.

The quasi-equilibrium, drift-diffusion equation 1.18 for purely diffusive spin systems apply here; there is no $\boldsymbol{j}_{\text{c}}$ (and therefore $\boldsymbol{j}_{\text{SHE},i}$) assuming negligible capacitive coupling between the HM and the stripline. The following equations define $\mu_s$, $\boldsymbol{j}_s$ in each layer:

$$\mu_{s,\text{buf}} = Ae^{-z/\lambda_{\text{buf}}} + Be^{z/\lambda_{\text{buf}}}, \tag{5.1}$$

$$\mu_{s,\text{HM}} = Ce^{-z/\lambda_{\text{HM}}} + De^{z/\lambda_{\text{HM}}}, \tag{5.2}$$

$$\boldsymbol{j}_{s,\text{buf}} = -\Psi_{\text{buf}}\left[Ae^{-z/\lambda_{\text{buf}}} - De^{z/\lambda_{\text{buf}}}\right], \tag{5.3}$$

$$\boldsymbol{j}_{s,\text{HM}} = -\Psi_{\text{HM}}\left[Ce^{-z/\lambda_{\text{HM}}} - De^{z/\lambda_{\text{HM}}}\right]. \tag{5.4}$$

Instead of the FM layer acting as the spin sink in the SHMR system, in spin pumping the FM now acts as a spin source, where the DC $\boldsymbol{j}_s$ is damped in the HM from induced precession at FMR. In this light, we apply the same boundary conditions depicted in figure 4.3 to solve for the four unknowns ($A$, $B$, $C$, $D$) of the spin system.

The spin current passing through the SUB|BUF interface is nil ($\boldsymbol{j}_{s,\text{buf}} = 0$) at z = 0:

$$\Psi_{\text{buf}}[B - A] = 0 \tag{5.5}$$

The spin current passing through the BUF|HM interface is equal ($\boldsymbol{j}_{s,\text{buf}} = \boldsymbol{j}_{s,\text{HM}}$) at z = d:

$$\Psi_{\text{buf}}\left[-Ae^{-d/\lambda_{\text{buf}}} + Be^{d/\lambda_{\text{buf}}}\right] = \Psi_{\text{HM}}\left[-Ce^{-d/\lambda_{\text{HM}}} + De^{d/\lambda_{\text{HM}}}\right] \tag{5.6}$$

The spin accumulation at the BUF|HM interface is equal ($\mu_{s,\text{buf}} = \mu_{s,\text{HM}}$) at z = d:

$$Ae^{-d/\lambda_{\text{buf}}} + Be^{d/\lambda_{\text{buf}}} = Ce^{-d/\lambda_{\text{HM}}} + De^{d/\lambda_{\text{HM}}} \tag{5.7}$$

The spin current passing through the HM|FM interface is equal ($\boldsymbol{j}_{\text{s,HM}} = \boldsymbol{j}_{\text{s,FM}}$) at z = p:

$$\Psi_{\text{HM}}\left[-Ce^{-p/\lambda_{\text{HM}}} + De^{p/\lambda_{\text{HM}}}\right] = \boldsymbol{j}_s^{\text{HM|FM}} \tag{5.8}$$

Where, according to Ando [17] the DC spin current at the interface injected into the HM is

$$\boldsymbol{j}_s^{\text{HM|FM}} = \frac{g_r e\gamma^2 {H_{\text{RF}}}^2 \hbar}{4\pi\alpha^2} \frac{[(4\pi \sin^2\theta_M M_s)\gamma + \sqrt{(4\pi M_s)^2\gamma^2 \sin^4\theta_M + 4\omega^2}]}{[(4\pi M_s)^2\gamma^2 \sin^4\theta_M + 4\omega^2]} . \tag{5.9}$$

$\gamma$ is the gyromagnetic ratio, $\alpha$ is the Gilbert damping constant, $\boldsymbol{M}_s$ is the saturation magnetisation and $\theta_M$ is the precession angle of that $\boldsymbol{M}$, $\omega$ is the angular microwave frequency ($2\pi \times f$), $\hbar$ is the reduced Planks constant and $\boldsymbol{H}_{\text{RF}}$ is the RF Oersted field experienced by the heterostructure induced by $\boldsymbol{j}_{c,\text{RF}}$ in the stripline of the CPW. With $\boldsymbol{M}$ strongly in-plane in these BUF|Pt($t$)|CoFeB(5) films, any perturbation from $\boldsymbol{H}_{\text{RF}} \ll \boldsymbol{H}_{\text{K}}^{\perp}$ such that $\theta_M \sim \theta_H = \frac{\pi}{2}$. We discuss the repercussions of the decision to fabricate thick $d_{\text{CoFeB}}$ = 5 nm devices in more detail later. The spin current from spin pumping at the HM|FM interface is then reduced to

$$\boldsymbol{j}_s^{\text{HM|FM}} = \frac{g_r e\gamma^2 {H_{\text{RF}}}^2 \hbar}{4\pi\alpha^2} \frac{[(4\pi M_s)\gamma + \sqrt{(4\pi M_s)^2\gamma^2 + 4\omega^2}]}{[(4\pi M_s)^2\gamma^2 + 4\omega^2]} . \tag{5.10}$$

Typically a precise value of the Gilbert damping constant $\alpha$ is extracted from linewidth broadening after the HM spin sink is deposited on the FM layer, however, in these experiments, no appreciable microwave absorption is measured. To reduce the number of free fitting parameters, we instead constrain the $\alpha \sim 1.04 \pm 0.08 \times 10^{-2}$ in agreement with recent literature, where Conca *et al.* [25] showed experimentally that the large $\alpha$ in Pt|CoFeB bilayers remains constant over $t$. $\boldsymbol{H}_{\text{RF}}$ is evaluated by solving the medium range field approximation for a current-carrying strip under the FM. This calculation is treated extensively in Appendix C.

Once $\mu_s$, $\boldsymbol{j}_s$ are known for both buffer and HM layers, the entire spin system is defined for the HM metal layers, and the expected $V_{\text{ISHE}}$ can be estimated. To calculate $V_{\text{ISHE}}$, the DC $\boldsymbol{j}_s(z)$ pumped across the HM|FM interface is integrated in both the buffer and the HM layer across their respective thicknesses to determine the overall charge current generated

$$\boldsymbol{j}_{c,i}^{\mathrm{ISHE}} = \theta_{\mathrm{SH},i} \int \boldsymbol{j}_{s,i}\, dz. \tag{5.11}$$

This assumes all the spin relaxation is by the ISHE into an observable $\boldsymbol{j}_{c,i}^{\mathrm{ISHE}}$ and there is no SML. However, if spin-flip scattering at the surface is present, these magnetoelectronic circuit theory models will underestimate $\theta_{\mathrm{SH}}$ for the HM layer. Since in all metallic systems the current travels in all conductive layers, shunting must also be accounted for. The current created in the system then is given by [222]

$$\boldsymbol{j}_{c,y} = \boldsymbol{j}_{c,\mathrm{buf}}^{\mathrm{ISHE}} + \boldsymbol{j}_{c,\mathrm{HM}}^{\mathrm{ISHE}} + \sum_i \boldsymbol{j}_{c,i}^{0}\ , \tag{5.12}$$

where $\boldsymbol{j}_{c,i}^{0} = \frac{V}{l\,\rho_i}$ for each conducting $i$ layer of the system when a constant voltage $V$ is established across the length $l$ of the bar. The total current in the system is just the integration of the $\boldsymbol{j}_{c,i}$ in each layer across their respective thicknesses

$$\boldsymbol{j}_{c,y}(t) = \int_0^d \left(j_{c,\mathrm{buf}}^{\mathrm{ISHE}} + \frac{V}{l\ \rho_{\mathrm{buf}}}\right) dz + \int_d^t \left(j_{c,\mathrm{HM}}^{\mathrm{ISHE}} + \frac{V}{l\ \rho_{\mathrm{HM}}}\right) dz + \frac{V\ d_{\mathrm{FM}}}{l\ \rho_{\mathrm{FM}}}\ . \tag{5.13}$$

In open circuit conditions when $\boldsymbol{j}_{c,y}$ = 0, the normalised, expected spin pumping voltage is

$$V_{\mathrm{SP}}(t) = l\ \frac{\int_0^d \boldsymbol{j}_{c,\mathrm{buf}}^{\mathrm{ISHE}}\, dz + \int_d^t \boldsymbol{j}_{c,\mathrm{HM}}^{\mathrm{ISHE}}\, dz}{\left(\frac{d_{\mathrm{buf}}}{\rho_{\mathrm{buf}}} + \frac{t}{\rho_{\mathrm{HM}}} + \frac{d_{\mathrm{FM}}}{\rho_{\mathrm{FM}}}\right)}\ . \tag{5.14}$$

## 5.4 The buffered Pt|CoFeB system

In this section, we highlight experimental findings of the $V_{\mathrm{ISHE}}$ lineshape spin pumping measurements performed on a series of (un)buffered Pt($t$)|CoFeB(5) bilayers. To correlate HM microstructure morphology to spin-dependent scattering in the Pt, we apply our extension of the existing spin pumping magnetoelectronic circuit theory to model the experimental data. To perform a direct comparison to the characterised buffer samples, and the thickness-dependent SHMR measurements in chapters 3-4, the same bilayer systems are fabricated at varying $t$. However, a thicker 5 nm FM layer than in the previous chapter is required to ensure consistent in-plane $\boldsymbol{M}$ across the series. To facilitate the comparison between measurements, we again depict Ta-, Ru- and (un) buffered Pt|CoFeB bilayer with their respective colour schemes as in Chapters 3-4.

### 5.4.1 The FMR spin pumping measurement with ISHE lineshape

In this section, spin pumping $V_{\mathrm{ISHE}}$ measurements are performed on the HM|FM bilayers by applying a microwave field $\boldsymbol{H}_{\mathrm{RF}}$ and sweeping the static field $\boldsymbol{H}_{\mathrm{X}}$ through CoFeB resonance field at $\boldsymbol{H}_{\mathrm{FMR}}$. $\boldsymbol{H}_{\mathrm{X}}$ is swept through $\pm\boldsymbol{H}_{\mathrm{FMR}}$ and the acquired rectified diode voltage $V_{\mathrm{Diode}}$ is fit with a function that combines two symmetric and two anti-symmetric Lorentzian functions, which occur at $\pm\boldsymbol{H}_{\mathrm{FMR}}$ respectively, for a more accurate estimation of $V_S$ and $V_{AS}$. In some samples, a small step in $V_{\mathrm{Diode}}$ is apparent, which has been attributed in literature to SR

effects [229]. An additional Boltzmann-type step function centred about $H_X$ = 0 is included to account for this step in the overall fitting function, which is given by

$$V_{\text{Diode}} = V_S \frac{(\Delta H)^2}{(H - H_{\text{FMR}})^2 + (\Delta H)^2} + V_{AS} \frac{-2(\Delta H)(H - H_{\text{FMR}})}{(H - H_{\text{FMR}})^2 + (\Delta H)^2} - V_S \frac{(\Delta H)^2}{(H + H_{\text{FMR}})^2 + (\Delta H)^2} + V_{AS} \frac{-2(\Delta H)(H + H_{\text{FMR}})}{(H + H_{\text{FMR}})^2 + (\Delta H)^2} + \frac{A}{(1 + e^{-kH})}, \quad (5.15)$$

where the first two terms define the symmetric and antisymmetric Lorentzian component for $+H_{\text{FMR}}$, the third and fourth, the symmetric and antisymmetric Lorentzian component for $-H_{\text{FMR}}$, and the last term, the Boltzmann step at $H_X$ = 0. In the Boltzmann fit, $A$ is the coefficient setting the size of the fit and $k$ sets the slant of the step.

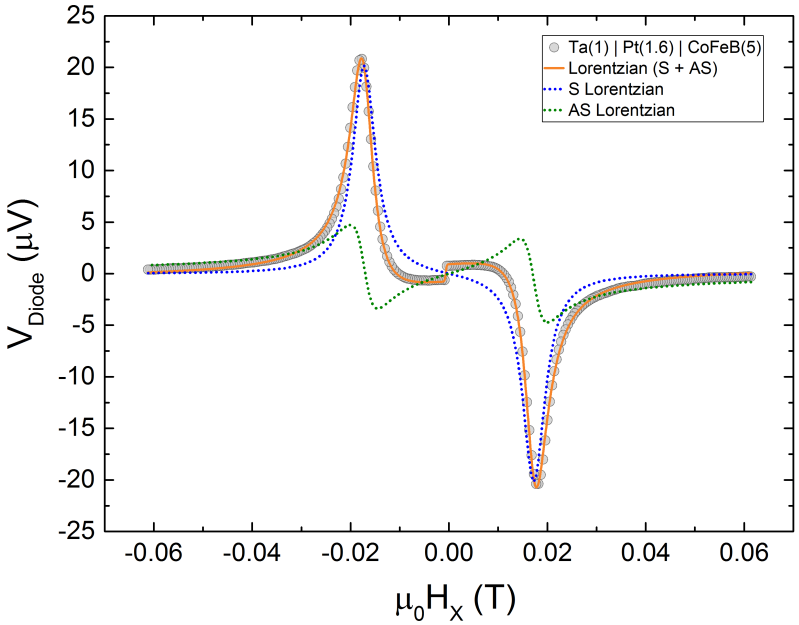


**Figure 5.5 Experimental $V_{\text{Diode}}$ spin pumping data measured on a Ta(1)|Pt(1.6)|CoFeB(5) sample and fit the pair of symmetric and antisymmetric Lorentzian curves as outlined in equation 5.15. The blue (green) dotted line fits the symmetric (antisymmetric) Lorentzian components.**

Figure 5.5 shows the raw diode voltage of a Ta(1)|Pt(1.6)|CoFeB(5) buffered bilayer measured in an ISHE lineshape spin pumping experiment as $H_X$ is swept through $\pm H_{\text{FMR}}$. The FMR conditions are given by the Kittel equation 1.8 in the FM. Once the resonance conditions are met at $H_X \sim H_{\text{FMR}}$, spin precession injects a DC $\boldsymbol{j}_s$ across the Pt|CoFeB interface and a $V_{\text{ISHE}}$ voltage is generated across the bar. At $\pm H_{\text{FMR}}$, the peak in diode voltage represents the summation of the symmetric and antisymmetric components of the Lorentzian fit, which are extracted using equation 5.15 with a four-parameter fit ($V_S$, $V_{AS}$, $A$, $k$). Notice, the Boltzmann step term about $H_X$ = 0 is required for an acceptable fit. The symmetric (blue) and antisymmetric (green) Lorentzian components comprising the overall fit (orange) are displayed with dotted fitting lines for a visual guide. Here, as in all samples, $V_S \gg V_{AS}$. Since $V_{AS}$ is purely signal from SR effects, this first indicates that the AHE and AMR components are small in these bilayers. This result is consistent with the electrical properties of the system, acknowledging that any induced $\boldsymbol{j}_c$ from the stripline will be

shunted primarily through the more conductive Pt layer due to the high resistivity of CoFeB, as shown in section 3.3.1.

However, the ISHE voltage yields a symmetric Lorentzian component, so the parasitic AHE and AMR components of the spin rectification effects in $V_S$ must also be explored. To do so, we measure a CoFeB(5) film with no Pt layer. Figure 5.6 shows the diode voltage of this film in comparison to that of the Ta(1)|Pt(1.6)|CoFeB(5) device. From fitting, the symmetric Lorentzian component of the CoFeB(5) device is $V_S$ = 0.557 μV, compared to $V_S$ = 20.3 μV of the Ta(1)|Pt(1.6)|CoFeB(5) device. Therefore, the parasitic SR component is only ~ 2.7% of the $V_S$ with the fixed $H_X$, suggesting that angular rotation measurements are not required. Additionally, both electrical and macroscopic magnetic properties remain consistent in CoFeB across the (un)buffered series, which suggests a constant injected spin current across the HM|FM interface. Hereby, it appears spin rectification effects are not significant in the buffered metallic bilayer series.

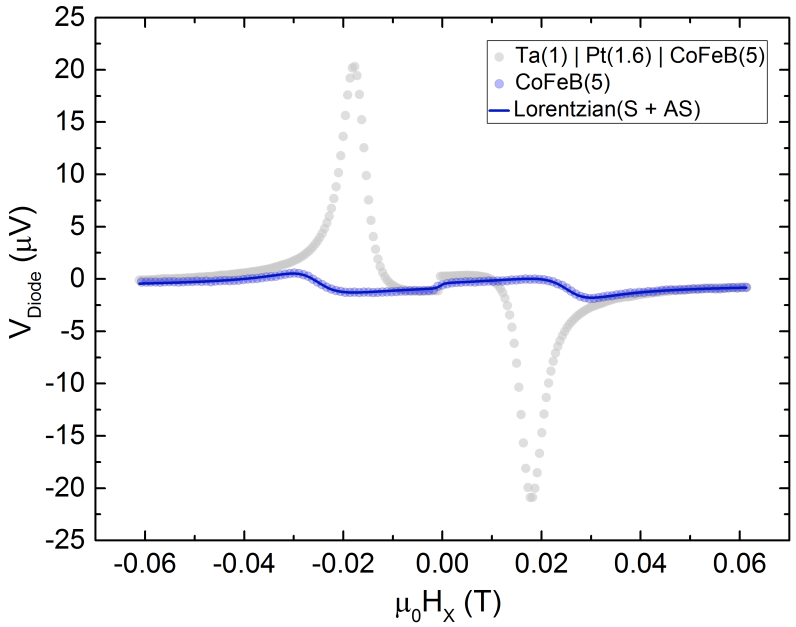


**Figure 5.6 Raw experimental $V_{Diode}$ spin pumping data of a CoFeB(5) sample fit to equation 5.15 compared with a reproduced raw data of a Ta(1)|Pt(1.6)|CoFeB(5) sample from figure 5.5.**

To further ensure the origin of $V_S$ is the ISHE, we test the possibility of the induced moment in the few Pt monolayers from the MPE adding to $V_S$. We spatially separate the HM and FM by fabricating and measuring a Pt|CoFeB sample with a spin-transparent 5 nm Cu spacer layer in between. There is little change found in $V_S$ when inserting the Cu spacer (see figure D.1 in Appendix D), which agrees well with new work [198] finding no discernable MPE in Pt|Co systems. The small change observed in $V_S$ between the two devices may be attributed to an imperfect spin-transparent Cu layer. Moreover, any small MPE component should not change dramatically across the (un)buffered series and, therefore, will remain ineffectual due to the comparative nature of this study. Hereby, we use $V_S \sim V_{ISHE}$ in the analysis below.

The final check required to confirm the validity of a spin pumping measurement is to show good coupling between the CPW and the sample such that the magnetisation dynamics in the FM follow the Kittel equation 1.8 at resonance. Figure 5.7 (a) shows linearity between $V_s$ of a Ta(1)|Pt(3)|CoFeB(5) device across the microwave power range spectrum suggesting good coupling between $H_{RF}$ and the CoFeB layer. Figure 5.7 (b) shows the correlation between microwave drive frequency and $H_{FMR}$ follows the Kittel equation.

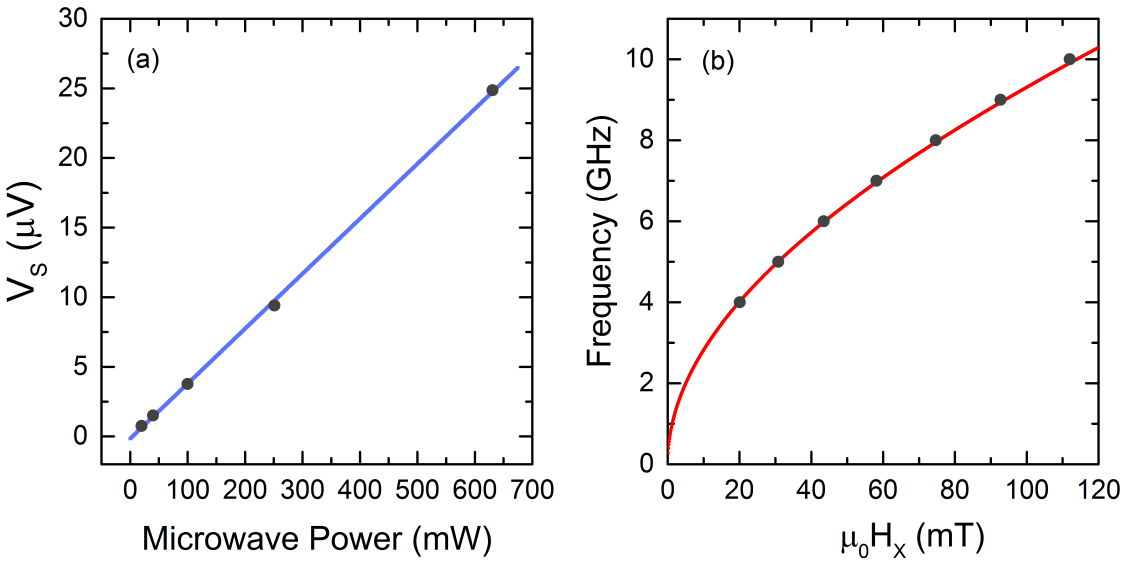


Figure 5.7 FMR conditions tested on a Ta(1)|Pt(3)|CoFeB(5) sample. (a) $V_s$ extracted from fitting raw $V_{Diode}$ plotted against microwave generator power. (b) Applied microwave frequency plotted against $H_{FMR}$ extracted from fitting raw $V_{Diode}$ at $(4\pi)M_{eff}$ = 1 T.

In spin pumping measurements, the device micromagnetics strongly affects the cone angle of precession in the FM and subsequently $j_s^{HM|FM}$ sunk by the HM layer. Thereby, changes in PMA arising from the buffered Pt(111) texture and $t$ as discussed in section 3.4.2 will affect the magnetisation dynamics. Therefore, it is imperative that in the thicker CoFeB samples with strong Pt(111) texture remain strongly in-plane and impervious to the effective anisotropy field $H_{K,eff}$. In the Kittel equation 1.8, the effective magnetisation $(4\pi)M_{eff}$ = $(4\pi)M_S - H_{K,eff}$ is strictly the magnetic field underpinning FMR. However, in the thick FM limit, magnetic properties are governed by bulk magnetic order, as opposed to thinner layers, which are closer to the SRT and influenced strongly by interface PMA. Liu *et al*. [232] proved that in the thick FM limit, $M_{eff} \sim M_S$ and PMA is not influential in setting the cone angle of precession.

Hereby, we fabricate (un)buffered series with thick 5 nm CoFeB, which are approximately 4 nm thicker than devices at the SRT, to ensure $M$ always lies strongly in-plane. A direct consequence of this is the applicability of the Kittel equation for FMR resonance in these buffered bilayers: any slight perturbation from $H_{FMR}$ has no significant time-averaged bearing on $\theta_M$, which remains in-plane ($\theta_M \sim \theta_H = \frac{\pi}{2}$). In figure 5.7 (b), we prove that even in a Ta(1)|Pt(3)|CoFeB(5) sample with significant PMA from the enhanced Pt(111) texture (and so $H_{K,eff}$), there is still good agreement with the Kittel equation where $M_{eff} \sim M_S$. Moreover,

the $(4\pi)M_{eff} \sim 1$ T fit from the Kittel equation in figure 5.7 (b) is corroborated with a VSM measurement on a continuous Ta(1)|Pt(3)|CoFeB(5) film (figure 3.10), confirming good agreement with magnetometry. Since the Ta-buffered bilayer has significant PMA, yet $M_{eff} \sim M_S$ still holds due to the bulk-like magnetic behaviour of the thick CoFeB layer, we use $(4\pi)M_{eff} \sim 1$ T in all magnetoelectronic circuit across all buffered bilayer series below.

### 5.4.2 Spin pumping in buffered HM|FM Bilayers

In this section, we fabricate and measure a series of (un)buffered Pt|CoFeB devices at varying $t$ to perform a HM thickness-dependent analysis and extract the $\theta_{SH}$ and $\lambda$. Spin pumping $V_{ISHE}$ signals are extracted from fitting lineshapes at $\pm H_{FMR}$, simultaneously, as outlined in the previous section. The microwave generator drives an $H_{RF}$ at $f$ = 4 GHz with a 28dBm (631 mW) AC current through the stripline for all devices measured. Figure 5.8 shows the raw diode voltage acquired for a range of unbuffered, Ta- and Ru-buffered Pt($t$)|CoFeB(5) bilayers a function of the sweeping, static field $H_X$.

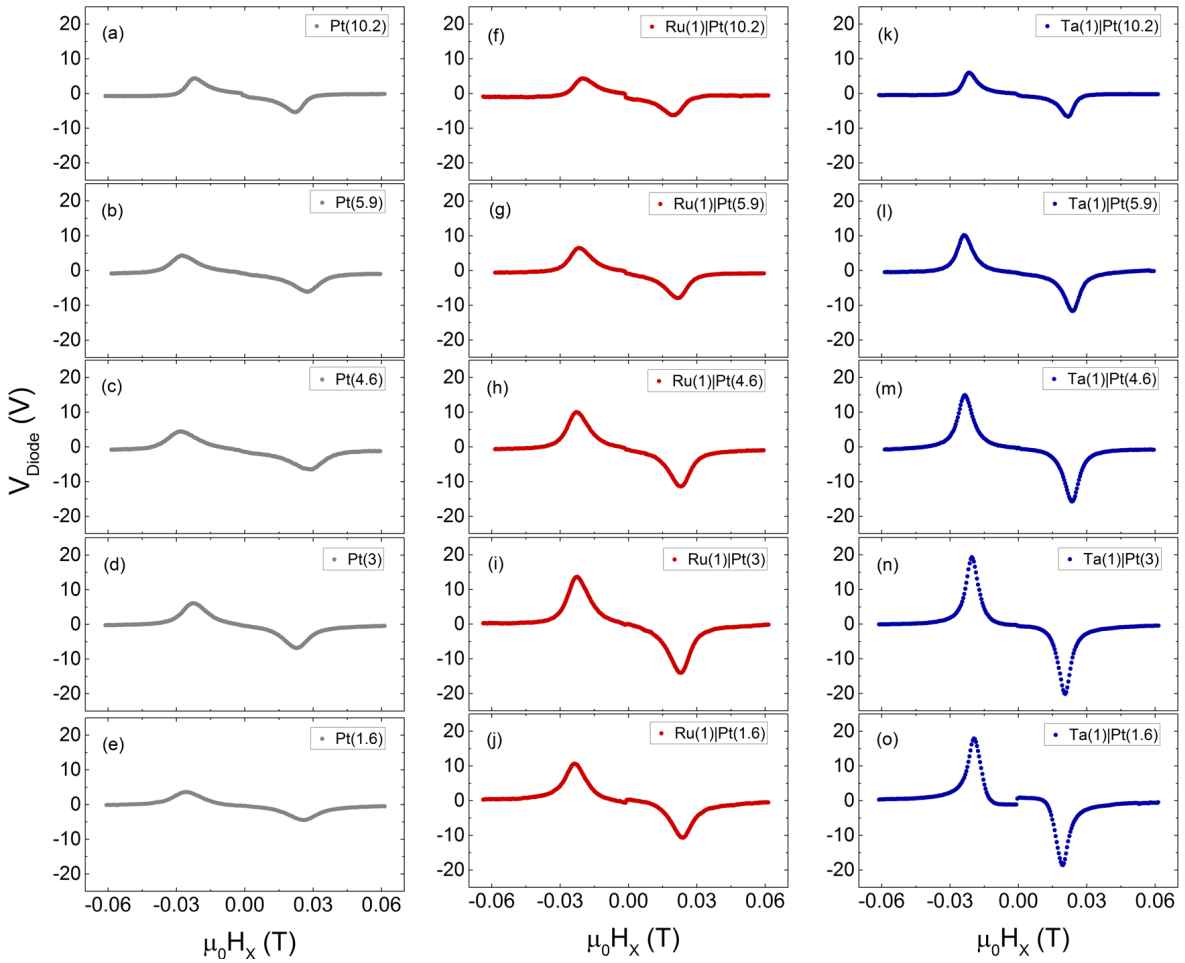


Figure 5.8. Spin pumping $V_{Diode}$ data plotted against field $H_X$ at varying t for: (a-e) unbuffered, (f-j) Ru-buffered and (k-o) Ta-buffered Pt($t$)|CoFeB(5) bilayers at $f$ = 4 GHz.

Note, a small background offset $V_{\text{Diode}}$ is removed from each measurement. In all samples, the $V_{\text{Diode}}$ is observed to decrease (increase) at $(\pm)H_{\text{FMR}}$ when the magnetic conditions of Kittel's equation are satisfied. The absolute magnitude of the Lorentzian lineshape at $\pm H_{\text{FMR}}$ is smaller in thicker $t$ = 10.2 nm devices than those with less Pt ($t \sim 3$ nm), as expected. We also observe a larger absolute magnitude of the $V_{\text{Diode}}$ lineshape at $\pm H_{\text{FMR}}$ from unbuffered to Ru-buffered to Ta-buffered devices. In figure 5.9, a thickness-dependent plot summarises the extracted $V_{\text{ISHE}} \sim V_S$ signals from equation 5.15 averaged from a set of at least two measurements at each Pt thickness for a comparison between each series of (un)buffered Pt(t)|CoFeB(5) multilayers.

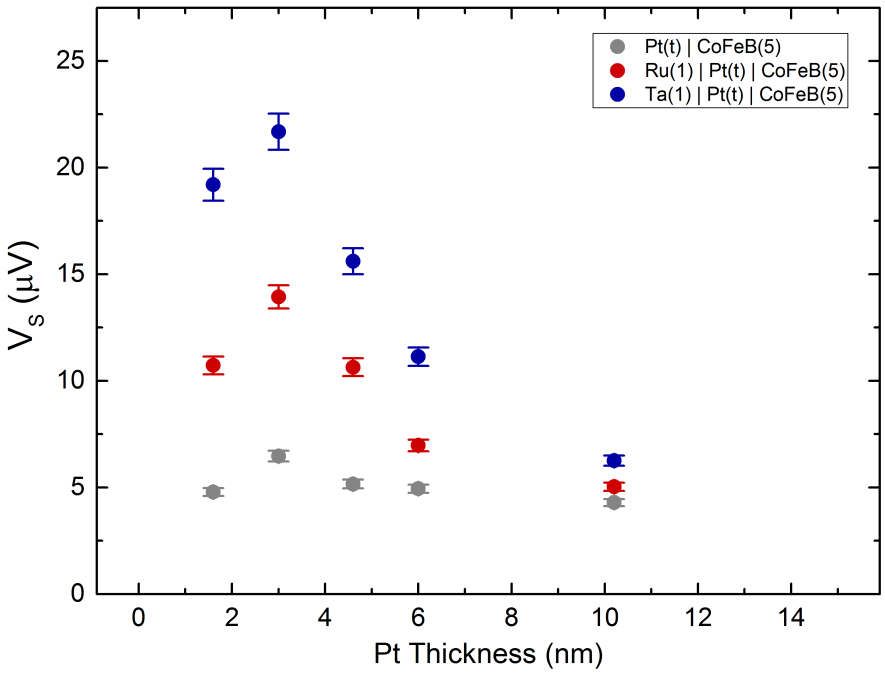


**Figure 5.9. Pt thickness-dependent $V_{\text{ISHE}} \sim V_S$ signals extracted from $V_{\text{Diode}}$ lineshape fitting with equation 5.15 for all (un)buffered Pt(t)|CoFeB(5) devices.**

It is clear from the extracted $V_S$ from fitting the $V_{\text{Diode}}$ lineshape that the larger magnitude at $\pm H_{\text{FMR}}$ from figure 5.8 corresponds directly to a larger symmetric component in figure 5.9. We observe common HM thickness-dependent behaviour in all series with the largest magnitude of $V_{\text{ISHE}}$ at $t \sim 2\lambda$ in the ultrathin limit and a fast falloff with thicker Pt devices. Again, this is directly a result of the exponential decay of $\mu_s$ in the HM layer from the Pt|CoFeB interface governed by equation 5.2. Under $t \sim 2\lambda$ the sustained spin polarisation still augments $\boldsymbol{j}_c^{\text{ISHE}}$ from equation 5.13, but once spins relax and $\mu_s \sim 0$ at $t > 2\lambda$, additional HM thickness does not add any significant ISHE component and effectively reduces the measured voltage.

In figure 5.9, we also observe that $V_S$ extracted values directly agree with the SHMR results from Chapter 4, where the Ta-buffered stacks are ~ 3 times as large as the unbuffered stacks at the peak ($t \sim 3$ nm), while the Ru-buffered stacks are approximately twice as large. The similarity is not coincidental, but rather because both measurement techniques rely on the ISHE to convert spin-to-charge. Again, the change in signal size in the ultrathin limit may be

correlated directly to the quality of the Pt film observed from the HAADF-STEM images in figure 3.4. At thicker HM devices ($t$ ~ 10 nm), we observe $V_S$ converging across all three (un)buffered series, which is consistent with HAADF-STEM microscopy. Here, the Pt film quality was observed to uniformly wet the surface regardless of the buffer layer.

The systematic error in $V_{\text{ISHE}}$ lineshape spin pumping measurement due to two sources. First is the sample placement on the CPW. Placement of the bar with length $l$ = 1.2 mm (similar to the width of the stripline $\mathbf{s}$ = 1.4 mm) is non-trivial since the sample is invert-mounted, face-down on the CPW. Without a visual aid, it is difficult to fix the bar both straight (in $\hat{\boldsymbol{y}}$) and centred within the stripline as desired. To determine the loading error, a reproducibility measurement was performed on a Ta(1)|Pt(3)|CoFeB(5) bar 10 times to calculate the standard error $\epsilon = \frac{100}{\mu_a}\frac{\sigma_{sd}}{\sqrt{n}}$, where $\sigma_{sd}$ is the standard deviation, $\mu_a$ is the sample average and $n$ is the number of samples. We found an $\epsilon \sim 2.5\%$ depending on the bar mounting. The lineshape fitting errors are small in comparison. The second source of error arises from the parasitic spin rectification signals present in $V_S$ when approximating $V_{\text{ISHE}} \sim V_S$, which is found to be $\epsilon \sim 3\%$. The error bars in Figure 5.8 display these errors added in quadrature. The real error may well be larger if the spin-dependent parameters in the CoFeB or the spin mixing conductance vary across the (un)buffered series.

### 5.4.3 Estimating spin-dependent parameters in spin pumping

We model the experimental spin pumping data this section with measured spin-dependent parameters of the HM buffers, $\theta_{\text{Ru}} \sim 0$, $\lambda_{\text{Ru}} \sim 2$ nm, $\theta_{\text{Ta}} \sim -0.0675$, $\lambda_{\text{Ta}} \sim 1.39$ nm from section 4.4.2 and estimated parameters from literature $P_{\text{CoFeB}} \sim 0.6$ [100], $\lambda_{\text{CoFeB}} \sim 1$ nm [213,214]. Similar to the previous chapter, we first attempt to fit the buffered Pt|CoFeB bilayer $V_{\text{ISHE}}$ spin pumping experimental data to equation 5.14 derived from the magnetoelectronic circuit theory model in section 5.2. The models shown in figure 5.10 are fit with the best set of constant Pt spin-dependent parameters for the Ta- and Ru-buffered bilayers.

In figure 5.10, it is clear that at constant Pt spin-dependent parameters, both models poorly fit the buffered data, albeit less so when $\rho_{\text{Pt}}$ is varied[5] to consider enhanced grain boundary and diffuse surface scattering in the ultrathin limit. Neither set of fits can model well the large $V_S$ magnitudes at $t \sim 2\lambda$ and the fast fall off at $t \sim 10$ nm, simultaneously. However, when we account for the change in spin-dependent parameters $\theta_{\text{SH}}$ and $\lambda$ with $\rho_{\text{Pt}}$ across $t$ in figure 5.11 for the buffered bilayers, the developed model follows the experimental data well.

[5] $\rho_{\text{Pt}}(t)$ is derived from empirically fitting the discrete experimental $\rho_{xx}$ data in figure 3.8 to obtain a continuous function.

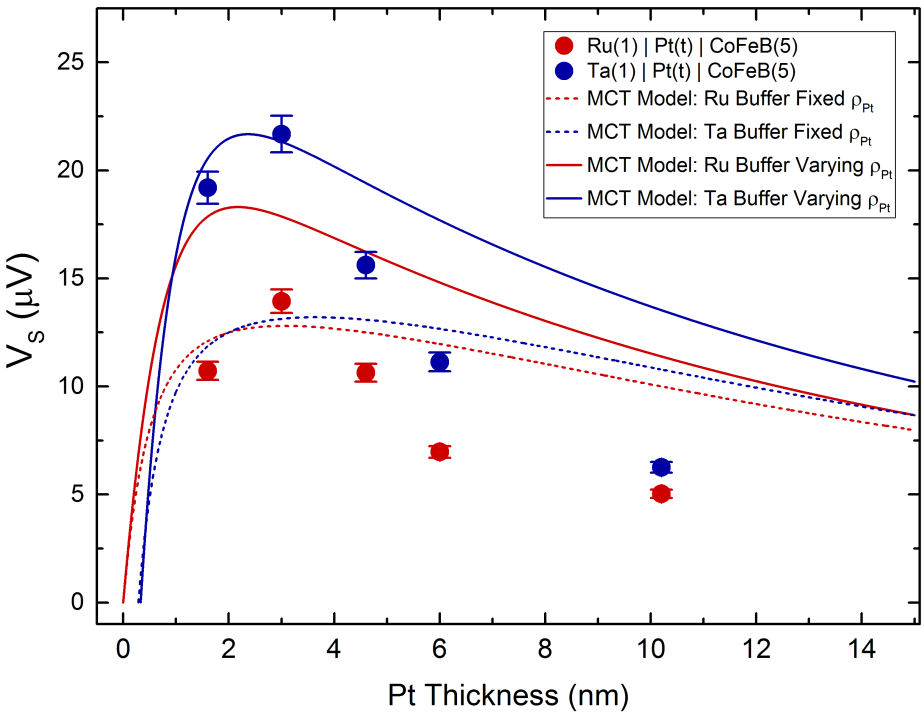


Figure 5.10 Pt thickness-dependent $V_{\mathrm{ISHE}} \sim V_S$ signals extracted from $V_{\mathrm{Diode}}$ lineshape for Ru- and Ta-buffered Pt(t)|CoFeB bilayers. The dashed lines represent the spin pumping model from equation 5.14, derived from magnetoelectronic circuit theory with a fixed $\rho_{\mathrm{Pt}}$ across $t$. The solid lines represent the model with $\rho_{\mathrm{Pt}}$ varying across $t$, as outlined in section 3.3.1. The spin mixing conductance is set as $g_r = 5 \times 10^{15}\ \Omega^{-1}\mathrm{m}^{-2}$ and a set of constant spin-dependent parameters are used, $\theta_{\mathrm{SH}} = 0.09$ and $\lambda = 5$ nm.

In figure 5.11, the magnetoelectronic circuit theory model developed in section 5.2 models the Ru- and Ta-buffered Pt|CoFeB bilayers well. Here, the recent indications that Pt is governed by Elliot-Yafet [84–87] spin relaxation and intrinsic spin scattering [67,68,74,87,143,211] prompt us to fix $\lambda\rho$ and $\sigma_{xy}^{\mathrm{SH}} = \frac{\theta_{\mathrm{SH}}}{\rho}$ constant, respectively. Therefore, in figure 5.11, the model sets $\lambda(t) = \lambda_{\mathrm{bulk}} \frac{\rho_{\mathrm{Pt,bulk}}}{\rho_{\mathrm{Pt}}(t)}$ and $\theta_{\mathrm{SH}}(t) = \theta_{\mathrm{SH,bulk}} \frac{\rho_{\mathrm{Pt}}(t)}{\rho_{\mathrm{Pt,bulk}}}$ from $\rho_{\mathrm{Pt}}(t)$ at each thickness to extract one set of bulk $\lambda$ and $\theta_{\mathrm{SH}}$ values, equivalent to the methodology applied in the previous chapter to model the buffered SHMR series. We find that when these mechanisms dominate, the buffered experimental data can be fit accurately in both thick and thin Pt bilayers down to $t \sim 3$ nm, simultaneously, unlike in figure 5.10. Because we use the identical heterostructure here as in the previous chapter for the buffered SHMR series, it follows that the possible explanations for the inability to correctly predict $V_{\mathrm{ISHE}}$ in ultrathin $t \sim 1.6$ films, as discussed in detail in section 4.4.4, are the same. Thereby, we again conclude that a slight decrease in $\sigma_{xy}^{\mathrm{SH}}$ or $g_r$ were the two most probable causes for the inaccurate prediction of the model at these thicknesses. Furthermore, in figure 5.11, we demonstrate that significantly different Ru- and Ta-buffered bilayer $V_{\mathrm{ISHE}}$ signals in the ultrathin limit can be fit well in figure 5.11 with the identical bulk spin-dependent $\theta_{\mathrm{SH}} = 0.086$ and $\lambda = 2$ nm, when considering $\rho_{\mathrm{Pt}}(t)$ and so $\lambda(t)$ and $\theta_{\mathrm{SH}}(t)$ for each series.

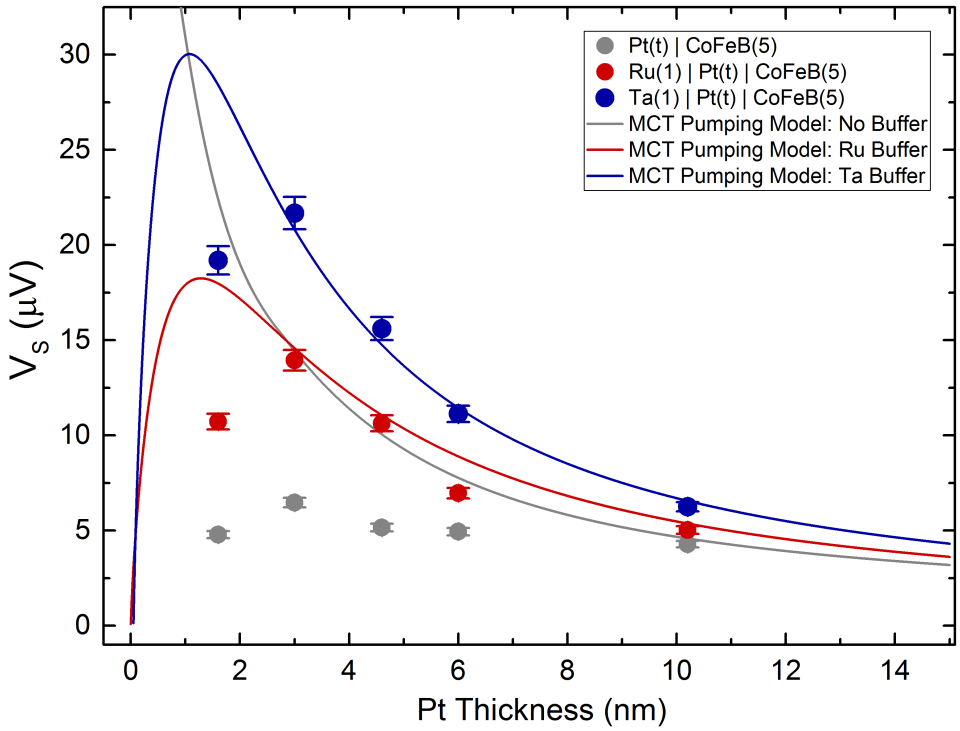


Figure 5.11 Pt thickness-dependent $V_{\mathrm{ISHE}} \sim V_S$ signals extracted from $V_{\mathrm{Diode}}$ lineshape for all (un)buffered Pt(t)|CoFeB bilayers. The solid lines represent the spin pumping model from equation 5.14, derived from magnetoelectronic circuit theory with varying $\rho_{Pt}$ across $t$. The spin mixing conductance is a constant $g_r = 5 \times 10^{15}\ \Omega^{-1}\mathrm{m}^{-2}$, while $\theta_{\mathrm{SH}}$ and $\lambda$ vary as a function of thickness, governed by Elliot-Yafet spin relaxation and intrinsic spin scattering.

In the case of unbuffered Pt|CoFeB, we find the model does not represent the experimental data whatsoever, similar to the previous chapter. In the ultrathin limit, we showed unbuffered Pt grown directly on $SiO_2$ has poor film quality and follows 3-D granular, Volmer-Weber-type growth in figure 3.4. In this case, an increase in $\rho_{\mathrm{Pt}}$ is due to percolated film growth and not proportional to stronger spin-dependent scattering. Therefore, a constant $\sigma_{xy}^{\mathrm{SH}}$ is not expected at low thickness ($t$ < 10 nm). However, at $t$ > 10 nm, when 2-D growth of unbuffered Pt occurs, the fit converges and models the experimental $V_{\mathrm{ISHE}}$ data well. This indicates that good layer-by-layer growth is restored and the intrinsic spin scattering and Elliot-Yafet mechanisms dominate once again.

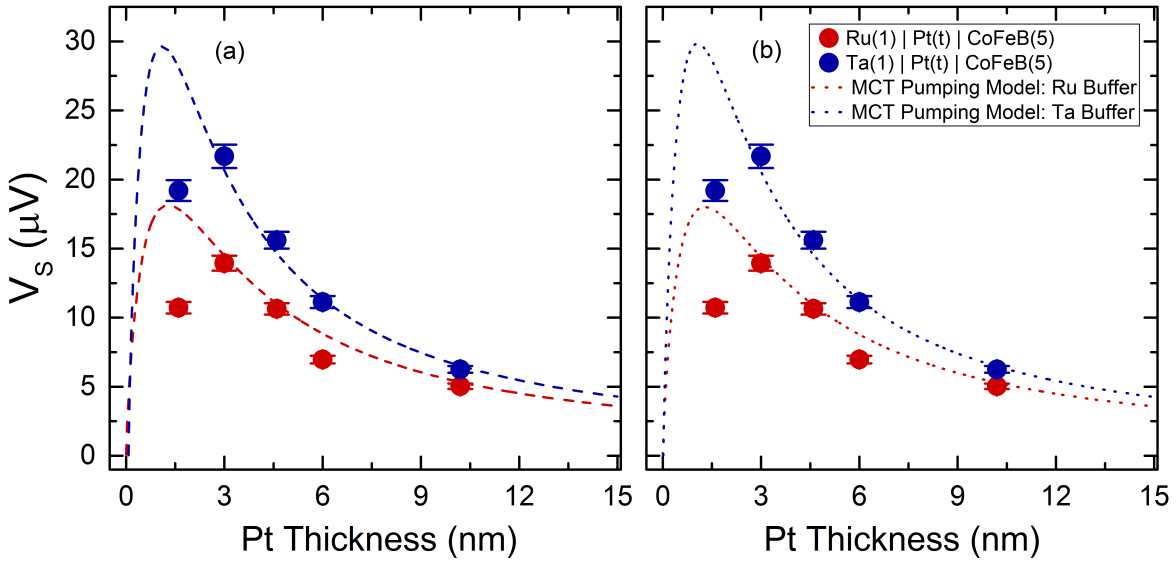


Figure 5.12 Pt thickness-dependent $V_{ISHE} \sim V_S$ signals extracted from $V_{Diode}$ lineshape for Ru- and Ta- buffered Pt(t)|CoFeB bilayers. The dashed fits represent the spin pumping model from equation 5.14 at varying $\rho_{Pt}(t)$, $\theta_{SH}(t)$ and $\lambda(t)$ in the Pt layer. The bulk spin diffusion length $\lambda$ = 2.48 nm from figure 5.11 fitting. (a) $g_r = 1 \times 10^{15}$ $\Omega^{-1}m^{-2}$ and the bulk $\theta_{SH}$ = 0.43, while in (b) $g_r = 9 \times 10^{15}$ $\Omega^{-1}m^{-2}$ and the bulk $\theta_{SH}$ = 0.047.

Figure 5.12 (a) and (b) shows two cases where vastly different $\theta_{SH}$ and $g_r$ values seemingly accurately model the buffered bilayers. This proves the inability to extract precise values of $\theta_{SH}$ and $g_r$ due to the codependence of $V_{ISHE}$. In fact, to properly estimate bulk spin-dependent parameters $\theta_{SH} = 0.086$ and $\lambda = 2$ nm of Pt, we fit all Ru- and Ta-buffered Pt|CoFeB bilayers in the thickness-dependent SHMR and spin pumping measurements simultaneously. Since the magnitude of $V_{ISHE}^{SP} \propto g_r\theta_{SH}$, while that of $\Delta R_{XX}^{SHMR} / R_{XX}^{0} \propto g_r\theta_{SH}^{2}$, we are able to decouple these parameters to find a unique solution. Therefore, these bulk spin-dependent values of Pt and the spin mixing conductance are capable of fitting a broad range of $V_{ISHE}$-dependent spin signals, which can be directly accounted for by considering the difference in HM microstructure morphology when Elliot-Yafet spin relaxation and intrinsic spin scattering dominate.

## 5.5 Conclusions

In this chapter, we performed HM-thickness dependent spin pumping measurements on (un)buffered Pt|CoFeB bilayers to understand the role of HM microstructure in $V_{\mathrm{ISHE}}$ lineshape spin pumping signal magnitudes. The spin pumping signals in the metallic bilayers were evaluated by fitting the ISHE induced voltage linewidth to a set of symmetric and antisymmetric Lorentzian functions. We demonstrated the spin rectification effects were small and not dominant in $V_S$, despite the difficulties of separating the pure ISHE signal from the symmetric component from parasitic spin rectification effects in metallic stacks noted in the recent literature. Additionally, using $V_{\mathrm{ISHE}} \sim V_S$, the Kittel equation confirmed good pumping conditions across different powers and microwave frequencies.

The HM thickness-dependent spin pumping measurements showed analogous results to those obtained with the SHMR: the peak signal size ($t \sim 3$ nm), was largest for Ta-buffered stacks, followed by Ru-buffered and the unbuffered stacks, respectively. This trend directly follows the quality of Pt film deposition characterised by HAADF-STEM and XRR in chapter 3. Thereby, we confirm that in spin pumping $V_{\mathrm{ISHE}}$ lineshape measurements, the spin-to-charge conversion of the ISHE is directly affected by HM microstructure.

To correlate changes in spin transport through spin-dependent properties with HM microstructure, current magnetoelectronic circuit theory was employed to created a BUF|HM|FM model and fit the experimental spin pumping data data. It was not possible to fit the buffered Pt|CoFeB devices well in both ultrathin and thicker ($t \sim 20$ nm) samples with a constant $\theta_{\mathrm{SH}}$ and $\lambda$. However, the data was well fit by varying both $\theta_{\mathrm{SH}}$ and $\lambda$, when the Elliot-Yafet spin relaxation and intrinsic spin scattering dominates in Pt. Additionally, it proved challenging to accurately evaluate $g_r$ and $\theta_{\mathrm{SH}}$ with spin pumping alone since both influences the ISHE voltage measured leading to a set of suitable values. However, when modelling Ru- and Ta-buffered Pt|CoFeB spin pumping data simultaneously with SHMR thickness-dependent data, the difference in signal dependence on $g_r$ and $\theta_{\mathrm{SH}}$ allowed for a self-consistent set of bulk spin-dependent parameters to be extracted. In so doing, we demonstrated that a single set of bulk HM spin-dependent parameters could be extracted from different measurement schemes at largely different signal sizes when adequately considering the difference in HM microstructure.

# 6 Spin current absorption in the ultrathin limit: Spin-orbit torque

## 6.1 Introduction

Spin-orbit torque arises from the accumulation of spin at the HM|FM interface from the SHE. Equivalent to SHMR, an in-plane charge current applied to a HM with large SOC drives a spin current across the interface. Instead of quantifying the HM resistivity change due to spin current reflection at the interface, SOT probes the amount of spin current injected into (and absorbed by) the FM, by quantifying the induced torque on $\boldsymbol{M}$. SOT in HM|FM bilayers has been shown to produce large effective fields [48,49,121,233], which comprise both a field-like and a damping-like component. When the effective fields generated by the SHE in the HM are large enough to overcome the effective anisotropy field in the FM, SOT may even exert enough torque on the FM to flip $\boldsymbol{M}$ [5,116–118], providing an exciting new opportunity in the magnetic recording industry. Additionally, low-current lock-in techniques have recently been developed [50,130] for devices with in-plane and perpendicular-to-plane magnetisation easy-axes, which elucidate both field-like and damping-like effective fields.

Currently, however, there are large discrepancies between the magnitudes of the effective field quantified from SOT measurements in literature [44,50,123,234], which makes SOT-MRAM difficult to implement. Interestingly, most of these experiments are performed on metallic bilayers with the HM fabricated directly on the substrate [5,118,199,221], where the HM microstructure and so the spin-dependent properties may be changing drastically. To account for the changes in the electrical properties of the HM layer, a new metric known as SOT efficiency was defined as $\xi \sim \frac{2e}{\hbar}\frac{j_s^{\mathrm{HM|FM}}}{j_{c,\mathrm{HM}}}$. Now heavily deployed [126,220,235,236], the SOT efficiency measurement is a useful tool for probing the spin Hall conductivity in HMs. Nguyen *et al*., utilise SOT efficiencies in this manner to find that $\sigma_{xy}^{\mathrm{SH}}$ is constant in Pt|Co bilayers, indicating spin scattering is dominated by intrinsic mechanisms in Pt [87]. In this same Pt|Co system, Pai *et al*., found that SOT efficiency depended strongly on the preparation of the Pt|FM bilayer [126], yet there has not been a study of the influence of HM microstructure morphology on spin-dependent properties with SOT to date.

In this chapter, we study the absorption of $\boldsymbol{j}_s$ in the FM with SOT measurements on the (un)buffered Pt|FM bilayers to correlate the magnitude of the induced effective fields to the Pt microstructure. With current-induced switching and low-current, lock-in techniques, we evaluate the damping-like and field-like effective fields induced by $\boldsymbol{j}_s$ from the SHE in the Pt. We find that due to experimental limitations during current-induced switching measurements, the low-current, lock-in techniques prove more suitable for extracting SOT effective fields in this work. Since the microstructure and so $\rho$ of the Pt layer is sensitive to

the seed layer in the ultrathin limit as shown in chapter 3, we account for the difference in $\rho_{Pt}$ across the (un)buffered Pt|FM bilayers by instead comparing $\frac{\Delta H_{SOT}}{j_{c,Pt}}$. In this vein, we compare $\sigma_{xy}^{SH}$ at varying Pt morphologies to corroborate the observations from chapters 4-5 that Pt is dominated by intrinsic spin scattering.

## 6.2 Experimental setup

The measurements in this chapter probe spin-orbit torque exerted on the FM layer with planar and anomalous hall voltages. The current flow in the HM driving the spin accumulation at the interface and the subsequent readout of the hall voltages are supplied and measured, respectively, by the spin transport rig outlined in section 2.3.1. The HM bilayers deposited in a Hall bar geometry are designed for transverse voltage measurements as illustrated in figure 6.1. The devices are temporarily fixed directly on one of the compact sample holders with Rubber Cement™ and wire bonded. The current leads are connected across the length of the bar, and the voltages leads are bonded across the width, transverse to $\boldsymbol{j}_{c,x}$.

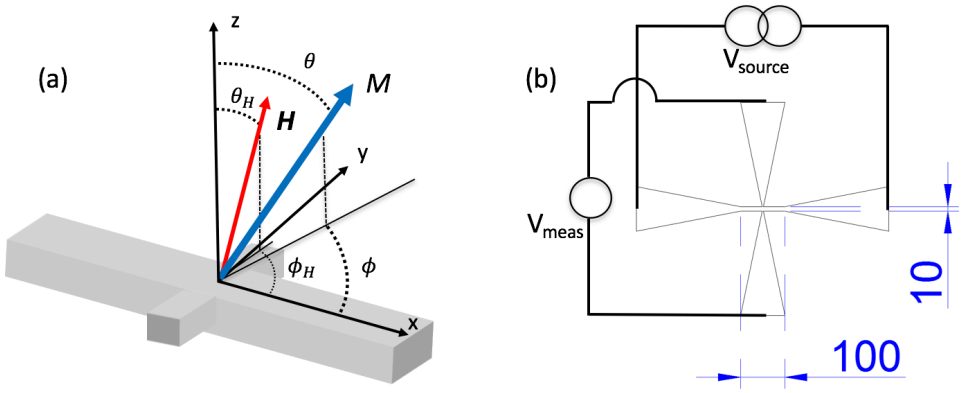


Figure 6.1 Schematic illustration of the (a) SOT measurement experiment and (b) the dimensions in μm of the Hall bar utilised in this chapter.

We conduct two different sets of experiments to determine the amount of SOT generated by each buffered HM bilayer: current-induced, SOT ferromagnetic switching and SOT effective field measurements with low-current, lock-in techniques. The SOT devices are fabricated in the Hall bar geometry depicted in figure 6.1 (b) for both experiments at room temperature, but require different instrumentation to drive current and measure Hall voltages. Figure 6.1 (a) illustrates a schematic of the Hall bar with the coordinate axes invoked for these SOT measurements. Before experimentation, we align $\boldsymbol{H}$ of the GMW 3470 electromagnet in the x-axis of the sample to one-tenth of a degree with the URS 150CC rotational stage. To align the sample and locate $\theta_H$ = 90° we apply a large $\mu_0 H \sim \pm$ 3 kG and minimise the transverse AHE signal from any perpendicular component $\boldsymbol{M}$.

To quantify the magnitude of the effective fields generated from the spin current absorption in the FM layer, we observe the change in $\boldsymbol{M}$ from spin-orbit torque with Hall measurements.

Since the FM conducts, an in-plane charge current flowing through the bilayer will generate Hall effects. Transverse voltage measurements $V_{XY}$ allow us to correlate the change in $\boldsymbol{M}$ both the perpendicular-to-plane component with the anomalous Hall effect ($V_{AHE}$) and the in-plane component with the planar Hall effect ($V_{PHE}$) following the symmetries outlined extensively in section 1.1.5. A purely PHE component of $V_{XY}$ is evaluated by rotation a small, in-plane ($\theta_H$ = 90°) field about $\phi$ and corresponds to a magnetisation change in the film plane. In contrast, the AHE component is evaluated by sweeping an $H_Z$ at $\theta_H$ = 0° and corresponds directly to changes in the out-of-plane component of $\boldsymbol{M}$. In this way, by controlling $\boldsymbol{M}$ with $\boldsymbol{H}$, we can relate the change in $V_{XY}$ to $\boldsymbol{M}$ in all directions, and so quantify the effective fields arising from the SHE in the HM.

The first of the two experiments conducted is current-induced, (field-assisted) SOT switching (CIS) on perpendicularly magnetised HM|FM bilayers. In CIS, large effective fields are required to overcome the effective anisotropy field of the FM film to reverse $\boldsymbol{M}$ with high applied DC currents. The current density required to switch a thin film FM layer is given by [200]

$$j_{c,x} = \frac{2e}{\hbar}\frac{M_s d_{FM}}{\theta_{SH}}\left(\frac{H_{k,eff}}{2} - \frac{H_X}{\sqrt{2}}\right). \tag{6.1}$$

where, $H_{k,eff}$ is the effective anisotropy field and $H_X$ is the symmetry-breaking field when $H_X \ll H_{k,eff}$. The symmetry-breaking field is required for deterministic, $\boldsymbol{M}$ switching [118,237]. Notice the switching current density is an extrinsic property: it is dependent on the amount of FM material through $d_{FM}$. Thereby, a large DC charge current applied across the length of the bar is supplied by the Keithley Sourcemeter 2400. We sweep to maximum applicable current magnitudes to induce SOT switching while measuring a transverse AC resistance without overloading $V_{Mixer}$ of the Lakeshore 3708. In these measurements, a slight out-of-plane component $H_Z$ from imperfect alignment biases the hysteresis loop, which is sometimes required to assist the SOT effective fields to switch the FM layer. This additional Zeeman term may be used to either assist or hinder the magnetisation reversal depending on the initial state $\pm M_Z$ and whether it is acting with or against the SOT effective field.

SOT effective field measurements, on the other hand, can decouple field-like $\Delta H_{FL}$ and damping-like $\Delta H_{DL}$ components of the induced SOT field by quantifying a change in $\boldsymbol{M}$ with Hall voltages without FM switching. Here, we use a low-current, lock-in techniques outlined in section 1.2.3 to measure bilayers with both easy-axis in-plane and out-of-plane magnetisation. We apply a constant sinusoidal voltage from the SRS 830 lock-in amplifier and measure the in-phase (0°) first harmonic $V_\omega$ component and the out-of-phase (90°) second harmonic $V_{2\omega}$ component, while the field is swept. In general, magnetoresistance measurements must be conducted with a constant applied current to not pick up spurious signals from a changing current. However, since we probe $V_{XY}$ in this experiment and we observe a maximum SHMR signal of 0.4% (and lower than that for AMR) in Pt|CoFeB bilayers from chapter 4, the applied current (and so SOT) will vary by only this value at most. In

addition, since offset $V_{XY}$ from the AHE and PHE are comparable to signal size, the maximum parasitic signal that could overlay the SOT measurement will again be a maximum of 0.4%. The larger uncertainties in this measurement scheme make the constant voltage source acceptable in this work.

In this chapter, the measured in- (out-of-) phase component is defined as the sinusoidal voltage in- (out-of-) phase to the applied sinusoidal voltage applied across the Hall bar. For easy-axis out-of-plane magnetic devices, the field is applied in-plane at $\theta_H$ = 90° in either $\hat{\boldsymbol{x}}$ ($\phi_H$ = 0°) or $\hat{\boldsymbol{y}}$ ($\phi_H$ = 90°) depending on the sample mounting. Prior to the sweep, the magnetisation is set by applying a 5 kG $\pm\mu_0 H_Z$ to fix an initial state $\pm M_Z$. Assuming the equilibrium magnetisation direction does not deviate significantly from the surface normal, we measure the harmonic Hall voltages and fit a parabola to the $V_\omega$ and a straight line to the $V_{2\omega}$. We extract measured SOT effective fields $\Delta H_{X(Y)}^{meas}$ on easy-axis out-of-plane magnetic layers from the harmonic Hall equations with equation 1.25.

For easy-axis in-plane magnetic layers, the field is applied to the film normal $\theta_H$ = 0° for the baseline $V_\omega$ measurements, and off-normal at $\theta_H$ = 9° for the $V_\omega$ and $V_{2\omega}$ measurements to induce planar and anomalous Hall signals. The observed $V_{2\omega}$ scales with $\theta_H$, so to increase the signal, yet still apply $H$ near to the film perpendicular, we choose $\theta_H$ = 9° similar to [130]. The second harmonic Hall voltage $V_{2\omega}$ measured at $\theta_H$ = 9° is fit to equation 1.27 to extract the field- and damping-like SOT effective fields $\Delta H_{Z(Y)}^{meas}$. Within equation 1.27, the equilibrium magnetisation angle from the normal of the sample $\theta_0$ is a function of $H$ and is evaluated as

$$\theta_0 = \cos^{-1}\left(\frac{V_{\omega(\theta_H=9°)}}{V_{AHE}}\right). \tag{6.2}$$

To ascertain the true SOT effective fields $\Delta H_{Z(Y)}$ from those extracted with fitting equation 1.27, we subtract the non-zero contribution from the Oersted field $H_{Z(Y)}^{OF}$ owing to the current flowing through the buffer and Pt constituent layers

$$\Delta H_{Z(Y)} = \Delta H_{Z(Y)}^{meas} - H_{Z(Y)}^{OF}. \tag{6.3}$$

$H_{Z(Y)}^{OF}$ is evaluated by solving the medium range field approximation for a current-carrying strip for each conducting layer. Each underlayer's effective $H_{Z(Y)}^{OF}$ at a finite distance from the FM layer is averaged over the height of the thin film FM bar, which is treated extensively in Appendix C. Note that since we assume minimal edge effects, the Oersted field doesn't affect the damping-like torque since $H_Z^{OF}$ = 0. On both sides of the bar, the perpendicular Oersted field is equal and opposite in all positions across the bar.

## 6.3 Current-induced spin-orbit torque switching

In this section, we show preliminary experimental observations of current-induced SOT switching with the AHE in different FM bilayers. To understand the role of microstructure on SOT, we buffer Pt|FM bilayers and observe both sharp FM switching about the magnetisation easy-axis- and smooth hard-axis- like switching with no coercivity. However, to extract a meaningful quantitative correlation between microstructure morphology and SOT there must be complete, coherent switching of the magnetisation in $\pm \boldsymbol{M}_Z$. Below we fabricate and measure different device variations, comprising multiple FM materials (Co and CoFeB) at varying thickness $d_{\mathrm{FM}}$ to achieve well-defined switching across the buffered Pt|FM bilayers.

### 6.3.1 Buffered Pt|Co bilayers

Much of the preliminary work on current-induced switching of FM layers was done on thin Co films ($\sim$ 6-7 Å). Thin Pt|Co devices are especially effective because of the significant PMA, which sets a perpendicular easy-axis in thin ($d_{\mathrm{Co}} \sim$ 7 Å) Co films, allowing for coercive, sharp, current-induced switching. Figure 6.1 shows current induced switching of (buffered) ultrathin Pt|Co films.

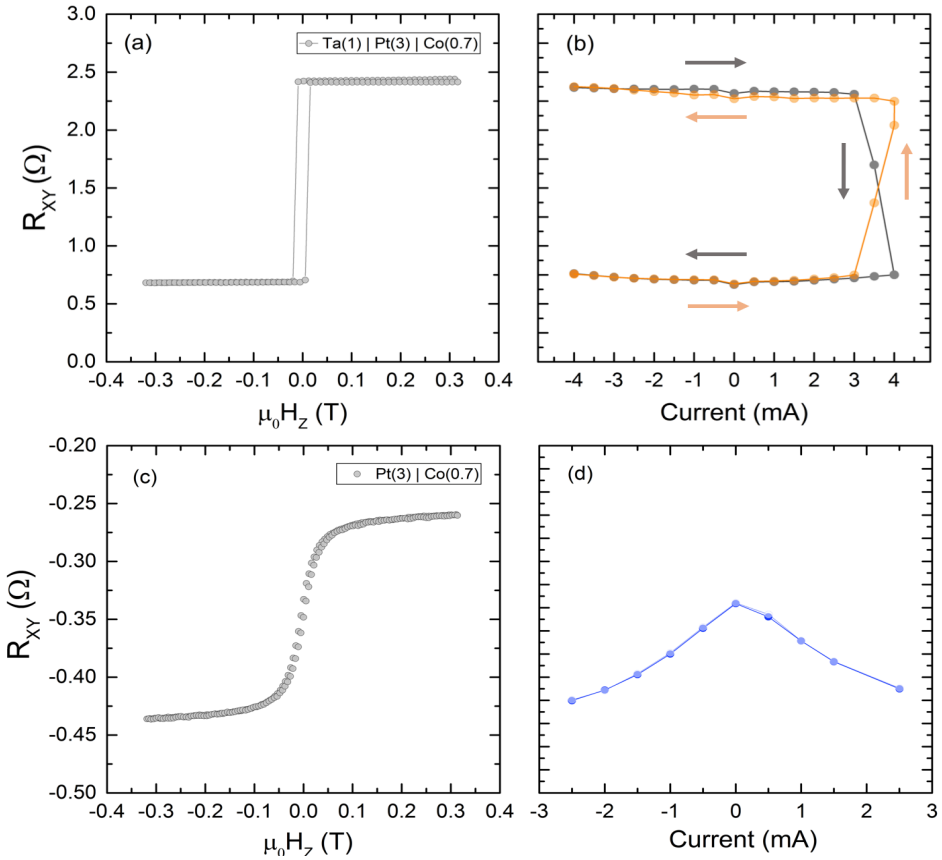


Figure 6.2 AHE resistances of a Ta(1)|Pt(3)|CoFeB(0.7) Hall bar with (a) an out-of-plane field sweep and (b) a current sweep with the Keithley Source Meter 2400. Current-induced switching of the Co layer follows the grey and orange arrows and is not reversible, but requires field-assistance to switch to $\pm \boldsymbol{M}_Z$. AHE resistances of a Pt(3)|CoFeB(0.7) Hall bar with (c) an out-of-plane field sweep and (d) a current sweep with the Keithley Source Meter 2400 with no observed current-induced switching.

Figure 6.2 (a) shows, indeed, a thin Ta(1)|Pt(3)|Co(0.7) Hall bar has an out-of-plane easy-axis $\boldsymbol{M}$ behaviour measured by $R_{XY}$ from the AHE, which allows for us to demonstrate sharp field-assisted switching from $\pm\boldsymbol{M}_Z$ in (b). However, it was not possible to switch $\boldsymbol{M}_Z$ in both directions at the applicable current densities ($\boldsymbol{j}_{c,\mathrm{HM}} < 10^{10}$ A/m$^2$), which would be observed as a closed loop at negative $\boldsymbol{j}_{c,x}$. This may be largely explained by the stronger uniaxial anisotropy in Co than in CoFeB, the magnitude of which is determined by the Pt|Co interaction near the interface. Since the $\boldsymbol{j}_{c,\mathrm{HM}}$ required to reserve a perpendicularly magnetised FM film is proportional to $\boldsymbol{M}_s\boldsymbol{H}_{k,\mathrm{eff}}$ from equation 6.1 and $\boldsymbol{H}_{k,\mathrm{eff}} = \frac{2\boldsymbol{K}_\perp}{\boldsymbol{M}_s}$, switching Co films with higher $\boldsymbol{K}_\perp$ are particularly difficult. Instead, figure 6.1 (b) shows good switching with an assisting field in $\boldsymbol{H}_Z$[6] from the misalignment of the symmetry-breaking field $\boldsymbol{H}_X$. Starting with $+\boldsymbol{M}_Z$ (represented by the grey data points), at $\mu_0\boldsymbol{H}_X = -1.1$ kG we observe the magnetisation flip to $-\boldsymbol{M}_Z$ with field-assistance at positive $\boldsymbol{j}_{c,x}$. Similarly, when the magnetisation is set to $-\boldsymbol{M}_Z$ and a positive $\mu_0\boldsymbol{H} = 1.1$ kG is applied (represented by the orange data points), the magnetisation is flipped to $+\boldsymbol{M}_Z$ with an applied current. This is in agreement with recent work that shows CIS without field-assisted switching in Pt|Co bilayers requires much larger current densities [237].

To work towards a complete buffered series we then fabricate and measure a Pt(3)|Co(0.7) Hall bar. Without the Ta buffer, the reduced Pt(111) texture significantly decreases PMA and $\boldsymbol{H}_K^\perp$. Figure 6.2 (c) shows the unbuffered bilayer no longer has an easy-axis out-of-plane at the same $d_{Co} \sim 7$ Å as the Ta-buffered device in (a). The strong rounding and lack of sharp coercive switching in $R_{XY}$ suggests the unbuffered device is easy-axis in-plane, but close to the SRT. In figure 6.2 (d), it is apparent that fully switching $\pm\boldsymbol{M}_Z$ is no longer possible with the applied current and a 0.7 nm Co layer cannot be used as the absorbing FM layer. Thinner Co layers would aid the perpendicular magnetisation, however, the microstructure of the Co changes here. At $d_{Co} \sim 5$ Å, the FM layer begins to lose continuity and the PMA is reduced further from increased quenching of the in-plane Co electronic orbitals. It can thereby be concluded that the typical Pt|Co bilayer was not suitable to observe full SOT switching across the buffer range.

### 6.3.2 Buffered Pt|CoFeB bilayers

The Pt|CoFeB bilayer is superior for SOT CIS than that of Pt|Co in multiple respects. Firstly, it is the identical HM|FM bilayer structure studied in chapters 4-5, such that there is no change in electrical or spin properties of the FM between measurement schemes. This allows for a direct comparison to spin pumping and SHMR measurements. Secondly,

[6] The precise evaluation of the magnitude of $\boldsymbol{H}_Z$ is non-trivial as it arises from a slight misalignment of the unidirectiontional symmetry-breaking field $\boldsymbol{H}_X$. This makes precise quantification of the SOT effective fields from CIS [125,245] in this system challenging.

$H_{k,CoFeB}$ is much lower than that of Co, requiring less SOT to reverse the magnetisation. Finally, the CoFeB layer is an order of magnitude more resistive than that of Co ($\rho_{CoFeB} \sim 133$ μΩ cm as opposed to Co $\rho_{CoFeB} \sim 17$ μΩ cm), which prevents current shunting and drives $\boldsymbol{j}_{c,x}$ to the Pt(3) underlayer, enhancing SOT.

We fabricate a Ta(1)|Pt(3)|CoFeB(0.7) Hall bar with ultrathin CoFeB, for the same arguments as above. However, the structural composition of deposited $Co_{60}Fe_{20}B_{20}$ is only 60% Co. It is important to remember that since the PMA arises in large part through the hybridisation of the large SOC in Pt 5*d* orbital with the 3*d* orbital in the Co at the interface, a significant of the PMA will be lost in the CoFeB system in comparison to the Co system at an equivalent FM thickness. In figure 6.3 (a), the AHE $R_{XY}$ signal at equivalent $d_{FM} \sim 7$ Å shows a device, which is easy-axis in-plane. However, the rounding at low applied fields between magnetic saturation states is indicative of a sample close to the SRT. The more rounded behaviour in the Pt|CoFeB device than the Pt|Co device from figure 6.2 (a), which showed a sharper transition between $\pm M_Z$, explained by the reduction of PMA and so $H_K^{\perp}$ in the Pt|CoFeB film.

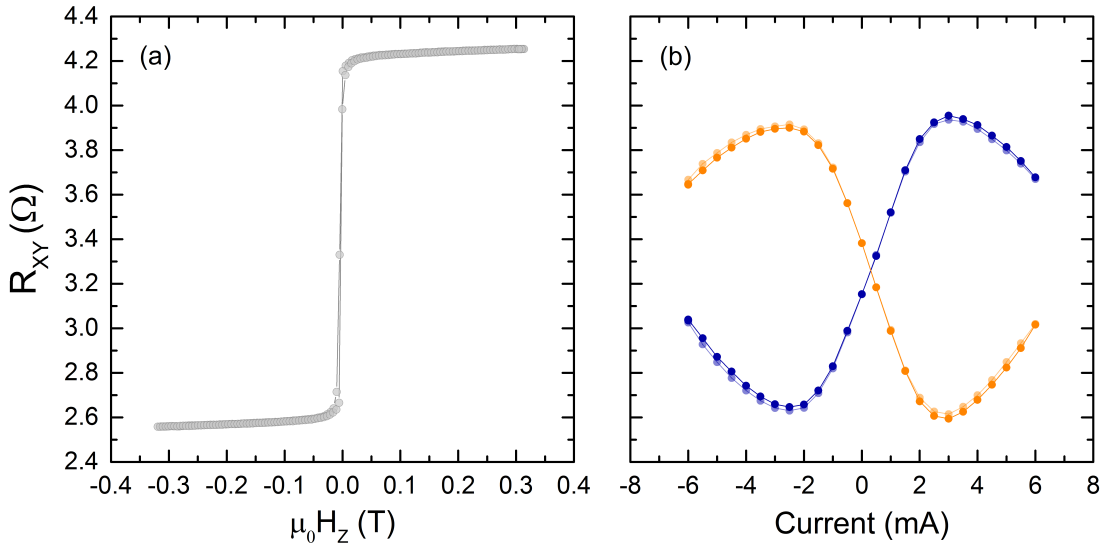


**Figure 6.3** AHE resistances of a Ta(1)|Pt(3)|CoFeB(0.7) Hall bar. (a) Out-of-plane field sweep showing full $R_{AHE}$ magnetisation switching. (b) Current-induced switching of the CoFeB magnetisation observed with $R_{AHE}$ symmetrically about the applied current of the Keithley Source Meter 2400. A symmetry-breaking field $\pm\mu_0 H_X$ = 2 kG is applied to give the blue(orange) magnetoresistance curves.

In figure 6.3 (b), the orange and blue points represent the AHE $R_{XY}$ signal evaluated at a symmetry-breaking field $\pm\mu_0 H_X \sim 2$ kG, respectively. The observed behaviour is in agreement with recent literature [238] for a bilayer with negligible coercivity. The lighter orange and blue points depict the $\boldsymbol{j}_{c,x}$ retrace, demonstrating that full switching can be accomplished without field assistance – unlike in the case of the Co|Pt bilayer – due to the reduced $M_{s,CoFeB}$. Note, $\boldsymbol{M}$ is pulled slightly in-plane by the symmetry-breaking field $H_X$ such that the AHE $R_{XY}$ signal of the current sweep is not expected to match fully that of the AHE $H_Z$ field sweep.

Here, the trace and retrace of $\boldsymbol{j}_{c,x}$ lie on top of one another due to the lack of coercivity in the sample and shows smooth, rounded switching across the applied current magnitudes. These results are unlike the coercive easy-axis out of plane bilayers which are often observed in literature to show sharp switching and hysteretic behaviour with respect to the applied current [123,237]. Again, this is explained by the fact that this Pt|CoFeB bilayer has reduced PMA and so is closer to the SRT, which promotes less-sharp switching behaviour than observed for the Pt|Co bilayer in figure 6.2 (b).

Again, to compare SOT in a complete series of (un)buffered Pt(3)|CoFeB(0.7) devices, we fabricate and measure an unbuffered Pt(3)|CoFeB(0.7) bilayer. However, the inherently low PMA induced at the Pt|CoFeB interface is only further reduced when removing the Ta buffer layer, which results in an easy-axis in-plane FM layer; this is not suitable for CIS switching measurements. Thinner $d_{\mathrm{CoFeB}} \sim 5$ Å devices were measured only to find similar growth issues arising as the Co case and so do not tend to favour interfacial PMA and out-of-plane magnetised films. Therefore, although we successfully demonstrate current-induced switching from SOT in both Pt|Co and Pt|CoFeB bilayers, the changes in anisotropy of the film due to altering the Pt(111) texture with buffers make it challenging to fabricate a self-consistent series of perpendicularly magnetised (un)buffered Pt|FM bilayers. Instead, we switch to low-current, harmonic Hall measurements, which no longer require magnetisation reversal. These experiments are more common for accurately extracting the magnitude of SOT effective fields and allow us to evaluate spin current absorption in the FM at different buffer conditions.

## 6.4 Harmonic Hall spin-orbit torque measurements in buffered Pt|CoFeB bilayers

In this section, we highlight experimental findings of the low-current, lock-in techniques to relate planar Hall and anomalous Hall effects to SOT effective fields in HM bilayers. To correlate HM microstructure to SOT fields, we mimic the (un)buffered Pt(3)|CoFeB bilayer systems explored in detail chapters 3-5. At $t \sim 3$ nm, the entire HM layer is effective at generating SOT to maximise the effective fields. First and second harmonic Hall voltages are measured for both in-plane and perpendicular-to-plane systems, depending on $d_{\mathrm{CoFeB}}$, to elucidate the dominant scattering mechanism. We compare the SOT effective fields within complete sets of (un)buffered bilayers at fixed $d_{\mathrm{CoFeB}}$, and discuss preliminary findings suggesting a dependence of SOT efficiency on $d_{\mathrm{CoFeB}}$. To facilitate the comparison between measurements, we depict Ta-, Ru- and (un) buffered Pt|CoFeB bilayer fits with their respective colour schemes as in chapters 3-5.

### 6.4.1 SOT effective field measurements on perpendicular, thin Pt|CoFeB bilayers

To extract the damping-like torque $\Delta H_X$ and field-like torque $\Delta H_Y$ from harmonic Hall voltages in a perpendicularly magnetised Pt|CoFeB bilayer, we first quantify 1st harmonic planar Hall voltage $V_{PHE}$ and anomalous Hall voltage $V_{AHE}$. Instead of measuring a change in the anomalous and planar Hall resistances, changes in voltage are measured as outlined in equation 1.24. In this way, we can accurately evaluate the Hall contributions without knowing the precise resistivity of CoFeB when applying a fixed voltage across the Hall bar.

In figure 6.4 (a), we rotate the electromagnet at $\mu_0 H$ = 5 kG about $\phi$ to measure the PHE on a Ta(1)|Pt(3)|CoFeB(1) device. A purely PHE follows $\sin 2\phi_H$ and $V_{PHE}$ is extracted from the amplitude of the sinusoidal fit. In figure 6.4 (b), a field normal to the sample plane $H_Z$ ($\theta_H$ = 0°) is swept to determine $V_{AHE}$, which is one half the voltage difference between $\pm M_Z$. Note, small background offsets voltages have been subtracted from figure 6.4 (a-b).

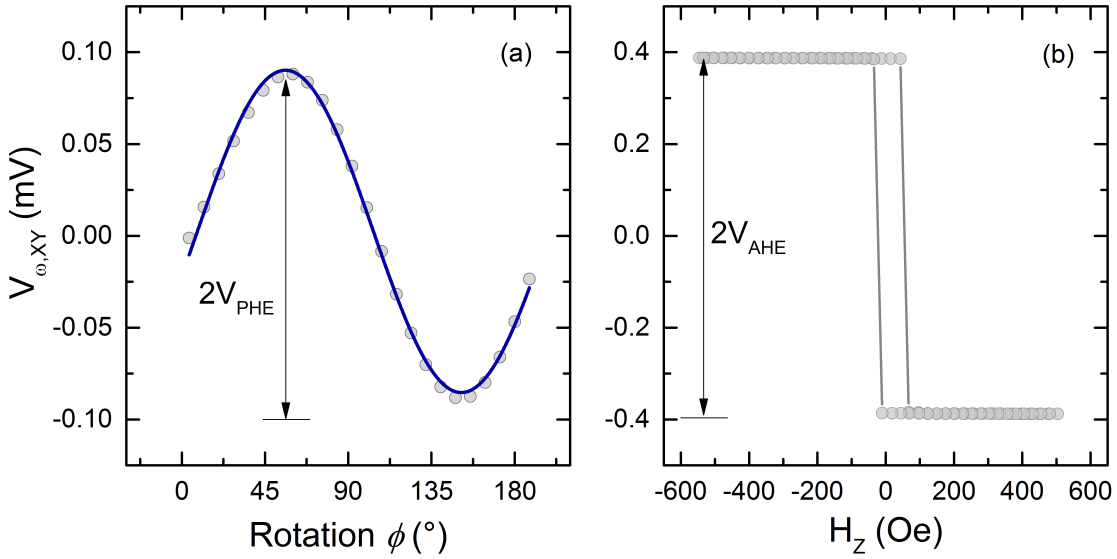


**Figure 6.4 (a) First harmonic PHE voltage measurement by rotating $\phi$ in the plane of the sample. (b). First harmonic AHE voltage measurement by sweeping the field perpendicular-to-plane ($\theta_H$ = 0°).**

The SOT effective fields are elucidated from a series of 1st and 2nd harmonic Hall voltage measurements shown in figure 6.5 (a-d). The film magnetisation is initially set in the $\pm M_Z$ before data acquisition, which denoted by the grey and blue data points, respectively. According to equation 1.25, $\Delta H_{X(Y)}$ is calculated from the derivative of the 2nd harmonic and the second derivative of the 1st harmonic Hall voltages. The $V_{2\omega}$ for both an $H_X$ and $H_Y$ shown in panels (a-b) are fit with linear equations to evaluate the magnitude of $\frac{\partial V_{2\omega}}{\partial H}$, while $V_\omega$ measured in panels (c-d) are fit with parabolae to evaluate $\frac{\partial^2 V_\omega}{\partial H^2}$. In figure 6.5 (c), the system is approaching the noise floor determined by $R_{XX}$ of the sample, yet the signal sizes at 10s of nV are still discernible enough to acquire a linear fit. For a longitudinal field, we

observe the slopes of $V_{2\omega}$ versus $H_X$ are the same for both $\pm M_Z$ in panel (a), while for transverse fields $H_Y$ in panel (c), there is a sign reversal. Panels (b) and (d) show $M$ slightly pulled into the plane for small applied fields, denoted by the $V_\omega$ rocking about $H$ = 0. The behaviour of the 1st and 2nd harmonic Hall voltages displayed in figure 6.5 are indentical to other HM|CoFeB bilayers measured in literature [239].

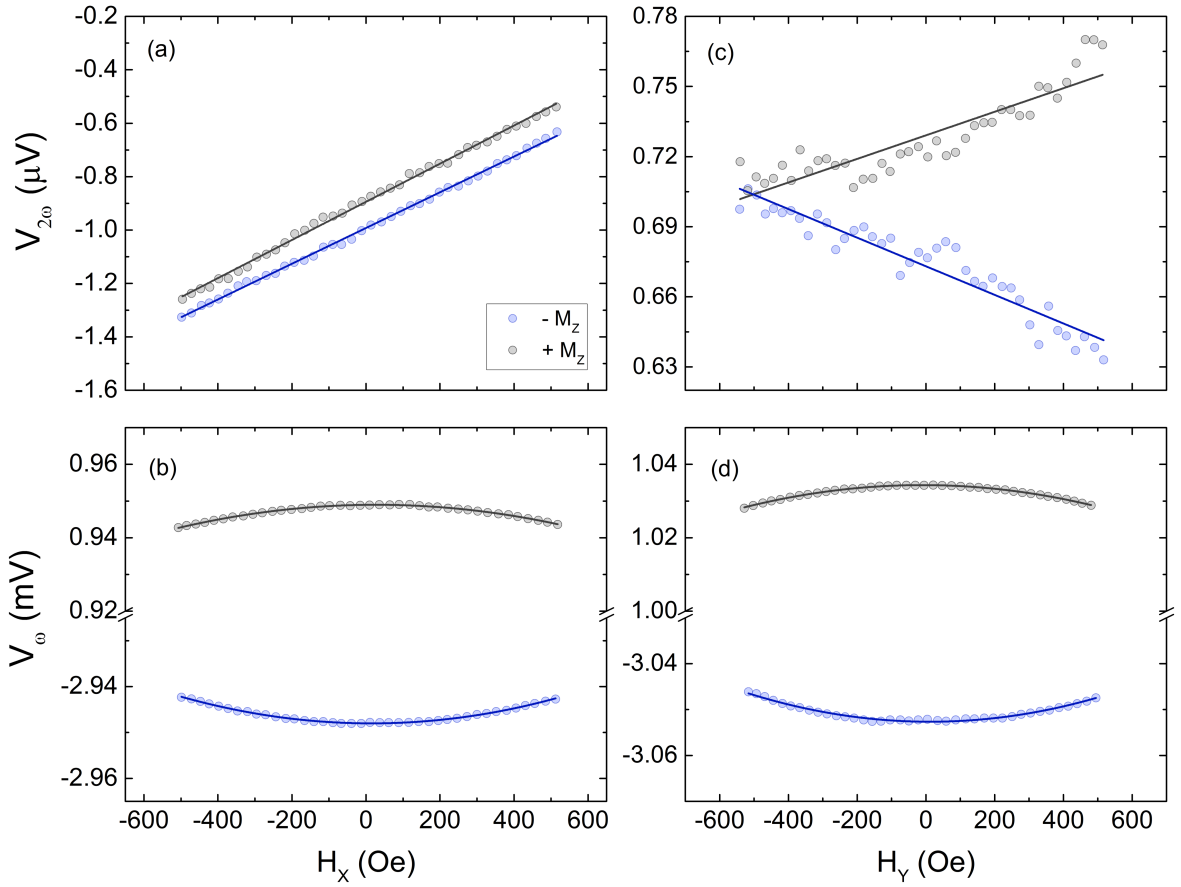


Figure 6.5 Transverse harmonic Hall voltages showing variation in field in an out-of-plane Ta(1)|Pt(3)|CoFeB(1) Hall bar. (a,c) 90° out-of-phase $V_{2\omega}$ voltages and (b,d) in-phase $V_\omega$ voltages measured with an applied $H_X$ and $H_Y$, respectively. The magnetisation is set prior to the experiment in the up (grey) state or the down (blue) state.

Table 6.1 Derivatives of harmonic hall voltages on a Ta(1)|Pt(3)|CoFeB(1) Hall bar for each magnetisation state $M_Z$ and the resultant damping-like ($\Delta H_X$) and field-like ($\Delta H_Y$) effective fields.

| Magnetisation State | Field Direction | $\frac{\partial V_{2\omega}}{\partial H} \times 10^{-11}$ (V/Oe) | $\frac{\partial^2 V_\omega}{\partial H^2} \times 10^{-11}$ (V/Oe$^2$) | $\Delta H_X$ (Oe) | $\Delta H_Y$ (Oe) |
|---|---|---|---|---|---|
| $+M_Z$ | $H_X$ | $71.2 \pm 0.6$ | $-2.0 \pm 0.1$ | $84 \pm 4$ | $43 \pm 2$ |
| | $H_Y$ | $5.4 \pm 0.4$ | $-2.3 \pm 0.1$ | | |
| $-M_Z$ | $H_X$ | $66.9 \pm 0.4$ | $2.2 \pm 0.1$ | $-80 \pm 4$ | $42 \pm 2$ |
| | $H_Y$ | $-6.1 \pm 0.3$ | $2.2 \pm 0.1$ | | |

Table 6.1 illustrates the estimated parameters from the harmonic hall measurements performed in Figure 6.5 used in order to quantify the damping-like torque $\Delta H_X$ exerted on the FM by the spin current generated in the Pt underlayer. $\Delta H_X$ can be evaluated with either $\pm M_Z$. Because $\Delta H_X$ depends on the direction of $M_Z$, we must invert the sign of the damping-like SOT for $-M_Z$ to exclude this effect, which is aligned with recent work [47,233]. We then take the average value. The uncertainty displayed in table 6.1 represents a systematic error arising from an inability to perfectly align the device at $\phi_H$ = 0°, 90° with sample placement on-chip and in $\theta_H$ = 90° with the rotation of the electromagnet. From fitting misaligned samples, this error is estimated as 5% and is added in quadrature to the standard measurement error between $\Delta H_X$ extracted at $\pm M_Z$ to arrive at $\Delta H_X$ = -82 $\pm$ 5 Oe. Note, here the Oersted field from the AC $\boldsymbol{j}_{c,x}$ flowing through the Pt underlayer does not affect the measured damping-like component. This damping-like SOT effective field magnitude agrees well with recent work done by Pai *et al*. in similar Pt|CoFeB bilayers with additional PMA from capping $AlO_X$ layer [124].

### 6.4.2 SOT effective field measurements on in-plane, thin Pt|CoFeB bilayers

When $d_{CoFeB}$ = 1.1 nm, the unbuffered and Ru-buffered Pt|CoFeB bilayers have insufficient PMA to remain easy-axis perpendicular-to-plane due to the suppression of Pt(111) texture. To complete the SOT effective field measurements on the series of thin, in-plane CoFeB (un)buffered bilayers, we follow the technique recently developed in [130] and outlined in section 1.2.3 to extract the damping-like SOT efficiency for easy-axis in-plane samples. To extract the damping-like torque $\Delta H_Z$ and field-like torque $\Delta H_Y$ in an easy-axis in-plane magnetised system, we again first quantify 1$^{st}$ harmonic $V_{PHE}$ and $V_{AHE}$ to attribute the observed change in $V_{XY}$ to slight variations in $\boldsymbol{M}$ from SOT. In this light, $V_\omega$ is measured in and out of the sample plane in figure 6.6. Note, small background offset voltages have been subtracted here.

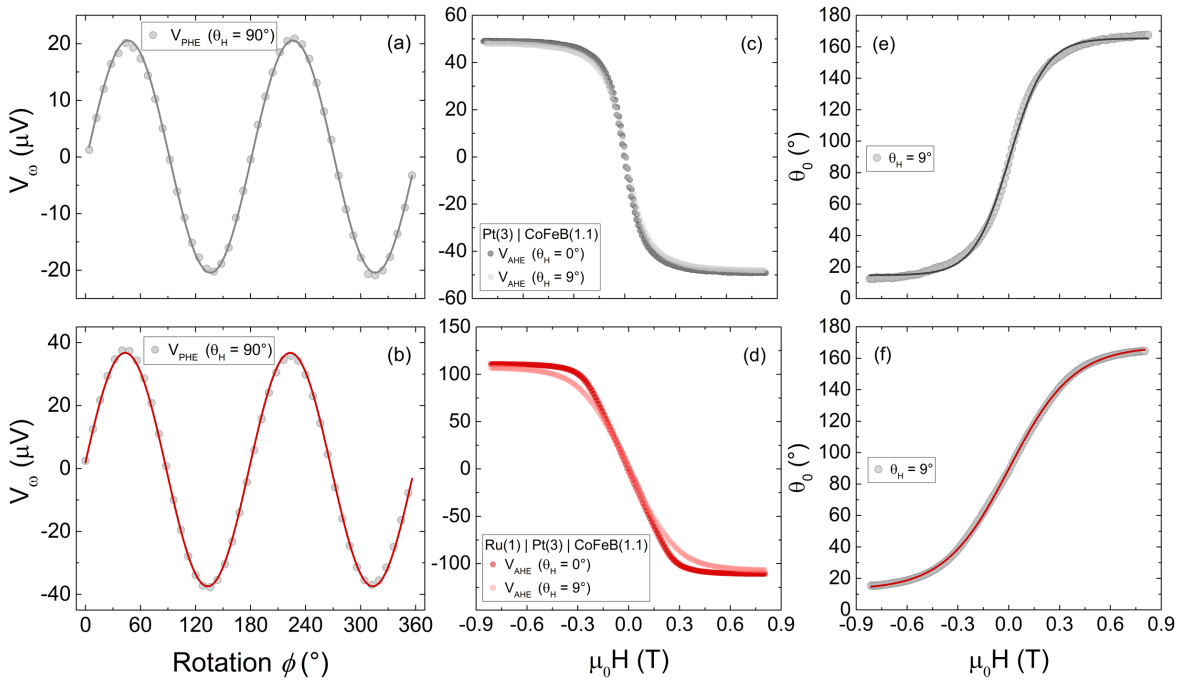


Figure 6.6 First harmonic (a,b) PHE voltage measurements by rotating $\phi$ in the plane of the sample and (c,d) AHE voltage measurements by sweeping the field perpendicular-to-plane (darker data points at $\theta_H$ = 0°) and slightly off perpendicular (lighter data points at $\theta_H$ = 9°) at $V_{app}$ = 0.5 V. (e,f) The equilibrium magnetisation angle $\theta_o$ plotted as a function of $\boldsymbol{H}$ and fit to a Boltzmann-type function.

In panels (a-b) we rotate the electromagnet about $\phi$ to measure the PHE on an unbuffered and Ru-buffered Pt(3)|CoFeB(1.1). To minimise any AHE component from slight sample holder misalignment a small field $\boldsymbol{H}$ = 100 Oe is applied. With negligible in-plane anisotropy $H_K^- \sim 0$ confirmed by magneto-optical Kerr measurements, the $\boldsymbol{M}$ is saturated and still pulled completely by the small $\boldsymbol{H}$. A purely PHE follows $\sin 2\phi_H$ and $V_{PHE}$ is extracted from the amplitude of the sinusoidal fit for both devices. In figure 6.6 (c-d), a field normal to the sample plane $\boldsymbol{H}_Z$ ($\theta_H$ = 0°) is swept to determine the $V_{AHE}$ of the unbuffered and Ru-buffered bilayers, respectively. Small spurious OHE components (typically on the order of $10^{-9}$ V/Oe) of $V_{XY}$, antisymmetric about $\boldsymbol{H}$ = 0, have been removed to observe $\boldsymbol{M}$ saturation correctly. The $V_{XY}$ from the AHE loops of the in-plane samples exhibits hard-axis behaviour, as expected. The Ru-buffered sample in panel (d) saturates at higher field values than the unbuffered samples in panel (c), which is indicative of more hard-axis-like behaviour without the Pt(111) texturing promoting PMA. From panels (c-d) the $H_K^\perp$ is extracted by finding the intercept of two straight lines drawn between either of the $\pm M_Z$ saturation plateaus and the linear portion of the low-field $V_{XY}$ behaviour.

We then rotate the sample off-normal to $\theta_H$ = 9° and obtain the $V_{XY}$ response (depicted by the lighter data points in panels (c-d)) in preparation for the SOT effective field measurements. The $V_{XY}$ at $\theta_H$ = 9° is always smaller than that at the film normal ($\theta_H$ = 0°) due to a small in-plane component of $\boldsymbol{M}$. The equilibrium magnetisation angle from the normal of the sample plane $\theta_o$ in the SOT measurement is extracted from fitting $V_{XY}$ at $\theta_H$ = 9° to equation 6.2. Figures 6.6 (e-f) show $\theta_o$ of the unbuffered and Ru-buffered bilayers, respectively. The equilibrium magnetisation is fit to a Boltzmann-type function to obtain $\theta_o(H)$ – an essential component when fitting the $V_{2\omega}$ to extract SOT effective field values.

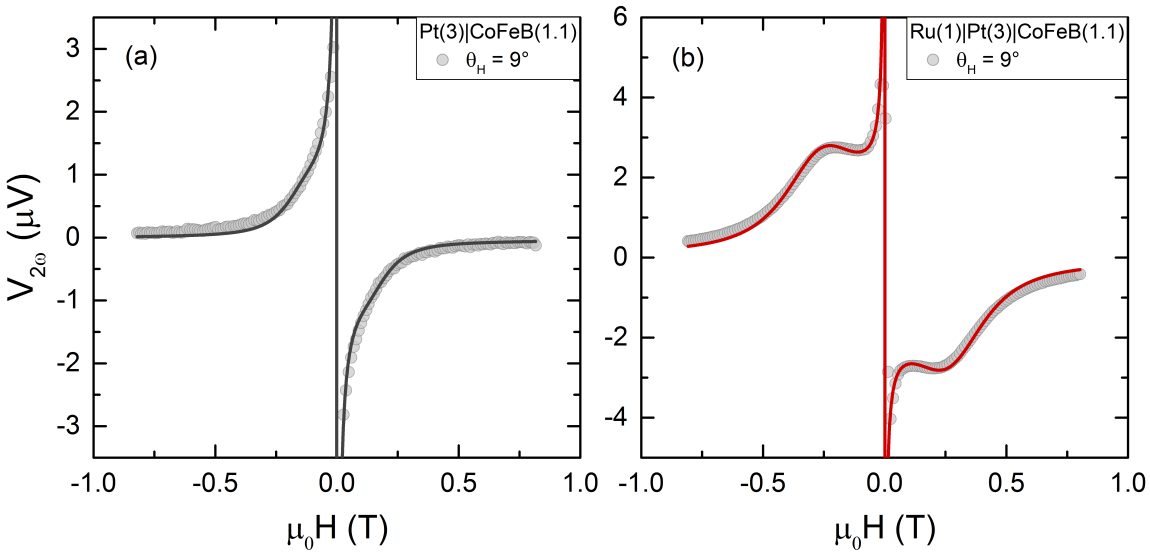


Figure 6.7 The out-of-phase component (90°) second harmonic Hall voltages at $\theta_H$ = 9° and $V_{app}$ = 4 V fit by equation 1.27 to extract $a_j$ and $b_j$.

Figure 6.7 (a-b) shows the out-of-phase component (90°) of $V_{2\omega}$ at $\theta_H$ = 9° for the unbuffered and Ru-buffered Pt(3)|CoFeB(1.1) bilayers, respectively. Note small background offset voltages have been subtracted here. These data display similar $V_{2\omega}$ behaviour at $\theta_H$ = 9° as [130] for in-plane magnetised samples. The medium-to-high field saturation is predominately set by $\Delta H_Z$ and $V_{AHE}$, while about $H$ = 0, $\Delta H_Y$ and $V_{PHE}$ dominate $V_{2\omega}$. The position of the shoulder in panel (b) is set by $H_K^{\perp}$ extracted from $V_{AHE}$ at $\theta_H$ = 0° and the height is set by the size of damping-like torque. The experimental data are fit to equation 1.27 with a two-parameter fit for $a_j$ and $b_j$. To extract the field-like and damping-like torque, we set $V_{XY} = I_c R_{XY}$ and $(\Delta H_Y, \Delta H_Z) = (b_j, a_j \sin\theta_0 \cos\phi_H)$ at $\theta_0 \sim 0°$. Note that a piecewise function is used for fitting since it is not appropriate to substitute negative field values into equation 1.27. Instead, we change $\theta_0, \theta_H, \phi_H$ to $\pi - \theta_0, \pi - \theta_H, \pi + \phi_H$, respectively, at $H$ < 0 [130].

Table 6.2 Measured damping-like ($\Delta H_Z^{meas}$) and field-like ($\Delta H_Y^{meas}$) effective fields from fitting Figure 6.6 second harmonic Hall voltage data to equation 1.27. The Oersted field $H_Y^{OF}$ is subtracted from the field-like component to give the SOT effective fields $\Delta H_Z$ and $\Delta H_Y$.

| Stack Structure | $\Delta H_Z^{meas}$ (Oe) | $\Delta H_Y^{meas}$ (Oe) | $H_Z^{OF}$ (Oe) | $H_Y^{OF}$ (Oe) | $\Delta H_Z$ (Oe) | $\Delta H_Y$ (Oe) |
|---|---|---|---|---|---|---|
| Pt(3)\|CoFeB(1.1) | -34 $\pm$ 2 | 4.7 $\pm$ 0.5 | 0 | -1.6 | -34 $\pm$ 2 | 6.3 $\pm$ 0.7 |
| Ru(1)\| Pt(3)\|CoFeB(1.1) | -101 $\pm$ 5 | 1.9 $\pm$ 0.2 | 0 | -2.9 | -101 $\pm$ 5 | 4.8 $\pm$ 0.5 |

SOT efficiencies extracted from the fits $\Delta H_{Z(Y)}^{meas}$ in figure 6.6 (a-b) are compiled in Table 6.2. Torques arising from the Oersted field via current driven through the Pt(3) underlayer and Ru-buffer layer is evaluated in Appendix C and subtracted from $\Delta H_{Z(Y)}^{meas}$ to get the tabulated effective SOT fields $\Delta H_{Z(Y)}$. With minimal edge effects, the Oersted field does not affect the damping-like torque since $H_Z^{OF} = 0$. In table 6.2, we demonstrate there is nearly three times as much damping-like torque in the Ru-buffered device as the unbuffered one. The magnitude of the damping-like effective field in an unbuffered Pt|CoFeB is in good agreement with that quoted in [130] for similar $\boldsymbol{j}_{c,x}$ in the HM layer. Additionally, $\Delta H_Y \ll \Delta H_Z$ for both samples with approximately an order of magnitude less effective field for the unbuffered stack and approximately two orders of magnitude less field for the Ru-buffered stack, respectively.

The tabulated error in these SOT measurements comprises the aformentioned systematic loading error of approximately 5% (estimated from fitting misaligned samples) added in quadrature to the fitting error of well-aligned samples. The field-like fitting error is notably high in compared to that of the damping-like error. The fit error does not account for deviation in $\theta_0$ from a Boltzmann, and as a result, the total error may well be larger than we estimate here. Since the $H_Y^{OF}$ is of the same order as $\Delta H_Y^{meas}$, it would be challenging to draw any convincing conclusions from the field-like torque. We focus on the damping-like SOT for comparison between samples in the following analyses for the remainder of this chapter.

### 6.4.3 Comparing SOT in thin Pt|CoFeB bilayers with different easy axes

To compare SOT effective fields in thin HM bilayers layers we consolidate the effective damping-like fields from table 6.1 and table 6.2 for the perpendicular Ta(1)|Pt(3)|CoFeB(1) and the in-plane Pt(3)|CoFeB(1.1) and Ru(1)|Pt(3)|CoFeB(1.1) devices. The CoFeB thickness of the Ta-buffered bilayer is reduced by 1 Å in $d_{CoFeB}$ to ensure good perpendicular magnetic behaviour. Table 6.3 illustrates the effective SOT damping-like torque $\Delta H_{DL}$ magnitudes for the perpendicular bilayer ($\Delta H_X$) and the in-plane bilayers ($\Delta H_Z$).

Table 6.3 Pt resistivity for each (un)buffered Pt|CoFeB bilayer highlighting the difference in current density within the Pt layer driving SOT with the effective fields and the normalised SOT damping-like effective field.

| Stack Structure | $\rho_{Pt}$ (μΩ cm) | $\lvert\Delta H_{DL}\rvert$ (Oe) | $\lvert\Delta H_{DL}\rvert / j_{c,Pt}$ (x $10^{-10}$) (Oe $A^{-1}$ $m^2$) |
|---|---|---|---|
| Pt(3)\|CoFeB(1.1) | 54 | $34 \pm 2$ | $4.1 \pm 0.4$ |
| Ru(1)\|Pt(3)\|CoFeB(1.1) | 32.4 | $101 \pm 5$ | $7.3 \pm 0.6$ |
| Ta(1)\|Pt(3)\|CoFeB(1) | 31 | $82 \pm 5$ | $5.6 \pm 0.5$ |

In Table 6.3 we observe a significant enhancement of the $\Delta H_{DL}$ in the buffered HM bilayers. The Ru-buffered bilayer shows a 3-fold increase, while that of Ta shows approximately 2.5 times the damping-like torque exerted on the CoFeB when compared to an unbuffered device. However, a better comparison between effective torques accounts for the change in microstructure morphology (and thereby conduction properties) of the Pt underlayer [124]. In Table 6.3, experimentally measured $\rho_{Pt}$ at $t$ = 3 nm are displayed to highlight the drastic increase in unbuffered Pt. In devices with larger $\rho_{Pt}$, $j_{c,Pt}$ is reduced at fixed applied voltages, which drives a smaller $j_s^{Pt|CoFeB}$ across the interface and, in turn, a smaller damping-like effective field is expected. Thereby, we compare the current-normalised damping-like effective field $\frac{\Delta H_{DL}}{j_{c,Pt}}$ instead. The error is displayed in table 6.3 is evaluated by adding the SOT effective field error to an error of the measured resistivity 6.5% in quadrature. The measurement error might well be larger than our estimation, which makes it difficult to state conclusively there is a difference in $\frac{\Delta H_{DL}}{j_{c,Pt}}$ across the (un)buffered bilayers.

While there is an observed variation in $\frac{\Delta H_{DL}}{j_{c,Pt}}$ at with different buffer layers, the trend is weak in comparison to the changes in $\frac{\Delta R_{XX}^{SHMR}}{R_{XX}^{0}}$ and $V_S$ signals in spin pumping measurements at $t$ = 3 nm displayed in chapters 4 and 5, respectively. Thereby, we conclude that there is little change in the overall SOT effective fields per unit current density in the HM. Since $\Delta H_{DL}$ directly results from $j_s^{Pt|CoFeB}$, we find that the charge-to-spin conversion efficiency is dependent on HM microstructure when the change in film resistivity is not considered. Moreover, when accounting for the change in $\rho_{Pt}$ in $\frac{\Delta H_{DL}}{j_{c,Pt}}$ we demonstrate that $\sigma_{xy}^{SH}$ is nearly constant and does not depend strongly on Pt morphology. This result is in agreement with the previous analyses of chapters 4-5, where the HM thickness-dependent SHMR and spin pumping measurements fit well to a constant $\sigma_{xy}^{SH}$. This is a strong indication that Pt is indeed dominated by intrinsic SH scattering in the moderately-dirty Pt regime.

### 6.4.4 Self-consistent SOT comparison on in-plane Pt|CoFeB bilayers

To confirm this result of a small variation in $\frac{\Delta H_{DL}}{j_{c,Pt}}$ across the thin (un)buffered Pt|CoFeB bilayers, which have a mixture of in-plane and perpendicular-to-plane magnetised CoFeB, we fabricate a series of samples with thicker CoFeB. At $d_{CoFeB}$ = 1.6 nm, all of the (un)buffered Pt(3)|CoFeB(1.6) bilayers have an in-plane easy-axis, which allows for a direct self-consistent comparison of the SOT effective fields. We repeat the methodology for the low-current, lock-in technique developed in [130], and used previously the previous section, to first characterise planar and anomalous Hall voltages $V_\omega$ of each thicker CoFeB bilayer.

Measured $V_\omega$ are shown in figure 6.8 (a-f) and used to extract the planar and anomalous Hall voltages as outlined in Figure 6.6, previously. Note, small background offset voltages have been subtracted here. In panels (a-c) the electromagnet is rotated about $\phi$ at $H$ = 100 Oe to extract the $V_{PHE}$, while the $V_{AHE}$ is extracted from the out-of-plane field sweep ($\theta_H$ = 0°) in panels (d-f). Similar to the thin, in-plane CoFeB samples, small spurious OHE components on the order of $10^{-9}$ V/Oe have been removed from measured $V_{XY}$ to correctly determine $M$ saturation. The $V_{XY}$ follows hard-axis-like behaviour at $\theta_H$ = 0° with varying degrees of PMA present depending on the buffer as expected. The slope of the straight line at low fields – representative of hard-axis-like switching – decreases from Ta- to Ru- to un-buffered bilayers, as the PMA and $H_K^\perp$ is reduced from decreasing Pt(111) texturing.

Again, we rotate the sample off-normal to $\theta_H$ = 9° to obtain the AHE response as depicted by the lighter data points in panels (d-f) so that the equilibrium magnetisation angle $\theta_0$ may be extracted from equation 6.2. Panels (g-i) show $\theta_0$ of the buffered bilayers, each fit to a Boltzmann-type function to obtain $\theta_0(H)$ used subsequently in equation 1.27 when fitting $V_{2\omega}$ SOT data.

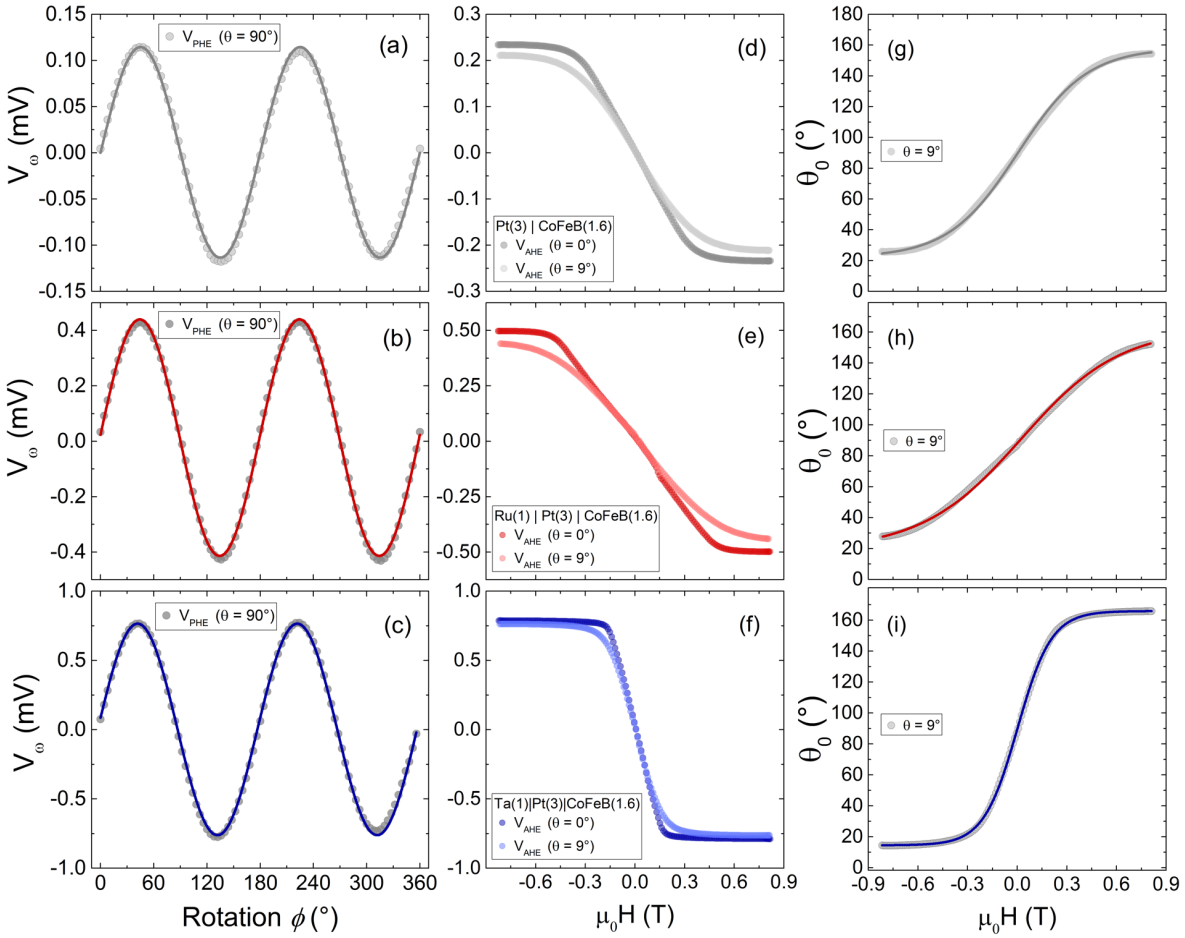


Figure 6.8 First harmonic (a-c) PHE voltage measurements by rotating $\phi$ in the plane of the sample and (d-f) AHE voltage measurements by sweeping the field perpendicular-to-plane (darker data points at $\theta_H$ = 0°) and slightly off perpendicular (lighter data points at $\theta_H$ = 9°) at $V_{app}$ = 1.5 V. (g-i) The equilibrium magnetisation angle $\theta_o$ plotted as a function of $\boldsymbol{H}$ and fit to a Boltzmann-type function.

Figure 6.9 (a-c) shows the out-of-phase component (90°) of $V_{2\omega}$ at $\theta_H$ = 9° for the unbuffered, Ru-buffered and Ta-buffered Pt(3)|CoFeB(1.6) bilayers, respectively. Note small background offset voltages have been subtracted here. Again, the $V_{2\omega}$ is fit to equation 1.27 with a piecewise function where we set $\theta_0$, $\theta_H$, $\phi_H$ to $\pi - \theta_0$, $\pi - \theta_H$, $\pi + \phi_H$, respectively, at $H <$ 0 [130] to extract the SOT effective fields $\Delta H_{Z(Y)}^{meas}$ compiled in Table 6.4.

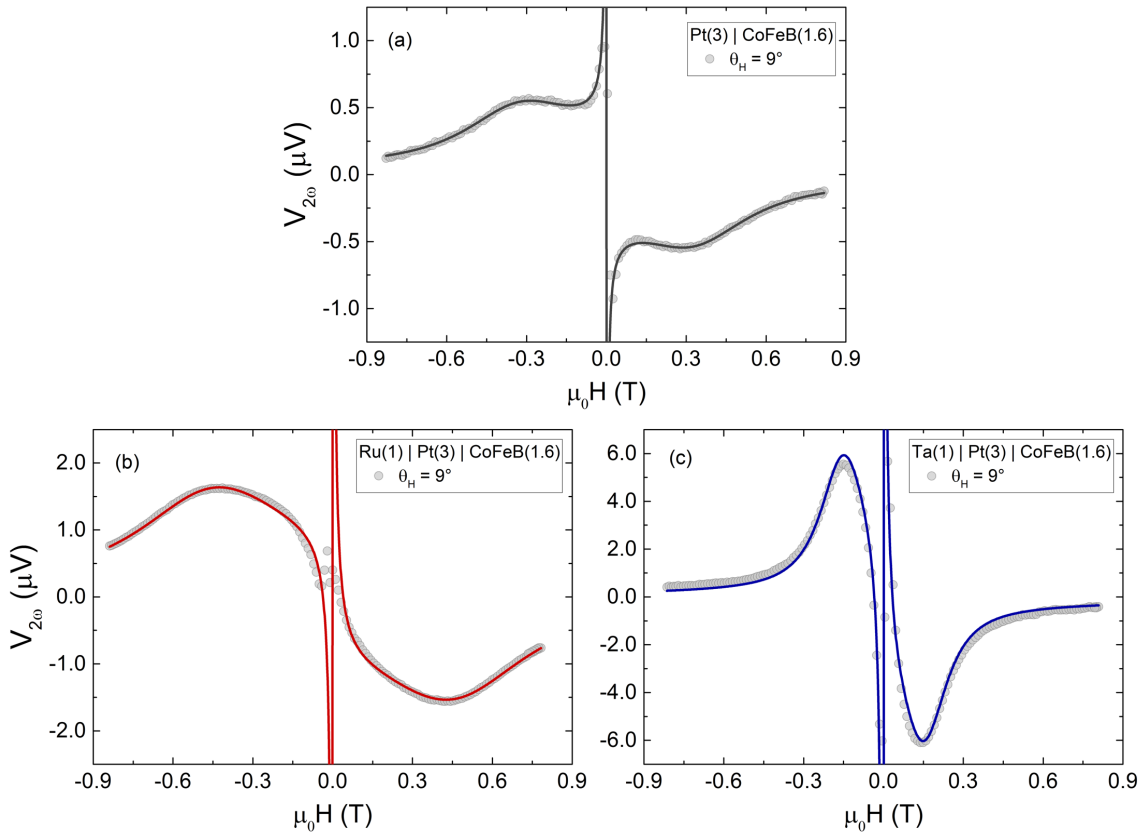


Figure 6.9 The out-of-phase component (90°) second harmonic Hall voltages at $\theta_H$ = 9° and $V_{app}$ = 4 V fit by equation 1.27 to extract $a_j$ and $b_j$ for all (un)buffered Pt(3)|CoFeB(1.6) bilayers.

Table 6.4 Measured damping-like ($\Delta H_Z^{meas}$) and field-like ($\Delta H_Y^{meas}$) effective fields from fitting Figure 6.9 second harmonic Hall voltage data to equation 1.27. The Oersted field is subtracted from the field-like component to give the SOT effective fields $\Delta H_Z$ and $\Delta H_Y$.

| Stack Structure | $\Delta H_Z^{meas}$ (Oe) | $\Delta H_Y^{meas}$ (Oe) | $H_Z^{OF}$ (Oe) | $H_Y^{OF}$ (Oe) | $\Delta H_Z$ (Oe) | $\Delta H_Y$ (Oe) |
|---|---|---|---|---|---|---|
| Pt(3)\|CoFeB(1.6) | -12.3 ± 0.6 | 0.1 ± 0.01 | 0 | -1.4 | -12.3 ± 0.6 | 1.5 ± 0.1 |
| Ru(1)\|Pt(3)\|CoFeB(1.6) | -25 ± 1 | -0.2 ± 0.02 | 0 | -2.6 | -25 ± 1 | 2.4 ± 0.1 |
| Ta(1)\|Pt(3)\|CoFeB(1.6) | -19 ± 1 | -0.4 ± 0.04 | 0 | -2.5 | -19 ± 1 | 2.2 ± 0.1 |

The methodology behind the Oersted field subtraction from $\Delta H_{Z(Y)}^{meas}$ to evaluate the true SOT effective fields and the measurement error estimation are equivalent to that described the previous section. We observe significantly more $\Delta H_Z$ in buffered bilayers than those unbuffered with damping-like SOT fields largest in Ru-buffered then Ta-buffered Pt(3)|CoFeB(1.6) devices, similar to the previous section. Again, the $\Delta H_Y \ll \Delta H_Z$ for all bilayers and since the estimated $H_Y^{OF} > \Delta H_Y^{meas}$, it would be challenging to draw any convincing conclusions from comparing the field-like torques.

Table 6.5 Pt resistivity for each (un)buffered Pt|CoFeB bilayer highlighting the difference in current density within the Pt layer driving SOT with the effective fields and the normalised SOT damping-like effective field.

| Stack Structure | $\rho_{Pt}$ (μΩ cm) | $\lvert\Delta H_{DL}\rvert$ (Oe) | $\lvert\Delta H_{DL}\rvert / j_{c,Pt}$ (x $10^{-10}$) (Oe $A^{-1}$ $m^2$) |
|---|---|---|---|
| Pt(3)\|CoFeB(1.6) | 54 | -12.3 ± 0.6 | 1.7 ± 0.1 |
| Ru(1)\|Pt(3)\|CoFeB(1.6) | 32.4 | -25 ± 1 | 2.0 ± 0.2 |
| Ta(1)\|Pt(3)\|CoFeB(1.6) | 31 | -19 ± 1 | 1.5 ± 0.1 |

Although the magnitude of $\Delta H_{DL}$ is significantly different for (un)buffered Pt|CoFeB bilayers, when we evaluate the more telling metric $\frac{\Delta H_{DL}}{j_{c,Pt}}$ in Table 6.5, we find the current-normalised, SOT effective fields of each device vary only slightly in magnitude, and have a nearly constant value. Across these thicker CoFeB bilayers, $\frac{\Delta H_{DL}}{j_{c,Pt}}$ is more consistent than the thinner CoFeB samples in Section 6.4.3 measured with different lock-in techniques, as expected. The experimentally measured $\rho_{Pt}$ at $t \sim 3$ nm is redisplayed to show that drastic increase of the unbuffered bilayer can immediately account for the reduction $\Delta H_{DL}$.

The near constant overall SOT effective field per unit current density in the Pt is initially surprising considering the vastly differing growth mode, and so microstructure, in the (un)buffered ultrathin Pt films. However, since the SOT effective field arises directly from the SHE in the Pt layer, a constant $\frac{\Delta H_{DL}}{j_{c,Pt}}$ indicates that $\sigma_{xy}^{SH}$ is constant in the Pt films, regardless of microstructure. This is consistent with the results found when modelling SHMR and spin pumping signals in chapters 4 and 5, which could only be accomplished adequately when $\sigma_{xy}^{SH}$ was constant. In contrast, if $\sigma_{xy}^{SH}$ was found to vary with $\rho_{Pt}$, a large extrinsic scattering component would be expected in Pt due to the enhanced surface and grain boundary scattering in the ultrathin limit between the (un)buffered films. Therefore, we conclude that intrinsic spin hall scattering must dominate in ultrathin Pt films.

### 6.4.5 SOT effective field FM depth dependence

Finally, we discuss one further question arising from the SOT damping-like effective field measurements compiled in table 6.3 and 6.5; Why are the magnitudes three to four times larger in thinner $d_{CoFeB} \sim 1.1$ nm CoFeB than those at $d_{CoFeB} = 1.6$ nm? This is in contrast to [233], who find a constant $\Delta H_{DL}$ from $d_{CoFeB} \sim 0.8$ to 1.4 nm. In the following analysis, we attempt to understand the precipitous drop in $\lvert\Delta H_{DL}\rvert$ across the 5 Å.

The effective damping-like torque is directly proportional to the total spin current absorbed by the FM layer. Recently, transverse spin current relaxation in FM has been shown to differ from the longitudinal $\boldsymbol{j}_s$ derivation from the drift-diffusion equation (1.18), which promotes different depth-dependent spin absorption. Ghosh *et al*. [135] observe a linear transverse $\boldsymbol{j}_s$ absorption as a function of $d_{FM}$ and a sharp transition to a plateau at the saturation value of

the spin mixing conductance. This is illustrated in figure 6.10 (a) and compared to the spin current absorption from longitudinal $\boldsymbol{j}_s$ absorption given by

$$j_{s,\mathrm{abs}}^{\mathrm{long}} \propto \int_0^{d_{\mathrm{FM}}} \frac{e^{-z/\lambda}}{\lambda}\,\mathrm{dz}. \tag{6.4}$$

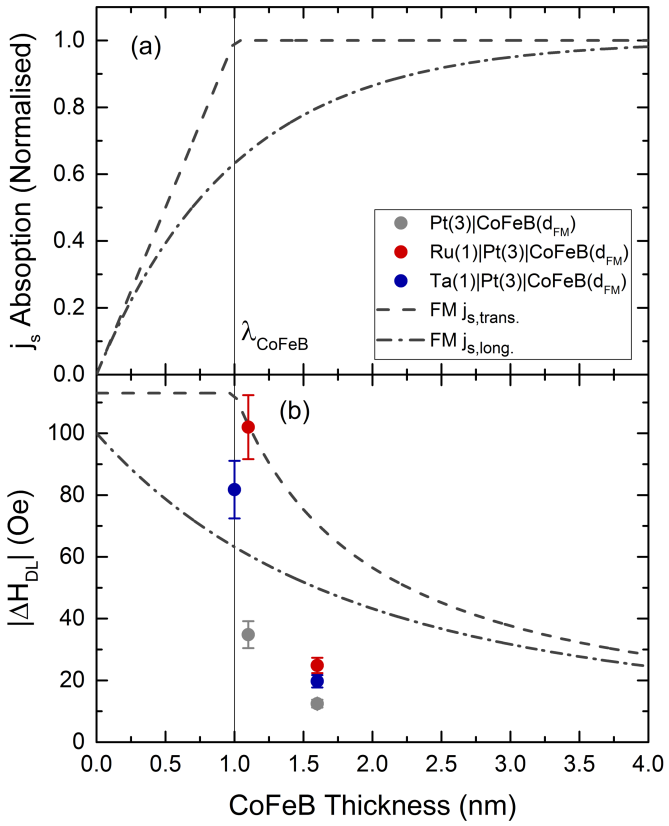


Figure 6.10 (a) Spin current absorption modelled with transverse spin relaxation behaviour found by [135] (dashed) and with classic longitudinal spin relaxation (dash-dot) in the FM. (b) Experimental SOT damping-like effective field data versus FM thickness modelled as a surface effect following $1/d_{\mathrm{FM}}$ following the transverse and longitudinal spin absorption functions in (a).

In figure 6.10 (b), $|\Delta H_{\mathrm{DL}}|$ values are reproduced from tables 6.3 and 6.5 and the $j_{s,\mathrm{abs}}$ is multiplied by $1/d_{\mathrm{FM}}$ to probe if the magnitude of effective SOT decays as a typical surface effect would. It is clear from the rapid drop of $|\Delta H_{\mathrm{DL}}|$ across the 0.5 nm thickness range that neither the longitudinal nor the transverse spin relaxation processes in FMs fit the observed data well, and the fall-off is faster than a $1/d_{\mathrm{FM}}$ surface effect. However, it can be said that the transverse spin relaxation depth dependence seems to better account for the observed precipitous decay after 1 nm unlike that of the longitudinal relaxation mechanism in these devices. It is clear from figure 6.10 that another interfacial effect may be augmenting fast fall-off of the surface effect, such as SML, which generates additional spin-flip scattering. For a more comprehensive study, this limited data set should be augmented with additional buffered Pt(3)|CoFeB($d$) bilayers.

## 6.5 Conclusions

We studied SOT effective fields in (un)buffered HM bilayers with current-induced SOT switching and with recently developed low-current, lock-in techniques to understand the role of HM microstructure in $\boldsymbol{j}_s$ absorption at the HM|FM interface. We first experimentally demonstrated current induced switching in Pt|Co and Pt|CoFeB bilayers with some notable differences. In Ta-buffered Pt(3)|Co(0.7) bilayers, large PMA created sharp SOT switching observed by the AHE, but required field-assistance due to large $\boldsymbol{M}_s$. In Ta-buffered Pt(3)|CoFeB(0.7) bilayers, reduced PMA resulted in a non-coercive FM film close to the SRT, but with reversible SOT switching due to a lower $\boldsymbol{M}_s$. Unfortunately, when completing the series of (un)buffered bilayers, neither the unseeded Pt(3)|Co(0.7) nor the Pt(3)|CoFeB(0.7) device would switch with the reduced PMA. Lowering $\boldsymbol{d}_{FM}$ in an attempt to increase PMA only had the opposite effect due to a lack of FM film continuity with only approximately one monolayer of deposited metal. Therefore, complete, coherent switching within a series of (un)buffered bilayers was not possible.

Instead, we quantified SOT effective fields with low-current, lock-in techniques which correlates changes in $\boldsymbol{M}$ from SOT to planar and anomalous harmonic Hall voltages. With these measurements, we were able to extract field-like, and damping-like SOT effective fields for (un)buffered Pt(3)|CoFeB($\boldsymbol{d}$) bilayers at $\boldsymbol{d}_{CoFeB} \sim 1.1$ nm and 1.6 nm. Due to the combination of small field-like effective field magnitudes and large uncertainties from the equivalent-symmetry Oersted field, it was challenging to draw conclusions for interfacial, field-like SOT and we focused on the bulk damping-like torque component.

In the thinner 1.1 nm CoFeB bilayers, the SOT effective fields had to be measured with a perpendicular (in-plane) harmonic Hall measurement for the un- and Ru-buffered (Ta-buffered) Pt|CoFeB bilayer because of the change in PMA, and so easy-axis, with different buffers. We observed significant differences in damping-like SOT effective fields, however, when accounting for the change in resistivity of the Pt film and $\frac{\Delta \boldsymbol{H}_{DL}}{\boldsymbol{j}_{\boldsymbol{c},Pt}}$ showed only weak variation across the (un)buffered bilayer. This suggests that there is little change to the $\Delta \boldsymbol{H}_{DL}$ per unit current density. To improve the accuracy of this conclusion, we measured a self-consistent series of thicker (un)buffered Pt(3)|CoFeB(1.6) bilayers, with the same in-plane harmonic Hall measurement technique. These measurements demonstrated that $\frac{\Delta \boldsymbol{H}_{DL}}{\boldsymbol{j}_{\boldsymbol{c},Pt}}$ only slightly varies across the series of (un)buffered samples in comparison to signals extracted by SHMR or spin pumping measurements. Indeed, it would be difficult to claim the extracted values are different. This strongly indicates that $\sigma_{xy}^{SH}$ is consistent regardless of Pt morphology, in agreement with the observations of chapters 4-5, and confirms intrinsic spin scattering seems to dominate these ultrathin Pt films.

Interestingly, $\Delta H_{DL}$ indicates a strong CoFeB depth-dependent spin current absorption, which disagrees with recent work [233]. To better understand the origin of the sharp decrease of $\Delta H_{DL}$ in ultrathin CoFeB, we explore more literature [102,135] focused on transverse spin current relaxation in FM and compare it to longitudinal relaxation derived directly from drift-diffusion equations. Neither processes seemed to fit the data well, assuming the fall-off in SOT damping-like effective field goes as a surface effect $1/d_{FM}$. However, transverse spin current relaxation better accounted for the quick fall-off of $\Delta H_{DL}$, suggesting it to be the dominant mechanism in these systems.

# 7 Conclusion

All-metallic spintronics is a substantial research field at present. As spin angular momentum transport is further explored, a myriad of new technological applications in novel SOT-MRAM hard drives, spin-based thermoelectric generators, and microwave communication and sensing devices [7–9], are becoming possible. The prototypical HM|FM metallic bilayer is particularly interesting from a technological point of view due to its low resistance-area product and non-volatility. With the ability to inject and detect pure spin currents, and manipulate FM moments, these inherently robust, energy-efficient devices are useful for probing a host of exciting new spin-mediated effects at the nanoscale. As a result, there is an insatiable urge to probe these exotic new effects in HM|FM bilayers. However, a significant amount of understanding behind the propagation of spin imbalance and the spin-to-charge conversion efficiencies in HMs at the nanoscale is still left lacking. This is readily apparent from the long-standing controversy in literature over the magnitudes of spin-dependent parameters $\lambda$ and $\theta_{SH}$ and in high spin-orbit coupled HMs [61]. Gaining insight into the reason for this discrepancy is an important step towards elucidating the principles governing spin transport at the nanoscale and paramount to the development of novel spintronic microelectronic devices.

Recently, it has become apparent that spin-dependent properties are changing drastically in the ultrathin limit [86,87]. In this limit, nano-fabrication of HM|FM by sputtering is particularly sensitive to growth conditions and the resultant film quality has been found to deviate strongly [151–154]. An accurate estimation of spin-dependent parameters $\theta_{SH}$ and $\lambda$ then becomes challenging. The growing evidence interlinking electrical and spin-dependent parameters [74,87] suggests that HM film microstructure may play an essential role in spin-transport. Up to now, a comprehensive study to understand the effect of HM microstructure on spin transport has not yet been completed and was the main motivation behind this work.

In this thesis, we investigated the role of HM microstructure morphology on spin transport properties within HM|FM bilayers (FM = Co, CoFeB; HM = W, Ta, Ru, Pt) by exploiting the sensitivity of the ultrathin films. The control of specific growth parameters such as the sputter chamber working pressure and the substrate surface wetting conditions allowed the precise tuning of HM morphology and microstructure. This was demonstrated with high-angle x-ray diffractometry, low angle x-ray reflectivity and high resolution scanning transmission electron microscopy. The XRD and XRR measurements showed that although increasing working pressure during Pt growth increased roughness and decreased Pt(111) texture, seeding Pt deposition with thin (1 nm) high-melting-point metals (Ru or Ta in this case) was more effective; diffractometry showed the complete suppression or large enhancement of Pt(111) texture depending whether a 1 nm Ru or a Ta buffer layer was deposited, respectively, between the 6 nm Pt films and the $SiO_2$ substrate. Additionally, XRR

measurements showed that a 1 nm Ta buffer below an ultrathin Pt layer decreased surface roughness by 3 fold, which preliminarily indicated that seeding thin Pt films drastically alters morphology.

To obtain direct evidence of this, changes in growth mode and film continuity from seeding ultrathin 1.6 and 3 nm Pt films were optically demonstrated with aberration-corrected, high angle annular dark field scanning electron microscopy. When Pt was deposited directly on $SiO_2$, the HAADF-STEM images showed noticeable grains, which were representative of island-like growth and classified as following a 3-D Volmer-Weber-type growth mode. However, when buffered with 1 nm of Ru, Pt film continuity increased. At $t \sim 1.6$ nm there were still observable grains, but at $t \sim 3$ nm, the film appeared to conform to the Ru buffer layer with good layer-by-layer growth. These well-wet Pt films follow 2-D van der Merwe growth mode. Finally, Ta buffering proved superior to that of Ru, allowing smooth, continuous 2-D VDM-type growth down to 1.6 nm of Pt.

Not surprisingly, these drastic changes in microstructure morphology in ultrathin Pt films correlated directly to resistivity. By measuring stack resistance across a Hall bar with well defined current and voltage directions, we extracted thin film Pt resistivities to find each (un)buffered series shows a large increase in the ultrathin limit. There was gradual a 2-3 fold resistivity increase from bulk Pt resistivity in Ru- and Ta- buffered films down to $t \sim 1.6$ nm. The gradual increase in resistivity at low thickness is explained well by Mayadas-Shatzkes and Fuchs-Sondheimer scattering theories. Fitting the two equations simultaneously to the (un)buffered series shows that both grain boundary and diffuse surface scattering account for the larger resistivity and that neither dominate in ultrathin Pt films. A larger enhancement was observed in the unbuffered Pt films, especially at $t \sim 1.6$ nm where the resistivity jumps to a value one order of magnitude higher than that of the bulk. This suggests that ultra-low thickness Pt films may be is under the percolation threshold.

Once we demonstrated the tunability of ultrathin Pt film morphology with Ru and Ta buffer layers, we correlated the effect of HM microstructure on spin transport and spin-dependent properties with a systematic set of spin Hall magnetoresistance, spin pumping and spin-orbit torque measurements on thin Pt|CoFeB films. We first performed HM-thickness dependent, angular spin Hall magnetoresistance measurements to determine the bulk spin-dependent parameters of constituent HM materials on unbuffered HM|FM bilayers. For crystalline HMs such as Pt, we made a surprising observation: standard magnetoelectronic circuit theory models fit experimental data at fixed $\rho_{Pt}$ deceptively well without considering the drastically enhanced resistivity in the ultrathin limit. Therefore we caution against extracting film parameters in unbuffered HM|FM bilayers with crystalline HM films.

We proceeded to measure a series of un-, Ru- and Ta- buffered HM|FM bilayers to demonstrate vastly different spin Hall magnetoresistances in the ultrathin limit over a range of constituent materials (Pt|Co, Pt|CoFeB and W|CoFeB). In Pt|Co(FeB) stacks, buffering strongly enhanced SHMR at $t \sim 3$ nm. In fact, in (un)buffered Pt|CoFeB bilayers, larger SHMR

signals were strongly correlated to film microstructure. At $t \sim 3$ nm, SHMR were more enhanced for Ta-buffered stacks, followed by Ru-buffered stacks than for unbuffered stacks. This trend directly follows the quality of Pt film deposition characterised by HAADF-STEM and XRR, suggesting that the spin-to-charge conversion of the ISHE is directly affected by HM microstructure.

To extract a set of spin-dependent parameters, we extended standard magnetoelectronic circuit theory models for metallic bilayers to include the seed layer only to find that there was poor agreement with experimental data at a fixed resistivity across $t$. No set of spin dependent-parameters could account for the enhanced SHMR in Ta-buffered ultrathin Pt|CoFeB films, nor could considering the varying $\rho_{Pt}$ in the ultrathin limit or an additional SUB|BUF interface resistance. However, in light of growing evidence that Pt is dominated by Elliot-Yafet spin relaxation and intrinsic spin scattering, we varied the effective spin-dependent parameters $\theta_{SH}$ and $\lambda$ with $\rho_{Pt}$ to find excellent agreement with experimental SHMR on buffered Pt|CoFeB bilayers down to $t \sim 3$ nm. Moreover, a single set of bulk spin-dependent parameters accurately predicted both Ru- and Ta- buffered Pt|CoFeB bilayers despite large differences in SHMR. This confirms that spin-dependent scattering and relaxation is directly correlated to HM microstructure.

Following the methodology from SHMR measurements, we performed HM-thickness dependent spin pumping measurements on (un)buffered Pt|CoFeB bilayers to understand the role of HM microstructure in determining $V_{ISHE}$ lineshape spin pumping signal magnitudes. Although spin pumping probes spin current injection from FM magnetisation dissipation, unlike that of SHMR, they both rely on the ISHE to measure voltage and so the spin-to-charge conversion efficiency in the HM is identical. The spin pumping signals in the metallic bilayers were evaluated by fitting the ISHE induced voltage linewidth to a set of symmetric and antisymmetric Lorentzian functions. After experimentally demonstrating that $V_{ISHE} \sim V_S$ for these measurements, the series of (un)buffered Pt|CoFeB bilayers were measured and compared. The results were analogous to those obtained with the SHMR: the peak signal size ($t \sim 3$ nm), was largest for Ta-buffered stacks, followed by Ru-buffered and the unbuffered stacks, respectively. This trend directly follows the quality of Pt film deposition characterised by HAADF-STEM and XRR, confirming the results obtained with SHMR.

The standard magnetoelectronic circuit theory spin pumping model was extended to include the buffer layer and applied to the experimental data. Again, good agreement with theory and experimental data was only possible after assuming Elliot-Yafet spin relaxation and intrinsic spin scattering dominates in the Pt layers for buffered Pt|CoFeB bilayers. Furthermore, individually fitting thickness-dependent SHMR and spin pumping signals to estimate the spin mixing conductance and $\theta_{SH}$, resulted in multiple, nonunique sets of values. Instead, we extracted a single set of parameters $g_r$ = 5 x $10^{15}$ $\Omega^{-1}m^{-2}$, $\lambda$ = 2 nm and $\theta_{SH}$ = 0.086 by simultaneously fitting the buffered Pt|CoFeB SHMR and spin pumping data, owing to their different $\theta_{SH}$-dependence. In so doing, we demonstrated that a single set of

bulk HM spin-dependent parameters could be extracted from different measurement schemes at largely different signal sizes when adequately considering the difference in HM microstructure.

Finally, we measured the magnitude of spin-orbit torque applied locally to the FM arising from spin current injection from the SHE in an adjacent HM film. We evaluated SOT effective fields in (un)buffered Pt|CoFeB bilayers to compare $\sigma_{xy}^{\mathrm{SH}}$ at varying Pt morphologies and corroborate the observations from SHMR and spin pumping experiments, which find that Pt is dominated by intrinsic spin scattering. To do so, we first demonstrated current induced switching in Ta-buffered Pt|Co and Pt|CoFeB bilayers, but could not measure a complete set of (un)buffered devices due to changes in PMA from strongly varying Pt(111) texture. Instead, we used low-current, lock-in techniques, which related field-like and damping-like effective fields to changes in $\boldsymbol{M}$ through planar and anomalous harmonic Hall voltage measurements.

We observed much larger damping-like effective fields for buffered Pt(3)|CoFeB($d$) bilayers at $d_{\mathrm{CoFeB}} \sim 1.1$ nm and 1.6 nm than for those unbuffered, but demonstrated that after considering the change in $\rho_{\mathrm{Pt}}$ for each device, $\frac{\Delta \boldsymbol{H}_{\mathrm{DL}}}{\boldsymbol{j}_{c,\mathrm{Pt}}}$ showed only weak variation across the (un)buffered bilayer. Indeed, it would be difficult to claim the extracted values are different. We concluded that there was little change to the $\Delta \boldsymbol{H}_{\mathrm{DL}}$ per unit current, which strongly indicates that $\sigma_{xy}^{\mathrm{SH}}$ is consistent regardless of Pt morphology. This is in agreement with the observations from SHMR and spin pumping measurements, and confirms intrinsic spin scattering dominates in these ultrathin Pt films.

Overall, with three different spin measurement schemes, we probed spin reflection and transmission through the HM|FM interface and the absorption of spin current into the FM layer to demonstrate the vital role of HM microstructure morphology in spin transport measurements. When not considering the change in HM resistivity, the SHMR, spin pumping and SOT measurements yield largely different spin signals, which are directly correlated to the quality of the HM microstructure. However, when HM resistivity is evaluated and considered, spin scattering and propagation may be accurately described with a single set of bulk spin-dependent parameters across different measurement schemes. We believe these results may provide a partial solution to the discrepancy of $\theta_{\mathrm{SH}}$ and $\lambda$ reported across the literature for crystalline highly spin-orbit coupled HMs like Pt.

There are multiple steps that can be taken to expand on this work and uncover the extent to which the discrepancies in spin-dependent parameters are correlated to HM microstructure. The first step could be simply expanding the phase space by characterising alternative HM films and subsequently measuring spin transport, by changing growth conditions such as the chamber working pressure during deposition, or by depositing HM films directly on different substrate materials. Indeed, this work already shows preliminarily that altering W microstructure correlates to a change in spin reflection at the HM|FM interface in SHMR. It

also demonstrates that Pt microstructure can be accurately controlled with the chamber working pressure during sputtered deposition. A series of spin transport measurements are required to confirm the effect of changing HM morphology without buffering the film. Furthermore, changing the substrate may prove to be another effective method to observe spin transport dependence on HM microstructure. For example, in HM|FMI systems such as the well studied Pt|YIG bilayer, the YIG layer acts as both the substrate and the FMI on top of which the Pt is deposited. SHMR measurements have been performed on these bilayers as well, and although the results are not outlined in this document, preliminary findings show that $\rho_{Pt}$ increases drastically in the ultrathin limit and SHMR behaviour follows that of the unbuffered Pt|Co(FeB) bilayers.

The next step would likely be to consider the largely unknown role of interfacial spin-orbit coupling in HM|FM bilayers. This thesis highlights only the crucial role of bulk HM spin-orbit effects and spin-dependent parameters on spin transport in multilayers. However, the coupling of intrinsic spin to angular momentum, and to the crystal lattice by Coulomb interactions at the interface may either act as a local spin source or sink in a way that is still poorly understood [129,240]. Interfacial SOC may affect all spin transport measurement schemes where spin transports through the HM|FM interface. Current magnetoelectronic circuit theory assumes that all spin relaxation comes from spin-dependent scattering in the bulk HM, but doesn't take into account the possibility of further spin-orbit scattering at the interface due to SML. This will act quench spin polarisation, although recent work [97] suggests this is not dominant in HM|FM bilayers when measuring SHMR. In contrast, in-plane charge currents may also create spin polarisation [4,241–243] at the interface with broken inversion symmetry like the Rashba-Edelstein effect, which may introduce an additional spin-orbit torque contribution to those arising from bulk spin Hall effects.

To evaluate interfacial SOC, the bulk spin-dependent effects must be separated from interface contributions. Current magnetoelectronic circuit theory does not consider spin-flip scattering processes at the interface. Given its wide applicability, it should be extended to include interfacial spin-orbit coupling to more accurately model spin transport in multilayers. Experimentally decoupling bulk and interfacial microstructure is a particularly challenging task because the surface structure typically follows that of the bulk. One possible method may be to selectively tune the interface roughness with $Ar^+$ ion milling. Depositing a thicker HM film and milling down leaves the bulk structure unaltered, but drastically changes the surface properties. Unlike in HM|FMI bilayers where the spin mixing conductance is limiting, in HM|FM bilayers $g_r$ is large, which makes it the ideal device to tune interface microstructure without having a large impact on spin transparency. Overall, further insight into the relative contributions of bulk and interfacial spin-orbit coupling is essential to microelectronic device design for technological applications.

# 8 References


[1] M. N. Baibich, J. M. Broto, A. Fert, F. N. Van Dau, F. Petroff, P. Etienne, G. Creuzet, A. Friederich, and J. Chazelas, Phys. Rev. Lett. **61**, 2472 (1988).

[2] J. S. Moodera, L. R. Kinder, T. M. Wong, and R. Meservey, Phys. Rev. Lett. **74**, 3273 (1995).

[3] J. Kim, P. Sheng, S. Takahashi, S. Mitani, and M. Hayashi, Phys. Rev. Lett. **116**, 097201 (2016).

[4] J. C. R. Sánchez, L. Vila, G. Desfonds, S. Gambarelli, J. P. Attané, J. M. De Teresa, C. Magén, and A. Fert, Nat. Commun. **4**, 2944 (2013).

[5] G. Yu, P. Upadhyaya, Y. Fan, J. G. Alzate, W. Jiang, K. L. Wong, S. Takei, S. A. Bender, L.-T. Chang, Y. Jiang, M. Lang, J. Tang, Y. Wang, Y. Tserkovnyak, P. K. Amiri, and K. L. Wang, Nat. Nanotechnol. **9**, 548 (2014).

[6] R. Lebrun, A. Ross, S. A. Bender, A. Qaiumzadeh, L. Baldrati, J. Cramer, A. Brataas, R. A. Duine, and M. Kläui, Nature **561**, 222 (2018).

[7] A. Slavin and V. Tiberkevich, IEEE Trans. Magn. **45**, 1875 (2009).

[8] A. Kirihara, K. Uchida, Y. Kajiwara, M. Ishida, Y. Nakamura, T. Manako, E. Saitoh, and S. Yorozu, Nat. Mater. **11**, 686 (2012).

[9] T. Kawahara, R. Takemura, K. Miura, J. Hayakawa, S. Ikeda, Y. Lee, R. Sasaki, Y. Goto, K. Ito, T. Meguro, F. Matsukura, H. Takahashi, H. Matsuoka, and H. Ohno, in *2007 IEEE Int. Solid-State Circuits Conf. Dig. Tech. Pap.* (IEEE, 2007), pp. 480–617.

[10] M. Saleem, *Quantum Mechanics* (IOP Publishing, 2015).

[11] P. A. M. (Paul A. M. Dirac, *The Principles of Quantum Mechanics* (Clarendon Press, 1981).

[12] J. S. Townsend, *A Modern Approach to Quantum Mechanics* (University Science Books, 2000).

[13] J. M. D. Coey, *Magnetism and Magnetic Materials* (Cambridge University Press, Cambridge, 2010).

[14] L. D. Landau and E. Lifshitz, Phys. Z. Sowjet. **8**, 153 (1935).

[15] T. L. Gilbert, IEEE Trans. Magn. **40**, 3443 (2004).

[16] O. Yalcin, in (IntechOpen, Rijeka, 2013), p. Ch. 1.

[17] K. Ando, S. Takahashi, J. Ieda, Y. Kajiwara, H. Nakayama, T. Yoshino, K. Harii, Y. Fujikawa, M. Matsuo, S. Maekawa, and E. Saitoh, J. Appl. Phys. **109**, 103913 (2011).

[18] C. Kittel, *Introduction to Solid State Physics* (Wiley, 2005).

[19] T. D. Rossing, J. Appl. Phys. **34**, 995 (1963).

[20] M. B. Jungfleisch, A. V. Chumak, A. Kehlberger, V. Lauer, D. H. Kim, M. C. Onbasli, C. A. Ross, M. Kläui, and B. Hillebrands, Phys. Rev. B **91**, 134407 (2015).

[21] M. Wu and A. F. (Axel F. Hoffmann, *Recent Advances in Magnetic Insulators : From Spintronics to Microwave Applications* (n.d.).

[22] G. Woltersdorf and B. Heinrich, Phys. Rev. B **69**, 184417 (2004).

[23] J. Lindner, K. Lenz, E. Kosubek, K. Baberschke, D. Spoddig, R. Meckenstock, J. Pelzl, Z. Frait, and D. L. Mills, Phys. Rev. B **68**, 060102 (2003).

[24] A. Azevedo, L. H. Vilela Leão, R. L. Rodriguez-Suarez, A. B. Oliveira, and S. M. Rezende, J. Appl. Phys. **97**, 10C715 (2005).

[25] A. Conca, B. Heinz, M. R. Schweizer, S. Keller, E. T. Papaioannou, and B. Hillebrands, Phys. Rev. B **95**, 174426 (2017).

[26] S. Keller, J. Greser, M. R. Schweizer, A. Conca, V. Lauer, C. Dubs, B. Hillebrands, and E. T. Papaioannou, Phys. Rev. B **96**, 024437 (2017).

[27] E. Saitoh, M. Ueda, H. Miyajima, and G. Tatara, Appl. Phys. Lett. **88**, 182509 (2006).

[28] N. F. Mott, Proc. R. Soc. A Math. Phys. Eng. Sci. **153**, 699 (1936).

[29] K. Tauber, M. Gradhand, D. V. Fedorov, and I. Mertig, Phys. Rev. Lett. **109**, 026601 (2012).

[30] A. Altland and B. Simons, *Condensed Matter Field Theory* (Cambridge University Press, Cambridge, 2006).

[31] Y. Kajiwara, K. Harii, S. Takahashi, J. Ohe, K. Uchida, M. Mizuguchi, H. Umezawa, H. Kawai, K. Ando, K. Takanashi, S. Maekawa, and E. Saitoh, Nature **464**, 262 (2010).

[32] B. Heinrich, C. Burrowes, E. Montoya, B. Kardasz, E. Girt, Y.-Y. Song, Y. Sun, and M. Wu, Phys. Rev. Lett. **107**, 066604 (2011).

[33] B. F. Miao, S. Y. Huang, D. Qu, and C. L. Chien, Phys. Rev. Lett. **112**, 236601 (2014).

[34] E. H. Hall, Am. J. Math. **2**, 287 (1879).

[35] E. H. Hall, London, Edinburgh, Dublin Philos. Mag. J. Sci. **12**, 157 (1881).

[36] N. Nagaosa, J. Sinova, S. Onoda, A. H. MacDonald, and N. P. Ong, Rev. Mod. Phys. **82**, 1539 (2010).

[37] M. I. Dyakonov and V. I. Perel, Phys. Lett. A **35**, 459 (1971).

[38] M. I. Dyakonov and V. I. Perel, J. Exp. Theor. Phys. Lett. Vol. 13, p.467 **13**, 467 (1971).

[39] J. E. Hirsch, Phys. Rev. Lett. **83**, 1834 (1999).

[40] L. Onsager, Phys. Rev. **37**, 405 (1931).

[41] K. M. Seemann, F. Freimuth, H. Zhang, S. Blügel, Y. Mokrousov, D. E. Bürgler, and C. M. Schneider, Phys. Rev. Lett. **107**, 086603 (2011).

[42] G. Binasch, P. Grünberg, F. Saurenbach, and W. Zinn, Phys. Rev. B **39**, 4828 (1989).

[43] X. Qiu, Z. Shi, W. Fan, S. Zhou, and H. Yang, Adv. Mater. **30**, 1705699 (2018).

[44] T. Suzuki, S. Fukami, N. Ishiwata, M. Yamanouchi, S. Ikeda, N. Kasai, and H. Ohno, Appl. Phys. Lett. **98**, 142505 (2011).

[45] E. van der Bijl and R. A. Duine, Phys. Rev. B **86**, 094406 (2012).

[46] U. H. Pi, K. Won Kim, J. Y. Bae, S. C. Lee, Y. J. Cho, K. S. Kim, and S. Seo, Appl. Phys. Lett. **97**, 162507 (2010).

[47] K.-W. Kim, S.-M. Seo, J. Ryu, K.-J. Lee, and H.-W. Lee, Phys. Rev. B **85**, 180404 (2012).

[48] X. Wang and A. Manchon, Phys. Rev. Lett. **108**, 117201 (2012).

[49] D. A. Pesin and A. H. MacDonald, Phys. Rev. B **86**, 014416 (2012).

[50] U. H. Pi, K. Won Kim, J. Y. Bae, S. C. Lee, Y. J. Cho, K. S. Kim, and S. Seo, Appl. Phys. Lett. **97**, 162507 (2010).

[51] S. Meyer, Y.-T. Chen, S. Wimmer, M. Althammer, T. Wimmer, R. Schlitz, S. Geprägs, H. Huebl, D. Ködderitzsch, H. Ebert, G. E. W. Bauer, R. Gross, and S. T. B. Goennenwein, Nat. Mater. **16**, 977 (2017).

[52] A. D. Avery, M. R. Pufall, and B. L. Zink, Phys. Rev. Lett. **109**, 196602 (2012).

[53] K. v. Klitzing, G. Dorda, and M. Pepper, Phys. Rev. Lett. **45**, 494 (1980).

[54] D. Hsieh, D. Qian, L. Wray, Y. Xia, Y. S. Hor, R. J. Cava, and M. Z. Hasan, Nature **452**, 970 (2008).

[55] D. R. Yennie, Rev. Mod. Phys. **59**, 781 (1987).

[56] C. M. Jaworski, J. Yang, S. Mack, D. D. Awschalom, R. C. Myers, and J. P. Heremans, Phys. Rev. Lett. **106**, 186601 (2011).

[57] K. Uchida, S. Takahashi, K. Harii, J. Ieda, W. Koshibae, K. Ando, S. Maekawa, and E. Saitoh, Nature **455**, 778 (2008).

[58] J. Xiao, G. E. W. Bauer, K. Uchida, E. Saitoh, and S. Maekawa, Phys. Rev. B **81**, 214418 (2010).

[59] H. Adachi, K. Uchida, E. Saitoh, and S. Maekawa, Reports Prog. Phys. **76**, 036501 (2013).

[60] M. Onoda and N. Nagaosa, J. Phys. Soc. Japan **71**, 19 (2002).

[61] A. Hoffmann, IEEE Trans. Magn. **49**, 5172 (2013).

[62] R. Karplus and J. M. Luttinger, Phys. Rev. **95**, 1154 (1954).

[63] N. Nagaosa, J. Phys. Soc. Japan **75**, 042001 (2006).

[64] G. Sundaram and Q. Niu, Phys. Rev. B **59**, 14915 (1999).

[65] T. Jungwirth, Q. Niu, and A. H. MacDonald, Phys. Rev. Lett. **88**, 207208 (2002).

[66] S. Onoda, N. Sugimoto, and N. Nagaosa, Phys. Rev. B **77**, 165103 (2008).

[67] T. Tanaka, H. Kontani, M. Naito, T. Naito, D. S. Hirashima, K. Yamada, and J. Inoue, Phys. Rev. B **77**, 165117 (2008).

[68] G. Y. Guo, S. Murakami, T.-W. Chen, and N. Nagaosa, Phys. Rev. Lett. **100**, 096401 (2008).

[69] H. Kontani, T. Tanaka, D. S. Hirashima, K. Yamada, and J. Inoue, Phys. Rev. Lett. **102**,

016601 (2009).

[70] J. Smit, Physica **24**, 39 (1958).

[71] L. Berger, Phys. Rev. B **2**, 4559 (1970).

[72] L. Berger, Phys. Rev. B **54**, 9353 (1996).

[73] P. J. de Visser, J. J. A. Baselmans, P. Diener, S. J. C. Yates, A. Endo, and T. M. Klapwijk, Phys. Rev. Lett. **106**, 167004 (2011).

[74] E. Sagasta, Y. Omori, M. Isasa, M. Gradhand, L. E. Hueso, Y. Niimi, Y. Otani, and F. Casanova, Phys. Rev. B **94**, 060412 (2016).

[75] A. Fert and S.-F. Lee, Phys. Rev. B **53**, 6554 (1996).

[76] S. Hershfield and H. L. Zhao, Phys. Rev. B **56**, 3296 (1997).

[77] P. C. van Son, H. van Kempen, and P. Wyder, Phys. Rev. Lett. **58**, 2271 (1987).

[78] S. Takahashi and S. Maekawa, J. Phys. Soc. Japan **77**, 031009 (2008).

[79] M. Johnson and R. H. Silsbee, Phys. Rev. Lett. **60**, 377 (1988).

[80] M. Johnson and R. H. Silsbee, Phys. Rev. Lett. **55**, 1790 (1985).

[81] T. Valet and A. Fert, Phys. Rev. B **48**, 7099 (1993).

[82] Y.-T. Chen, S. Takahashi, H. Nakayama, M. Althammer, S. T. B. Goennenwein, E. Saitoh, and G. E. W. Bauer, J. Phys. Condens. Matter **28**, 103004 (2016).

[83] A. Kiss, L. Szolnoki, and F. Simon, Sci. Rep. **6**, 22706 (2016).

[84] Y. Liu, Z. Yuan, R. J. H. Wesselink, A. A. Starikov, and P. J. Kelly, Phys. Rev. Lett. **113**, 207202 (2014).

[85] Y. Niimi, D. Wei, H. Idzuchi, T. Wakamura, T. Kato, and Y. Otani, Phys. Rev. Lett. **110**, 016805 (2013).

[86] K. Roy, Phys. Rev. B **96**, 174432 (2017).

[87] M.-H. Nguyen, D. C. Ralph, and R. A. Buhrman, Phys. Rev. Lett. **116**, 126601 (2016).

[88] R. J. Elliott, Phys. Rev. **96**, 266 (1954).

[89] Y. Yafet, Phys. Lett. A **98**, 287 (1983).

[90] E. Y. (Evgeny Y. . Tsymbal and I. Zutic, *Handbook of Spin Transport and Magnetism* (CRC Press, 2012).

[91] H. Jiao and G. E. W. Bauer, Phys. Rev. Lett. **110**, 217602 (2013).

[92] C. O. Avci, K. Garello, A. Ghosh, M. Gabureac, S. F. Alvarado, and P. Gambardella, Nat. Phys. **11**, 570 (2015).

[93] A. Brataas, G. E. W. Bauer, and P. J. Kelly, Phys. Rep. **427**, 157 (2006).

[94] A. Brataas, Y. V. Nazarov, and G. E. W. Bauer, Phys. Rev. Lett. **84**, 2481 (2000).

[95] M. Weiler, M. Althammer, M. Schreier, J. Lotze, M. Pernpeintner, S. Meyer, H. Huebl, R. Gross, A. Kamra, J. Xiao, Y.-T. Chen, H. Jiao, G. E. W. Bauer, and S. T. B.

Goennenwein, Phys. Rev. Lett. **111**, 176601 (2013).

[96] Y. Tserkovnyak, A. Brataas, and G. E. W. Bauer, Phys. Rev. Lett. **88**, 117601 (2002).

[97] M. Kawaguchi, D. Towa, Y.-C. Lau, S. Takahashi, and M. Hayashi, Appl. Phys. Lett. **112**, 202405 (2018).

[98] K. Eid, D. Portner, J. A. Borchers, R. Loloee, M. Al-Haj Darwish, M. Tsoi, R. D. Slater, K. V. O'Donovan, H. Kurt, W. P. Pratt, and J. Bass, Phys. Rev. B **65**, 054424 (2002).

[99] J. Bass and W. P. Pratt, J. Phys. Condens. Matter **19**, 183201 (2007).

[100] S. Y. Huang, X. Fan, D. Qu, Y. P. Chen, W. G. Wang, J. Wu, T. Y. Chen, J. Q. Xiao, and C. L. Chien, Phys. Rev. Lett. **109**, 107204 (2012).

[101] K.-S. Ryu, S.-H. Yang, L. Thomas, and S. S. P. Parkin, Nat. Commun. **5**, 3910 (2014).

[102] M. Caminale, A. Ghosh, S. Auffret, U. Ebels, K. Ollefs, F. Wilhelm, A. Rogalev, and W. E. Bailey, Phys. Rev. B **94**, 014414 (2016).

[103] M. Suzuki, H. Muraoka, Y. Inaba, H. Miyagawa, N. Kawamura, T. Shimatsu, H. Maruyama, N. Ishimatsu, Y. Isohama, and Y. Sonobe, Phys. Rev. B **72**, 054430 (2005).

[104] X. Jia, K. Liu, K. Xia, and G. E. W. Bauer, EPL (Europhysics Lett. **96**, 17005 (2011).

[105] W. J. Antel, M. M. Schwickert, T. Lin, W. L. O'Brien, and G. R. Harp, Phys. Rev. B **60**, 12933 (1999).

[106] F. Wilhelm, P. Poulopoulos, G. Ceballos, H. Wende, K. Baberschke, P. Srivastava, D. Benea, H. Ebert, M. Angelakeris, N. K. Flevaris, D. Niarchos, A. Rogalev, and N. B. Brookes, Phys. Rev. Lett. **85**, 413 (2000).

[107] J. Vogel, A. Fontaine, V. Cros, F. Petroff, J.-P. Kappler, G. Krill, A. Rogalev, and J. Goulon, Phys. Rev. B **55**, 3663 (1997).

[108] Y. Yang, B. Wu, K. Yao, S. Shannigrahi, B. Zong, and Y. Wu, J. Appl. Phys. **115**, 17C509 (2014).

[109] W. Zhang, M. B. Jungfleisch, W. Jiang, Y. Liu, J. E. Pearson, S. G. E. te Velthuis, A. Hoffmann, F. Freimuth, and Y. Mokrousov, Phys. Rev. B **91**, 115316 (2015).

[110] J.-C. Rojas-Sánchez, N. Reyren, P. Laczkowski, W. Savero, J.-P. Attané, C. Deranlot, M. Jamet, J.-M. George, L. Vila, and H. Jaffrès, Phys. Rev. Lett. **112**, 106602 (2014).

[111] L. J. Zhu, D. C. Ralph, and R. A. Buhrman, Phys. Rev. B **98**, 134406 (2018).

[112] J. C. Slonczewski, J. Magn. Magn. Mater. **159**, L1 (1996).

[113] A. Brataas, A. D. Kent, and H. Ohno, Nat. Mater. **11**, 372 (2012).

[114] D. C. Ralph and M. D. Stiles, J. Magn. Magn. Mater. **320**, 1190 (2008).

[115] K. Xia, P. J. Kelly, G. E. W. Bauer, A. Brataas, and I. Turek, Phys. Rev. B **65**, 220401 (2002).

[116] L. Liu, C.-F. Pai, Y. Li, H. W. Tseng, D. C. Ralph, and R. A. Buhrman, Science **336**, 555 (2012).

[117] X. Qiu, K. Narayanapillai, Y. Wu, P. Deorani, D.-H. Yang, W.-S. Noh, J.-H. Park, K.-J. Lee,

H.-W. Lee, and H. Yang, Nat. Nanotechnol. **10**, 333 (2015).

[118] I. M. Miron, K. Garello, G. Gaudin, P.-J. Zermatten, M. V. Costache, S. Auffret, S. Bandiera, B. Rodmacq, A. Schuhl, and P. Gambardella, Nature **476**, 189 (2011).

[119] Z. Diao, D. Apalkov, M. Pakala, Y. Ding, A. Panchula, and Y. Huai, Appl. Phys. Lett. **87**, 232502 (2005).

[120] J. Hayakawa, S. Ikeda, Y. M. Lee, R. Sasaki, T. Meguro, F. Matsukura, H. Takahashi, and H. Ohno, Jpn. J. Appl. Phys. **44**, L1267 (2005).

[121] A. Manchon and S. Zhang, Phys. Rev. B **78**, 212405 (2008).

[122] P. M. Haney, H.-W. Lee, K.-J. Lee, A. Manchon, and M. D. Stiles, Phys. Rev. B **87**, 174411 (2013).

[123] L. Liu, C.-F. Pai, Y. Li, H. W. Tseng, D. C. Ralph, and R. A. Buhrman, Science **336**, 555 (2012).

[124] C.-F. Pai, M. Mann, A. J. Tan, and G. S. D. Beach, Phys. Rev. B **93**, 144409 (2016).

[125] X. Fan, H. Celik, J. Wu, C. Ni, K.-J. Lee, V. O. Lorenz, and J. Q. Xiao, Nat. Commun. **5**, 3042 (2014).

[126] C.-F. Pai, Y. Ou, L. H. Vilela-Leão, D. C. Ralph, and R. A. Buhrman, Phys. Rev. B **92**, 064426 (2015).

[127] K. Garello, I. M. Miron, C. O. Avci, F. Freimuth, Y. Mokrousov, S. Blügel, S. Auffret, O. Boulle, G. Gaudin, and P. Gambardella, Nat. Nanotechnol. **8**, 587 (2013).

[128] S. Zhang and Z. Li, Phys. Rev. Lett. **93**, 127204 (2004).

[129] V. P. Amin and M. D. Stiles, Phys. Rev. B **94**, 104419 (2016).

[130] M. Hayashi, J. Kim, M. Yamanouchi, and H. Ohno, Phys. Rev. B **89**, 144425 (2014).

[131] B. Heinrich, Y. Tserkovnyak, G. Woltersdorf, A. Brataas, R. Urban, and G. E. W. Bauer, Phys. Rev. Lett. **90**, 187601 (2003).

[132] Y. Tserkovnyak, A. Brataas, G. E. W. Bauer, and B. I. Halperin, Rev. Mod. Phys. **77**, 1375 (2005).

[133] A. Brataas, Y. Tserkovnyak, G. E. W. Bauer, and B. I. Halperin, Phys. Rev. B **66**, 060404 (2002).

[134] O. Mosendz, V. Vlaminck, J. E. Pearson, F. Y. Fradin, G. E. W. Bauer, S. D. Bader, and A. Hoffmann, Phys. Rev. B **82**, 214403 (2010).

[135] A. Ghosh, S. Auffret, U. Ebels, and W. E. Bailey, Phys. Rev. Lett. **109**, 127202 (2012).

[136] S. Mizukami, Y. Ando, and T. Miyazaki, Phys. Rev. B **66**, 104413 (2002).

[137] S. Mizukami, Y. Ando, and T. Miyazaki, J. Magn. Magn. Mater. **226–230**, 1640 (2001).

[138] Y.-T. Chen, S. Takahashi, H. Nakayama, M. Althammer, S. T. B. Goennenwein, E. Saitoh, and G. E. W. Bauer, Phys. Rev. B **87**, 144411 (2013).

[139] C. Hahn, G. de Loubens, O. Klein, M. Viret, V. V. Naletov, and J. Ben Youssef, Phys. Rev. B **87**, 174417 (2013).

[140] Y. Yin, D.-S. Han, M. C. H. de Jong, R. Lavrijsen, R. A. Duine, H. J. M. Swagten, and B. Koopmans, Appl. Phys. Lett. **111**, 232405 (2017).

[141] J. Liu, T. Ohkubo, S. Mitani, K. Hono, and M. Hayashi, Appl. Phys. Lett. **107**, 232408 (2015).

[142] S. Cho, S. C. Baek, K.-D. Lee, Y. Jo, and B.-G. Park, Sci. Rep. **5**, 14668 (2015).

[143] M. Isasa, A. Bedoya-Pinto, S. Vélez, F. Golmar, F. Sánchez, L. E. Hueso, J. Fontcuberta, and F. Casanova, Appl. Phys. Lett. **105**, 142402 (2014).

[144] H. Nakayama, M. Althammer, Y.-T. Chen, K. Uchida, Y. Kajiwara, D. Kikuchi, T. Ohtani, S. Geprägs, M. Opel, S. Takahashi, R. Gross, G. E. W. Bauer, S. T. B. Goennenwein, and E. Saitoh, PRL **110**, 206601 (2013).

[145] N. Vlietstra, J. Shan, V. Castel, B. J. van Wees, and J. Ben Youssef, Phys. Rev. B **87**, 184421 (2013).

[146] L. Lang, X. Qiu, and S. Zhou, Sci. Rep. **8**, 329 (2018).

[147] J. Fischer, O. Gomonay, R. Schlitz, K. Ganzhorn, N. Vlietstra, M. Althammer, H. Huebl, M. Opel, R. Gross, S. T. B. Goennenwein, and S. Geprägs, Phys. Rev. B **97**, 014417 (2018).

[148] Ø. Johansen, H. Skarsvåg, and A. Brataas, Phys. Rev. B **97**, 054423 (2018).

[149] Y. Ji, J. Miao, Y. M. Zhu, K. K. Meng, X. G. Xu, J. K. Chen, Y. Wu, and Y. Jiang, Appl. Phys. Lett. **112**, 232404 (2018).

[150] K. Uchida, S. Takahashi, K. Harii, J. Ieda, W. Koshibae, K. Ando, S. Maekawa, and E. Saitoh, Nature **455**, 778 (2008).

[151] H. N. Shah, R. Jayaganthan, and D. Kaur, (2013).

[152] V. K. Arepalli, Y. Shin, and J. Kim, Superlattices Microstruct. **122**, 253 (2018).

[153] C. T. Campbell, Surf. Sci. Rep. **27**, 1 (1997).

[154] A. Pimpinelli and J. Villain, *Physics of Crystal Growth* (Cambridge University Press, Cambridge, 1998).

[155] W. Zhang, W. Han, X. Jiang, S.-H. Yang, and S. S. P. Parkin, Nat. Phys. **11**, 496 (2015).

[156] T. Kimura, Y. Otani, T. Sato, S. Takahashi, and S. Maekawa, Phys. Rev. Lett. **98**, 156601 (2007).

[157] A. Azevedo, L. H. Vilela-Leão, R. L. Rodríguez-Suárez, A. F. Lacerda Santos, and S. M. Rezende, Phys. Rev. B **83**, 144402 (2011).

[158] K. Kondou, H. Sukegawa, S. Mitani, K. Tsukagoshi, and S. Kasai, Appl. Phys. Express **5**, 073002 (2012).

[159] K. Uchida, Z. Qiu, T. Kikkawa, R. Iguchi, and E. Saitoh, Appl. Phys. Lett. **106**, 052405 (2015).

[160] M. Althammer, S. Meyer, H. Nakayama, M. Schreier, S. Altmannshofer, M. Weiler, H. Huebl, S. Geprägs, M. Opel, R. Gross, D. Meier, C. Klewe, T. Kuschel, J.-M. Schmalhorst, G. Reiss, L. Shen, A. Gupta, Y.-T. Chen, G. E. W. Bauer, E. Saitoh, and S. T. B.

Goennenwein, Phys. Rev. B **87**, 224401 (2013).

[161] K. Ando, S. Takahashi, K. Harii, K. Sasage, J. Ieda, S. Maekawa, and E. Saitoh, Phys. Rev. Lett. **101**, 036601 (2008).

[162] S. Swann, Phys. Technol. **19**, 67 (1988).

[163] P. . Kelly and R. . Arnell, Vacuum **56**, 159 (2000).

[164] S. Foner, Rev. Sci. Instrum. **30**, 548 (1959).

[165] D. J. (David J. Griffiths, *Introduction to Electrodynamics* (n.d.).

[166] A. Zieba and S. Foner, Rev. Sci. Instrum. **53**, 1344 (1982).

[167] H. Stanjek and W. Häusler, Hyperfine Interact. **154**, 107 (2004).

[168] S. J. Pennycook and P. D. (Peter D. Nellist, *Scanning Transmission Electron Microscopy : Imaging and Analysis* (Springer, 2011).

[169] P. Hartel, H. Rose, and C. Dinges, Ultramicroscopy **63**, 93 (1996).

[170] M. Cattani, A. R. Vaz, R. S. Wiederkehr, F. S. Teixeira, M. C. Salvadori, and I. G. Brown, Surf. Rev. Lett. **14**, 87 (2007).

[171] A. F. Mayadas and M. Shatzkes, Phys. Rev. B **1**, 1382 (1970).

[172] K. Fuchs and N. F. Mott, Math. Proc. Cambridge Philos. Soc. **34**, 100 (1938).

[173] G. N. Gould and L. A. Moraga, Thin Solid Films **10**, 327 (1972).

[174] M. J. Jeng, W. K. Lei, W. L. Ku, L. B. Chang, C. W. Wu, Y. T. Lu, and S. C. Hu, Adv. Mater. Res. **213**, 161 (2011).

[175] K. Srinivas, M. Manivel Raja, D. V. Sridhara Rao, and S. V. Kamat, Thin Solid Films **558**, 349 (2014).

[176] P. R. LeClair, Fundamental Aspects of Spin Polarized Tunnelling, Eindhoven University of Technology, 2002.

[177] J. Kanak, M. Czapkiewicz, T. Stobiecki, M. Kachel, I. Sveklo, A. Maziewski, and S. van Dijken, Phys. Status Solidi **204**, 3950 (2007).

[178] J. J. Thomson, in *Proc. Cambridge Philos. Soc* (1901), pp. 120–123.

[179] S. Dutta, K. Sankaran, K. Moors, G. Pourtois, S. Van Elshocht, J. Bömmels, W. Vandervorst, Z. Tőkei, and C. Adelmann, J. Appl. Phys. **122**, 025107 (2017).

[180] M. Cattani and M. C. Salvadori, Surf. Rev. Lett. **11**, 283 (2004).

[181] J. S. Agustsson, U. B. Arnalds, A. S. Ingason, K. B. Gylfason, K. Johnsen, S. Olafsson, and J. T. Gudmundsson, J. Phys. Conf. Ser. **100**, 082006 (2008).

[182] M. C. SALVADORI, A. R. VAZ, R. J. C. FARIAS, and M. CATTANI, Surf. Rev. Lett. **11**, 223 (2004).

[183] E. H. Sondheimer, Adv. Phys. **1**, 1 (1952).

[184] A. F. Mayadas, M. Shatzkes, and J. F. Janak, Appl. Phys. Lett. **14**, 345 (1969).

[185] S. Pütter, S. Geprägs, R. Schlitz, M. Althammer, A. Erb, R. Gross, and S. T. B.

Goennenwein, Appl. Phys. Lett. **110**, 012403 (2017).

[186] C. T. Campbell, Surf. Sci. Rep. **27**, 1 (1997).

[187] K. Krupski, M. Moors, P. Jóźwik, T. Kobiela, A. Krupski, K. Krupski, M. Moors, P. Jóźwik, T. Kobiela, and A. Krupski, Materials (Basel). **8**, 2935 (2015).

[188] J.-G. Choi, J. W. Lee, and B.-G. Park, Phys. Rev. B **96**, 174412 (2017).

[189] L. Wang, R. J. H. Wesselink, Y. Liu, Z. Yuan, K. Xia, and P. J. Kelly, Phys. Rev. Lett. **116**, 196602 (2016).

[190] V. Elofsson, B. Lü, D. Magnfält, E. P. Münger, and K. Sarakinos, J. Appl. Phys. **116**, 044302 (2014).

[191] P. M. Martin, *Handbook of Deposition Technologies for Films and Coatings : Science, Applications and Technology.* (Elsevier Science, 2009).

[192] Y. Shiratsuchi, M. Yamamoto, and S. D. Bader, Prog. Surf. Sci. **82**, 121 (2007).

[193] S. Mangin, D. Ravelosona, J. A. Katine, M. J. Carey, B. D. Terris, and E. E. Fullerton, Nat. Mater. **5**, 210 (2006).

[194] T. Suzuki, S. Fukami, K. Nagahara, N. Ohshima, and N. Ishiwata, IEEE Trans. Magn. **44**, 2535 (2008).

[195] K.-U. Demasius, T. Phung, W. Zhang, B. P. Hughes, S.-H. Yang, A. Kellock, W. Han, A. Pushp, and S. S. P. Parkin, Nat. Commun. **7**, 10644 (2016).

[196] Q. Hao and G. Xiao, Phys. Rev. Appl. **3**, 034009 (2015).

[197] J. R. Sambles, K. C. Elsom, and D. J. Jarvis, Phil. Trans. R. Soc. Lond. A **304**, 365 (1982).

[198] L. J. Zhu, D. C. Ralph, and R. A. Buhrman, Phys. Rev. B **98**, 134406 (2018).

[199] C.-F. Pai, L. Liu, Y. Li, H. W. Tseng, D. C. Ralph, and R. A. Buhrman, Appl. Phys. Lett. **101**, 122404 (2012).

[200] G. Fischer, H. Hoffmann, and J. Vancea, Phys. Rev. B **22**, 6065 (1980).

[201] D. Josell, S. H. Brongersma, and Z. Tőkei, Annu. Rev. Mater. Res. **39**, 231 (2009).

[202] E. C. Stoner and E. P. Wohlfarth, Philos. Trans. R. Soc. A Math. Phys. Eng. Sci. **240**, 599 (1948).

[203] S. Foner, Rev. Sci. Instrum. **45**, 1181 (1974).

[204] T. Vemulkar, Fluid Suspended Magnetic Microdiscs with Interfacial Perpendicular Anisotropy, University of Cambridge, 2016.

[205] W.-G. Wang, M. Li, S. Hageman, and C. L. Chien, Nat. Mater. **11**, 64 (2012).

[206] P. Bruno, Phys. Rev. B **39**, 865 (1989).

[207] D. Weller, Y. Wu, J. Stöhr, M. G. Samant, B. D. Hermsmeier, and C. Chappert, Phys. Rev. B **49**, 12888 (1994).

[208] D. Weller, H. Brändle, and C. Chappert, J. Magn. Magn. Mater. **121**, 461 (1993).

[209] M. T. Johnson, J. H. Bloemen, J. A. Den Broeder, and J. J. De Vries, *Magnetic Anisotropy*

*in Metallic Multilayers* (1996).

[210] K. Wang, M.-C. Wu, S. Lepadatu, J. S. Claydon, C. H. Marrows, and S. J. Bending, J. Appl. Phys. **110**, 083913 (2011).

[211] M. Morota, Y. Niimi, K. Ohnishi, D. H. Wei, T. Tanaka, H. Kontani, T. Kimura, and Y. Otani, Phys. Rev. B **83**, 174405 (2011).

[212] M. Getzlaff, J. Bansmann, and G. Schönhense, Solid State Commun. **87**, 467 (1993).

[213] Y. Li, W. Cao, and W. E. Bailey, Phys. Rev. B **94**, 174439 (2016).

[214] J. Zhang, P. Levy, S. Zhang, and V. Antropov, Phys. Rev. Lett. **93**, 256602 (2004).

[215] W. T. Soh, B. Peng, and C. K. Ong, J. Phys. D. Appl. Phys. **47**, 285001 (2014).

[216] W. Zhang, V. Vlaminck, J. E. Pearson, R. Divan, S. D. Bader, and A. Hoffmann, Appl. Phys. Lett. **103**, 242414 (2013).

[217] E. Saitoh, M. Ueda, H. Miyajima, and G. Tatara, Appl. Phys. Lett. **88**, 182509 (2006).

[218] D.-J. Kim, S.-I. Kim, S.-Y. Park, K.-D. Lee, and B.-G. Park, Curr. Appl. Phys. **14**, 1344 (2014).

[219] C. T. Boone, J. M. Shaw, H. T. Nembach, and T. J. Silva, J. Appl. Phys. **117**, 223910 (2015).

[220] M.-H. Nguyen, K. X. Nguyen, D. A. Muller, D. C. Ralph, and R. A. Buhrman, Appl. Phys. Lett. **106**, 222402 (2015).

[221] G. Mihajlović, O. Mosendz, L. Wan, N. Smith, Y. Choi, Y. Wang, and J. A. Katine, Appl. Phys. Lett. **109**, 192404 (2016).

[222] O. Mosendz, J. E. Pearson, F. Y. Fradin, G. E. W. Bauer, S. D. Bader, and A. Hoffmann, Phys. Rev. Lett. **104**, 046601 (2010).

[223] Z. Feng, J. Hu, L. Sun, B. You, D. Wu, J. Du, W. Zhang, A. Hu, Y. Yang, D. M. Tang, B. S. Zhang, and H. F. Ding, Phys. Rev. B **85**, 214423 (2012).

[224] S. R. Marmion, M. Ali, M. McLaren, D. A. Williams, and B. J. Hickey, Phys. Rev. B **89**, 220404 (2014).

[225] X. Wang, G. E. W. Bauer, B. J. van Wees, A. Brataas, and Y. Tserkovnyak, Phys. Rev. Lett. **97**, 216602 (2006).

[226] K. Ando, T. Yoshino, and E. Saitoh, Appl. Phys. Lett. **94**, 152509 (2009).

[227] L. Bai, P. Hyde, Y. S. Gui, C.-M. Hu, V. Vlaminck, J. E. Pearson, S. D. Bader, and A. Hoffmann, Phys. Rev. Lett. **111**, 217602 (2013).

[228] H.-S. Song, K.-D. Lee, J.-W. Sohn, S.-H. Yang, S. S. P. Parkin, C.-Y. You, and S.-C. Shin, Appl. Phys. Lett. **103**, 022406 (2013).

[229] M. Harder, Y. Gui, and C.-M. Hu, Phys. Rep. **661**, 1 (2016).

[230] R. Iguchi and E. Saitoh, J. Phys. Soc. Japan **86**, 011003 (2017).

[231] K. Kang, Pure Spin Current and Charge Transport in Conjugated Polymers, 2017.

[232] X. Liu, W. Zhang, M. J. Carter, and G. Xiao, J. Appl. Phys. **110**, 033910 (2011).

[233] J. Kim, J. Sinha, M. Hayashi, M. Yamanouchi, S. Fukami, T. Suzuki, S. Mitani, and H. Ohno, Nat. Mater. **12**, 240 (2013).

[234] I. Mihai Miron, G. Gaudin, S. Auffret, B. Rodmacq, A. Schuhl, S. Pizzini, J. Vogel, and P. Gambardella, Nat. Mater. **9**, 230 (2010).

[235] L. Liu, T. Moriyama, D. C. Ralph, and R. A. Buhrman, Phys. Rev. Lett. **106**, 036601 (2011).

[236] L. Liu, C.-T. Chen, and J. Z. Sun, Nat. Phys. **10**, 561 (2014).

[237] L. Liu, O. J. Lee, T. J. Gudmundsen, D. C. Ralph, and R. A. Buhrman, Phys. Rev. Lett. **109**, 096602 (2012).

[238] F. Luo, S. Goolaup, W. C. Law, S. Li, F. Tan, C. Engel, T. Zhou, and W. S. Lew, Phys. Rev. B **95**, 174415 (2017).

[239] J. Kim, J. Sinha, M. Hayashi, M. Yamanouchi, S. Fukami, T. Suzuki, S. Mitani, and H. Ohno, Nat. Mater. **12**, 240 (2013).

[240] V. P. Amin and M. D. Stiles, Phys. Rev. B **94**, 104420 (2016).

[241] S. D. Ganichev, E. L. Ivchenko, V. V. Bel'kov, S. A. Tarasenko, M. Sollinger, D. Weiss, W. Wegscheider, and W. Prettl, Nature **417**, 153 (2002).

[242] Y. K. Kato, R. C. Myers, A. C. Gossard, and D. D. Awschalom, Phys. Rev. Lett. **93**, 176601 (2004).

[243] A. Y. Silov, P. A. Blajnov, J. H. Wolter, R. Hey, K. H. Ploog, and N. S. Averkiev, Appl. Phys. Lett. **85**, 5929 (2004).

[244] T. J. Silva, C. S. Lee, T. M. Crawford, and C. T. Rogers, J. Appl. Phys. **85**, 7849 (1999).

[245] S. Fukami, T. Anekawa, C. Zhang, and H. Ohno, Nat. Nanotechnol. **11**, 621 (2016).

# Appendix A

In this section, we detail the complete retrofit of the continuous flow MicrostatHe2 cryostat for electrical measurements at low and room temperatures. Thin film device resistance $R_{XX}$ is largely susceptible to small changes in ambient temperature. This causes thermal drift of the background voltage, which is parasitic to magnetoresistance measurements. At RT, $R_{XX}$ of a 20 nm Pt Hall bar is found to change dramatically overnight and is correlated directly with the change in ambient room temperature in figure A.1.

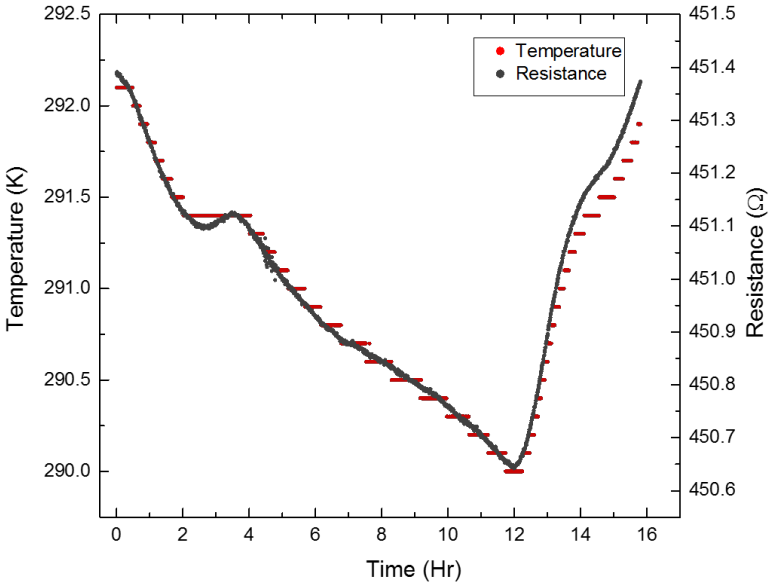


Figure A.1 $R_{XX}$ acquired by the Lakeshore 3708 resistance bridge across a 20 nm Pt Hall bar and temperature acquired by the TC 5035 temperature controller of the cryostat.

To limit thermal drift or to perform low-temperature spintronic measurements, the continuous flow MicrostatHe2 cryostat was re-engineered with specialised wiring. The cold finger was redesigned to have good thermal contact with the sample. In this way, a significant thermal gradient in $\hat{\boldsymbol{z}}$ may be established, which allows for spin caloritronic measurements such as the spin Seebeck effect. The final design is illustrated in the AutoDesk Inventor schematic in figure A.2.

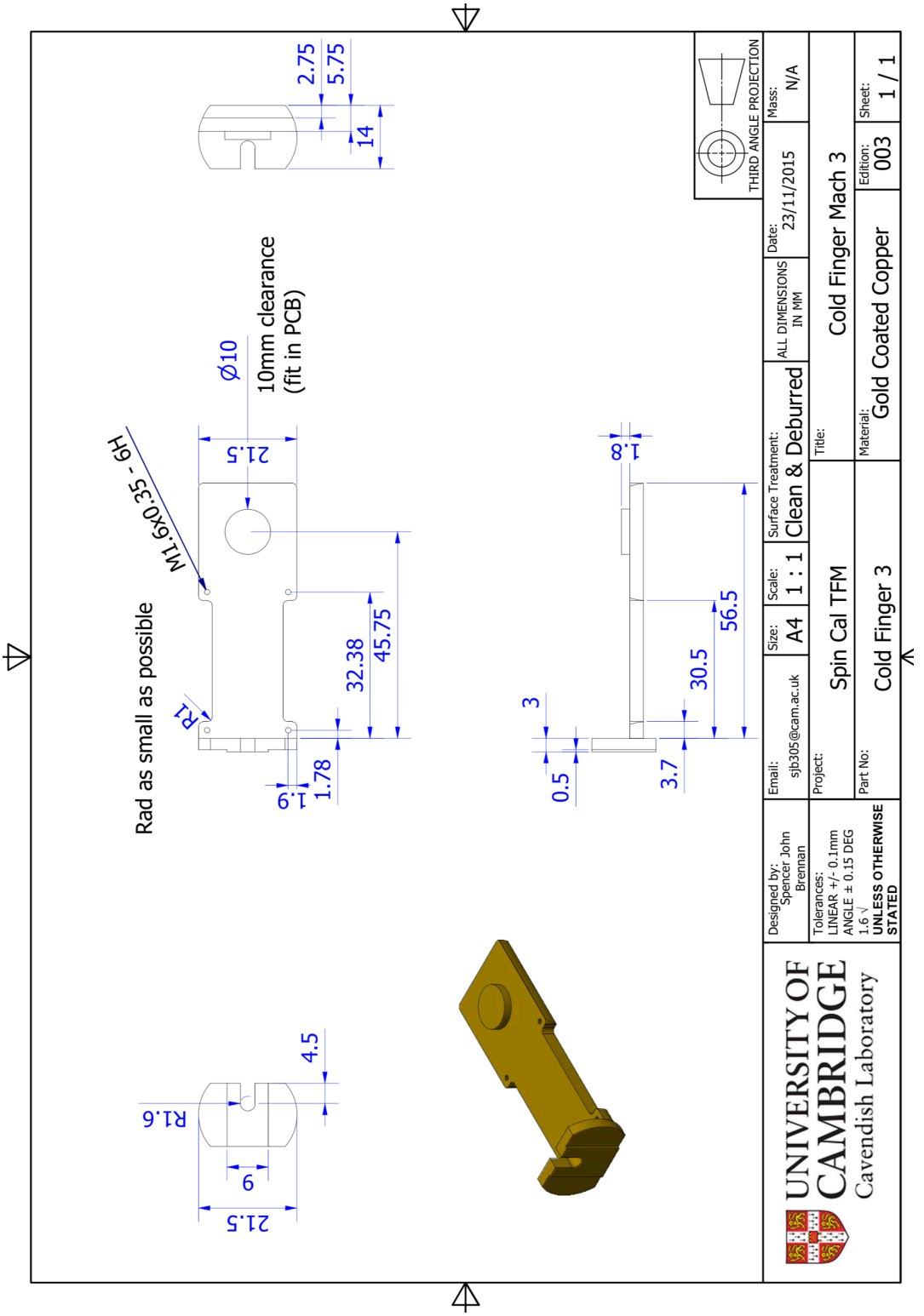


Figure A.2 AutoDesk Inventor schematic with dimensions in mm used to fabricate the final design of the retrofit cold finger.

To ensure good heat transfer between the sample and the cold finger heat sink, the sample bottom is stuck on a notched Cu puck (figure A.4) with Apiezon N cryostat thermal grease. Typically, samples are fixed directly onto the die cavity of a leadless chip carrier (LCC) for wire bonding; however, the ceramic has low thermal conductivity. Therefore we bored the middle of a 44 contact Kyocera LCC and inserted the puck to create a thermally conductive chip carrier in $\hat{\boldsymbol{z}}$. When the LCC is snapped into the Andon chip socket, the puck is contacted at the top of the Cu pedestal protruding cold finger, which completes the thermal circuit. This can be visualised in figure A.3.

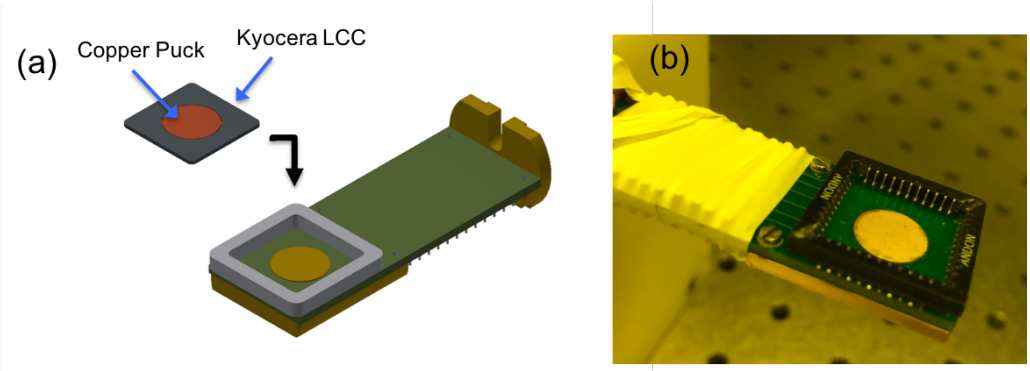


Figure A.3 (a) Schematic illustration of the bored Kyocera LCC fit tightly with the thin Cu puck. The LCC is clipped down into the Andon chip socket to make good thermal contact to the cold finger pedestal. (b) An image of the Andon chip socket soldered to the PCB board, which is screwed into the retrofitted cold finger. The white electrical tape covers the pins and wires carrying the signals to the loom. The Cu cold finger has been gold plated to protect against oxidation on thermal cycling.

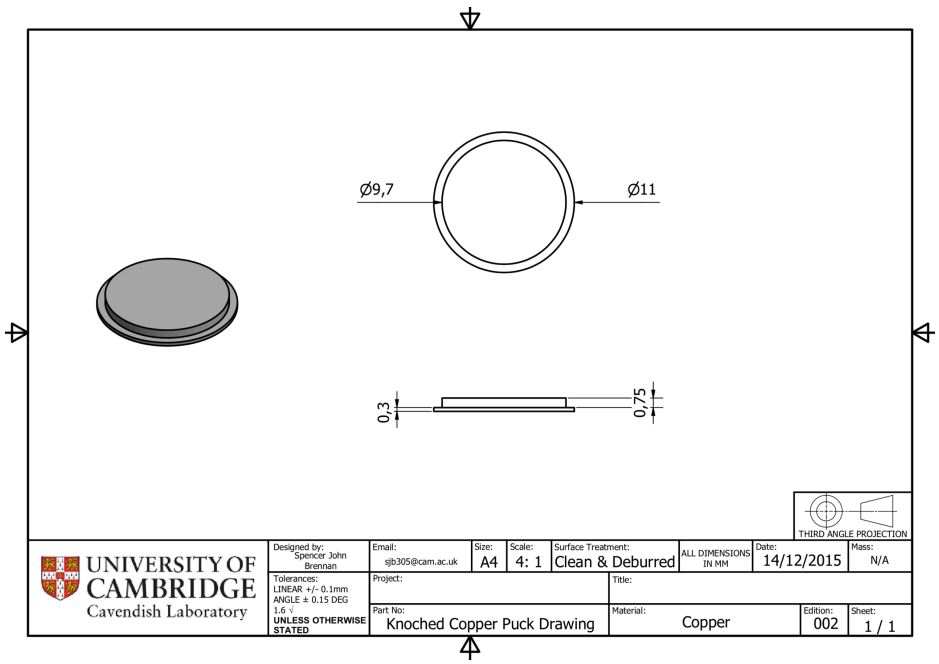


Figure A.4 AutoDesk Inventor schematic with dimensions in mm used to fabricate a set of notched copper pucks.

Electrically, a device is top-contacted with a F&S Bondtec 5332 wedge wire bonder, to the contact pads on the LCC. The LCC is push-fit into a custom chip socket designed by Andon Electronics Corp as shown in figure A.3 (a). Beryllium copper pins in the chip socket were chosen to prevent fracture upon thermal cycling, while the gold contacts prevent oxidation. Spatial constraints permitted only 24 contacts of the LCC to be wired. Thereby, six 4-T devices or twelve 2-T devices may be contacted and measured at one time without opening the cryostat. Additionally, spatial constraints set by the radiation shield limited the design in both in all directions, requiring a compact, low-profile solution. Therefore, the Andon chip socket was ground on the edges to reduce bulk, allowing it to fit inside the radiation shield. An image of the mounted chip socket is seen in figure A.3 (b).

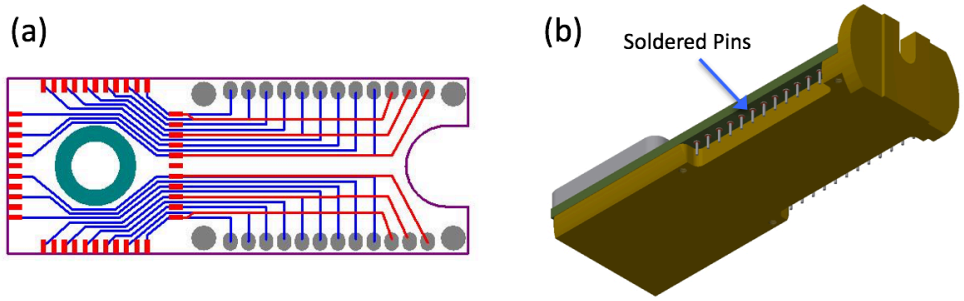


Figure A.5 An illustration of the current-carrying tracks on the custom PCB from the pins under the chip socket (on the left) to the soldered pins (on the right). (b). An illustrated design image of the bottom of the cold finger with two banks of protruding metal pins. These were carefully wired with the thin manganin wires.

The chip socket was soldered onto a custom printed circuit board (PCB) made of FR-4 (a reinforced epoxy laminate), which was chosen for its similar thermal expansion coefficient to Cu to minimise any thermal strain at low temperatures. The track design is illustrated in figure A.5 (a) and shows the protected electrical signals being transported from the Andon chip socket to one of the two 12-pin banks located along the side of the PCB. Pins were soldered into the PCB, protruding down from the bottom of the board where the cold finger is notched as seen in figure A.5 (b). Fine gauge wires were meticulously soldered onto the pins to ensure there was no contact ($R$ > MΩ) between each other and the cold finger.

Determining the wiring for low-temperature measurements to be used inside the MicrostatHe2 is more complicated than considerations at RT for the following reasons:

1. Soldered joints tend to experience wear from thermal cycling and high tin-based solders become brittle over time.
2. The resistivity of the current carrying wire changes, and therefore voltages cannot be considered equal at different temperatures. The residual-resistivity ratio (RRR) highlights this and is defined by the amount of resistivity change from RT to 0 K.
3. Current carrying wires with high thermal conductivities shunt heat, creating spurious thermal gradients.

Since the solder joints cannot be minimised, a solder with low Seebeck coefficient was chosen (97% indium – 3% silver) to reduce thermoelectric voltages. Although a differential measurement should cancel offset thermoelectric voltages, a small spurious signal pick-up will always ensue. The joints should then be covered with a noble metal (such as Au) to prevent oxidation.

A fine gauge manganin wire loom (comprised of 12 twisted pairs of 100 µm gauge wires) was chosen and soldered to the protruding pins in figure A.5 (b) to ensure there was no contact ($R$ > MΩ) between each other and the cold finger. With the small gauge and thermal conductivity ($k$ = 0.5 W/m) 100 times lower than Cu wire, it is a poor thermal conductor. Moreover, the RRR of manganin is nearly 1, allowing voltages to be compared accurately at different temperatures. Fine gauge manganin wires were meticulously soldered onto the pins to ensure there was no contact ($R$ > MΩ) between each other and the cold finger.

The loom was wrapped around the cryostat base and fed up to the top where it terminated with a custom, hermetically sealed Fischer connector. A heavy duty cable, which can be visualised in figure 2.4 (b) of the main text, transports the signal from the cryostat head to the cryostat breakout box. The cable terminates at a secure military connector at the back of the cryostat breakout box. Inside, each contact of the military connector is wired to one of the 24 grounded BNC connectors at the front of the box to be probed by any of the measurement instruments via BNC.

# Appendix B

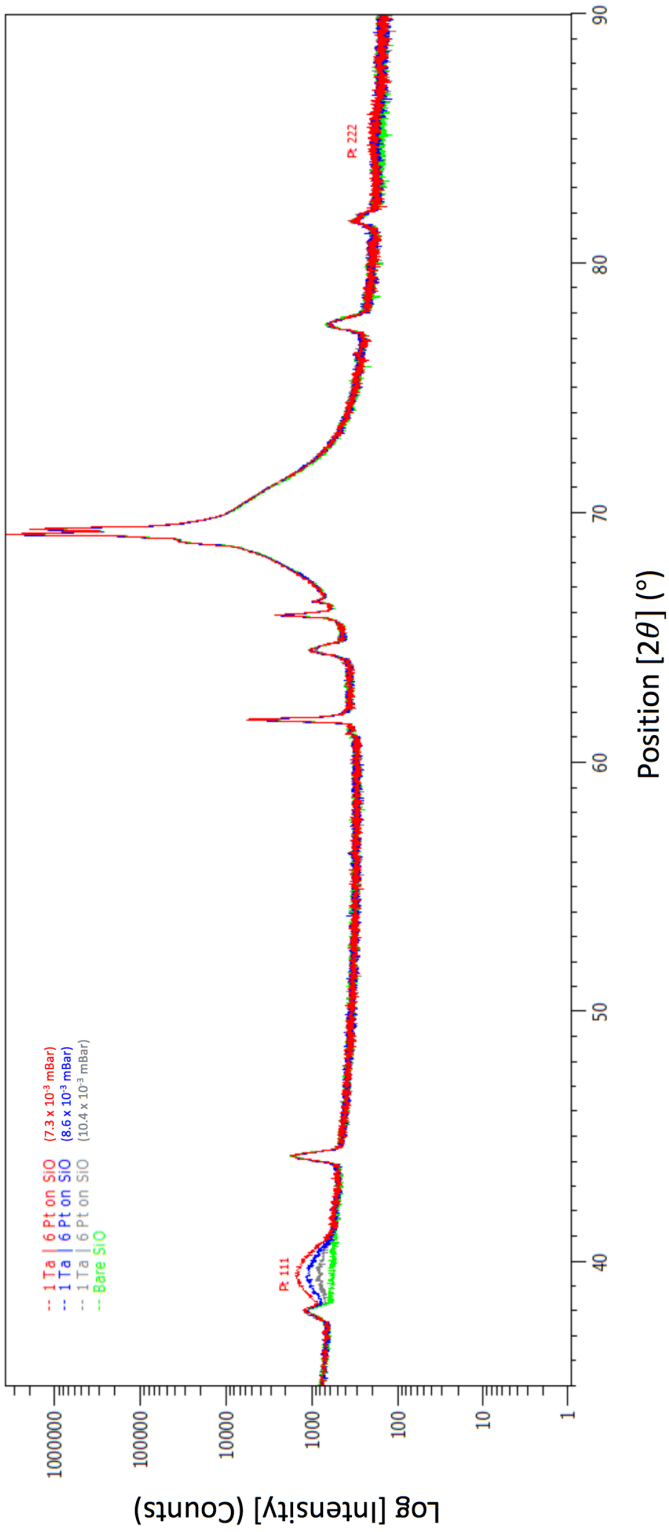


Figure B.1 A full, high-angle $\theta/2\theta$ x-ray diffractometry scan recorded for a series of ~ 10 mm x 10 mm continuous Ta(1)|Pt(6)|CoFeB(1.85)|Ru(1) films grown at varying working pressure.

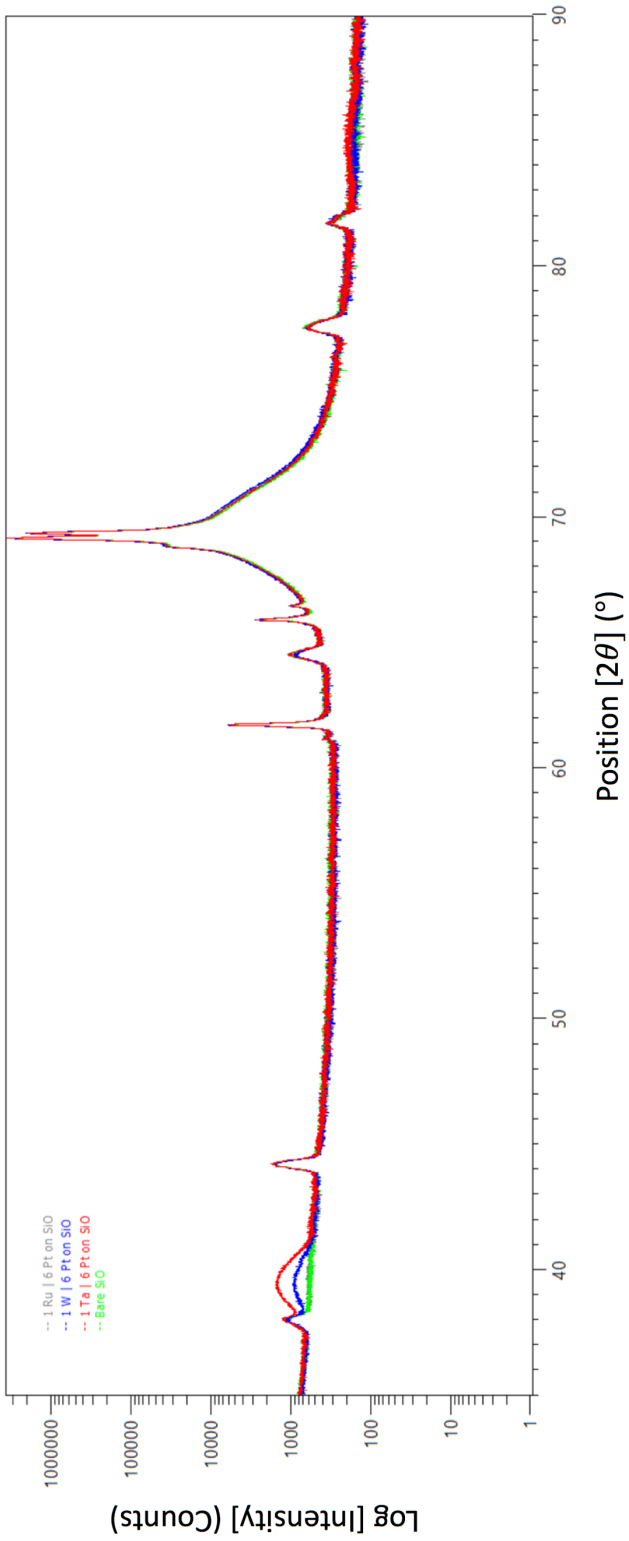


Figure B.2 A full, high-angle $\theta/2\theta$ x-ray diffractometry scan recorded for a series of ~ 10 mm x 10 mm continuous (un)buffered Pt films.

Table B.1 Lateral grain size (observable by eye) of ultrathin Pt films measured with ImageJ™ approximated from figure HAADF-STEM imaging in figure 3.4 for different buffer conditions.

| Buffer | Pt Thickness (nm) | Approximate Lateral Grain Size (nm) | Estimated Grain Scaling Parameter $C$ |
|---|---|---|---|
| – | 1.6 | $3.6 \pm 0.4$ | 2.9 |
| | 3.0 | $7 \pm 1$ | |
| Ru (1 nm) | 1.6 | $6 \pm 1$ | 4.8 |
| | 3.0 | – | |
| Ta (1 nm) | 1.6 | – | – |
| | 3.0 | – | |

In figure 3.4 (a-c), a series of the grains (observable by eye) were measured in ImageJ™ to coarsely quantify the average lateral grain size $D$ for each film and displayed in table B.1. It becomes too challenging to discern grains by eye in figure 3.4 (d-f) due to improved wetting, which hinders the estimation of grain size. We observe a larger lateral grain size in the Ru-buffered Pt(1.6) film than in the unbuffered Pt(1.6) film, as expected. The 3-D Volmer-Weber-type growth dominating in unbuffered, ultrathin Pt deposition promotes clustering and thereby a smaller grain size. In contrast, when aided by a 1 nm Ru buffer, wetting is more favourable for the ultrathin Pt film and the grain size increases. Grain size has been found to depend on film thickness [170,197], which follows

$$D = \left[\frac{1}{D_{\text{bulk}}} + \frac{1}{C\,t}\right]. \tag{B.1}$$

Here, the un-, Ru-buffered Pt ultrathin films are fit with a bulk grain size $D_{\text{bulk}} \sim 30$ nm from literature [181] and the fit parameter $C$ is bounded between 0.5 and 5 [197]. $C$ is fit to approximately 2.9 and 4.8 for the unbuffered and Ru-buffered Pt films, respectively. However, since only 1 point is discernable for the Ru-buffered Pt and two points for unbuffered Pt, the extracted $C$ values are likely inaccuracy. Furthermore, these lateral grain sizes estimated from figures 3.4 (a-c) are observed only by HAADF-STEM image contrast. Since imaging is performed in cross-section of the lamella cut by the FIB, the scattered electrons depend directly on the lamella thickness. Therefore, the estimated grain size is an upper-bound due to convolution in the depth of the sample. To estimate the deviation in lamella thickness across samples, we performed Energy Electron Loss Spectroscopy (EELS) to find the lamella range between 65 – 110 nm thick. Thus, it is challenging to precisely compare between samples, and we only estimate $D(t)$ to better understand the contribution of grain boundary scattering in ultrathin Pt films in section 3.3.2.

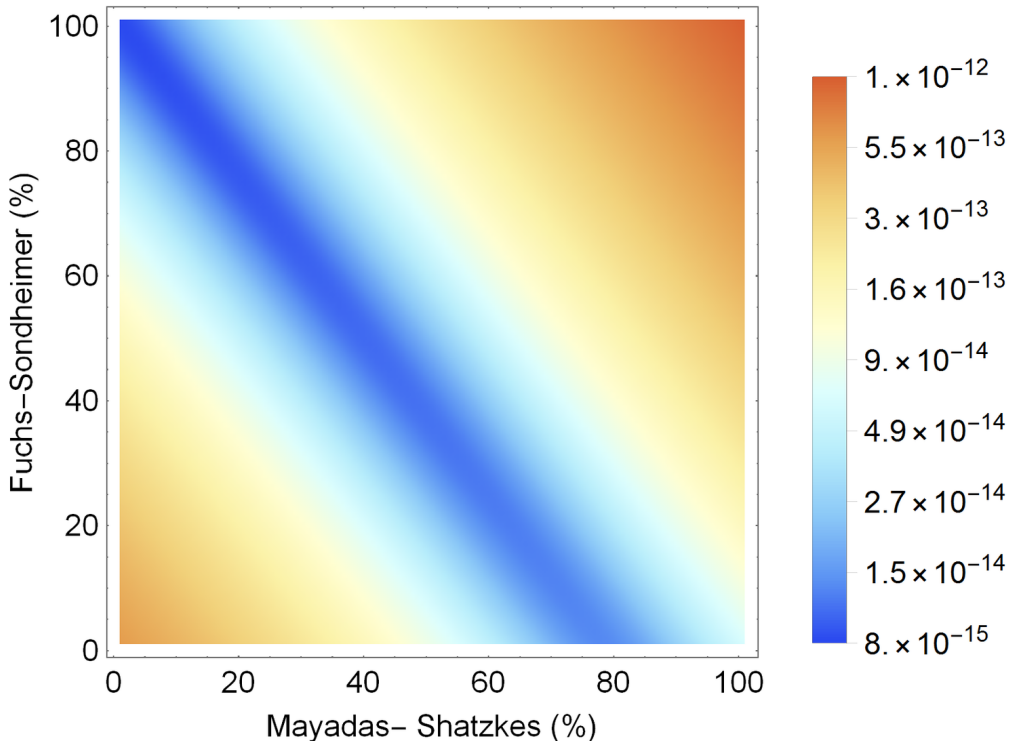


Figure B.3 A log density (colour map) plot of residuals calculated for the weighting pre-factors in the scattering mechanism analysis of unbuffered Pt resistivity with components of the Fuchs-Sondheimer surface scattering model and Mayadas-Shatzkes grain boundary scattering model on the x- and y-axis, respectively.

The residual analysis of the weighted pre-factors of the Fuchs-Sondheimer and the Mayadas-Shatzkes models from equation 3.1 and 3.2, respectively. The total Pt resistivity is fit to

$$\rho_{\mathrm{Pt}} = C_{FS}\rho_{FS} + C_{MS}\rho_{MS}\,, \tag{B.2}$$

where $C_{FS}$ and $C_{MS}$ are the pre-factors of the scattering models of the Fuchs-Sondheimer and the Mayadas-Shatzkes model, respectively, with weighting values from 0 to 1. The log colour map in figure B.3 displays the residual analysis with $C_{FS}$ and $C_{MS}$ on the x- and y-axis respectively. It is clear there is a distinct low residual solution of the log plot (represented by the blue stripe) at the near-diagonal, assuming $l_0 \sim 11$ nm, $R = 0.5$, $p = 0$ and $D_{\mathrm{bulk}} \sim 30$ nm. The residuals along this dark blue do not deviate by more than a factor of two from each other and therefore it is challenging to make any claims about a dominant mechanism in electron scattering in unbuffered, ultrathin Pt films.

# Appendix C

To calculate an average Oersted field $H^{OF}$ generated from a current carrying, thin film wire on a nearby thin film, we adapted equations from [130,244] for a field induced with a medium-range field approximation. Note that since we assume minimal edge effects, the perpendicular Oersted field is equal and opposite in all positions across the bar. Therefore, we denote the field as $H_Y^{OF}$. To calculate the field over the space directly above a current carrying wire, the average Oersted field (in Oe) is given by integrating the field across the thickness $t$ and width $w$ of the desired layer (or space) and dividing by the area following

$$H_Y^{OF}(y,z) = \frac{\boldsymbol{j}_c \times 10^{-3}}{w\,t} \int_0^t \int_{-\frac{w}{2}}^{\frac{w}{2}} C_1^+ + C_1^- - (C_2^+ + C_2^-)\; dzdy\,, \tag{C.1}$$

$$C_1^{\pm}(y,z) = 2(z+t_u)\arctan\left(\frac{{}^{w}/_{2} \pm y}{z+t_u}\right) + ({}^{w}/_{2} \pm y)\ln[({}^{w}/_{2} \pm y)^2 + (z+t_u)^2]\,,$$

$$C_2^{\pm}(y,z) = 2z\arctan\left(\frac{{}^{w}/_{2} \pm y}{z}\right) + ({}^{w}/_{2} \pm y)\ln[({}^{w}/_{2} \pm y)^2 + (z)^2],$$

$\boldsymbol{j}_c$ and $t_u$ is the current density and the thickness of the current-carrying film, respectively. Strictly speaking, $t$ and $w$ are may not be the same dimensions as the current carrying underlayer. When there is a spacer between the current-carrying film and space of interest experiencing the Oersted field, we take the same approach as equation C.1. However, now we integrate the $H_Y^{OF}$ equation for current flowing through the entire height plus the spacer ($t_s$)) for $F_1^{\pm}$ and that without the spacer $t_s$. In this case, $C_2^{\pm}$ cancels and the Oersted field is given by

$$H_Y^{OF}(y,z) = \frac{\boldsymbol{j}_c \times 10^{-3}}{w\,t} \int_0^t \int_{-\frac{w}{2}}^{\frac{w}{2}} F_1^+ + F_1^- - (C_1^+ + C_1^-)\; dydz\,, \tag{C.2}$$

$$F_1^{\pm}(y,z) = 2(z+t_u+t_s)\arctan\left(\frac{{}^{w}/_{2} \pm y}{z+t_u+t_s}\right) + ({}^{w}/_{2} \pm y)\ln[({}^{w}/_{2} \pm y)^2 + (z+t_u+t_s)^2].$$

Hereby, Oersted fields generated from current carrying films may be calculated with varying thicknesses of height between the film and the surrounding space of interest. In spin pumping, an ~ 100 µm space is estimated between the sample and the microstrip coplanar waveguide. Therefore, equation C.2 is used to calculate $H_Y^{OF}$ for the each of the stripline constituent layers: an 18 µm Cu layer capped by the 17 µm Sn layer. The current density flowing through each of the constituent layers is

$$\boldsymbol{j}_{c,i} = \frac{R_{\text{Tot}}}{R_i}\frac{P_{\text{RF}}}{V\rho_i l_{\text{strip}}}, \tag{C.3}$$

where $R_{\text{Tot}}$ is the total resistance across the stripline, $R_i$ is the resistance of the constituent layer, $P_{\text{RF}}$ = 0.631 W is the power of the microwave generator and $l_{\text{strip}}$ = 54.64 mm is the length of the stripline.

When calculating Oersted fields for spin-orbit torque effective fields, both equations C.1 and C.2 are used. For the majority $H_Y^{OF}$ field generated by the Pt underlayer directly in contact with the FM layer, equation C.1 is deployed. For the buffered samples, an additional $H_Y^{OF}$ is calculated with equation C.2 added to the component from the Pt layer.

# Appendix D

To determine the presence of the magnetic proximity effect in the (un)buffered Pt|CoFeB bilayers, we measured a Pt(1.6)|CoFeB(5) with and without a spin-transparent 5 nm Cu spacer layer in between the HM and FM for comparison. Figure D.1 shows the $V_{\text{Diode}}$ for both devices.

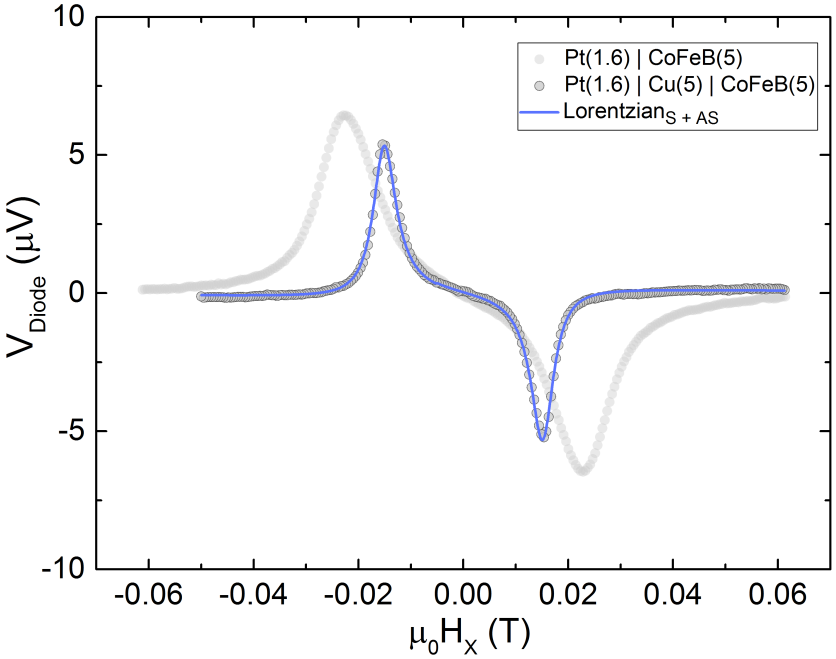


Figure D.1 Experimental spin pumping data of the raw diode voltage measured on a Pt(1.6)|Cu(5)|CoFeB(5) sample fit to a pair of symmetric and antisymmetric Lorentzian curves with equation 5.15. The raw diode voltage of a Pt(1.6)| CoFeB(5), is displayed for comparative purposes.

The resulting extracted symmetric voltages are $V_S$ = 6.47 μV and 5.43 μV in devices without and with the 5 nm Cu spacer layer, respectively. The difference in $V_S$ may be attributed to an imperfect spin-transparent Cu layer. Moreover, the comparative nature of this study between (un)buffered series should nullify any effects consistent across the series.